ANISOTROPIC CHARACTERIZATION OF ASPHALT MIXTURES IN COMPRESSION

A Dissertation

by

YUQING ZHANG

Submitted to the Office of Graduate Studies of
Texas A&M University
in partial fulfillment of the requirements for the degree of

DOCTOR OF PHILOSOPHY

Approved by:

Chair of Committee,	Robert L. Lytton
Committee Members,	Dallas N. Little
	Zachary C. Grasley
	Anastasia H. Muliana
	Rong Luo
Head of Department,	John Niedzwecki

December 2012

Major Subject: Civil Engineering

ABSTRACT

Rutting is one of the major distresses in asphalt pavements and it increases road roughness and traps water, which leads to wet-weather accidents due to the loss of tire-pavement friction and hydroplaning. The fundamental mechanisms of rutting have not been well addressed because of the complexity of asphalt mixtures. A comprehensive characterization of the asphalt mixtures in compression was accomplished by mechanistically modeling the inherent anisotropy, viscoelasticity, viscoplasticity and viscofracture of the material.

The inherent anisotropy due to preferentially oriented aggregates was characterized by a microstructural parameter (i.e., modified vector magnitudes) which could be rapidly and accurately measured by lateral surface scanning tests and physically related to anisotropic modulus ratio. The anisotropic viscoelasticity was represented by complex moduli and Poisson's ratios in separate orthogonal directions that were determined by an efficient testing protocol. Master curve models were proposed for the magnitude and phase angle of these complex variables. The viscoplasticity were intensively modeled by an anisotropic viscoplastic model which incorporated 1) modified effective stresses to account for the inherent and stress-induced anisotropy; 2) a new model to provide a smooth and convex yield surface and address the material cohesion and internal friction; 3) a non-associated flow rule to consider the volumetric dilation; and 4) a temperature and strain rate dependent strain hardening function. The viscofracture resulting from the crack growth in compression led to the stress-induced anisotropy and was characterized by anisotropic damage densities, the evolution of which was modeled by the anisotropic pseudo J-integral Paris' laws.

Results indicated that the undamaged asphalt mixtures were inherently anisotropic and had vertical to horizontal modulus ratios from 1.2 to 2.0 corresponding to the modified vector

magnitudes from 0.2 and 0.5. The rutting would be underestimated without including the inherent anisotropy in the constitutive modeling. Viscoelastic and viscoplastic deformation developed simultaneously while the viscofracture deformation occurred only during the tertiary flow, which was signaled by the increase of phase angle. Axial and radial strain decomposition methods were proposed to efficiently separate the viscoplasticity and viscofracture from the viscoelasticity. Rutting was accelerated by the occurrence of cracks in tertiary flow. The asphalt mixture had a brittle (splitting cracks) or ductile (diagonal cracks) fracture when the air void content was 4% and 7%, respecitvely. The testing protocol that produced the material properties is efficient and can be completed in one day with simple and affordable testing equipment. The developed constitutive models can be effectively implemented for the prediction of the rutting in asphalt pavements under varieties of traffic, structural, and environmental conditions.

DEDICATION

To my parents and my wife for their love, patience and encouragement

ACKNOWLEDGEMENTS

I would like to express my deepest gratitude to my advisor and committee chair, Dr. Robert L. Lytton, for his constant support, guidance, knowledge, and encouragement on both academic and personal sides. Dr. Lytton is a great professor and I could not finish the research without his help. I am so lucky and proud to be one of his students.

My sincere appreciation and thanks go to Dr. Dallas N. Little for his continuous support, motivation and valuable insights throughout the whole project. I also would like to thank Dr. Zachary C. Grasley and Dr. Anastasia H. Muliana for serving in my committee and providing me with fruitful comments on my work. Special thanks to Dr. Rong Luo for not only being a specialist on my committee, but sharing her knowledge, friendship and encouragement with me.

My appreciation is extended to Mr. Jeff Perry for his great help on my tests. I also want to thank my colleagues: Xue Luo, Yasser Koohi, Yunwei Tong, Hakan Sahin, Grover Allen, Litao Liu, Fan Yin, Fan Gu, Meng Ling and many others. I could never forget to thank my best friends: Le Zhang, Yue Liu and Yang Liu. Their friendship was one of the most valuable gifts I have received in College Station.

I would like to acknowledge the financial support provided by the Federal Highway Administration (FHWA) and the Western Research Institute (WRI) through the Asphalt Research Consortium (ARC) that makes this research possible.

NOMENCLATURE

AASHTO	American Association of State Highway and Transportation Officials
ASCE	American Society of Civil Engineers
ASTM	American Society for Testing and Materials
D-P	Drucker-Prager (yield surface model)
DBN	Di Benedetto (yield surface model)
DDM	Destructive Dynamic Modulus Test
DPI	Dots Per Inch
DPFSE	Dissipated Pseudo Fracture Strain Energy
DPPSE	Dissipated Pseudo Plastic Strain Energy
DPSE	Dissipated Pseudo Strain Energy
ED-P	Extended Drucker-Prager (yield surface model)
EM-N	Extended Matsuoka-Nakai (yield surface model)
FWD	Falling Weight Deflectometer
GPR	Ground Penetrating Radar
HISS	Hierarchical Single-Surface (yield surface model)
IDT	Indirect Tensile Test
LMLC	Lab-Mixed-Lab-Compacted
LVDT	Linear Variable Differential Transformer
M-C	Mohr-Coulomb (yield surface model)
MTS	Material Testing System
NDM	Nondestructive Dynamic Modulus Test
NHL	NuStar Asphalt and Texas Hanson Limestone Mixture

PG	Performance Grading
RaTT	Rapid Triaxial Test
TCS	Triaxial Compressive Strength Test
TRB	Transportation Research Board
TxDOT	Texas Department of Transportation
UCC	Uniaxial Compressive Creep Test
UCS	Uniaxial Compressive Strength Test
UTM	Universal Testing Machine
VHL	Valero Asphalt and Texas Hanson Limestone Mixture
X-ray CT	X-ray Computed Tomography
ZLL	Zhang-Luo-Lytton (yield surface model)

TABLE OF CONTENTS

Page

LIST OF FIGURES

Page

LIST OF TABLES

Page

CHAPTER I

INTRODUCTION

BACKGROUND

An asphalt mixture exhibits very complicated behaviors when it is subjected to a compressive load. When the compressive load is sufficiently small, e.g., the total strain is controlled to less than 150 microstrains in compression (Levenberg and Uzan 2004), damages such as permanent deformation and cracking may be avoided and the asphalt mixture behaves as an anisotropic viscoelastic solid. As the compressive load increases, the stress and strain have a nonlinear relationship which may be caused by not only the material relaxation but also the stress-induced damages including viscoplastic deformation and viscofracture cracking (i.e., a time-dependent fracture).

Permanent deformation (rutting) and fracture (cracking) are two major distresses of asphalt pavements. Rutting appears as a surface depression in the wheel paths, one primary source of which is the accumulation of the plastic and viscoplastic deformation in asphalt layers due to the inability to withstand the stress caused by traffic loading (Lytton et al. 1993). Rutting traps water and leads to wet-weather accidents due to loss of tire-pavement friction and hydroplaning. With the repeated applications of the traffic loads, energy is accumulated in the asphalt mixture due to the work done by the traffic loads during the primary and secondary stages of the rutting. The accumulated energy will initiate and propagate cracks in the tertiary stage of rutting and result in tertiary flow (Lytton 2000; Zhou and Scullion 2002). The cracking accompanying rutting in return accelerates the development of permanent deformation and eventually reduces the service life of the in-service pavements. Therefore, fundamentally mechanistic modeling and laboratory evaluation of the permanent deformation and the

associated viscofracture for the asphalt mixtures can contribute significantly to the design and analysis of the asphalt pavements for the purpose of better field performance and longer service life.

The permanent deformation and the associated fracture of asphalt mixtures primarily results from the irrecoverable viscoplastic deformation and damages which has been investigated carefully using continuum mechanics (Sides et al. 1985; Uzan 1996; Levenberg and Uzan 2004). Sousa et al. (1993; 1994) proposed a nonlinear viscoelastic damage model to predict the permanent deformation of the asphalt mixture which included a volumetric component accounting for densification of air voids and a deviatoric component responsible for a softening or hardening process. Florea (1994b; 1994a) developed an associated and a non-associated viscoplastic model to describe the mechanical properties of the asphalt mixtures. Schapery (1997; 1999) employed thermodynamic principles incorporated with internal state variables to develop the constitutive relations that account for the effects of viscoelasticity, viscoplasticity, growing damage and aging. Based on Schapery's viscoplastic continuum model, Gibson et al. (2003) investigated the properties of asphalt mixtures in an unconfined compressive state and Chehab et al. (2003) predicted the responses of asphalt mixtures in a uniaxial tensile condition. Masad and some other researchers (Huang et al. 2007; Saadeh et al. 2007; Masad et al. 2008b; Darabi et al. 2011) employed Schapery's nonlinear viscoelastic model (Schapery 1969) and the Perzyna's viscoplastic model (Perzyna 1971) associated with a damage density function to characterize the properties of the asphalt mixtures and yielded a good agreement between the laboratory testing results and the finite element simulations.

PROBLEM STATEMENT

Characterizations of an asphalt mixture in compression include two parts namely the nondestructive characterization and the destructive characterization of the material properties. The nondestructive properties of the asphalt mixtures in compression include the anisotropic viscoelasticity and the inherent anisotropy that is caused by the preferential orientation of aggregates. The destructive properties of asphalt mixtures consist of the anisotropic viscoplasticity and the anisotropic viscofracture that is caused by the different crack areas projected in different directions. The following subsections briefly summarize the problems existing in the literature on the aforementioned four topics that are viscoelasticity, anisotropy, viscoplasticity and viscofracture. Details of those problems are addressed in the chapter corresponding to each topic.

Problems of Anisotropic Viscoelastic Characterization

Asphalt mixtures are typical time and temperature dependent materials, the nondestructive properties of which are normally characterized with creep compliance, relaxation modulus, dynamic modulus and phase angle according to viscoelastic theory. These nondestructive material properties provide a basis for quantifying how far the damages such as plasticity and fracture depart from the undamaged state. Thus a comprehensive description and an accurate laboratory measurement for these nondestructive material properties are strongly needed; however, some problems that appear in the existing literature are summarized as follows:

a) The compressive and tensile viscoelastic properties of the undamaged asphalt mixtures are not separately characterized even though they are significantly distinct in terms of the magnitude, phase angle, and anisotropy.

b) The master curve models for the magnitude of the dynamic modulus are well addressed in the literature. Nevertheless, no perfect models are available to construct the master curve for the phase angle of the dynamic modulus as well as the master curves for the magnitude and phase angle of complex Poisson's ratio.

c) Rapid and efficient testing methods are needed to accurately determine the anisotropic complex modulus and the anisotropic complex Poisson's ratios when asphalt mixtures are in compression.

Problems of Inherent Anisotropic Characterization

The anisotropy of an asphalt mixture is defined as a difference in physical properties, such as modulus and Poisson's ratio, when the asphalt mixture is measured in different directions. According to the origins of anisotropy, granular materials, such as soils, aggregate base and asphalt mixtures, consist of two types of anisotropy: i) inherent anisotropy and ii) stress-induced anisotropy (Adu-Osei 2000; Masad et al. 2002; Kim et al. 2005; Underwood et al. 2005). The inherent anisotropy of the asphalt mixture is attributed to the preferential orientation of aggregates along the horizontal direction that is perpendicular to the compaction direction. The inherent anisotropy of the asphalt mixture has been demonstrated to be significant using laboratory and field tests. Taking into account the inherent anisotropy in the continuum damage models produced more accurate predictions of pavement rutting. However, several problems occur in the characterization of the inherent anisotropy for the asphalt mixtures.

(a) Only the inclination of coarse aggregates was considered for the characterization of the inherent anisotropy of asphalt mixtures, which, however, is properly attributed to the inclination, size, and sphericity of both coarse and fine aggregates.

(b) A nondestructive imaging system with high resolution is required to obtain the aggregate properties of the asphalt mixtures for the purpose of determining the inherent anisotropy.

(c) A constitutive method is needed to incorporate the inherent anisotropy into the continuum mechanistic modeling of the asphalt mixtures so that the inherent anisotropy is accounted for in the viscoplastic and viscofracture characterization.

Problems of Anisotropic Viscoplastic Characterization

The permanent deformation is the major damage when asphalt mixtures are in compression. The mechanisms of the permanent deformation have been investigated for decades using multiple theories and methods including the phenomenological empirical methods (Perl et al. 1983; Mahboub 1990; Uzan 1996; Qi and Witczak 1998) and the mechanistic theories that consist of viscoelastic damage models (Sousa et al. 1993; Ramsamooj and Ramadan 1999) and elasto-viscoplastic damage models (Chehab et al. 2003; Schwartz et al. 2004; Nguyen et al. 2007; Darabi et al. 2011). The models that use mechanistic constitutive equations to model the material characteristics utilize the fundamental engineering properties of materials as input in the models, which can be applied to different types of materials in different pavement structures, different traffic and environmental conditions. Thus the mechanistic models, especially the viscoelastic-viscoplastic-damage models are becoming more and more appealing to researchers as well as the civil engineers. However, these mechanistic models are still far away from being widely used because of some problems in the models themselves and the difficulties in acquiring the fundamental engineering material properties required by the models. Specifically, the problems associated with viscoplastic characterization include:

a) The anisotropy including the inherent anisotropy and the stress-induced anisotropy must be accounted for in the constitutive modeling of the asphalt mixtures. Otherwise, the

permanent deformation and fatigue cracking will be underestimated if assuming that asphalt mixtures in compression are isotropic.

b) A more comprehensive constitutive model is needed to characterize a variety of the viscoplastic properties of the asphalt mixtures including the hydrostatic stress-dependent yield surface that satisfies the requirements of smoothness and convexity, viscoplastic potential based on a non-associated flow rule, viscoplastic strain hardening and the temperature and strain rate dependence.

c) A systematic testing protocol and analyzing formulations are required to rapidly and accurately determine the parameters of the constitutive model and relate those model parameters to the measurable and understandable material engineering properties.

Problems of Anisotropic Viscofracture Characterization

The asphalt mixture experiences the primary, secondary and tertiary deformation stages when it is subjected to a destructive load in compression. The permanent deformation accumulates during all of the three stages while the microcracks are initiated during the secondary stage and grow into macrocracks in the tertiary stage. The increase of the crack size that mainly occurs in the tertiary stage leads to the loss of the intact material area, which is the major reason for the degradation of modulus. The area projection of the cracks differs in the vertical direction and in the horizontal direction, which results in different modulus degradation and produces the stress-induced anisotropy in the asphalt mixtures. The loss of intact material increases the true stress which will yield more viscoplastic deformation. The problems associated with the viscofracture characterization are:

a) Very few efforts are made in the investigation of the anisotropic viscofracture in the tertiary deformation and the mechanisms are not clearly revealed for the tertiary flow,

which in fact is not a plastic flow but the extra permanent strain that is caused by the formation and growth of cracks.

b) The anisotropic viscofracture that happens in the tertiary stage has a significant contribution to permanent deformation and has not been well considered in the constitutive modeling of the asphalt mixture.

c) The viscofracture strain that is caused by the crack growth in the tertiary stage needs to be separated from the viscoelastic strain and the viscoplastic strain for the purpose of an accurate characterization of the viscofracture and its evolution.

RESEARCH OBJECTIVES

The general objective of this research is to provide the engineers and researchers with fundamental mechanical models and efficient, reliable, and user-friendly testing methods to comprehensively characterize the engineered properties of the asphalt mixtures in compression and promote the understanding to the road performance of the materials. The problems mentioned in the section of problem statement will be resolved in this dissertation and specifically, the research objectives include:

a) Develop an efficient testing protocol working on a single asphalt mixture to determine the anisotropic complex modulus and complex Poisson's ratio and formulate rational master curve models for the magnitude and phase angle of the complex variables;

b) Propose a reasonable parameter and the corresponding testing method to characterize the inherent anisotropy of the asphalt mixture due to the preferential orientation of aggregates in the mixture and relate the proposed parameter to the physical properties.

c) Model the constitutive behaviors of the asphalt mixtures using a comprehensive equation which is capable of accounting for the viscoelasticity, viscoplasticity, viscofracture and the anisotropy of the materials.

d) Develop a systematic testing protocol and analyzing formulations to rapidly and accurately determine the parameters of the constitutive model and relate the parameters of the constitutive model to the measurable and understandable engineering material properties.

DISSERTATION OUTLINE

This dissertation combines four journal papers that have been published or in press and one paper that has been submitted for review. Some of the contents in this dissertation are slightly modified from the papers to avoid unnecessary repetitions of information and to improve the article flow. More continuation studies to those papers are also included in this dissertation to present a complete characterization of the asphalt mixture in compression. This dissertation is written according to the format of the ASCE's *Journal of Materials in Civil Engineering*, as well as the guidelines provided in the Texas A&M University Thesis Manual. The sign conventions used in this dissertation consider the compressive and extensive stresses and strains to be positive and the tensile stresses and strains to be negative. The organizations of this dissertation are as follows:

Chapter I is an introduction which contains background, problem statement, research objectives and dissertation outline.

Chapter II is a paper published in the ASCE's *Journal of Transportation Engineering* (Zhang et al. 2012a). This chapter presents the characterization of the anisotropic viscoelasticity of the asphalt mixtures, which includes the development of the master curve models, design of

the testing protocols and the anisotropic analysis of the complex variables of the asphalt mixtures.

Chapter III is a paper published in the ASCE's *Journal of Materials in Civil Engineering* (Zhang et al. 2011). This chapter presents a formulation of the modified vector magnitude for the characterization of the inherent anisotropy, a testing method for the determination of the aggregate properties as well as the construction and the verification of the relationship between the anisotropic parameter and the anisotropic modulus ratio.

Chapter IV is a paper published in the ASCE's *Journal of Materials in Civil Engineering* (Zhang et al. 2012b). This chapter presents a new method to efficiently and accurately perform the strain decomposition on the total strain measured in a destructive test on asphalt mixture in compression. The viscoplastic strain and the viscofracture strain are separated from the viscoelastic strain and then implemented in the damage characterizations in the following chapters.

Chapter V presents a comprehensive viscoplastic yield surface model for the asphalt mixture in compression. The model is capable of completely characterizing a variety of the viscoplastic yielding properties of the asphalt mixture. The corresponding parameter determining methods are also presented and some of the model parameters are related to the engineered material properties. Part of this chapter related to the temperature and strain rate dependent yield surface was summarized in a paper that had been submitted for presentation in the forthcoming 92nd TRB meeting and publication in the *Transportation Research Record: Journal of the Transportation Research Board*.

Chapter VI presents a comprehensive anisotropic viscoplastic constitutive modeling of the asphalt mixture. A modified effective stress is defined and used in the formulation of the extended Perzyna-type viscoplastic model. A generalized yield surface model, non-associated

viscoplastic flow rule and a temperature and strain rate dependent strain hardening function are employed in the viscoplastic modeling. Testing methods and theoretical relationships are provided to determine the model parameters. The effect of the anisotropy on the permanent deformation of the asphalt mixture is discussed based on the model and the testing results.

Chapter VII presents the characterization of the anisotropic viscofracture of the asphalt mixture in compression. The anisotropic (axial and radial) damage densities are determined using dissipated pseudo strain energy (DPSE) balance equations and geometric method. Anisotropic pseudo J-integral Paris' laws are proposed to model the evolution of the viscofracture. Part of this chapter associated with the axial viscofracture characterization was summarized in a paper that had been accepted for publication on the ASCE's *Journal of Materials in Civil Engineering* (Zhang et al. 2012c).

Chapter VIII presents overall summaries and conclusions of the dissertation. Recommendations for future studies are also suggested in this chapter.

CHAPTER II

ANISOTROPIC VISCOELASTICITY OF UNDAMAGED ASPHALT MIXTURES[*]

OVERVIEW

A test protocol and a data analysis method are developed in this chapter based on anisotropic linear viscoelastic theory to characterize the anisotropic viscoelastic properties of undamaged asphalt mixtures. The test protocol includes three nondestructive tests: 1) uniaxial compressive creep test, 2) indirect tensile creep test, and 3) the uniaxial tensile creep test. All three tests are conducted on asphalt mixtures at three temperatures (10, 20 and 30 ℃) to determine the tensile and compressive properties at each temperature and then to construct the master curve of each property. The determined properties include: magnitude and phase angle of the compressive complex modulus and Poisson's Ratio in the vertical direction and in the horizontal plane, respectively, magnitude and phase angle of the tensile complex modulus.

The test results indicate that all tested asphalt mixtures have significantly different tensile properties from compressive properties. The peak value of the master curve of the tensile complex modulus phase angle is within a range from 65 to 85 degrees while the peak value of the compressive moduli phase angle in both directions ranges from 35 to 55 degrees. In addition, the undamaged asphalt mixtures exhibit distinctively anisotropic properties in compression. The magnitude of the compressive modulus in the vertical direction is approximately 1.2 ~ 2 times of the magnitude of the compressive modulus in the horizontal plane. Dynamic modulus tests are

[*]Reprinted with permission from ASCE: "Anisotropic Viscoelastic Properties of Undamaged Asphalt Mixtures." by Yuqing Zhang, Rong Luo and Robert L. Lytton, 2012, *Journal of Transportation Engineering*, 138(1), 75-89. Copyright [2012], ASCE.

performed to verify the results of the proposed test protocol. The test results from the proposed test protocol match well with those from the dynamic tests.

INTRODUCTION

An asphalt mixture that performs well in service must be designed to resist the damage done by both traffic and weather. The damage takes many forms such as fatigue, rutting, aging, and moisture damage among others. In addition, the successfully designed mixture has the ability to heal some of the damage that occurs. A careful evaluation of the damage resistance and healing properties of an asphalt mixture must be done in the laboratory prior to its being constructed as a pavement surface. Damage to such a mixture is evaluated as a departure from "undamaged" properties. Thus, an important aspect of all successful asphalt mixture design is in determining the undamaged properties of the mixture to use as a "bench mark" for all damage that is done by subsequent testing.

This chapter presents a rapid and efficient method of evaluating the compressive properties of undamaged asphalt mixtures. In previous related work, the tensile viscoelastic properties of an undamaged asphalt mixture were carefully studied and a novel approach was developed to accurately and quickly determine the master curve of the complex modulus and the phase angle of the undamaged asphalt mixture in tension (Luo and Lytton 2010). This chapter presents a continuation of that work, which develops a comprehensive method to characterize both viscoelastic isotropic properties of undamaged asphalt mixtures in tension and viscoelastic anisotropic properties of the undamaged asphalt mixtures in compression.

The reason for characterizing tensile properties and compressive properties separately is that the tensile properties of an undamaged asphalt mixture are significantly different from the compressive properties of the same undamaged asphalt mixture. When an asphalt mixture is

subjected to a nondestructive tensile load, it has been found to be approximately isotropic (Underwood et al. 2005). In other words, the tensile properties of asphalt mixtures are approximately independent of direction. This is reasonable because the asphalt binder or mastic, which is recognized as an isotropic material, plays a key role when the asphalt mixture is under a tensile load. In contrast, when the asphalt mixture is in compression, it has been experimentally proved to be significantly anisotropic.

Anisotropy is the property of being directionally dependent. The anisotropy of an asphalt mixture can be defined as the difference in physical properties, such as modulus and Poisson's ratio, when the asphalt mixture is loaded in different directions. For example, the modulus in the vertical direction (compaction direction) was found to be 1.26 times larger than that in the horizontal plane perpendicular to the compaction direction based on the back-calculation of the modulus of the asphalt layer in the field (Oh et al. 2006). Motola and Uzan (2007) conducted dynamic modulus tests on 8 field specimens and found the dynamic modulus in the vertical direction could be as large as 1.5 times the dynamic modulus in the horizontal plane. They also found that, at a 5% significance level, the dynamic moduli statistically had the same mean value in the two directions in the horizontal plane. This finding suggests that the asphalt mixture is a transversely isotropic material whose physical properties are symmetric about the vertical direction that is normal to the horizontal plane of isotropy.

The inherent anisotropy of an undamaged asphalt mixture was found to be mainly attributed to the preferential orientation of aggregates (Masad et al. 2002; Masad et al. 2005). Figure 2-1 illustrates the preferential orientation of aggregates in a field core from an asphalt pavement. The top view of the field core specimen shows a more circular cutting face of the aggregates, while the side view shows a more flat cutting face. This fact demonstrates that the aggregates tend to "lay down" during compaction and that the long dimension of the aggregates

has a preferential direction in the horizontal plane. As a result, the properties of the asphalt mixture in the vertical direction are different from those in the horizontal plane.

(a) Top View

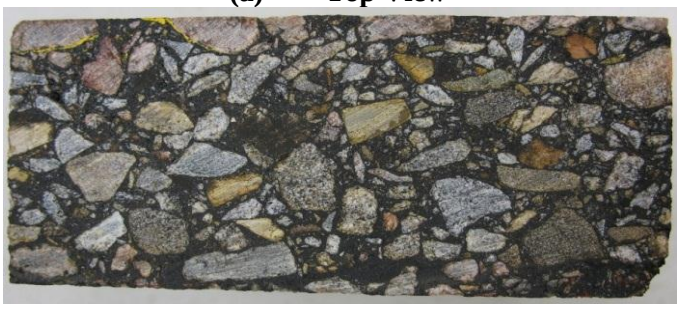

(b) Side View

Figure 2-1 Cutting faces of a field cored asphalt mixture sample: (a) Top view and (b) Side view

Research efforts have been documented in the literature on investigating the anisotropic properties of the asphalt mixture under compressive loading. One approach was to core cylindrical specimens compacted by a gyratory compactor in the vertical and horizontal directions, respectively, and then to test the specimens separately to obtain the properties in the vertical direction and in the horizontal direction (Mamlouk et al. 2002; Masad et al. 2005;

Underwood et al. 2005; Wagoner and Braham 2008). Using this approach to obtain the anisotropic properties may introduce significant sample to sample variability. Another documented approach was to fabricate a cubic specimen and to test it in different directions (Wang et al. 2005). This approach successfully eliminates the sample to sample errors but a complicated servo-controlled true triaxial test device was required to conduct the true triaxial tests on the cubic specimens.

For the purpose of using more accessible test equipment to efficiently measure the anisotropic properties of an asphalt mixture without introducing sample to sample errors, this chapter proposes three nondestructive tests on a single asphalt mixture specimen to the obtain the complex modulus and complex Poisson's ratio in the vertical direction and in the horizontal plane. In order to obtain the properties of the undamaged asphalt mixture, all tests should be conducted in the small strain domain with an empirical endurance limit of approximately 100 microstrains in tension and 150 microstrains in compression (Levenberg and Uzan 2004). As long as the asphalt mixture is tested under the endurance limit, the asphalt mixture can be characterized as a linearly viscoelastic material. In this study, the strains of the tested asphalt mixture specimen are carefully controlled under the endurance limits in all tests. At the end of all tests, additional dynamic tests are conducted on the same specimens to confirm that no damage is introduced to the specimens by verifying that the magnitude and phase angle of the complex moduli do not change.

This chapter is organized as follows. The next section details the theoretical formulations of the anisotropic viscoelastic properties of the asphalt mixture. Then the configurations and procedures of the three tests are developed based on the theoretical formulations. The following section presents the analysis of the test data and the determination of the magnitude and phase angle of the complex moduli and complex Poisson's ratio at each

test temperature. In the succeeding section, master curves of the magnitudes and phase angles are constructed using the time-temperature superposition principle and are then verified using the dynamic test. The final section concludes the main results of this chapter.

ANISOTROPIC VISCOELASTIC FORMULATIONS OF ASPHALT MIXTURES

The most general anisotropic form of linearly elastic constitutive relations is given by the generalized Hooke's law (Ding et al. 2006):

$$\varepsilon_{ij} = S_{ijkl}\sigma_{kl} \qquad i, j, k, l = 1, 2, 3 \tag{2-1}$$

where σ_{ij} and ε_{ij} are the linear stress and strain tensors and S_{ijkl} is a compliance tensor. For a transversely isotropic material, the material properties are symmetric with respect to an axis which is normal to an isotropic plane. As shown in Figure 2-2, the symmetric axis is the vertical axis 01, the anisotropic plane is vertical plane 012 and 013, and the isotropic plane is the horizontal plane 023 in which the properties of materials are identical in all horizontal directions. For an isotropic material, the material properties are the same in all directions.

When an asphalt mixture is under compressive loading, the material properties are symmetric about the compaction direction that is the vertical axis, which is perpendicular to the horizontal plane that is the plane of isotropy. In other words, the properties of the asphalt mixture in the horizontal plane are the same in all directions within the horizontal plane but different from the properties in the vertical direction. Using the coordinates in Figure 2-2, the constitutive relations for a transversely isotropic and linearly elastic material can be formulated as (Christensen 2005):

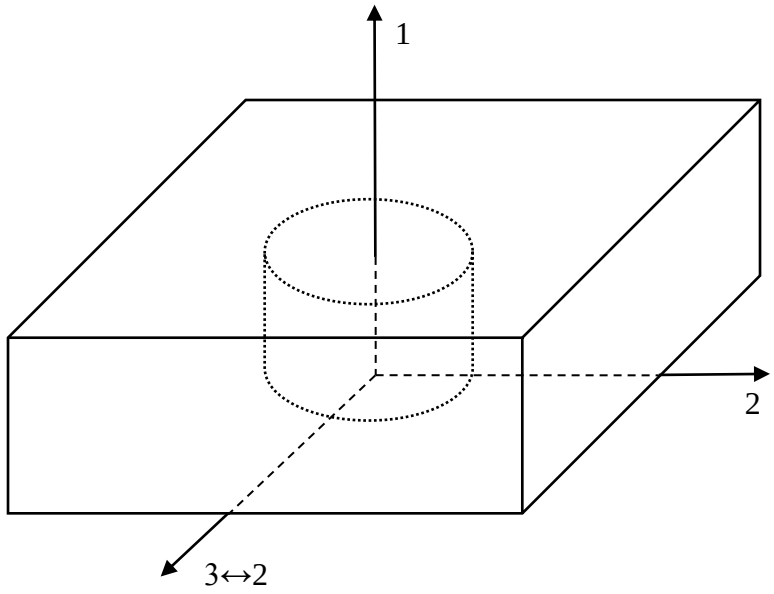

Figure 2-2 Coordinate system of transversely isotropic material

$$\begin{bmatrix} \varepsilon_{11} \\ \varepsilon_{22} \\ \varepsilon_{33} \\ \varepsilon_{12} \\ \varepsilon_{23} \\ \varepsilon_{31} \end{bmatrix} = \begin{bmatrix} \frac{1}{E_{11}} & -\frac{\nu_{21}}{E_{22}} & -\frac{\nu_{21}}{E_{22}} & 0 & 0 & 0 \\ -\frac{\nu_{12}}{E_{11}} & \frac{1}{E_{22}} & -\frac{\nu_{23}}{E_{22}} & 0 & 0 & 0 \\ -\frac{\nu_{12}}{E_{11}} & -\frac{\nu_{23}}{E_{22}} & \frac{1}{E_{33}} & 0 & 0 & 0 \\ 0 & 0 & 0 & \frac{1}{G_{12}} & 0 & 0 \\ 0 & 0 & 0 & 0 & \frac{2(1+\nu_{23})}{E_{22}} & 0 \\ 0 & 0 & 0 & 0 & 0 & \frac{1}{G_{12}} \end{bmatrix} \begin{bmatrix} \sigma_{11} \\ \sigma_{22} \\ \sigma_{33} \\ \sigma_{12} \\ \sigma_{23} \\ \sigma_{31} \end{bmatrix} \tag{2-2}$$

where,

$$\frac{\nu_{12}}{E_{11}} = \frac{\nu_{21}}{E_{22}} \tag{2-3}$$

and ε_{ij} is strain, σ_{ij} is stress, E_{ij} is Young's modulus, v_{ij} is Poisson's ratio, and G_{ij} is shear modulus; in the subscript *ij*, the first index *i* refers to the coordinate of imposed stress or strain and the second index *j* refers to the response direction. Equation 2-2 has five independent constants: E_{11}, E_{22}, v_{12}, v_{23}, and G_{12}, four of which (except G_{12}) can be used to characterize the anisotropy of an asphalt mixture if assuming that the asphalt mixture is linearly elastic. Thus, substituting Equation 2-3 into Equation 2-2 yields:

$$\begin{bmatrix} \varepsilon_{11} \\ \varepsilon_{22} \\ \varepsilon_{33} \end{bmatrix} = \begin{bmatrix} \frac{1}{E_{11}} & -\frac{\nu_{21}}{E_{22}} & -\frac{\nu_{21}}{E_{22}} \\ -\frac{\nu_{12}}{E_{11}} & \frac{1}{E_{22}} & -\frac{\nu_{23}}{E_{22}} \\ -\frac{\nu_{12}}{E_{11}} & -\frac{\nu_{23}}{E_{22}} & \frac{1}{E_{22}} \end{bmatrix} \begin{bmatrix} \sigma_{11} \\ \sigma_{22} \\ \sigma_{33} \end{bmatrix} \tag{2-4}$$

Equation 2-4 is the constitutive relation for the asphalt mixture in compression, which behaves as a transversely isotropic material. Equation 2-4 indicates that four independent constants are required for the asphalt mixture in compression, including $E_{11}^C, E_{22}^C, \nu_{12}^C, \nu_{23}^C$, in which the superscript *C* indicates the material property in compression. In contrast, because the anisotropy of the asphalt mixture is negligible in tension (Underwood et al. 2005), the asphalt mixture can be regarded as an isotropic material when it is under tensile loading. In other words, when the asphalt mixture is in tension, $E_{11} = E_{22}$ and $\nu_{12} = \nu_{23}$ in Equation 2-4. This fact indicates that only two independent constants are required for the asphalt mixture in tension, which are E_{11}^T, ν_{12}^T, where the superscript *T* indicates a property in tension. As a result, there are a total of six independent material constants for an asphalt mixture, four of which are compressive properties including $E_{11}^C, E_{22}^C, \nu_{12}^C, \nu_{23}^C$, and the other two are tensile properties including E_{11}^T, ν_{12}^T.

Equations 2-1 through 2-4 are elastic formulations for an asphalt mixture. These equations can be converted to the viscoelastic formulations in order to characterize the asphalt mixture since the properties of the asphalt mixture are frequency-dependent. The six independent constants ($E_{11}^{C}, E_{22}^{C}, \nu_{12}^{C}, \nu_{23}^{C}, E_{11}^{T}, \nu_{12}^{T}$) in the elastic formulations are no longer constants in the viscoelastic formulations. Instead, they are frequency-dependent variables as follows:

- compressive complex modulus in the vertical direction $E_{11}^{C*}(\omega)$;
- compressive complex Poisson's ratio in the vertical plane $\nu_{12}^{C*}(\omega)$;
- compressive complex modulus in the horizontal plane $E_{22}^{C*}(\omega)$;
- compressive complex Poisson's ratio in the horizontal plane $\nu_{23}^{C*}(\omega)$;
- tensile complex modulus $E_{11}^{T*}(\omega)$; and
- tensile complex Poisson's ratio $\nu_{12}^{T*}(\omega)$.

where the superscript "*" indicates the complex variables, and ω is frequency in rad/sec.

If a prescribed strain ε is applied to a linearly viscoelastic material, the stress-strain relationship can be derived as (Findley et al. 1989):

$$\sigma(t) = \int_0^t E(t-\xi)\frac{\partial \varepsilon(\xi)}{\partial \xi} d\xi \tag{2-5}$$

where, $\sigma(t)$ is time-dependent stress; $E(t)$ is relaxation modulus; $\varepsilon(t)$ is prescribed strain; and ξ is a dummy variable which is less than or equal to *t*. Let $\overline{f}(s)$ or $\mathcal{L}\{f(t)\}$ denote the Laplace transform of the function $f(t)$, where *s* is the transform variable in Laplace domain and the Laplace transform is defined as:

$$\bar{f}(s) = \mathcal{L}\{f(t)\} = \int_{0^-}^{\infty} e^{-st} f(t)\, dt \tag{2-6}$$

Applying the Laplace transform to Equation 2-5 yields:

$$\bar{\sigma}(s) = s\bar{E}(s)\bar{\varepsilon}(s) \tag{2-7}$$

Equation 2-7 is the Laplace transform of the one-dimensional constitutive relation that can also be derived based on the Elastic-Viscoelastic Correspondence Principle (Findley et al. 1989). According to the correspondence principle, elastic solutions can be converted into viscoelastic solutions by taking the Laplace transform of the time-dependent stress (or force) and strain (or displacement) and taking the Carson transform, also defined as an s-multiplied Laplace transform, of the modulus and Poisson's ratio (Schapery and Park 1999; Tschoegl et al. 2002; Lakes and Wineman 2006). Specifically, $\sigma(t), \varepsilon(t), E(t)$ and $\nu(t)$ are replaced by $\bar{\sigma}(s)$, $\bar{\varepsilon}(s)$, $s\bar{E}(s)$, and $s\bar{\nu}(s)$ respectively, where the upper script bar indicates the Laplace transforms of the corresponding variables. Therefore, applying the correspondence principle to Equation 2-4 obtains:

$$\begin{bmatrix} \bar{\varepsilon}_{11}(s) \\ \bar{\varepsilon}_{22}(s) \\ \bar{\varepsilon}_{33}(s) \end{bmatrix} = \begin{bmatrix} \dfrac{1}{s\bar{E}_{11}(s)} & -\dfrac{s\bar{\nu}_{12}(s)}{s\bar{E}_{11}(s)} & -\dfrac{s\bar{\nu}_{12}(s)}{s\bar{E}_{11}(s)} \\ -\dfrac{s\bar{\nu}_{12}(s)}{s\bar{E}_{11}(s)} & \dfrac{1}{s\bar{E}_{22}(s)} & -\dfrac{s\bar{\nu}_{23}(s)}{s\bar{E}_{22}(s)} \\ -\dfrac{s\bar{\nu}_{12}(s)}{s\bar{E}_{11}(s)} & -\dfrac{s\bar{\nu}_{23}(s)}{s\bar{E}_{22}(s)} & \dfrac{1}{s\bar{E}_{22}(s)} \end{bmatrix} \begin{bmatrix} \bar{\sigma}_{11}(s) \\ \bar{\sigma}_{22}(s) \\ \bar{\sigma}_{33}(s) \end{bmatrix} \tag{2-8}$$

If a uniaxial quasi-static load is applied to the asphalt mixture along the vertical axis, $\bar{\sigma}_{11}(s) \neq 0$, $\bar{\sigma}_{22}(s) = \bar{\sigma}_{33}(s) = 0$, then solving Equation 2-8 yields:

$$\bar{E}_{11}(s) = \frac{\bar{\sigma}_{11}(s)}{s\bar{\varepsilon}_{11}(s)} \tag{2-9}$$

$$\bar{\nu}_{12}(s) = -\frac{\bar{\varepsilon}_{22}(s)}{s\bar{\varepsilon}_{11}(s)} \tag{2-10}$$

where Equation 2-9 is consistent with Equation 2-7. Applying the inverse Laplace transform, which is denoted by $\mathcal{L}^{-1}\{f(t)\}$, to Equation 2-9 and Equation 2-10, the relaxation modulus and Poisson's ratio are determined as:

$$E_{11}(t) = \mathcal{L}^{-1}\left(\frac{\bar{\sigma}_{11}(s)}{s\bar{\varepsilon}_{11}(s)}\right) \tag{2-11}$$

$$\nu_{12}(t) = \mathcal{L}^{-1}\left(-\frac{\bar{\varepsilon}_{22}(s)}{s\bar{\varepsilon}_{11}(s)}\right) \tag{2-12}$$

In practice, the load applied on the pavement is not a quasi-static load, but a dynamic load such as a moving traffic load. Therefore, it is convenient to use oscillatory rather than static loading. If the input is an axial oscillatory strain with a sinusoidal form (Christensen 2003):

$$\varepsilon_{11}^{*}(t) = \varepsilon_1(\cos\omega t + i\sin\omega t) = \varepsilon_1 e^{i\omega t} \tag{2-13}$$

where ε_1 is axial strain amplitude, ω is the frequency of the input vibration, and $i = \sqrt{-1}$ represents the imaginary axis of the complex variable, then the stress response will lead the strain by a phase angle of φ_{E^*} which denotes the phase angle of the complex modulus of the viscoelastic pavement material. The corresponding stress can be expressed as:

$$\sigma_{11}^{*}(t) = \left|E^{*}(\omega)\right|\varepsilon_1\left[\cos\left(\omega t + \varphi_{E^*}\right) + i\sin\left(\omega t + \varphi_{E^*}\right)\right] = \left|E^{*}(\omega)\right|\varepsilon_1 e^{i\left(\omega t + \varphi_{E^*}\right)} \tag{2-14}$$

where $E^{*}(\omega)$ is the complex modulus, and $\left|E^{*}(\omega)\right|$ is the magnitude of $E^{*}(\omega)$. Dividing Equation 2-14 by Equation 2-13 yields:

$$E^{*}(\omega) = \left|E^{*}(\omega)\right|e^{i\varphi_{E^*}} = \left|E^{*}(\omega)\right|\left(\cos\varphi_{E^*} + i\sin\varphi_{E^*}\right) \tag{2-15}$$

The complex modulus in Equation 2-15 can be written as:

$$E^*(\omega) = E' + iE'' \tag{2-16}$$

where E' is the storage modulus, $= \left|E^*(\omega)\right| \cos\varphi_{E^*}$; and E'' is the loss modulus, $= \left|E^*(\omega)\right| \sin\varphi_{E^*}$. The magnitude and phase angle, $\left|E^*\right|$ and φ_{E^*} can be determined using E' and E'' as follows:

$$\left|E^*\right| = \sqrt{E'^2 + E''^2} \tag{2-17}$$

$$\varphi_{E^*} = \arctan\left(\frac{E''}{E'}\right) \tag{2-18}$$

If the horizontal strain is measured, the horizontal strain is determined as (Di Benedetto et al. 2007a):

$$\varepsilon_{22}^*(t) = \varepsilon_2\left[\cos\left(\omega t + \pi + \varphi_{\nu^*}\right) + i\sin\left(\omega t + \pi + \varphi_{\nu^*}\right)\right] = -\varepsilon_2 e^{i\left(\omega t + \varphi_{\nu^*}\right)} \tag{2-19}$$

where ε_2 is the horizontal strain amplitude, and φ_{ν^*} is the phase angle of the complex Poisson's ratio, $\nu^*(\omega)$. Using $\left|\nu^*\right|$ to denote the magnitude of $\nu^*(\omega)$, dividing Equation 2-19 by Equation 2-13 obtains:

$$\nu^*(\omega) = -\frac{\varepsilon_{22}^*}{\varepsilon_{11}^*} = \frac{\varepsilon_2}{\varepsilon_1} e^{i\varphi_{\nu^*}} = \left|\nu^*\right|\left(\cos\varphi_{\nu^*} + i\sin\varphi_{\nu^*}\right) = \nu' + i\nu'' \tag{2-20}$$

where ν' is the storage Poisson's ratio, $= \left|\nu^*\right| \cos\varphi_{\nu^*}$; and ν'' is the loss Poisson's ratio, $= \left|\nu^*\right| \sin\varphi_{\nu^*}$. Both the magnitude and phase angle of the Poisson's ratio, $\left|\nu^*\right|$ and φ_{ν^*} can be calculated as:

$$\left|\nu^*\right| = \sqrt{\nu'^2 + \nu''^2} \tag{2-21}$$

$$\varphi\left(\nu^*\right) = \arctan\left(\frac{\nu''}{\nu'}\right) \tag{2-22}$$

The complex modulus and the relaxation modulus have the following relationship (Findley et al. 1989; Park and Schapery 1999; Schapery and Park 1999):

$$E^*\left(\omega\right) = i\omega\mathcal{L}\left\{E\left(t\right)\right\}_{s=i\omega} = \left[s\bar{E}\left(s\right)\right]_{s=i\omega} \tag{2-23}$$

Similarly, the complex Poisson's ratio can be determined using the relaxation Poisson's ratio (Tschoegl et al. 2002).

$$\nu^*\left(\omega\right) = i\omega\mathcal{L}\left\{\nu\left(t\right)\right\}_{s=i\omega} = \left[s\bar{\nu}\left(s\right)\right]_{s=i\omega} \tag{2-24}$$

Equations 2-23 and 2-24 indicate that the complex modulus and complex Poisson's ratio can be determined using creep tests rather than the dynamic test. Equations 2-9 and 2-10 make it possible to use the Laplace transforms of stresses and strains to determine the Laplace transforms of the modulus and Poisson's ratio, which are then substituted into Equations 2-23 and 2-24 to calculate the complex modulus and complex Poisson's ratio. Equations 2-17, 2-18, 2-21 and 2-22 are used to calculate the magnitude and phase angle of the complex modulus and complex Poisson's ratio, respectively.

MASTER CURVE MODELS FOR COMPLEX MODULUS AND POISSON'S RATIO

To characterize the viscoelastic properties of asphalt mixtures in a wider range of temperature and frequency, it is preferred to construct the master curves for the magnitude and phase angle of the complex modulus and complex Poisson's ratio. When constructing the master curves, the undamaged asphalt mixture is considered as a linearly viscoelastic material so that the time-temperature superposition principle is employed. This principle states that the effect of temperature on the time-dependent material is equivalent to an increasing (decreasing) of the frequency at a temperature below (above) the reference temperature. Therefore, the master

curves can be constructed by conducting tests at multiple temperatures and shifting the data to the reference temperature.

The CAM model (Marasteanu and Anderson 1999) shown in Equation 2-25 has proved to be able to successfully construct the master curve of the magnitude of the complex modulus (Luo and Lytton 2010). The CAM model will be used later in this chapter to formulate the master curves of the magnitudes of both compressive complex modulus and the tensile complex modulus.

$$\left|E^*(\omega)\right| = \frac{E_g}{\left[1+\left(\frac{\omega_{cE}}{\omega \cdot 10^{C_E(T-T_r)}}\right)^{\frac{\log 2}{R_E}}\right]^{\frac{R_E}{\log 2}}} \tag{2-25}$$

where E_g = glassy modulus of the asphalt mixture, MPa; ω_{cE} = crossover frequency of the asphalt mixture for modulus, rad/sec; R_E = rheological index of the asphalt mixture for modulus; and C_E = slope of temperature shift factor for modulus. The CAM model in Equation 2-25 yields a rising "S-shaped" curve for the magnitude of the complex modulus that approaches the horizontal glassy modulus an asymptote of E_g.

It is found in this study that the magnitude of the complex Poisson's ratio decreases as the frequency increases, which will be shown in later sections. In addition, the magnitude curve has an "inverse S" shape. Therefore, a formula in the similar form of the CAM model is developed to construct the master curve of the magnitude of the complex Poisson's ratio, as shown in Equation 2-26. The model presents a falling S-shaped curve on the frequency domain and is named as the Inverse S Model.

$$\left|\nu^*(\omega)\right| = \frac{\nu_g}{\left[1+\left(\frac{\omega \cdot 10^{C_\nu (T-T_r)}}{\omega_{c\nu}}\right)^{\frac{\log 2}{R_\nu}}\right]^{\frac{R_\nu}{\log 2}}} \tag{2-26}$$

where ν_g = glassy Poisson's ratio of the asphalt mixture; $\omega_{c\nu}$ = crossover frequency of the asphalt mixture for Poisson's ratio, rad/sec; R_ν = rheological index for Poisson's ratio; and C_ν = slope of temperature shift factor for Poisson's ratio.

For the master curve of the phase angle of the complex modulus, Bahia et al. (Bahia et al. 2001; Luo and Lytton 2010) developed a model (see Equation 2-27) that presents a bell-shaped curve which is symmetric on a log-log plot of phase angle versus frequency. The Williams-Landel-Ferry (WLF) function is recommended to calculate the time-temperature shift factor for Bahia's model.

$$\varphi_E = \frac{\varphi_{mE}}{\left\{1+\left[\frac{\log\left(\frac{\omega_{mE}}{\omega \cdot 10^{\frac{C_1(T-T_r)}{C_2+(T-T_r)}}}\right)}{R_{\varphi E}}\right]^2\right\}^{\frac{m}{2}}} \tag{2-27}$$

where φ_{mE} = the maximum phase angle for modulus, degrees; ω_{mE} = the frequency when φ_{mE} occurs, rad/sec; m, $R_{\varphi E}$ = fitting parameters for modulus phase angle; T_r = reference temperature; and C_1 and C_2 = regression constants in WLF function.

It is reasonable to use a bell-shaped curve to model the master curve of the phase angle of the complex modulus because the phase angle approaches zero at a frequency of zero or infinity. In other words, a viscoelastic solid, such as the asphalt mixture, behaves as an elastic

solid at extremely low or high frequencies. However, for an asphalt mixture, the master curve of the phase angle of may not be symmetric on a log-log plot of the phase angle versus the frequency. As a result, a more general model (see Equation 2-28) is developed and is named as the β-model for the phase angle of both complex modulus and complex Poisson's ratio. This model also produces a bell-shaped curve but the curve is not constrained to be symmetric on the plot of phase angle versus the logarithm of frequency.

$$\varphi = \frac{\varphi_{max}}{Exp\left\{\left(\frac{\beta+1}{\beta}\right)\left[\left(\frac{\omega_R}{\omega\cdot\alpha_T}\right)^{\beta}-1\right]\right\}\left(\frac{\omega\cdot\alpha_T}{\omega_R}\right)^{\beta+1}} \tag{2-28}$$

where φ_{max} = the maximum phase angle, degrees; ω_R = the reference frequency where φ_{mE} occurs, rad/sec. β = fitting parameter that determine curvature of the phase angle master curve; α_T = time-temperature shift factor, e.g. $\log\alpha_T = \frac{C_1(T-T_r)}{C_2+(T-T_r)}$ if the WLF model was used.

When $\varphi_{max} > 0$, Equation 2-28 produces a bell-shaped curve function that is applicable for the master curve of the phase angle of the complex modulus; while $\varphi_{max} < 0$, Equation 2-28 yields an inverted bell-shaped curve function that is applicable for the master curve of the phase angle of the complex Poisson's ratio.

TEST CONFIGURATIONS AND DATA ANALYSIS

Based on the viscoelastic formulations detailed in the previous section, a test protocol with three test scenarios is developed to determine the six independent variables: $E_{11}^{C*}(\omega)$, $\nu_{12}^{C*}(\omega)$, $E_{22}^{C*}(\omega)$, $\nu_{23}^{C*}(\omega)$, $E_{11}^{T*}(\omega)$, and $\nu_{12}^{T*}(\omega)$. The test protocol includes the uniaxial compressive creep test, uniaxial tensile creep test and indirect tensile creep test. To investigate

the influence of mixture volumetrics and aging on the anisotropic viscoelastic characteristics, the three tests are respectively conducted on 16 asphalt mixture specimens that vary in the following conditions:

- Two types asphalt binder: labeled as AAM and AAD in the Strategic Highway Research Program (SHRP) Materials Reference Library (MRL) (Jones 1993);
- Two air void contents: 4% and 7% (variation within ±0.5%); and
- Two aging periods: unaged and continuously aged asphalt mixtures at 60 ℃ for 6 months.

Two replicate specimens are prepared for each combination of the above three varying conditions. For each specimen, the gradation for the aggregates is a Type C dense gradation specified by Texas Department of Transportation (TxDOT) (TxDOT 2004). The optimum asphalt content is calculated based on the TxDOT test procedure (TxDOT 2008). The asphalt mixture is compacted using the Superpave gyratory compactor to fabricate cylindrical specimens that are 150 mm in diameter and 175 mm in height. Then the specimens are cored to 100 mm in diameter and cut to 150 mm in height. During the three tests, the compressive creep test is firstly conducted on the specimens (150 mm in height, 100 mm in diameter), which is followed by the indirect tensile test. Then the specimens with 150 mm height are cut to 100 mm in height and the tensile creep test is finally conducted on the specimens (100mm height, 100mm diameter). The purpose of using the specimens that are 100 mm in height and 100 mm in diameter in the tensile creep test is to eliminate the effect of the non-uniform air void distribution on the tensile properties (Luo and Lytton 2010). The specimen compacted by the Superpave gyratory compactor has a higher air void content near the top and bottom of the compacted cylindrical specimen and an approximately uniform air void content in the middle part of the specimen. If a 150 mm high specimen is used in the tensile test, the non-uniform air void distribution will result

in significant variations on the tensile properties of asphalt mixtures. Although the height to diameter ratio of 2 or 1.5 is preferred in order to minimize the constraint effect of the end caps (Witczak et al. 2000), the end cap constraint effect can be neglected in the middle part of the 100 mm high specimen under a uniaxial tensile load.

All three tests on each specimen are conducted at three temperatures (10 ℃, 20 ℃ and 30 ℃) in order to construct the master curves of the magnitude and phase angle of the complex modulus and complex Poisson's ratio. Specimens are conditioned in an environmental chamber at the testing temperature for at least two hours before being tested to assure that the specimen temperature has reached equilibrium. In addition, all three tests are nondestructive so the specimens are not damaged in any one of the three tests and can be reused in succeeding destructive tests for its fatigue and healing properties. To avoid damaging the specimens, the specimen strains in each test are controlled below 100 microstrains; the corresponding applied load is determined based on testing conditions and shown in Table 2-1.

Table 2-1 Applied Load at Different Testing Conditions

Testing Methods	Mixture Type	10 ℃		20 ℃		30 ℃	
		4%	7%	4%	7%	4%	7%
Compressive and Tensile Creep (kPa)	AAD	70	50	30	20	15	10
	AAM	70	50	50	30	30	15
Indirect Tensile Creep (N)	AAD	500	500	300	300	150	150
	AAM	700	500	400	300	200	150

In each of the three creep tests, the applied load is kept constant for 60 sec. The reasons of using a 60 sec creep period include: 1) a longer time of creep would introduce damage to the

specimens; 2) the unstable transient material response at the early portion of creep usually vanishes within 1 second since the step loading reaches a constant level within this short period; 3) the unstable creep data is not used to calculate the properties; instead, testing data from 5 sec to 60 sec are stable and reliable and they are employed in the calculation; and 4) a short creep test saves testing time.

Uniaxial Compressive Creep Test

The first test in the proposed test protocol is the uniaxial compressive creep test, which determines the compressive complex modulus in the vertical direction, $E_{11}^{C*}(\omega)$, and the compressive complex Poisson's ratio in vertical plane, $\nu_{12}^{C*}(\omega)$. Both the magnitude and phase angle of $E_{11}^{C*}(\omega)$ and $\nu_{12}^{C*}(\omega)$ were calculated as functions of frequency.

The Universal Testing Machine (UTM) is employed to conduct the uniaxial compressive creep test on specimens with a height of 150 mm and a diameter of 100 mm. The test configuration is shown in Figure 2-3, in which two vertical linear variable differential transformers (LVDTs) are mounted on the middle part of the asphalt mixture specimen with a gauge length of 90 mm to measure the vertical deformation of the specimen, and one LVDT is fitted on a bracelet which surrounds the specimen to record the change of the specimen's circumference. A constant load, the magnitude of which is referred to Table 1, is applied to the specimen and held for 60 sec. The constant load is expressed as in Equation 2-29. The same test procedure is repeated three times in order to reduce the test variability. There is lengthy rest period between two repeating tests to assure the full recovery of the viscoelastic strains.

$$\sigma_{11}(t) = \sigma_0 = constant \tag{2-29}$$

The vertical strain is computed using the average vertical deformation divided by the vertical gauge length. The horizontal strain is calculated using the change of the circumference divided by the original circumference of the specimen. The vertical strains and horizontal strains of all three repeating tests are presented in Figure 2-4, in the legend of which "Horizontal 1" represents the horizontal strain of the 1st repeating test, "Vertical 2" is the vertical strain of the 2nd repeating test, and so on.

Figure 2-3 Configuration of the compressive creep test

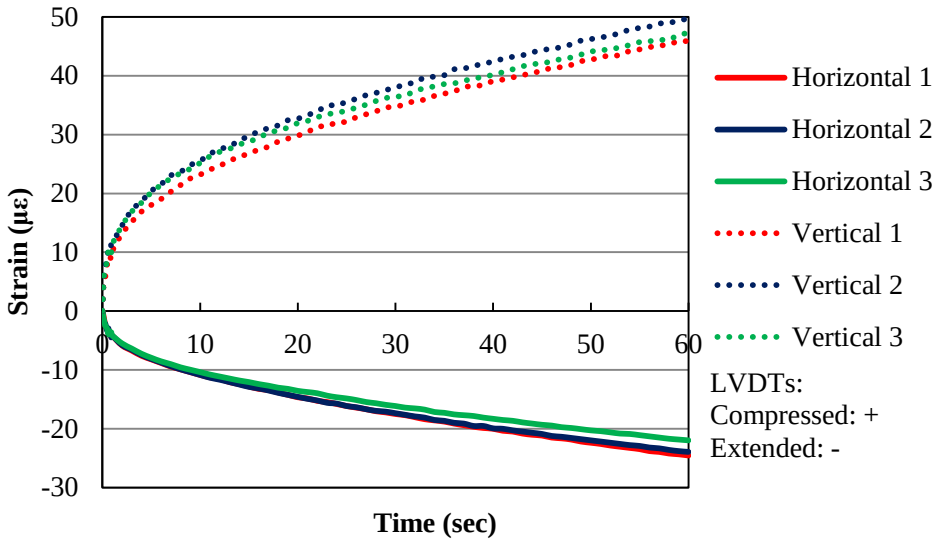

Figure 2-4 Vertical strains and horizontal strains in the uniaxial compressive creep test

As illustrated in Figure 2-4, the three curves of the vertical strain are close to each other and the three curves of the horizontal strain are also close to each other. This fact indicates that the three repeating tests produce similar results; therefore, the uniaxial compressive creep test proves to be repeatable. The average of the three vertical strain curves and the average of the three horizontal strain curves are then used for the following calculation. The average vertical strain and the average horizontal strain are firstly modeled using Equations 2-30 and 2-31, respectively:

$$\varepsilon_{11}(t) = a_1\left(1 - e^{-b_1 \cdot t}\right) + c_1 \tag{2-30}$$

$$\varepsilon_{22}(t) = a_2\left(1 - e^{-b_2 \cdot t}\right) + c_2 \tag{2-31}$$

where t is the loading time; $\sigma_{11}(t) = \sigma_0$ is the constant compressive load in the vertical direction; $\varepsilon_{11}(t)$ is the time-dependent average vertical strain; $\varepsilon_{22}(t)$ is the time-dependent average horizontal strain; e is the base of the natural logarithm; and a_1, b_1, c_1, a_2, b_2, and c_2 are

fitting parameters. By fitting the raw data to the strain models, all the fitting parameters are determined and the R-squared values of the strain models are found to be larger than 0.97, which indicates the goodness of the model fit. Applying the Laplace transform to Equations 2-29, 2-30 and 2-31 yields:

$$\bar{\sigma}_{11}(s) = \frac{\sigma_0}{s} \tag{2-32}$$

$$\bar{\varepsilon}_{11}(s) = \frac{b_1(a_1 + c_1) + c_1 s}{s(s + b_1)} \tag{2-33}$$

$$\bar{\varepsilon}_{22}(s) = \frac{b_2(a_2 + c_2) + c_2 s}{s(s + b_2)} \tag{2-34}$$

Then substituting Equations 2-32 and 2-33 into Equation 2-9 and then into Equation 2-23 obtains:

$$\begin{aligned} E_{11}^{C*}(\omega) &= \left[s\bar{E}_{11}^{C}(s) \right]_{s=i\omega} = \left[\frac{\bar{\sigma}_{11}(s)}{\bar{\varepsilon}_{11}(s)} \right]_{s=i\omega} = \left[\frac{\sigma_0(s + b_1)}{b_1(a_1 + c_1) + c_1 s} \right]_{s=i\omega} \\ &= \frac{\sigma_0 \left[b_1^2(a_1 + c_1) + \omega^2 c_1 \right]}{b_1^2(a_1 + c_1)^2 + c_1^2 \omega^2} + i \cdot \frac{\sigma_0 a_1 b_1 \omega}{b_1^2(a_1 + c_1)^2 + c_1^2 \omega^2} \end{aligned} \tag{2-35}$$

where the real part is $E_{11}^{C\prime}(\omega) = \frac{\sigma_0 \left[b_1^2(a_1 + c_1) + \omega^2 c_1 \right]}{b_1^2(a_1 + c_1)^2 + c_1^2 \omega^2}$, the imaginary part is

$E_{11}^{C\prime\prime}(\omega) = \frac{\sigma_0 a_1 b_1 \omega}{b_1^2(a_1 + c_1)^2 + c_1^2 \omega^2}$, the magnitude of $E_{11}^{C*}(\omega)$ is $\left| E_{11}^{C*} \right| = \sqrt{\left(E_{11}^{C\prime} \right)^2 + \left(E_{11}^{C\prime\prime} \right)^2}$, and the phase angle of $E_{11}^{C*}(\omega)$ is $\varphi_{E_{11}^{C*}} = \arctan\left(\frac{E_{11}^{C\prime\prime}}{E_{11}^{C\prime}} \right)$.

Similarly, $\nu_{12}^{C*}(\omega)$ is determined by substituting Equations 2-33 and 2-34 into Equation 2-10 and then into Equation 2-24:

$$\begin{aligned} \nu_{12}^{C*}(\omega) &= \left[s\bar{\nu}_{12}^{C}(s) \right]_{s=i\omega} = \left[-\frac{\bar{\varepsilon}_{22}(s)}{\bar{\varepsilon}_{11}(s)} \right]_{s=i\omega} \\ &= \left[-\frac{(s+b_1)\left[b_2(a_2+c_2)+c_2 s \right]}{(s+b_2)\left[b_1(a_1+c_1)+c_1 s \right]} \right]_{s=i\omega} \\ &= -\frac{(i\omega+b_1)\left[b_2(a_2+c_2)+c_2 i\omega \right]}{(i\omega+b_2)\left[b_1(a_1+c_1)+c_1 i\omega \right]} \end{aligned} \tag{2-36}$$

By simplifying Equation 2-36, the real part and imaginary part of $\nu_{12}^{C*}(\omega)$ can be estimated and $\nu_{12}^{C*}(\omega)$ is expressed as $\nu_{12}^{C*}(\omega) = \nu_{12}^{C\prime}(\omega) + i \cdot \nu_{12}^{C\prime\prime}(\omega)$. Then the magnitude of $\nu_{12}^{C*}(\omega)$ is calculated as $\left|\nu_{12}^{C*}\right| = \sqrt{\left(\nu_{12}^{C\prime}\right)^2 + \left(\nu_{12}^{C\prime\prime}\right)^2}$, and the phase angle of $\nu_{12}^{C*}(\omega)$ is estimated as $\varphi\left(\nu_{12}^{C*}\right) = \arctan\left(\frac{\nu_{12}^{C\prime\prime}}{\nu_{12}^{C\prime}}\right)$.

The magnitude and phase angle of both $E_{11}^{C*}(\omega)$ and $\nu_{12}^{C*}(\omega)$ are complex functions of the frequency. Since time-dependent test data are obtained from the creep test in this study, the loading time needs to be converted to the corresponding frequency so that the frequency-dependent magnitude and phase angle can be calculated. Schapery (1965) developed a straightforward method of approximation for the Laplace transform of the time function $f(t)$.

$$f(t) = \left[s\bar{f}(s) \right]_{s=\frac{1}{2t}} \tag{2-37}$$

Comparing Equations 2-23 or 2-24 with Equation 2-37 yields:

$$\omega = \frac{1}{2t} \tag{2-38}$$

Since the testing data used in the calculation are within a loading time from 5 to 60 sec, the corresponding frequency is 0.0083 rad/sec to 0.1 rad/sec based on Equation 2-38. Then the

raw stress and strain data measured at three temperatures are used to determine the frequency-dependent magnitude and phase angle of $E_{11}^{C*}(\omega)$ and $\nu_{12}^{C*}(\omega)$ using Equations 2-29 to 2-36. The master curves of $\left|E_{11}^{C*}\right|$ and $\varphi_{E_{11}^{C*}}$ are constructed at a reference temperature of 20 ℃ using the CAM model in Equation 2-25 and the β-model in Equation 2-28, respectively. Figure 2-5 shows an example of $\left|E_{11}^{C*}\right|$ determined at each temperature as well as how they shift horizontally to construct the master curve of $\left|E_{11}^{C*}\right|$ at a reference temperature of 20 ℃. It shows that the asphalt mixture has a higher value of $\left|E_{11}^{C*}\right|$ at a lower temperature or higher frequency. This finding agrees with what have been documented in the literature.

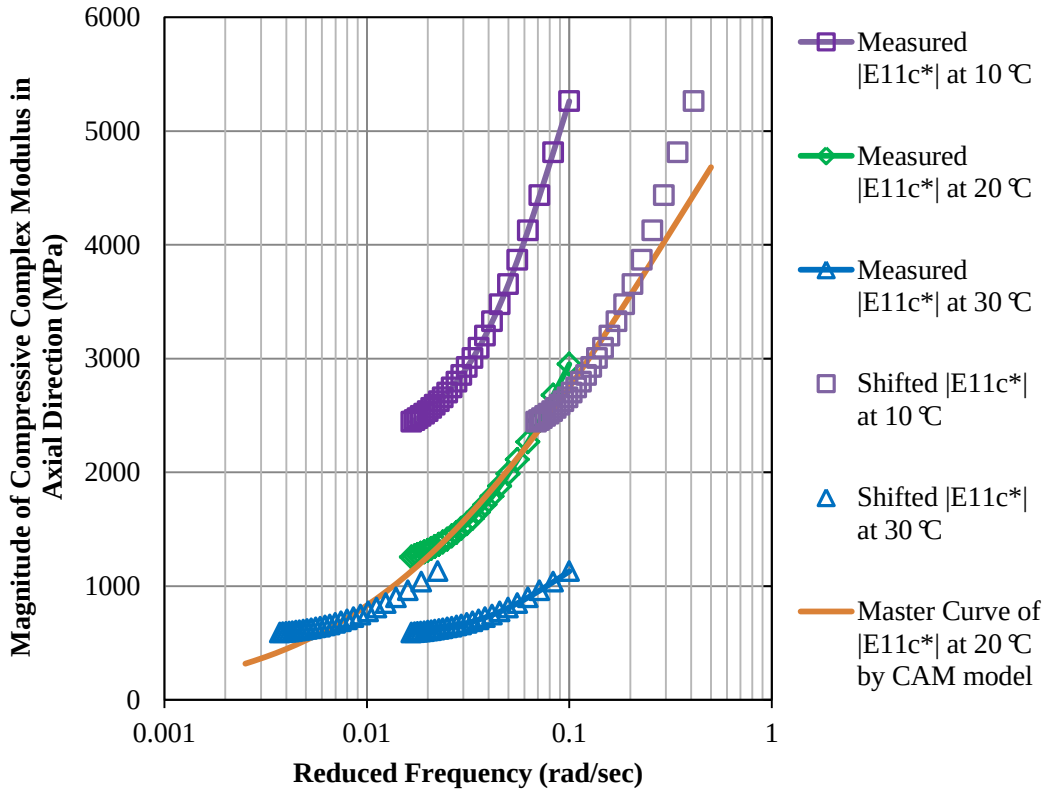

Figure 2-5 Magnitude of the E_{11}^{C*} at different temperatures and master curve at 20 ℃

Figure 2-6 illustrates an example of $\varphi_{E_{11}^{C*}}$ determined at each temperature and two master curves of $\varphi_{E_{11}^{C*}}$ at a reference temperature of 20 ℃, one of which is constructed using Equation 2-27, and the other is constructed using Equation 2-28.

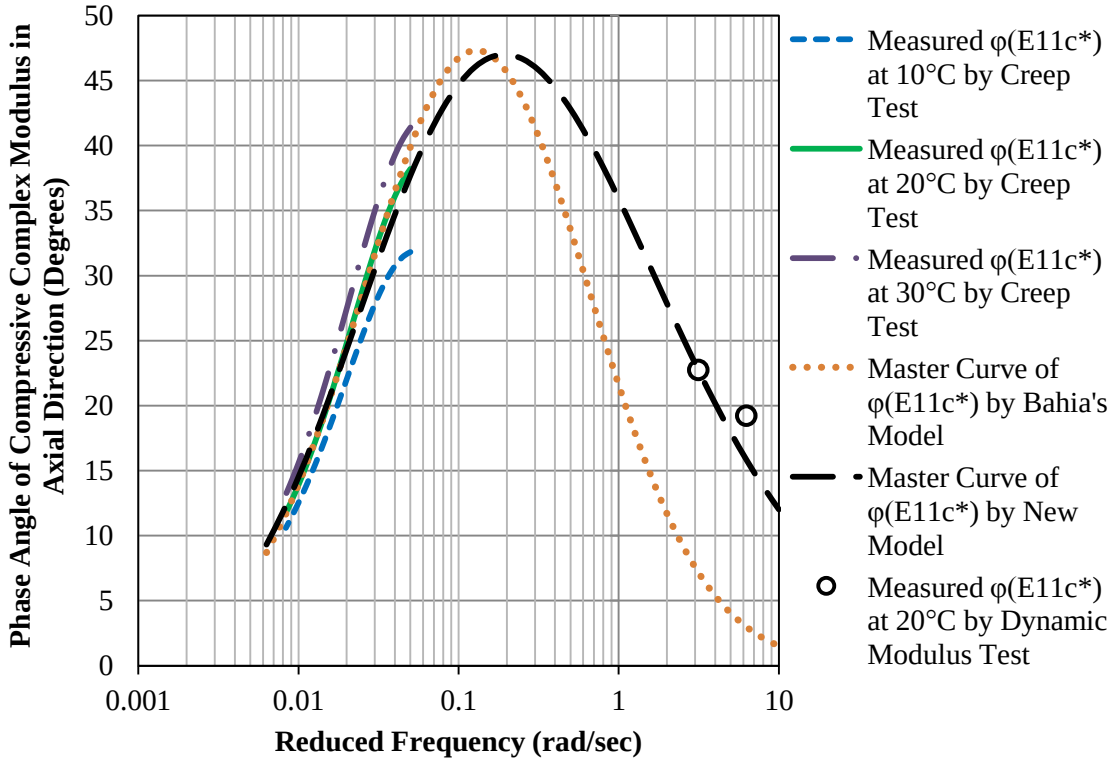

Figure 2-6 Phase angle of the E_{11}^{C*} at different temperatures and master curve at 20 ℃

In order to validate the results of the proposed uniaxial compressive creep test, nondestructive dynamic modulus tests are conducted on the same asphalt specimens at 20 ℃. A variety of frequencies are used in the dynamic test including 0.5 and 1 Hz, which correspond to 3.14 and 6.28 rad/sec, respectively. The stress amplitudes of the haversine loading wave are 50 kPa at 3.14 rad/sec and 70 kPa at 6.28 rad/sec. The $\left|E_{11}^{C*}\right|$ and $\varphi_{E_{11}^{C*}}$ measured by the dynamic

tests at the two frequencies are compared to those determined by the proposed uniaxial compressive creep test. Figure 2-7 and Figure 2-8 show the comparison of $\left|E_{11}^{C*}\right|$ and $\varphi_{E_{11}^{C*}}$ respectively, of asphalt mixtures with different binder type, air void content and aging periods. For any type of asphalt mixture, both $\left|E_{11}^{C*}\right|$ and $\varphi_{E_{11}^{C*}}$ as determined by the proposed uniaxial compressive creep test match those measured by the dynamic test very well. This demonstrates that the proposed test method effectively determines $E_{11}^{C*}(\omega)$. In addition, $\varphi_{E_{11}^{C*}}$ measured by the dynamic test at the two frequencies are also plotted as black circles in Figure 2-6. The two black circles in Figure 2-6 are close to the master curve constructed using Equation 2-28, but they do not well match the master curve constructed using Equation 2-27. Consequently, the asymmetric Equation 2-28 is more appropriate model of constructing the master curve of the phase angle of the complex modulus.

The master curves of $\left|\nu_{12}^{C*}\right|$ and $\varphi_{E_{11}^{C*}}$ are also constructed at a reference temperature of 20 ℃ using Equation 2-26 and Equation 2-28, respectively. Figure 2-9 shows an example of $\left|\nu_{12}^{C*}\right|$ at three test temperatures and how they shift horizontally to construct the master curve at a reference temperature of 20 ℃. This figure indicates that the asphalt mixture has a higher $\left|\nu_{12}^{C*}\right|$ at a higher temperature or lower frequency. Figure 2-9 also illustrates that Equation 2-26 is appropriate to construct the master curve of $\left|\nu_{12}^{C*}\right|$. Figure 2-10 presents an example of $\varphi_{E_{11}^{C*}}$ at the three test temperatures and the constructed master curve at a reference temperature of 20 ℃. The values of $\varphi_{E_{11}^{C*}}$ are negative based on the definition in Equation 2-22.

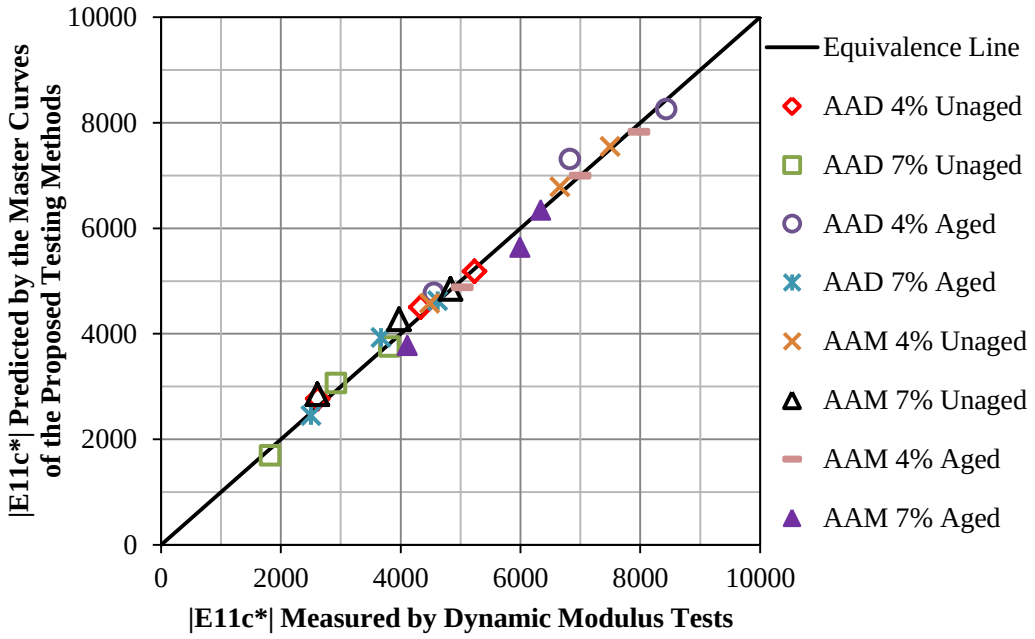

Figure 2-7 Comparison of magnitudes of E_{11}^{C*} predicted by master curves with that measured in dynamic modulus tests for different asphalt mixtures

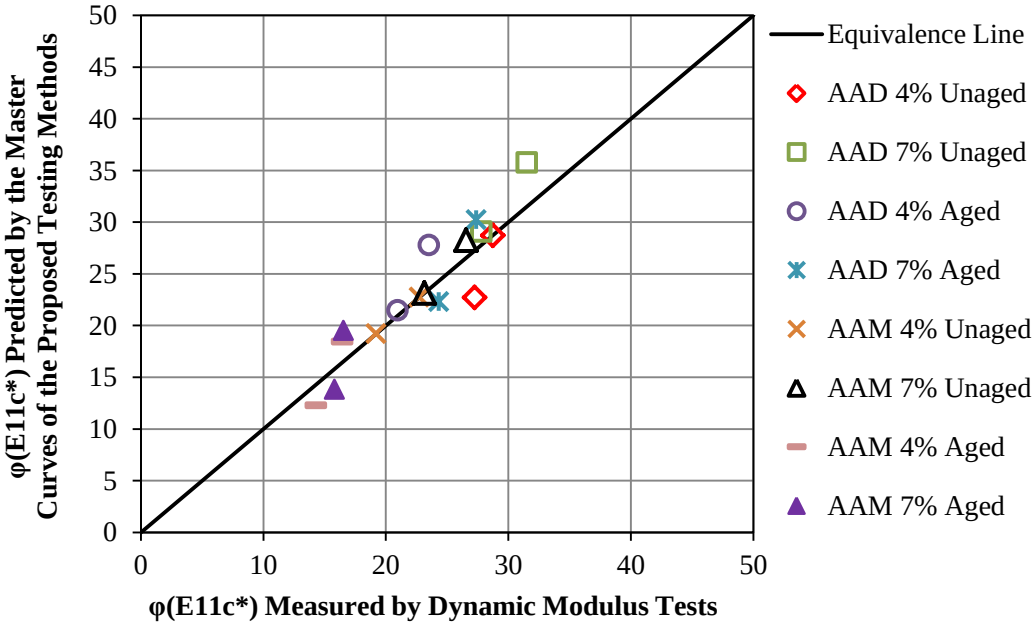

Figure 2-8 Comparison of phase angles of E_{11}^{C*} predicted by master curves with that measured in dynamic modulus tests for different asphalt mixtures

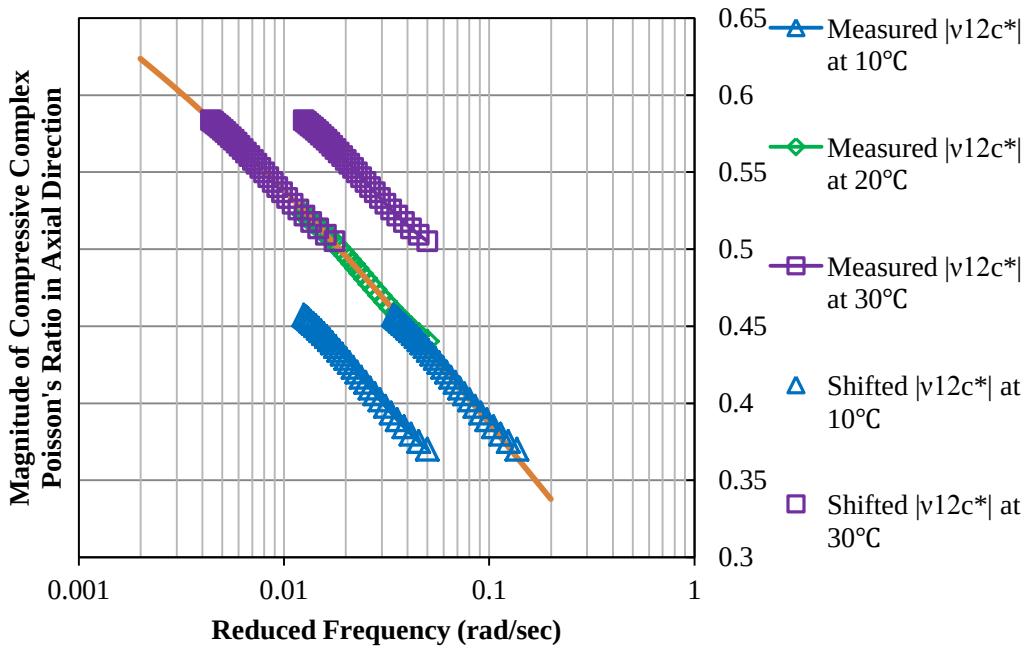

Figure 2-9 Magnitude of the ν_{12}^{C*} at different temperatures and master curve at 20 ℃

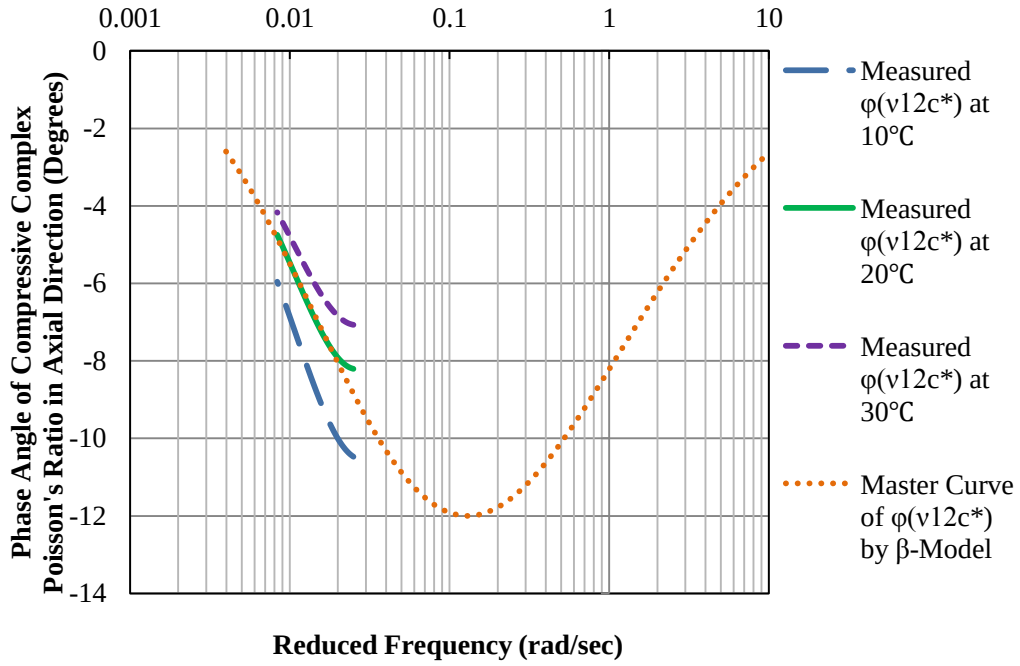

Figure 2-10 Phase angle of the ν_{12}^{C*} at different temperatures and master curve at 20 ℃

Uniaxial Tensile Creep Test

The uniaxial tensile creep test is the third test (after the uniaxial compressive creep test and the indirect tensile creep test) in the sequence of the proposed test protocol. This test is conducted on the specimens with 100 mm in height and 100 mm in diameter to determine the tensile complex modulus $E_{11}^{T*}(\omega)$ and the tensile complex Poisson's ratio $\nu_{12}^{T*}(\omega)$ in terms of four complex functions of frequency: 1) the magnitude of the tensile complex modulus, $\left|E_{11}^{T*}\right|$, 2) the phase angle of the tensile complex modulus, $\varphi_{E_{11}^{T*}}$, 3) the magnitude of the tensile complex Poisson's ratio, $\left|\nu_{12}^{T*}\right|$, and 4) the phase angle of the tensile complex Poisson's ratio, $\varphi_{\nu_{12}^{T*}}$. The reason that the chapter presents the uniaxial tensile creep test before the indirect tensile creep test is that the uniaxial tensile creep test can independently measure the tensile properties of the asphalt mixtures, which will be used together with the results of the indirect tensile creep test to determine the compressive properties of the asphalt mixtures in the horizontal plane.

The uniaxial tensile creep test is conducted on the specimens using the Material Testing System (MTS), as shown in Figure 2-11. A set of end caps are glued to the top surface and bottom surface of each specimen, and then the specimen is set up in the environmental chamber of the MTS by connecting the end caps to the loading frame. Three vertical LVDTs and a bracelet LVDT are mounted in the middle part of the specimen. The gauge length of the vertical LVDTs is 50 mm. A constant tensile load is applied to the specimen for 60 sec. The magnitude of the tensile load varies with the specimens and temperatures and is summarized in Table 2-1. Similar to the uniaxial compressive creep test, the uniaxial tensile creep test is also repeated three times on each specimen to verify the repeatability of the test. Figure 2-12 presents the measured vertical strains and horizontal strains of the three repeating tests. In this figure, the measured vertical strains from the three repeating tests are close to each other, and the measured

horizontal strains from the three repeating tests almost overlap each other. This fact proves that the uniaxial tensile creep test is also repeatable.

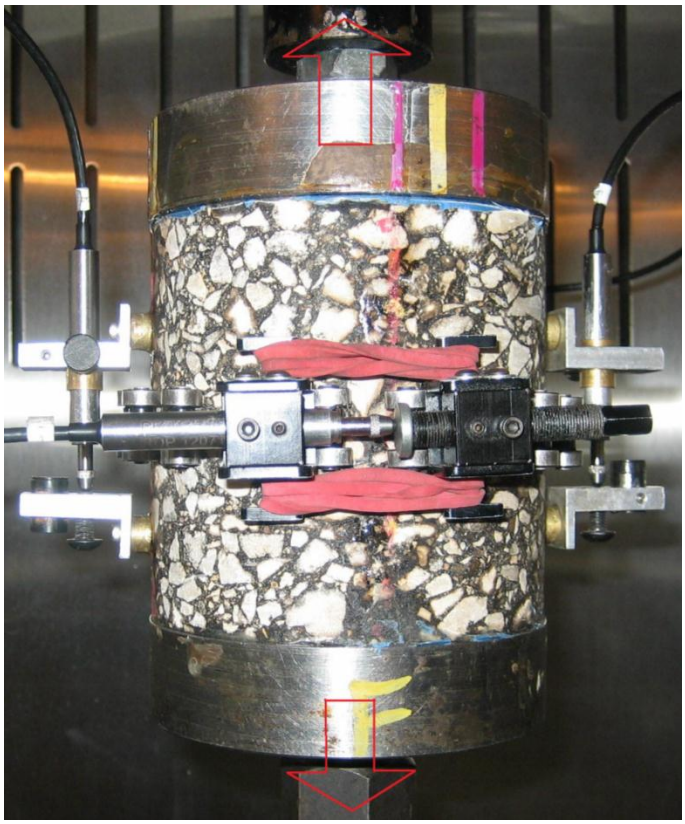

Figure 2-11 Configuration of the uniaxial tensile creep test

The same procedure of using Equations 2-29 through 2-36 to determine $E_{11}^{C*}(\omega)$ and $\nu_{12}^{C*}(\omega)$ also applies to the calculation of $E_{11}^{T*}(\omega)$ and $\nu_{12}^{T*}(\omega)$. Based on the stress and strain data measured at the three testing temperatures, $\left|E_{11}^{T*}\right|$, $\varphi_{E_{11}^{T*}}$, $\left|\nu_{12}^{T*}\right|$ and $\varphi_{\nu_{12}^{T*}}$ are all determined as complex functions of frequency. Then the CAM model (Equation 2-25) and the β-model (Equation 2-28) are employed to construct the master curves of $\left|E_{11}^{T*}\right|$ and $\varphi_{E_{11}^{T*}}$ at a reference

temperature of 20 ℃, respectively. The Inverse S model (Equation 2-26) and the β-model (Equation 2-28) are also used to construct the master curves of $\left|\nu_{12}^{T*}\right|$ and $\varphi_{\nu_{12}^{T*}}$ at the same reference temperature of 20 ℃, respectively. All master curves of $E_{11}^{T*}(\omega)$ and $\nu_{12}^{T*}(\omega)$ are plotted in Figure 2-16 through Figure 2-19 and are compared to those of the compressive properties in both the vertical direction and the horizontal plane in later sections.

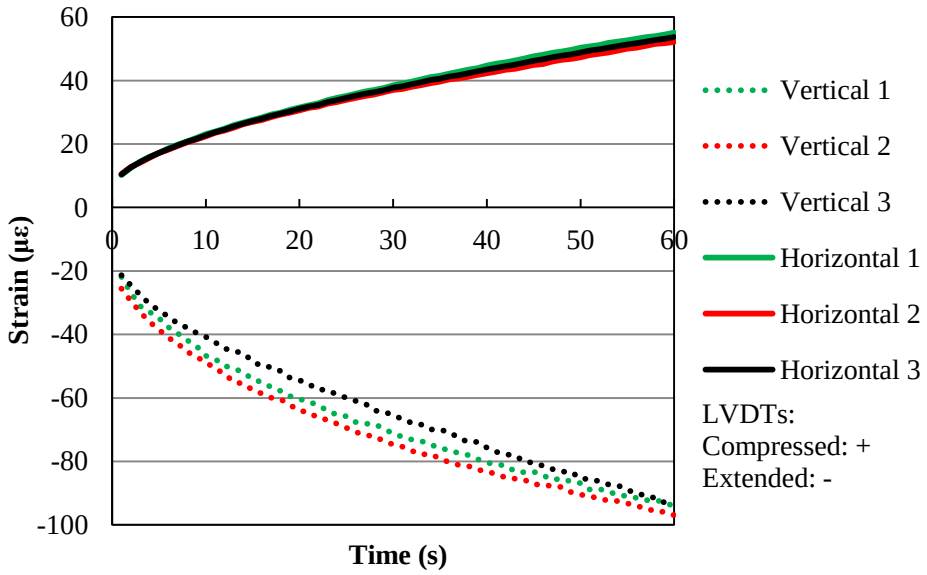

Figure 2-12 Vertical strains and horizontal strains in the uniaxial tensile creep test

Indirect Tensile Creep Test

The indirect tensile (IDT) creep test is used together with the uniaxial compressive creep test and the uniaxial tensile creep test to determine the compressive complex modulus in the horizontal plane $E_{22}^{C*}(\omega)$ and the compressive complex Poisson's ratio in the horizontal plane $\nu_{23}^{C*}(\omega)$. The compressive properties in the vertical direction and the tensile properties determined by the aforementioned two tests serve as known parameters in the calculation of

$E_{22}^{C*}(\omega)$ and $\nu_{23}^{C*}(\omega)$. Again, $E_{22}^{C*}(\omega)$ and $\nu_{23}^{C*}(\omega)$ are presented in terms of four complex functions of frequency: 1) magnitude of the compressive complex modulus in the horizontal plane, $\left|E_{22}^{C*}\right|$, 2) phase angle of the compressive complex modulus in the horizontal plane, $\varphi_{E_{22}^{C*}}$, 3) magnitude of the compressive complex Poisson's ratio in the horizontal plane, $\left|\nu_{23}^{C*}\right|$, and 4) phase angle of the compressive complex Poisson's ratio in the horizontal plane, $\varphi_{\nu_{23}^{C*}}$.

The IDT test has been widely used to determine the properties of the asphalt mixture. Mirza evaluated the Poisson's ratio and elastic modulus of an asphalt mixture using the IDT test (Mirza et al. 1997). Zhang incorporated the elastic-viscoelastic correspondence principle and Fourier transforms to obtain linear viscoelastic solutions of the asphalt mixture properties using the IDT test (Zhang et al. 1997). Kim developed an analytical solution for the dynamic modulus in terms of the magnitude and phase angle of the dynamic modulus using the linear viscoelasticity theory based on the IDT test results (Kim et al. 2004). Even though the IDT test has been employed as a convenient method of evaluating the mechanical properties of the asphalt mixtures, several problems in the previous research need to be addressed.

First, the anisotropy of the asphalt mixture was not taken into account in the IDT tests reported in the literature. Many studies assumed the asphalt mixture as an isotropic material. Thus, only a direction-independent modulus was used in the constitutive relations to analyze the IDT test results.

Second, the tensile modulus was not separated from the compressive modulus in previous studies in spite of the fact that they differed from each other significantly. If addressing the difference between the tensile properties and the compressive properties, the constitutive relation must be changed. Using the plane stress problem as an example, the constitutive relation should be:

$$\varepsilon_x = \frac{1}{E_{xx}^T}\sigma_x - \frac{\nu_{xy}^C}{E_{yy}^C}\sigma_y \text{ for plane stress} \quad (2\text{-}39)$$

If σ_x is a tensile stress, a tensile modulus E_{xx}^T should be used to calculate a tensile strain. Similarly, since σ_y is a compressive stress, a compressive modulus E_{yy}^C and compressive Poisson's ratio ν_{xy}^C should be used to calculate the compressive strain.

Third, the assumption of plane strain or plain stress was used in the previous studies. However, neither plane strain nor plane stress applies to the IDT test because the length of the cylinder specimen is neither large enough to lead to a plane strain situation nor small enough to be treated as the plane stress case. Thus, a three-dimensional constitutive relation should be established for the IDT test. In order to address the three limitations of the previous studies, a novel set-up of the IDT test is developed and its configuration is shown in Figure 2-13.

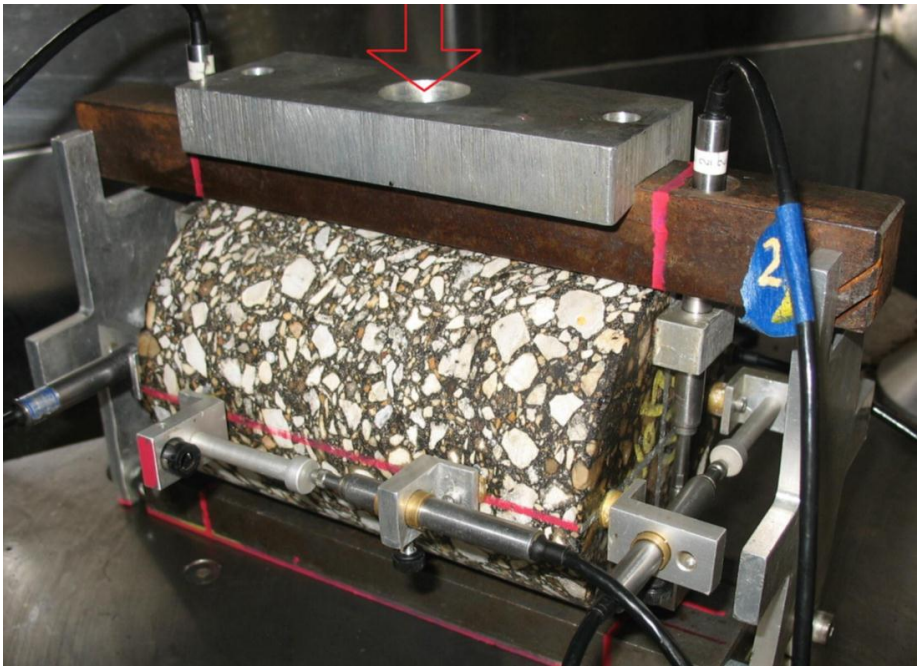

Figure 2-13 Configuration of the indirect tensile creep test

The asphalt mixture specimen has a height of 150 mm and a diameter of 100 mm. Six LVDTs are mounted on the specimen, including: 1) two vertical LVDTs glued along the vertical axis to measure the vertical compressive deformations, U_y, 2) two radial LVDTs glued along the radial axis to measure the radial tensile deformations, U_x, and 3) two axial LVDTs glued along the axial axis on the two lateral sides of the specimen to record the axial tensile deformations, U_z. During the test, a constant compressive load is applied by the UTM in the direction of the arrow in Figure 2-13. This load is applied to the specimen through a steel bar with a flat bottom surface along the generatrix of the cylindrical specimen. The contact surface between the steel bar and the specimen is small enough so that the applied load can be considered as a line load. The constant load is held for 60 sec on the specimen in each IDT test. The magnitude of the applied load for each specimen at each temperature is listed in Table 2-1. This IDT test is also repeated three times on each specimen.

A schematic illustration of the IDT test setup is plotted in Figure 2-14, in which a three-dimensional coordinate system is established with the origin located at the center of the front surface. In the coordinate system, the 1(z) axis is the axial axis of the specimen, the 2(y) axis is the vertical axis, and the 3(x) axis is the radial axis. The specimen diameter is denoted as *D*, *D*=*AB*=*CD*=100 mm; the specimen height is denoted as *L*, *L*=*CE*=*DF*=150 mm; the line load is p, $p = P/L$, where P is the concentrated load applied by the UTM. The gauge length of the vertical LVDTs is *2h*, which is 75 mm. The gauge length of the radial LVDTs is *2r*, which is also 75 mm. The gauge length of the axial LVDTs is *2l*, which is 90 mm. Figure 2-15 illustrates the measured deformations in the vertical direction, the radial direction and the axial direction in the three repeating tests. The IDT creep test also proves to be repeatable.

The stress distribution in a cylindrical specimen with a line load applied as in the IDT test has been well analyzed in the available literature, and a closed-form solution has developed for the stress distribution (Ye et al. 2009). Based on this closed-form solution of the stress distribution, the stress components on axis CD (y axis, $x = 0$) are:

$$\sigma_{33}^{CD} = -\frac{2P}{\pi LD} \tag{2-40}$$

$$\sigma_{22}^{CD} = \frac{2P}{\pi LD}\left(\frac{D}{\frac{D}{2}-y}+\frac{D}{\frac{D}{2}+y}-1\right) \tag{2-41}$$

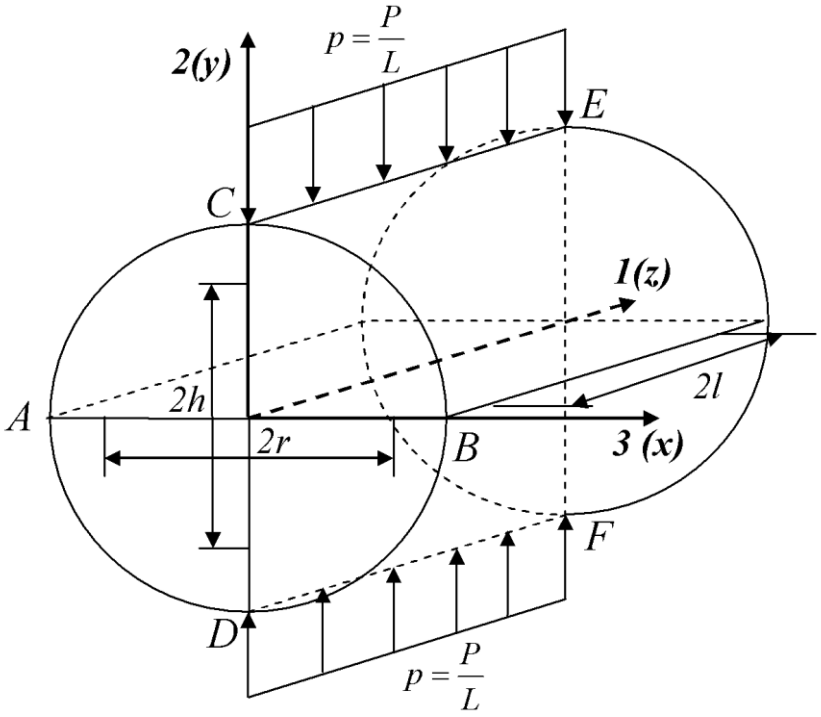

Figure 2-14 Schematic illustration of the indirect tensile creep test

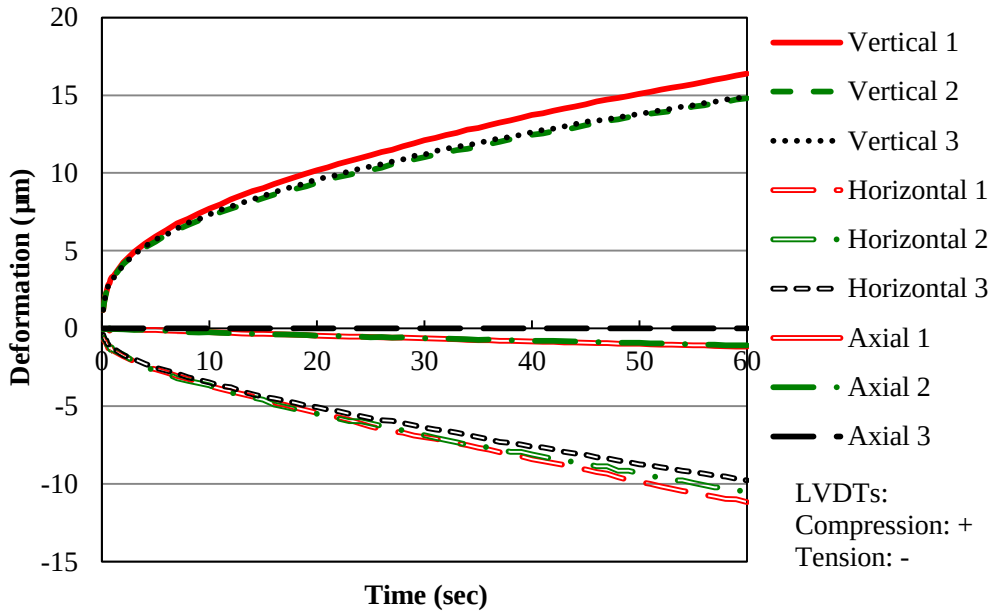

Figure 2-15 Deformations along vertical axis (U_y), horizontal axis (U_x), and axial axis (U_z) in the indirect tensile creep test

When $y = 0$, the stress components on axis AB (x axis) are obtained as:

$$\sigma_{33}^{AB} = \frac{2P}{\pi LD}\left[\frac{16D^2x^2}{\left(4x^2+D^2\right)^2} - 1\right] \tag{2-42}$$

$$\sigma_{22}^{AB} = \frac{2P}{\pi LD}\left[\frac{4D^4}{\left(4x^2+D^2\right)^2} - 1\right] \tag{2-43}$$

After the determination of the stress components, the three-dimensional anisotropic elastic stress-strain relations are developed while including the difference between the tensile properties and the compressive properties. On axis CD, the stress-strain relation is as follows:

$$\begin{bmatrix} \varepsilon_{11}^{CD} \\ \varepsilon_{22}^{CD} \\ \varepsilon_{33}^{CD} \end{bmatrix} = \begin{bmatrix} \frac{1}{E_{11}^T} & -\frac{\nu_{12}^C}{E_{11}^C} & -\frac{\nu_{12}^T}{E_{11}^T} \\ -\frac{\nu_{12}^T}{E_{11}^T} & \frac{1}{E_{22}^C} & -\frac{\nu_{23}^T}{E_{22}^T} \\ -\frac{\nu_{12}^T}{E_{11}^T} & -\frac{\nu_{23}^C}{E_{22}^C} & \frac{1}{E_{22}^T} \end{bmatrix} \begin{bmatrix} \sigma_{11}^{CD} \\ \sigma_{22}^{CD} \\ \sigma_{33}^{CD} \end{bmatrix} \tag{2-44}$$

On axis AB, the constitutive relation is shown in Equation 2-45:

$$\begin{bmatrix} \varepsilon_{11}^{AB} \\ \varepsilon_{22}^{AB} \\ \varepsilon_{33}^{AB} \end{bmatrix} = \begin{bmatrix} \frac{1}{E_{11}^{T}} & -\frac{\nu_{12}^{C}}{E_{11}^{C}} & -\frac{\nu_{12}^{T}}{E_{11}^{T}} \\ -\frac{\nu_{12}^{T}}{E_{11}^{T}} & \frac{1}{E_{22}^{C}} & -\frac{\nu_{23}^{T}}{E_{22}^{T}} \\ -\frac{\nu_{12}^{T}}{E_{11}^{T}} & -\frac{\nu_{23}^{C}}{E_{22}^{C}} & \frac{1}{E_{22}^{T}} \end{bmatrix} \begin{bmatrix} \sigma_{11}^{AB} \\ \sigma_{22}^{AB} \\ \sigma_{33}^{AB} \end{bmatrix} \tag{2-45}$$

On the right side of either Equation 2-44 or Equation 2-45, the elements in the first and the third columns of the compliance matrix are determined by tensile properties because σ_{11}^{CD}, σ_{33}^{CD}, σ_{11}^{AB} and σ_{33}^{AB} are tensile stresses, while the elements in the second column of each compliance matrix are determined by compressive properties since σ_{22}^{CD} and σ_{22}^{AB} are compressive stresses. As mentioned before, the anisotropy of the asphalt mixture is negligible when it is under a pure tensile load (Underwood et al. 2005), Equations 2-46 and 2-47 are valid:

$$E_{11}^{T} = E_{22}^{T} \tag{2-46}$$

$$\upsilon_{12}^{T} = \upsilon_{23}^{T} \tag{2-47}$$

Equation 2-44 can be used to solve for ε_{22}^{CD} as follows:

$$\varepsilon_{22}^{CD} = \left(\frac{1}{E_{22}^{C}} - \frac{\nu_{12}^{C}\nu_{12}^{T}}{E_{11}^{C}}\right)\sigma_{22}^{CD} - \left(\frac{\nu_{23}^{T}}{E_{22}^{T}} + \frac{\left(\nu_{12}^{T}\right)^{2}}{E_{11}^{T}}\right)\sigma_{33}^{CD} - \varepsilon_{11}^{CD}\nu_{12}^{T} \tag{2-48}$$

The vertical compressive deformation on axis CD, U_y, is then calculated by integrating the strain ε_{22}^{CD} along the gauge length from $-h$ to $+h$:

$$U_y = \int_{-h}^{h} \varepsilon_{22}^{CD} dy \tag{2-49}$$

Substituting Equation 2-48 into Equation 2-49 yields:

$$U_y = A\left(\frac{1}{E_{22}^{C}} - \frac{\nu_{12}^{C}\nu_{12}^{T}}{E_{11}^{C}}\right)P - B\left(\frac{\nu_{23}^{T}}{E_{22}^{T}} + \frac{\left(\nu_{12}^{T}\right)^{2}}{E_{11}^{T}}\right)P + C \tag{2-50}$$

where:

$$A = \frac{1}{P}\int_{-h}^{h} \sigma_{22}^{CD} dy = \frac{2}{\pi L}\left[\ln\left(\frac{D+2h}{D-2h}\right)^2 - \frac{2h}{D}\right]; \tag{2-51}$$

$$B = \frac{1}{P}\int_{-h}^{h} \sigma_{33}^{CD} dy = -\frac{4h}{\pi LD}; \text{and} \tag{2-52}$$

$$C = \int_{-h}^{h} -\varepsilon_{11}^{CD} \nu_{12}^{T} dy = -2h\varepsilon_{11}^{CD}\nu_{12}^{T} = -\frac{h}{l} U_z \nu_{12}^{T} \tag{2-53}$$

In Equation 2-53, the axial strain ε_{11}^{CD} is computed by dividing U_z by the axial gauge length, *2l*, since the tensile strain distribution within the axial gauge length is uniform under the line load. Solving Equation 2-50 for the radial elastic compressive modulus produces:

$$E_{22}^{C} = \frac{1}{\frac{\nu_{12}^{C}\nu_{12}^{T}}{E_{11}^{C}} + \frac{U_y}{AP} + \frac{h}{l}\frac{U_z\nu_{12}^{T}}{AP} + \frac{B\nu_{12}^{T}\left(1+\nu_{12}^{T}\right)}{AE_{11}^{T}}} \tag{2-54}$$

Similarly, ε_{33}^{AB} is computed using Equation 2-45:

$$\varepsilon_{33}^{AB} = -\left(\frac{\nu_{23}^{C}}{E_{22}^{C}} + \frac{\nu_{12}^{C}\nu_{12}^{T}}{E_{11}^{C}}\right)\sigma_{22}^{AB} + \left(\frac{1}{E_{22}^{T}} - \frac{\left(\nu_{12}^{T}\right)^2}{E_{11}^{T}}\right)\sigma_{33}^{AB} - \varepsilon_{11}^{AB}\nu_{12}^{T} \tag{2-55}$$

The radial tensile deformation, U_x, on axis AB is determined by integrating ε_{33}^{AB} over the gauge length from $-r$ to r:

$$U_x = \int_{-r}^{r} \varepsilon_{33}^{AB} dy = -K\left(\frac{\nu_{23}^{C}}{E_{22}^{C}} + \frac{\nu_{12}^{C}\nu_{12}^{T}}{E_{11}^{C}}\right)P + M\left(\frac{1}{E_{22}^{T}} - \frac{\left(\nu_{12}^{T}\right)^2}{E_{11}^{T}}\right)P + N \tag{2-56}$$

where:

$$K = \frac{1}{P}\int_{-r}^{r} \sigma_{22}^{AB} dy = \frac{4}{\pi L}\arctan\left(\frac{2r}{D}\right) + \frac{8rD}{\pi L\left(4r^2+D^2\right)} - \frac{4r}{\pi LD} \tag{2-57}$$

$$M = \frac{1}{P}\int_{-r}^{r} \sigma_{33}^{AB} dy = \frac{4}{\pi L}\arctan\left(\frac{2r}{D}\right) - \frac{8rD}{\pi L\left(4r^2+D^2\right)} - \frac{4r}{\pi LD} \text{ and} \tag{2-58}$$

$$N = \int_{-r}^{r} -\varepsilon_{11}^{AB} \nu_{12}^{T} dy = -2r\varepsilon_{11}^{AB} \nu_{12}^{T} = -\frac{r}{l} U_z \nu_{12}^{T} \tag{2-59}$$

Solving Equation 2-56 for the elastic Poisson's ratio in the horizontal plane yields:

$$\nu_{23}^{C} = E_{22}^{C} \left[\frac{M\left[1-\left(\nu_{12}^{T}\right)^2\right]}{KE_{11}^{T}} - \frac{\nu_{12}^{C}\nu_{12}^{T}}{E_{11}^{C}} - \frac{rU_z\nu_{12}^{T} + lU_x}{lKP} \right] \tag{2-60}$$

Applying the elastic-viscoelastic correspondence principle to Equations 2-54 and 2-60 obtains:

$$s\bar{E}_{22}^{C} = \frac{1}{\frac{s\bar{\nu}_{12}^{C} s\bar{\nu}_{12}^{T}}{s\bar{E}_{11}^{C}} + \frac{\bar{U}_y}{A\bar{P}} + \frac{h}{l}\frac{\bar{U}_z s\bar{\nu}_{12}^{T}}{A\bar{P}} + \frac{Bs\bar{\nu}_{12}^{T}\left(1+s\bar{\nu}_{12}^{T}\right)}{As\bar{E}_{11}^{T}}} \tag{2-61}$$

$$s\bar{\nu}_{23}^{C} = s\bar{E}_{22}^{C} \left[\frac{M\left[1-\left(s\bar{\nu}_{12}^{T}\right)^2\right]}{K \cdot s\bar{E}_{11}^{T}} - \frac{s\bar{\nu}_{12}^{C} \cdot s\bar{\nu}_{12}^{T}}{s\bar{E}_{11}^{C}} - \frac{r\bar{U}_z \cdot s\bar{\nu}_{12}^{T} + l\bar{U}_x}{lK\bar{P}} \right] \tag{2-62}$$

where A, B, K and M are constants calculated using Equations 2-51, 2-52, 2-57 and 2-58; $\bar{P}$ is the Laplace transform of the constant load, $\bar{P} = P/s$; $\bar{E}_{11}^{C}$, $\bar{E}_{11}^{T}$, $\bar{\nu}_{12}^{C}$, and $\bar{\nu}_{12}^{T}$ are Laplace transforms of the corresponding time-dependent variables, which are determined in the uniaxial compressive creep tests and uniaxial tensile creep tests; and $\bar{U}_x$, $\bar{U}_y$ and $\bar{U}_z$ are Laplace transforms of the U_x, U_y and U_z which are respectively measured using the radial LVDTs, vertical LVDTs and axial LVDTs, and are modeled using Equation 2-63:

$$U(t)_{x,y,or,z} = a_u\left(1-e^{-b_u \cdot t}\right) + c_u \tag{2-63}$$

where a_u, b_u, and c_u are the fitting parameters. Applying the Laplace transform to Equation 2-63 yields:

$$\bar{U}(s)_{x,\,y,\,or,\,z} = \frac{b_u(a_u + c_u) + c_u s}{s(s + b_u)} \tag{2-64}$$

After determining all variables in Equations 2-61 and 2-62, substituting Equations 2-61 and 2-62 into Equations 2-23 and 2-24 yields:

$$E_{22}^{C*}(\omega) = \left[s\bar{E}_{22}^{C}(s) \right]_{s=i\omega} = \left[\frac{1}{\frac{s\bar{\nu}_{12}^{C} s\bar{\nu}_{12}^{T}}{s\bar{E}_{11}^{C}} + \frac{\bar{U}_y}{A\bar{P}} + \frac{h}{l}\frac{\bar{U}_z s\bar{\nu}_{12}^{T}}{A\bar{P}} + \frac{Bs\bar{\nu}_{12}^{T}\left(1 + s\bar{\nu}_{12}^{T}\right)}{As\bar{E}_{11}^{T}}} \right]_{s=i\omega} \tag{2-65}$$

$$\nu_{23}^{C*}(\omega) = \left[s\bar{\nu}_{23}^{C}(s) \right]_{s=i\omega} = s\bar{E}_{22}^{C} \left[\frac{M\left[1 - \left(s\bar{\nu}_{12}^{T}\right)^2\right]}{K \cdot s\bar{E}_{11}^{T}} - \frac{s\bar{\nu}_{12}^{C} \cdot s\bar{\nu}_{12}^{T}}{s\bar{E}_{11}^{C}} - \frac{r\bar{U}_z \cdot s\bar{\nu}_{12}^{T} + l\bar{U}_x}{lK\bar{P}} \right]_{s=i\omega} \tag{2-66}$$

Although it is a mathematical challenge to obtain the closed-form solutions of Equations 2-65 and 2-66, it is convenient to use the software MATLAB to determine the real part and imaginary part of the complex variables of $E_{22}^{C*}(\omega)$ and $\nu_{23}^{C*}(\omega)$. Subsequently, $\left|E_{22}^{C*}\right|$, $\varphi_{E_{22}^{C*}}$, $\left|\nu_{23}^{C*}\right|$, and $\varphi_{\nu_{23}^{C*}}$ are determined respectively using Equations 2-17, 2-18, 2-21 and 2-22 at the three test temperatures, and their master curves are also constructed at a reference temperature of 20 ℃ using Equations 2-25, 2-28, 2-26 and 2-28, respectively. These master curves are plotted in Figure 2-16 through Figure 2-19.

COMPARISON OF TENSILE AND COMPRESSIVE PROPERTIES

By conducting the three tests detailed in former sections, the viscoelastic tensile properties and the anisotropic viscoelastic compressive properties are determined in terms of six parameters including E_{11}^{C*}, ν_{12}^{C*}, E_{11}^{T*} ν_{12}^{T*}, E_{22}^{C*} and ν_{23}^{C*}. Master curves are constructed for the

magnitude and phase angle of the six parameters at a reference temperature of 20 ℃ using Equations 2-25, 2-26 and 2-28, and are plotted in Figure 2-16 through Figure 2-19. The model parameters of all master curves are summarized in Table 2-2.

Figure 2-16 plots the master curves of $\left|E_{11}^{C*}\right|$, $\left|E_{11}^{T*}\right|$ and $\left|E_{22}^{C*}\right|$; each master curve has an S-shaped curve on the log scale of the frequency, which agrees with what is reported in the literatures (Findley et al. 1989; Christensen 2003; Kim et al. 2004; Di Benedetto et al. 2007a). Figure 2-17 shows the master curves of $\varphi_{E_{11}^{C*}}$, $\varphi_{E_{11}^{T*}}$ and $\varphi_{E_{22}^{C*}}$, which are bell-shaped curves on the log scale of the frequency. The bell-shaped master curves of the phase angle of the complex moduli were also obtained using dynamic modulus tests and were reported in the literature (Levenberg and Shah 2008; Biligiri et al. 2010).

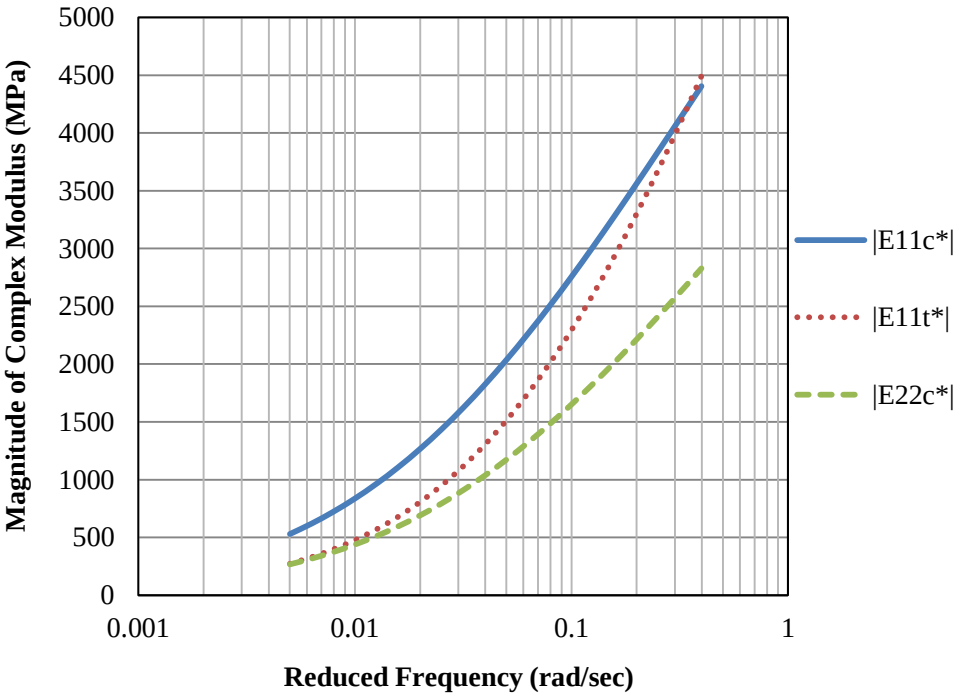

Figure 2-16 Master curves for the magnitude of E_{11}^{C*}, E_{11}^{T*} and E_{22}^{C*} at 20 ℃

Figure 2-17 also indicates that Equation 2-27 predicts very low phase angles (close to zero) of the compressive complex moduli in the normal frequency range from 3.14 to 6.28 rad/sec (from 0.5 Hz to 1 Hz), while the β-model yields more reasonable phase angles within the same frequency range. The tensile complex modulus shows a significantly larger phase angle than the compressive complex moduli at any given frequency in Figure 2-17. This is reasonable because it is mainly the asphalt binder or mastic that takes the tensile load when the asphalt mixture is in tension; therefore the asphalt mixture in tension is more viscous, which leads to a larger phase angle. In contrast, when the asphalt mixture is in compression, it is mainly the aggregates that take the compressive load. As a result, the asphalt mixture is less viscous in compression, which results in a smaller phase angle.

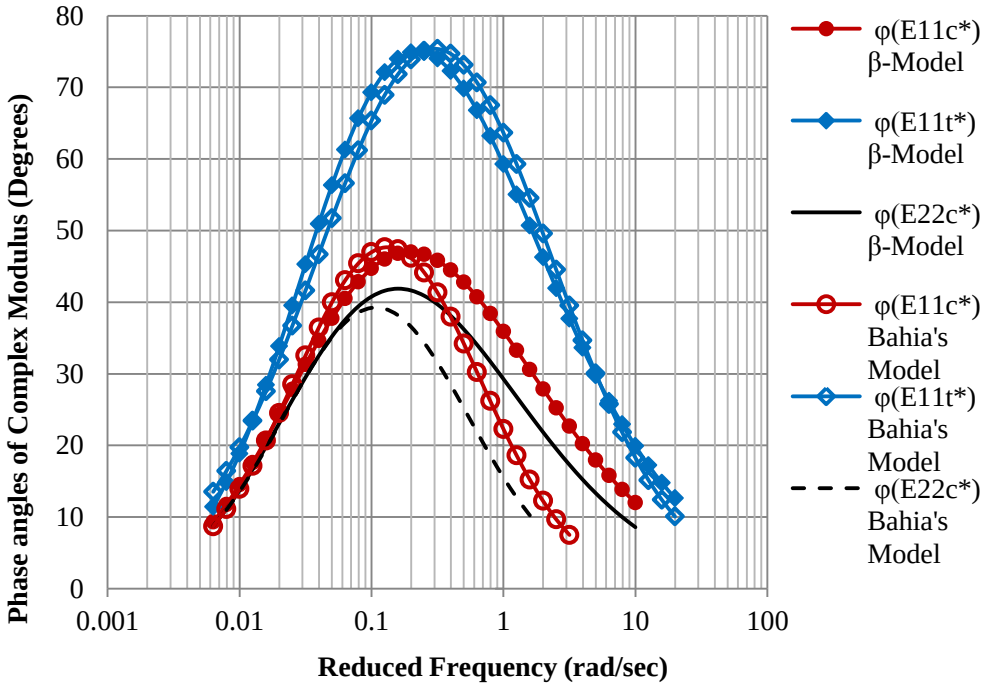

Figure 2-17 Master curves for the phase angle of E_{11}^{C*}, E_{11}^{T*} and E_{22}^{C*} at 20 ℃

Table 2-2 Values of Parameters in Master Curves

Complex Modulus	**Parameters**		E_{11}^{C*}		E_{22}^{C*}		E_{11}^{T*}	
Magnitude (CAM model)	E_g (MPa)		9933		7251		8500	
	ω_{cE} (rad/sec)		0.038		0.067		0.169	
	R_E		0.747		0.726		0.454	
	C_E		-0.062		-0.023		-0.048	
Phase Angle	Bahia's Model	β-Model	Bahia's Model	β - Model	Bahia's Model	β - Model	Bahia's Model	β - Model
	φ_{mE}	φ_{max}	47.32	47.0	39.3	41.89	75.4	75.0
	ω_{mE}	ω_R	0.129	0.194	0.108	0.159	0.301	0.224
	$R_{\varphi E}$	β	6.629	0.186	6.454	0.199	7.383	0.194
	m	---	88.20	---	83.70	---	68.15	---
	C_1		-1.343		-0.749		-0.168	
	C_2		-225.5		-225.3		-25.5	
Complex Poisson's Ratio	**Parameters**		ν_{12}^{C*}		ν_{23}^{C*}		ν_{12}^{T*}	
Magnitude (Inverse S model)	ν_g		0.846		1.0		1.0	
	$\omega_{c\nu}$ (rad/sec)		35.00		0.479		3.01	
	R_ν		1.173		0.509		0.949	
	C_ν		-0.044		-0.022		-0.061	
Phase Angle (β -Model)	φ_{max} (degree)		-12.0		-23.0		-23.23	
	ω_R (rad/sec)		0.130		0.301		0.359	
	β		0.174		0.101		0.071	
	C_1		-0.323		-200.7		-2.156	
	C_2		-26.58		-6000.1		-42.89	

Figure 2-18 plots the master curves of $\left|\nu_{12}^{C*}\right|, \left|\nu_{12}^{T*}\right|$ and $\left|\nu_{23}^{C*}\right|$ at the reference temperature of 20 ℃. Each master curve has an inverse S shape on the log scale of the frequency, which decreases as the frequency increases. The values of $\left|\nu_{12}^{C*}\right|, \left|\nu_{12}^{T*}\right|$ and $\left|\nu_{23}^{C*}\right|$ are relatively high since they are plotted in a relative low frequency range from 0.001 rad/sec to 0.1 rad/sec

corresponding to 0.00016 Hz to 0.016 Hz. The values in Figure 2-18 are considered to be reasonable because it has been reported in the literatures that the Poisson's ratio of a transversely isotropic elastic material has the following relations (Pickering 1970; Christensen 2005):

$$\nu_{12}^2 < \left(\frac{1-\nu_{23}}{2}\right)\left(\frac{E_{11}}{E_{22}}\right) < \frac{E_{11}}{E_{22}} \tag{2-67}$$

$$-1 < \nu_{23} < 1 \tag{2-68}$$

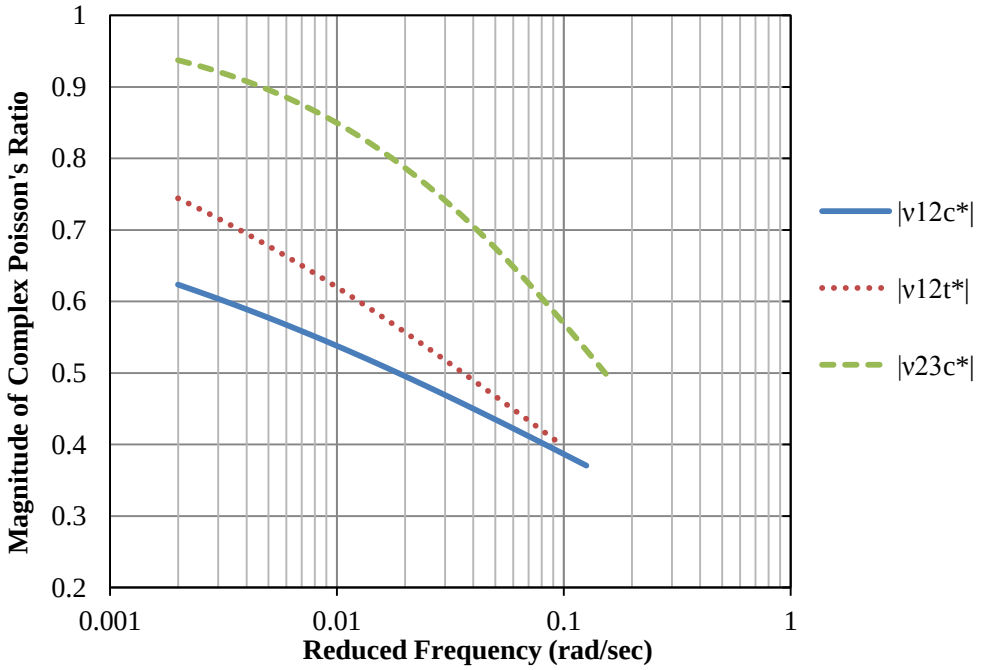

Figure 2-18 Master curves for the magnitude of ν_{12}^{C*}, ν_{12}^{T*} and ν_{23}^{C*} at 20 ℃

Based on the test results of the 16 test specimens, $\left|E_{11}^{C*}\right|$ is approximately 1.2~2 times of $\left|E_{22}^{C*}\right|$ at a given frequency. Thus, $\left|\nu_{12}^{C*}\right| < \sqrt{1.2} = 1.1$. Figure 2-18 shows that the calculated $\left|\nu_{12}^{C*}\right|$ is less than 1 in a wide frequency range, which agrees with Equation 2-67. In addition, Figure 2-

18 also shows that $\left|\nu_{23}^{C*}\right|$ is less than 1 in a wide frequency range; this finding agrees with Equation 2-68, which indicates $-1<\left|\nu_{23}^{C*}\right|<1$. Also, Table 2-2 shows that the values of ν_g for $\left|\nu_{23}^{C*}\right|$, the maximum value of the horizontal Poisson's ratio is 1.0, also agreeing with Equation 2-68. Figure 2-19 plots the master curves of $\varphi_{\nu_{12}^{C*}}$, $\varphi_{\nu_{12}^{T*}}$ and $\varphi_{\nu_{23}^{C*}}$ at the reference temperature of 20 ℃. Each master curve has a reversed bell-shaped curve on the log scale of the frequency, which agrees with what is reported in the literature (Di Benedetto et al. 2007a).

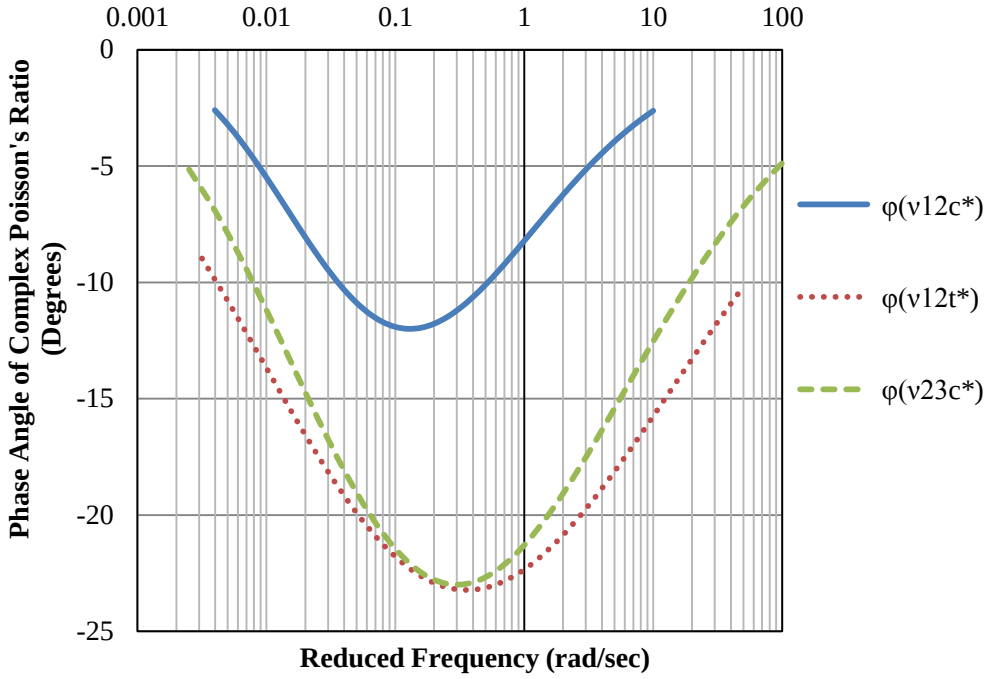

Figure 2-19 Master curves for the phase angle of ν_{12}^{C*}, ν_{12}^{T*} and ν_{23}^{C*} at 20 ℃

To evaluate the effects of the binder type, air void content and aging period on $\left|E_{11}^{C*}\right|$, $\left|E_{11}^{T*}\right|$ and $\left|E_{22}^{C*}\right|$, the values of $\left|E_{11}^{C*}\right|$, $\left|E_{11}^{T*}\right|$ and $\left|E_{22}^{C*}\right|$ at the frequency of 0.1 rad/sec on the master

curves of the total of 16 specimens are selected as the representative modulus magnitudes. Figure 2-20 plots the representative modulus magnitude of each specimen and the average representative modulus magnitude of the two replicates at each combination of the binder type, air void content and aging period. Figure 2-20 shows that the specimens with the AAM binder are stiffer than the specimens with the AAD binder. When the air void content increases from 4% to 7%, $\left|E_{11}^{C*}\right|$, $\left|E_{11}^{T*}\right|$ and $\left|E_{22}^{C*}\right|$ all decrease. The aged asphalt mixtures have higher moduli than the unaged specimens. For any combination of binder type, air void content and aging period, $\left|E_{11}^{C*}\right|$ is always larger than $\left|E_{22}^{C*}\right|$; the ratio of $\left|E_{11}^{C*}\right|$ to $\left|E_{22}^{C*}\right|$ ranges from 1.2 to 2, which proves that asphalt mixtures have significant anisotropy under a compressive load.

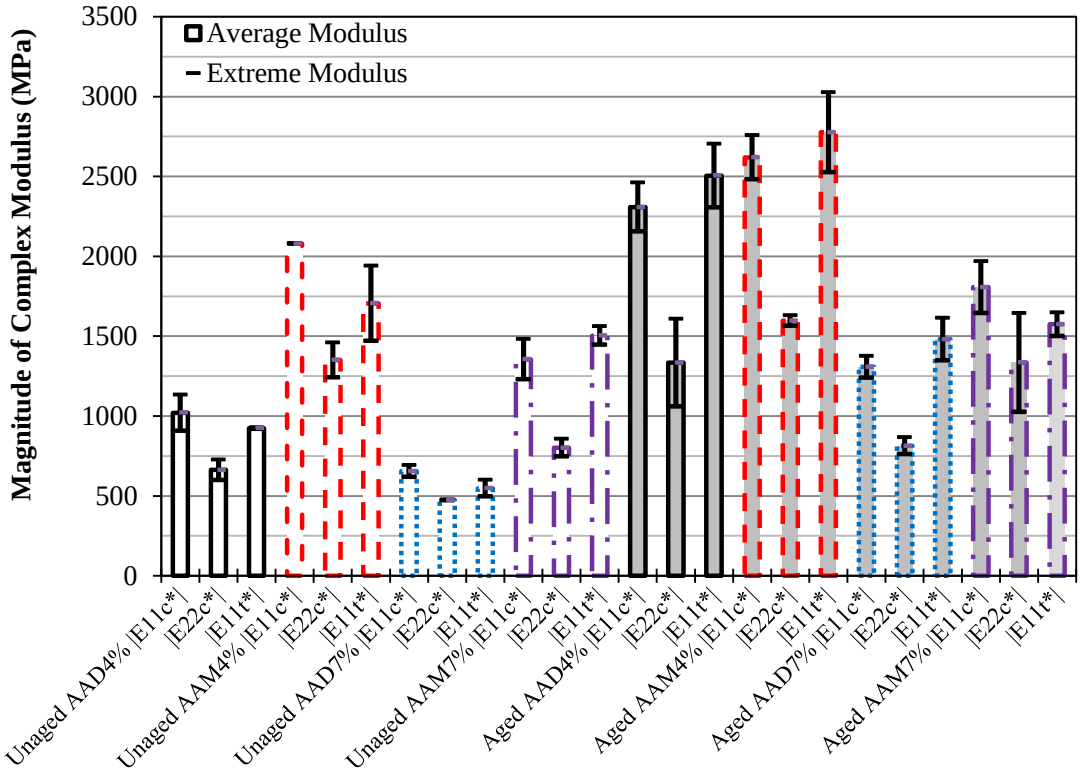

Figure 2-20 Comparison of the magnitude of E_{11}^{C*}, E_{11}^{T*} and E_{22}^{C*} at 0.1 Hz and 20 ℃

Figure 2-21 plots the peak value of the phase angle master curve of every specimen as well as the average peak value of the two replicates of each type of asphalt mixture. It can be seen from Figure 2-21 that the peak values of $\varphi_{E_{11}^{C*}}$ and $\varphi_{E_{22}^{C*}}$ are close to each other, both of which are in a range of 35 to 55 degrees, while $\varphi_{E_{11}^{T*}}$ always has a higher peak value ranging from 65 to 85 degrees. These findings can also be explained by the stronger viscoelasticity of asphalt mixture in tension but less viscoelasticity in compression as stated before.

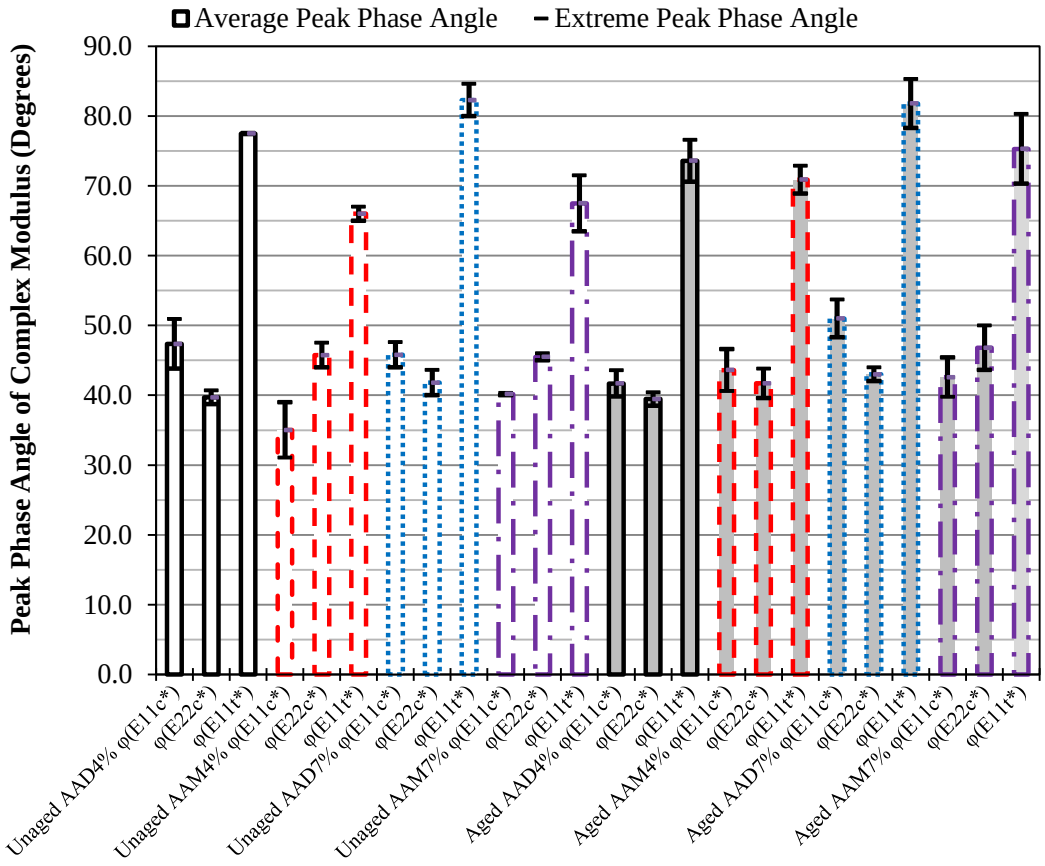

Figure 2-21 Comparison of the peak phase angles of the E_{11}^{C*}, E_{11}^{T*} and E_{22}^{C*} at 20 ℃

SUMMARIES AND CONCLUSIONS

This chapter develops a test protocol and data analysis method based on anisotropic linear viscoelastic theory to characterize the anisotropic viscoelastic properties of undamaged asphalt mixtures. A total of 16 asphalt mixture specimens are tested in this study with two replicates at each of the two binder types (AAD and AAM), two air void contents (4% and 7%) and two aging periods (unaged and 6-month aging at 60 ℃). The test protocol includes three nondestructive tests: 1) the uniaxial compressive creep test, in which a uniaxial constant compressive load is applied to the cylindrical asphalt mixture specimen for 60 sec, and the vertical strains and the horizontal strains are recorded by the LVDTs; 2) the indirect tensile creep test, in which a constant compressive load is applied to the specimen for 60 sec, and the deformations are measured in the vertical, radial and axial directions; 3) the uniaxial tensile creep test, in which a uniaxial constant tensile load is applied to the specimen while the vertical and horizontal strains are measured. These tests are conducted on all specimens at three temperatures (10, 20 and 30 ℃).

The uniaxial compressive creep test determines E_{11}^{C*} and ν_{12}^{C*} independently, and the uniaxial tensile creep test determines E_{11}^{T*} and ν_{12}^{T*} independently. These properties are used together with the results of the indirect tensile creep test are used to calculate E_{22}^{C*} and ν_{23}^{C*}. Master curves are constructed for the magnitude and phase angle of these six parameters. Calculation results indicate that all tested asphalt mixtures have significantly different tensile properties from compressive properties. The peak value of the phase angle of the master curve of the tensile complex modulus is within a range from 65 to 85 degrees while the peak values of the compressive moduli phase angle in both directions range from 35 to 55 degrees. In addition, the

undamaged asphalt mixtures exhibit distinctively anisotropic properties in compression. It is found that $\left|E_{11}^{C*}\right|$ is approximately 1.2 ~ 2 times of $\left|E_{22}^{C*}\right|$.

Dynamic modulus tests are performed at 0.5 and 1 Hz to verify the results of the proposed test protocol. The predicted $\left|E_{11}^{C*}\right|$ and $\varphi_{E_{11}^{C*}}$ from the master curves constructed by the proposed test protocol match well those measured by the dynamic test for the asphalt mixtures with different binder types, air void contents and aging periods.

Compared to the traditional anisotropic test methods using multiple specimens cored in different directions, the newly proposed triple testing protocols are much quicker and more efficient. First, creep tests instead of dynamic tests are used to obtain the anisotropic complex modulus and Poisson's ratio. Second, only one cylindrical specimen is needed for the three tests, which eliminates the sample to sample error and reduces the quantity of testing materials. Third, each test is finished in a short testing period (only 1 min). Finally, strains are controlled under the endurance limit of 100 microstrains so no damage is introduced to the specimen. Therefore, the same specimen may be reused in the future destructive fatigue, rutting and healing tests.

CHAPTER III

MICROSTRUCTURE-BASED INHERENT ANISOTROPY OF ASPHALT MIXTURES*

OVERVIEW

Asphalt mixtures are demonstrated to be anisotropic materials in both laboratory and field tests. The anisotropy of asphalt mixtures consists of inherent anisotropy and stress-induced anisotropy. In previous work, the inherent anisotropy of asphalt mixtures was quantified using only the inclination angles of the coarse aggregate particles in the asphalt mixtures. However, the inclination of fine aggregates also has a contribution to the inherent anisotropy of the asphalt mixtures. Moreover, the contribution to the inherent anisotropy of each aggregate may not be the same as in the previous work but will depend on the size, orientation and sphericity of the aggregate particle.

This chapter quantifies the internal microstructure of the aggregates in the asphalt mixtures using an aggregate-related geometric parameter, the vector magnitude. The original formulation of the vector magnitude, which addresses only the orientation of coarse aggregates, is modified to take into account not only the coarse aggregate orientation, but also the size, orientation and sphericity of coarse and fine aggregates. This formulation is applied to cylindrical Lab-Mixed-Lab-Compacted (LMLC) asphalt mixture specimens varying in asphalt binder type, air void content and aging period. The vertical modulus and the horizontal modulus are also measured using nondestructive tests.

A relationship between the modified vector magnitude and the modulus ratio of the vertical modulus to the horizontal modulus is developed to quantify the influence of the inherent microstructure of the aggregates on the anisotropy of the mixtures. The modulus ratio is found to depend solely on the aggregate characteristics including the inclination angle, size and sphericity, and it is independent of the asphalt binder type, air void content and aging period. The inclination angle itself proves to be insufficient to quantify the inherent anisotropy of the asphalt mixtures.

INTRODUCTION

Anisotropy of a material is the property of being directionally dependent. The anisotropy of an asphalt mixture can be defined as a difference in physical properties, such as modulus and Poisson's ratio, when the asphalt mixture is measured in different directions. According to the origins of anisotropy, granular materials, such as soils, aggregate base and asphalt mixtures, consist of two types of anisotropy: i) inherent anisotropy and ii) stress-induced anisotropy (Adu-Osei 2000; Masad et al. 2002; Kim et al. 2005; Underwood et al. 2005). The inherent anisotropy of the asphalt mixture is attributed to the preferential orientation of aggregates. Since the aggregates tend to "lie flat" during compaction of asphalt mixtures as shown in Figure 2-1, the major axis (longest diameter) of the aggregate has a preferential direction in the horizontal plane. The stress-induced anisotropy is caused by the concentration of the contact normal of the material particles (e.g., soils, sands and aggregates) (Oda 1993). In this study, the stress-induced anisotropy of the asphalt mixture is believed as the result of crack growth under load applications. The increase of the crack surface area leads to the loss of the intact material area, which causes the modulus degradation. The projection area of the crack differs in different directions, which results in different lost area and true stresses in different directions and

produces the stress-induced anisotropy in the asphalt mixture. Because the two types of anisotropy have different mechanisms, the inherent anisotropy and the stress-induced anisotropy have to be investigated separately. The focus of this chapter is investigating the inherent anisotropy of asphalt mixtures and the stress-induced anisotropy is investigated in Chapter VII. In order to avoid the influence of the stress-induced anisotropy and to obtain the pure inherent anisotropy, all asphalt mixture specimens are tested within small strains in this study so that no crack grows in the asphalt mixture specimens in the test.

The inherent anisotropy of the asphalt mixture has been demonstrated to be significant using laboratory and field tests. Levenberg and Uzan (2004) conducted small strain (below 150 microstrains) hydrostatic compression tests on lab compacted cylindrical samples and found that the asphalt mixture was 1.5 times stiffer in the vertical direction than that in the horizontal direction. Ramos-Aparicio and Oh et al. (Ramos-Aparicio 2004; Oh et al. 2006) backcalculated 106 groups data of ground penetrating radar (GPR) and falling weight deflectometer (FWD) field tests of asphalt pavement and found the anisotropic modulus ratio (the ratio of vertical modulus to the horizontal modulus) to be an average of 1.26. One point that needs to be noted is that asphalt mixtures exhibit significant inherent anisotropy only when they are in compression; when an asphalt mixture is under tensile loading, it behaves approximately isotropically (Underwood et al. 2005; Wagoner and Braham 2008). Therefore, this chapter studies the inherent anisotropy of asphalt mixtures under compressive loading only.

The inherent anisotropy of the asphalt mixture needs to be taken into account during the performance analysis of asphalt pavements because both fatigue cracking and plastic deformation may be underestimated if using the assumption of asphalt mixtures being isotropic in compression. Wang et al. (2005) conducted triaxial tests on cubic field samples and showed significant differences in vertical and horizontal stiffness. They further analyzed the pavement

responses in a finite element pavement program using the anisotropic moduli and isotropic modulus, separately. They found larger tensile and shear stresses in the pavement when using the anisotropic moduli than those using the isotropic modulus. Oh et al. (2006) modeled the asphalt pavement using both anisotropic moduli and isotropic modulus for the asphalt layers. Their modeling results indicated that the pavement rutting predicted using the anisotropic moduli matched well with the measured pavement rutting which exceeded the rutting predicted using the isotropic modulus.

To address the preferred orientation of geological structures, a parameter of vector magnitude was firstly introduced by Curray (1956) for quantification of the two dimensional orientation data. Subsequent researchers (Oda and Nakayama 1989; Oda 1993) addressed the inherent anisotropy of soils in terms of the inclination of soil particles by using the concept of vector magnitude which was then used to formulate a microstructure-based fabric tensor to modify the effective stress in the soils during a continuum damage analysis. The similar fabric anisotropy concepts were employed to describe the granular sands and soils properties such as the inherent anisotropy, the directions of principal stresses and the anisotropic elastic deformation (Wong and Arthur 1985; Houque and Tatsuoka 1998; Yoshimine et al. 1998). Recently, by direct application of the fabric tensor, anisotropic behavior of granular soils is successfully simulated by a number of elasto-plastic constitutive models (Li and Dafalias 2002; Dafalias et al. 2004; Lashkari and Latifi 2007; Loukidis and Salgado 2009).

The same formulations of the vector magnitude and the fabric tensor were applied to asphalt mixtures (Masad et al. 2002; Masad and Button 2004; Tashman et al. 2005a; Dessouky et al. 2006; Saadeh et al. 2007). The preferential orientation of the coarse aggregates in the asphalt mixtures was evaluated using X-ray Computed Tomography (X-ray CT) and was then quantified using the vector magnitude. Subsequently, the fabric tensor was formulated based on the vector

magnitude to modify the effective stress in the asphalt mixture during a continuum damage analysis. The fabric tensor formulated using the vector magnitude proved to be an effective indicator of the inherent anisotropy of asphalt mixtures. Taking into account the inclination of coarse aggregates in the continuum damage model produced more accurate predictions of pavement rutting.

However, the inherent anisotropy of asphalt mixtures is not attributed only to the inclination of coarse aggregates. The inclination of fine aggregates also has a contribution to the inherent anisotropy. Moreover, the contribution to the inherent anisotropy of each aggregate may not be the same but will depend on the size, and sphericity as well as the orientation of the aggregate particle. All of these three parameters have to be addressed when quantifying the inherent anisotropy of an asphalt mixture. In other words, the microstructure-based fabric tensor should address not only the inclination of coarse aggregates but the size, orientation and sphericity of both coarse aggregates and fine aggregates whose size is between1.18 mm and 4.75 mm. In order to characterize the fine aggregates, an imaging system with high resolution is required to scan the asphalt mixtures. The images produced by the X-ray CT may not have high enough quality in terms of dots per inch (DPI). Consequently, other imaging methods need to be investigated that can provide higher quality images. In addition, instead of indirectly addressing the inherent anisotropy by using the fabric tensor to modify the effective stress in the material, it is desirable to establish a direct relationship between the inherent anisotropy and the anisotropic moduli of the asphalt mixtures.

This chapter investigates the inherent anisotropy of asphalt mixtures in terms of the size, orientation and sphericity of aggregate particles. These geometric characteristics of aggregates are formulated in a modified vector magnitude to construct the microstructure-based fabric tensor. The next section details the formulation of the modified vector magnitude and the fabric

tensor, which is followed by the laboratory measurement of the modified vector magnitude. The followed section presents a relationship between the modified vector magnitude and the ratio of the vertical modulus to the horizontal modulus, which is then verified based on the laboratory measurements. The final section summarizes the major findings of this chapter.

FORMULATION OF FABRIC TENSOR AND VECTOR MAGNITUDE

The original formulation of the component of the fabric tensor, F_{ij}, which was developed to quantify the inherent anisotropy, is given in Equation 3-1 (Oda and Nakayama 1989; Oda 1993):

$$F_{ij} = \int_{\Omega} m_i m_j E(m)\, d\Omega \qquad (i,\ j = 1,2,3;\ \Omega = 4\pi) \tag{3-1}$$

where m_i and m_j (i, j = 1, 2, 3) = components of a unit vector $\vec{m}$ projected on the orthogonal reference axes x_i (i = 1, 2, 3); Ω = a solid angle corresponding to the entire surface of a unite sphere; and $E(m)$ = probability density function that describes the spatial distribution of the vector $\vec{m}$. For transversely isotropic granular media, the $E(m)$ is neglected and the fabric tensor [F_{ij}] is formulated as:

$$\left[F_{ij}\right] = \begin{bmatrix} F_1 & 0 & 0 \\ 0 & F_2 & 0 \\ 0 & 0 & F_3 \end{bmatrix} = \frac{1}{3+\Delta} \begin{bmatrix} 1-\Delta & 0 & 0 \\ 0 & 1+\Delta & 0 \\ 0 & 0 & 1+\Delta \end{bmatrix} \tag{3-2}$$

where Δ = vector magnitude that is used to quantify the directional distribution of particles and is calculated by:

$$\Delta = \frac{1}{M} \sqrt{\left(\sum_{k=1}^{M} \sin 2\theta_k \right)^2 + \left(\sum_{k=1}^{M} \cos 2\theta_k \right)^2} \tag{3-3}$$

where M = number of particles on an image; θ_k = inclination angle of the major axis of the k^{th} particle measured from the horizontal axis in the image. Oda further interpreted the fabric tensor and emphasized that each particle could be defined by two unit vectors n_i^k and n_j^k which are identical in trend but in opposite directions. Then the fabric tensor in Equation 3-1 can be written as $F_{ij} = \frac{1}{2M}\sum_{k=1}^{2M} n_i^k n_j^k$ which is capable of yielding the same expression for vector magnitude as Equation 3-3.

When applying the formulations of fabric tensor and vector magnitude to asphalt mixtures (Masad et al. 2002; Masad and Button 2004; Tashman et al. 2005a; Dessouky et al. 2006; Saadeh et al. 2007), the vector magnitude, Δ, was used to quantify the directional distribution of coarse aggregates. The number ($k = 1, 2, \cdots\cdots, M$) and inclination angle (θ_k) of the coarse aggregates were obtained by photographing the cut surface or scanning the asphalt mixture using the X-ray CT. The side view of the core sample in Figure 2-1 is re-plotted in Figure 3-1 which illustrates the definition of the aggregate inclination angle in the asphalt mixture.

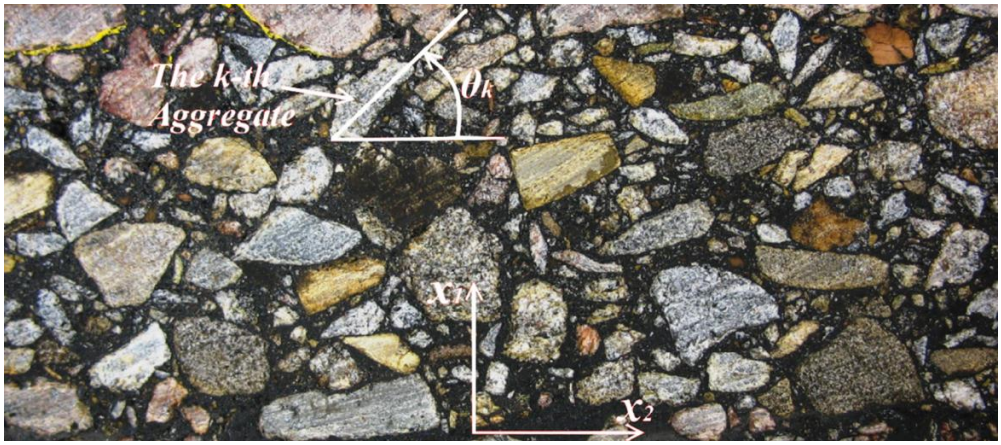

Figure 3-1 Vertical section of an asphalt mixture field core showing aggregate orientation

In Figure 3-1, x_1 is the compaction direction and x_2 is the horizontal direction that is normal to the compaction direction; $-90^o \le \theta_k \le 90^o$. Theoretically, the value of Δ ranges from 0 to 1: $\Delta = 0$ indicates that the aggregates are completely randomly distributed so that the asphalt mixture is isotropic; $\Delta = 1$ implies that all aggregates are oriented in one direction.

The formulations of the fabric tensor and vector magnitude shown in Equations 3-2 and 3-3 are designated for fine-grained materials with approximately uniform particle size, such as soils. These formulations may not be directly applied to aggregates in an asphalt mixture, which do not have uniform particle size or uniform shape. Instead, the fabric tensor and the vector magnitude should be modified so it can address not only the inclination of coarse aggregates but also the size, orientation and sphericity of both coarse and fine aggregates.

The modification of the fabric tensor and the vector magnitude are detailed as follows. First, a vector $\vec{a}^{(k)}$ is introduced to represent the *k*-th aggregate in the asphalt mixture system:

$$\vec{a}^{(k)} = a^{(k)}\vec{n}^{(k)} \qquad k = 1, 2, \cdots, M; \tag{3-4}$$

where $\vec{n}^{(k)}$ = unit vector indicating the orientation of the aggregate, and it has two components in the two dimensional (2-D) orthogonal coordinate system:

$$\begin{cases} n_1^{(k)} = \cos\left(x_1, \vec{n}^{(k)}\right) = \sin\theta_k \\ n_2^{(k)} = \cos\left(x_2, \vec{n}^{(k)}\right) = \cos\theta_k \end{cases} \tag{3-5}$$

$a^{(k)}$ = normalized magnitude of the aggregate addressing the effects of the aggregate size and sphericity, where the aggregate size is characterized by the aggregate area ($\rho^{(k)}$) on the scanned image of the asphalt mixture and the aggregate sphericity is described by the aspect

ratio, $\lambda^{(k)}$ ($\lambda^{(k)}$ = ratio of the longest dimension to the shortest dimension). If set $A_0 \equiv \sum_{k=1}^{M}\left(\rho^{(k)}\lambda^{(k)}\right)$, $a^{(k)}$ can be expressed as:

$$a^{(k)} = \frac{\rho^{(k)}\lambda^{(k)}}{A_0} = \frac{\rho^{(k)}\lambda^{(k)}}{\sum_{k=1}^{M}\left(\rho^{(k)}\lambda^{(k)}\right)} \tag{3-6}$$

Second, the component of the fabric tensor is redefined in the 2-D coordinate system as:

$$\bar{F}_{ij} = \int_{\Omega} a^{(k)}\vec{n}_i^{(k)}\vec{n}_j d\Omega \qquad \left(i,\ j = 1,2;\quad \Omega = 2\pi\right) \tag{3-7}$$

In fact, the 2-D fabric tensor ($\left[\bar{F}_{ij}\right]$) can be interpreted as the quantitative estimate of the influence of an aggregate (with magnitude of $a^{(k)}$ and orientation of $\vec{n}_i^{(k)}$) on a specific direction ($\vec{n}_j$). The aggregate magnitude ($a^{(k)}$) is introduced to replace the probability density function $E(m)$ in Equation 3-1 and to represent the effects of the aggregate size and sphericity on the inherent anisotropy. The fabric tensor has three independent components:

$$\begin{cases} \bar{F}_{11} = \dfrac{1}{A_0}\sum_{k=1}^{M}\left[\rho^{(k)}\lambda^{(k)}\sin^2\theta^{(k)}\right] \\ \bar{F}_{12} = \bar{F}_{21} = \dfrac{1}{A_0}\sum_{k=1}^{M}\left[\rho^{(k)}\lambda^{(k)}\sin\theta^{(k)}\cos\theta^{(k)}\right] \\ \bar{F}_{22} = \dfrac{1}{A_0}\sum_{k=1}^{M}\left[\rho^{(k)}\lambda^{(k)}\cos^2\theta^{(k)}\right] \end{cases} \tag{3-8}$$

Then two principal values of the 2-D fabric tensor can be calculated because the fabric tensor is a symmetric second order tensor. Solving the characteristic equation $\left|\bar{F}_{ij} - F\delta_{ij}\right| = 0$ yields:

$$\begin{Bmatrix} \bar{F}_1 \\ \bar{F}_2 \end{Bmatrix} = \frac{\bar{F}_{11} + \bar{F}_{22}}{2} \mp \sqrt{\frac{1}{4}\left(\bar{F}_{11} - \bar{F}_{22}\right)^2 + \bar{F}_{12}^2} = \frac{1 \mp \Delta'}{2} \tag{3-9}$$

where Δ' = the modified vector magnitude that is formulated as:

$$\Delta' = \frac{1}{A_0}\sqrt{\left(\sum_{k=1}^{M} \rho^{(k)} \lambda^{(k)} \sin 2\theta_k\right)^2 + \left(\sum_{k=1}^{M} \rho^{(k)} \lambda^{(k)} \cos 2\theta_k\right)^2} \tag{3-10}$$

where $A_0 = \sum_{k=1}^{M}\left(\rho^{(k)} \lambda^{(k)}\right)$, $\rho^{(k)}$ = area of k-th aggregate on the image of the asphalt mixture, and $\lambda^{(k)}$ = aspect ratio of k-th aggregate. As can be seen from Equation 3-10, the modified vector magnitude addresses the effects of the aggregate size, orientation and sphericity of both coarse aggregates and fine aggregates on the inherent anisotropy. By comparing Equation 3-10 to Equation 3-3, the modified vector magnitude can be interpreted as follows: the effect of the inclination angle on the anisotropy of an asphalt mixture is emphasized or de-emphasized based on the aggregate size (area) and sphericity (aspect ratio). For example, if the aggregate is larger or more flat and elongated, the inclination angle will contribute more anisotropy to the mixture. If the aggregate is smaller or has a more rounded shape, the net effect is to decrease the influence of the inclination angle on anisotropy. The next section will detail the test procedure for characterizing these aggregate characteristics to determine the modified vector magnitude.

Using the same approach reported in the literature (Oda and Nakayama 1989), the 2-D fabric tensor is transferred to a 3-D fabric tensor ($\left[F'_{ij}\right]$) as shown in Equation 3-11 that has a similar form to the original 3-D fabric tensor shown in Equation 3-2. This fabric tensor ($\left[F'_{ij}\right]$) can be employed when using continuum mechanics principles to study asphalt mixtures or granular bases.

$$\left[F'_{ij}\right]=\begin{bmatrix} F'_1 & 0 & 0 \\ 0 & F'_2 & 0 \\ 0 & 0 & F'_3 \end{bmatrix}=\frac{1}{3+\Delta'}\begin{bmatrix} 1-\Delta' & 0 & 0 \\ 0 & 1+\Delta' & 0 \\ 0 & 0 & 1+\Delta' \end{bmatrix} \quad (3\text{-}11)$$

DETERMINATION OF MODIFIED VECTOR MAGNITUDE

In order to determine the modified vector magnitude formulated in Equation 3-10, aggregate characteristics must be measured including the inclination angle (θ_k), cutting surface area ($\rho^{(k)}$), and aspect ratio ($\lambda^{(k)}$). In the previous research (Masad et al. 2002), only the inclination angle was measured on the cutting surface of Lab-Mixed-Lab-Compacted (LMLC) asphalt mixture specimens. Specifically, the LMLC specimens were cut into vertical sections or horizontal sections that were photographed using a digital camera or scanned using the X-ray CT to obtain the images of the sections. If using this technique to measure the aggregate characteristics, the specimens would be damaged in the cutting process and could not be reused in the future tests. Consequently, additional specimens have to be fabricated and tested for their physical properties such as modulus and Poisson's ratio in order to establish the relationship between the microstructure and physical properties of the asphalt mixtures. This would also introduce sample to sample error. In addition, the images scanned by the X-ray CT may not have sufficient resolution to distinguish certain types of aggregates (such as limestone) from the asphalt mastic if the density of the aggregates is not significantly different from the asphalt mastic that consists of the asphalt binder, fine aggregates and mineral powder. As a result, a nondestructive test is desired to provide images of the asphalt mixture specimens with a sufficient resolution for the purpose of saving materials, eliminating sample to sample errors and obtaining more accurate aggregate characteristics.

Experimental Design and Image Analysis

To address this research need, an efficient and economical test is developed in this study to nondestructively measure the aggregate characteristics (θ_k, $\rho^{(k)}$ and $\lambda^{(k)}$). The minimum size of the aggregates that is characterized in this study is chosen to be 1.18 mm, which is the size of No. 16 sieve. This minimum size of aggregates is selected because the aggregates smaller than 1.18 mm have relatively negligible contribution to the anisotropy of the asphalt mixture and they can be considered to be imbedded in the asphalt binder to form the isotropic asphalt mastic according to the literature (You and Buttlar 2004). Therefore, a portable optical scanner with a maximum resolution of 600 dots per inch (DPI) is utilized to obtain the asphalt mixture images, which clearly capture the image of the aggregates as small as 1.18 mm. The procedure of the proposed test is detailed as follows.

Firstly, the same 16 LMLC asphalt mixture specimens that were sued in the anisotropic viscoelastic characterization (Chapter II which performed nondestructive tests) were employed in the inherent anisotropic characterization (Chapter III).

Secondly, each specimen is laid horizontally on an automatic rotator as shown in Figure 3-2. A speed controller is connected to the motor to control the speed of the rotator. The portable scanner is installed on top of the specimen to scan the lateral surface of the cylindrical specimen while the specimen is rotating on the rotator.

After scanning the entire lateral surface of the specimen, the scanner produces an image with 150 mm in height and 314 mm in width, as illustrated in Figure 3-3 (a). This image is then analyzed using the software Image-Pro Plus to identify the aggregates within the asphalt mixture, which are presented in Figure 3-3 (b).

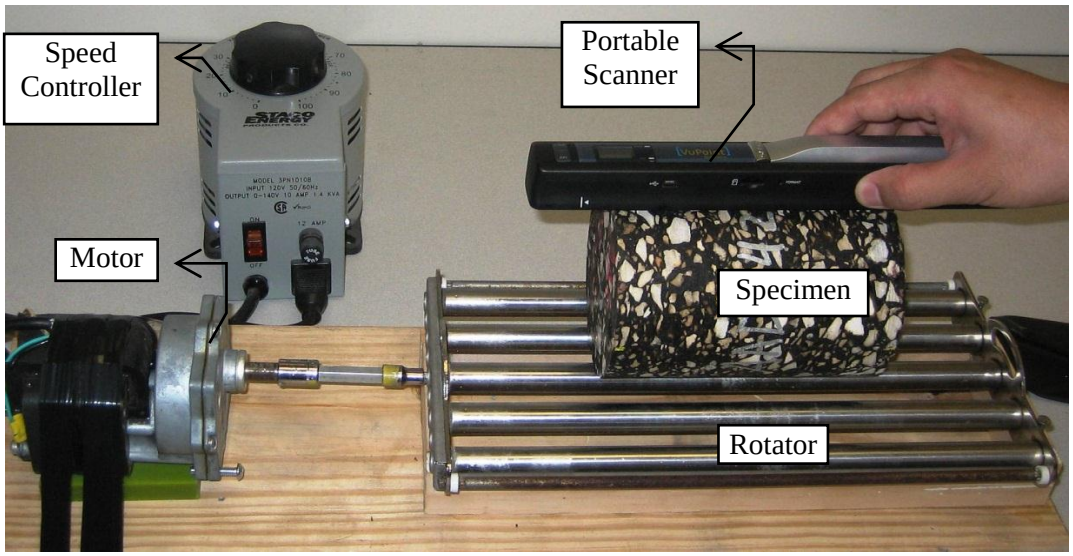

Figure 3-2 Configuration of lateral surface scanning of an asphalt mixture sample

Thirdly, after identifying the aggregate particles, the image is further processed using Image-Pro Plus (MediaCybernetics 2000) to determine the characteristics of each aggregate as follows:

- Inclination angle (θ_k): angle between the horizontal axis and the major axis of the ellipse equivalent to the aggregate particle, $-90^o \le \theta_k \le 90^o$ (see Figure 3-4 (a));
- Cutting surface area ($\rho^{(k)}$): area of the cutting surface of the aggregate (see Figure 3-4 (b)); and
- Aspect ratio ($\lambda^{(k)} = a/b$): ratio of the major axis to the minor axis of the ellipse equivalent to the aggregate particle (see Figure 3-4 (c)).

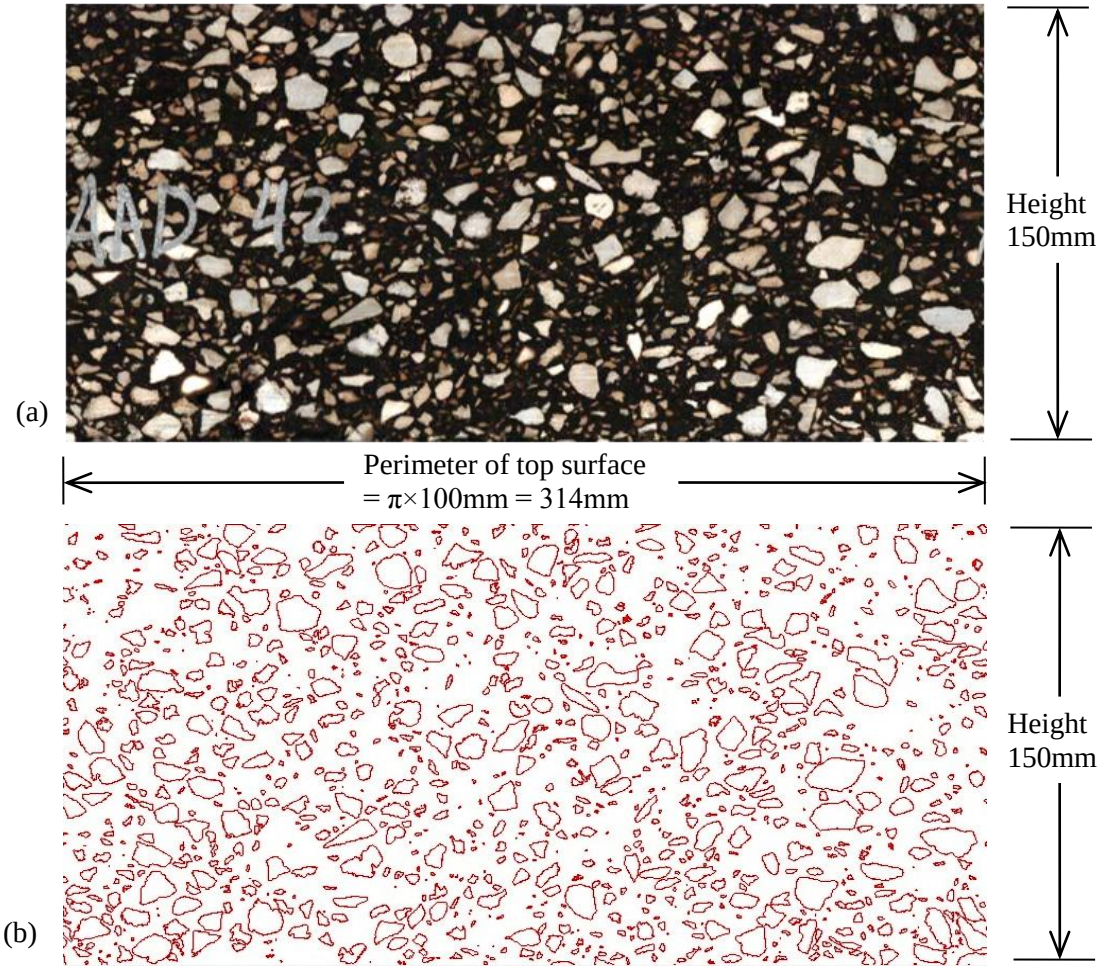

Figure 3-3 Lateral surface of a cylinder asphalt mixture sample (a) Original scan (b) Plot of outline of aggregates

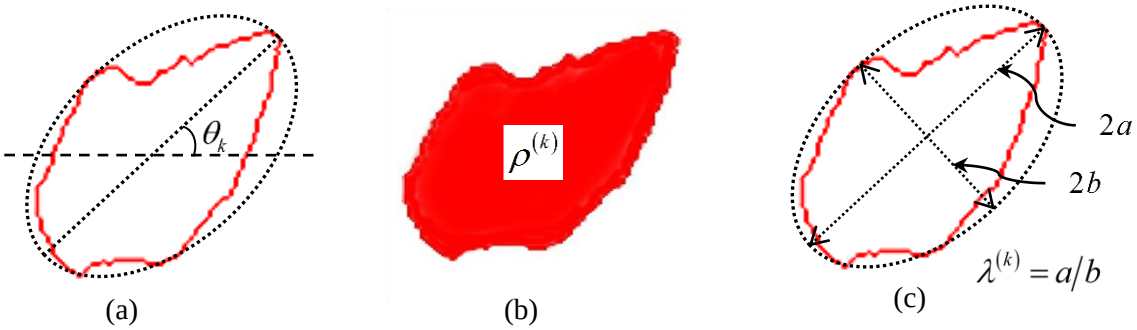

Figure 3-4 Measurements of k-th aggregate characteristics (a) Inclination Angle (b) Cutting surface area (c) Aspect ratio

Results of Modified Vector Magnitude

Based on the aforementioned experimental design, the lateral surface scanning test and image analysis were performed on each of the asphalt mixture specimens. The absolute values of the measured aggregates' inclination angles ($|\theta_k|$) are classified into 9 intervals: $[0^\circ, 10^\circ]$, $(10^\circ, 20^\circ]$, $(20^\circ, 30^\circ]$, $(30^\circ, 40^\circ]$, $(40^\circ, 50^\circ]$, $(50^\circ, 60^\circ]$, $(60^\circ, 70^\circ]$, $(70^\circ, 80^\circ]$, and $(80^\circ, 90^\circ]$. Then the percentage of the aggregates in each interval is calculated using the number of aggregates in the corresponding interval divided by the total number of aggregates measured on the lateral surface of the specimen. Statistical analysis is performed on the calculation results of all 16 specimens to determine the average, maximum and minimum percentage in each interval of the 16 specimens, which are illustrated in Figure 3-5.

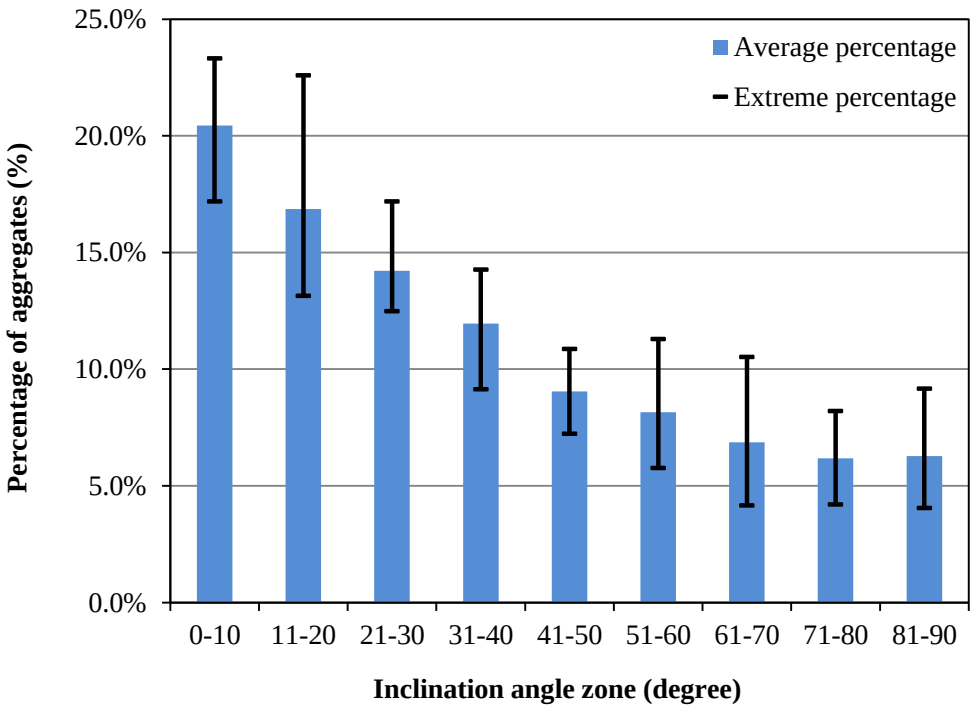

Figure 3-5 Distribution of aggregate inclination angles of asphalt mixtures

Figure 3-5 shows that an average of approximately 20% of the aggregates has an inclination angle between -10 °and 10 °, and two-thirds of the aggregates have an inclination angle between -45 °and 45 °. Since a small inclination angle indicates the aggregate lies flat in the horizontal direction, the measurements demonstrate that the aggregates have a preferential distribution in the horizontal direction that is perpendicular to the compaction direction.

Finally, the modified vector magnitude (Δ') is calculated for all 16 specimens based on the measured θ_k, $\rho^{(k)}$ and $\lambda^{(k)}$ according to Equation 3-10, and the values of Δ' are tabulated in Table 3-1. The values of the original vector magnitude (Δ) are also calculated that address only the inclination angles of the aggregates in the scanned image.

Table 3-1 Vector Magnitudes of Measured Asphalt Mixture Specimens

Aging Period	Binder	Air Void Content	Replicate Specimen	Δ'	Δ
0 Month Aging	AAD	4%	No.1	0.236	0.029
			No.2	0.310	0.053
		7%	No.1	0.258	0.039
			No.2	0.236	0.038
	AAM	4%	No.1	0.315	0.019
			No.2	0.301	0.051
		7%	No.1	0.267	0.008
			No.2	0.254	0.018
6 Month Aging	AAD	4%	No.1	0.450	0.171
			No.2	0.386	0.082
		7%	No.1	0.376	0.154
			No.2	0.381	0.116
	AAM	4%	No.1	0.364	0.162
			No.2	0.410	0.141
		7%	No.1	0.435	0.147
			No.2	0.425	0.142

Comparing Δ to Δ' in Table 3-1, the value of Δ' is significantly larger than the value of Δ; in certain cases, they are not even in the same order. As stated in previous sections, a smaller value of the vector magnitude indicates that the aggregates are more randomly

distributed in the mixture so the mixture is less anisotropic while a larger value of the vector magnitude implies that the aggregates are more horizontally oriented. Therefore, the fact of Δ being significantly smaller than Δ' demonstrates that the original formulation of the vector magnitude (Δ) substantially underestimates the inherent anisotropy of the asphalt mixtures. In other words, the inclination angle itself is not sufficient to quantify the inherent anisotropy of asphalt mixtures. The size and sphericity of the aggregates must be addressed to more accurately quantify the mixture's inherent anisotropy.

RELATIONSHIP BETWEEN VECTOR MAGNITUDE AND MODULUS RATIO

It is desired to develop the relationship between the modified vector magnitude (Δ') and the modulus ratio ($\left|E_{11}^*\right| / \left|E_{22}^*\right|$) in order to quantify the inherent anisotropy of the asphalt mixtures. This subsection presents the theoretical derivation and the experimental verification.

Derivation of Theoretical Relationship

The development of the relationship between Δ' and $\left|E_{11}^*\right| / \left|E_{22}^*\right|$ starts from the general polynomial relation between the elastic modulus tensor and the fabric tensor of an elastic material (Cowin 1985; Tobita and Yanagisawa 1992). In the case of granular materials such as soils, aggregate base and asphalt mixtures, the high order terms in the polynomial function can be neglected and the elastic relation becomes (Oda and Nakayama 1989; Oda 1993; Tashman et al. 2004):

$$C_{ijkl} = 2b_6\delta_{ik}\delta_{jl} + 4b_7F'_{ik}\delta_{lj} \qquad i, j, k, l = 1, 2, 3 \tag{3-12}$$

where C_{ijkl} = elastic modulus tensor; δ_{ij} = Kronecker delta; $\left[F'_{ik}\right]$ is the 3-D fabric tensor given in Equation 3-11; b_6 and b_7 are material parameters which can be determined using Equation 3-13 (Oda and Nakayama 1989).

$$\begin{cases} b_6 = \dfrac{1}{4} - \dfrac{\mu}{2}\sqrt{2D_2} \\ b_7 = \dfrac{3}{4}\mu\sqrt{2D_2} \end{cases} \tag{3-13}$$

where μ = experimentally determined parameter; and D_2 = second invariant of the deviatoric fabric tensor. Since the deviatoric fabric tensor can be calculated using Equation 3-14:

$$F''_{ij} = F_{ij}' - \frac{1}{3}F'_{kk}\delta_{ij} = \frac{2\Delta'}{3\left(3+\Delta'\right)}\begin{bmatrix} -2 & 0 & 0 \\ 0 & 1 & 0 \\ 0 & 0 & 1 \end{bmatrix} \tag{3-14}$$

The second invariant of the deviatoric fabric tensor (D_2) is determined using Equation 3-15:

$$D_2 = \frac{1}{2}F''_{ij}F''_{ji} = \frac{4\Delta'^2}{3\left(3+\Delta'\right)^2} \tag{3-15}$$

Let σ_{ij} be the stress tensor and ε_{kl}^{el} be the elastic strain tensor, the constitutive relation for an elastic material is:

$$\sigma_{ij} = C_{ijkl}\varepsilon_{kl}^{el} \qquad i,j,k,l = 1,2,3 \tag{3-16}$$

The truncated format of the constitutive relation in Equation 3-16 is shown as:

$$\sigma_m = C_{mn}\varepsilon_n^{el} \qquad m,n = 1,2,3,4,5,6 \tag{3-17}$$

For a cross-anisotropically elastic material, the truncated format of the constitutive relations with the normal stresses and strains only is:

$$\begin{pmatrix}\sigma_1\\ \sigma_2\\ \sigma_3\end{pmatrix}=\begin{bmatrix}C_{11} & C_{12} & C_{12}\\ C_{12} & C_{22} & C_{23}\\ C_{12} & C_{23} & C_{22}\end{bmatrix}\begin{pmatrix}\varepsilon_1\\ \varepsilon_2\\ \varepsilon_3\end{pmatrix} \tag{3-18}$$

in which C_{11} and C_{22} are functions of the modulus and Poisson's ratio, and shown as.

$$C_{11}=\frac{E_{11}\left(1-\nu_{22}\right)}{1-\nu_{22}-2\nu_{12}\nu_{21}} \tag{3-19}$$

$$C_{22}=\frac{E_{22}\left(E_{11}-\nu_{12}^2E_{22}\right)}{E_{11}\left(1+\nu_{22}\right)\left(1-\nu_{22}-2\nu_{12}\nu_{21}\right)} \tag{3-20}$$

where E_{11} = elastic modulus in the x_1 direction; E_{22} = elastic modulus in the x_2 direction; and ν_{ij} = Poisson's ratio in the ij plane. In the mean time, $C_{ijkl}=C_{mn}$ is a function of F'_{ik} according to Equation 3-12. Therefore, C_{11} and C_{22} are also functions of F'_{11} and F'_{22}, respectively, as shown in Equations 3-21 and 3-22.

$$C_{11}=C_{1111}=2b_6+4b_7F'_{11} \tag{3-21}$$

$$C_{22}=C_{2222}=2b_6+4b_7F'_{22} \tag{3-22}$$

Substituting Equations 3-11, 3-13, 3-19 and 3-20 into Equations 3-21 and 3-22 yields:

$$-3\sqrt{6}\mu\left(\sqrt{D_2}\right)^2=\frac{\left(1-\nu_{22}\right)E_{22}}{\left(1-\nu_{22}-2\nu_{12}\nu_{21}\right)}\left(\sqrt{\frac{E_{11}}{E_{22}}}\right)^2-\frac{\left(1-\nu_{12}\nu_{21}\right)E_{22}}{\left(1+\nu_{22}\right)\left(1-\nu_{22}-2\nu_{12}\nu_{21}\right)} \tag{3-23}$$

where $\frac{\nu_{12}}{E_{11}}=\frac{\nu_{21}}{E_{22}}$ is used. Equation 3-23 indicates an approximate linear relation between $\sqrt{D_2}$ and $\sqrt{E_{11}/E_{22}}$, which may have the following form:

$$\sqrt{D_2}=\frac{2\sqrt{3}\Delta'}{3\left(3+\Delta'\right)}=k\left(\sqrt{\frac{E_{11}}{E_{22}}}-1\right)+b \tag{3-24}$$

where k and b are the slope and intercept of the fitting line, respectively.

When applying this relation to asphalt mixtures, the ratio of the representative moduli at a specific frequency ($\left|E_{11}^*\right|/\left|E_{22}^*\right|$) will be used to replace E_{11}/E_{22} in Equation 3-24. The boundary conditions are as follows:

- If $\Delta' = 0$, then $\sqrt{D_2} = 0$, the aggregates are randomly distributed and the material is isotropic, which indicates $\left|E_{11}^*\right|/\left|E_{22}^*\right|$ = 1;
- If $\Delta' = 1$, then $\sqrt{D_2} = \frac{1}{2\sqrt{3}}$, the aggregates orients along one direction, the material is fully cross-anisotropic, and the modulus ratio ($\left|E_{11}^*\right|/\left|E_{22}^*\right|$) has the maximum value (let $\max\left\{\left|E_{11}^*\right|/\left|E_{22}^*\right|\right\} \equiv q$).

Employing these two boundary conditions in Equation 3-24 to solve for k and b yields:

$$\begin{cases} k = \dfrac{\sqrt{3}}{6\left(\sqrt{q}-1\right)} \\ b = 0 \end{cases} \tag{3-25}$$

Substituting Equation 3-25 into Equation 3-24, the relationship between Δ' and $\left|E_{11}^*\right|/\left|E_{22}^*\right|$ is developed as:

$$\Delta' = \frac{3\left(\sqrt{\dfrac{\left|E_{11}^*\right|}{\left|E_{22}^*\right|}}-1\right)}{4\left(\sqrt{q}-1\right)-\left(\sqrt{\dfrac{\left|E_{11}^*\right|}{\left|E_{22}^*\right|}}-1\right)} \tag{3-26}$$

Experimental Verification of the Relationship

Based on the measurements of the vertical and horizontal complex modulus in Chapter II, the modulus ratio ($\left|E_{11}^{*}\right|/\left|E_{22}^{*}\right|$) is calculated for each replicate of the mixture with the same asphalt binder, air void content and aging period. The frequency of the vertical modulus and horizontal modulus ranges from 0.05 Hz to 50 Hz in order to determine the modulus ratios at a variety of frequencies. Then the mean and standard deviation of the modulus ratio over the frequency range is calculated and plotted against the modified vector magnitude (Δ'), as illustrated in Figure 3-6, in which each diamond represents the average $\left|E_{11}^{*}\right|/\left|E_{22}^{*}\right|$ of a specimen.

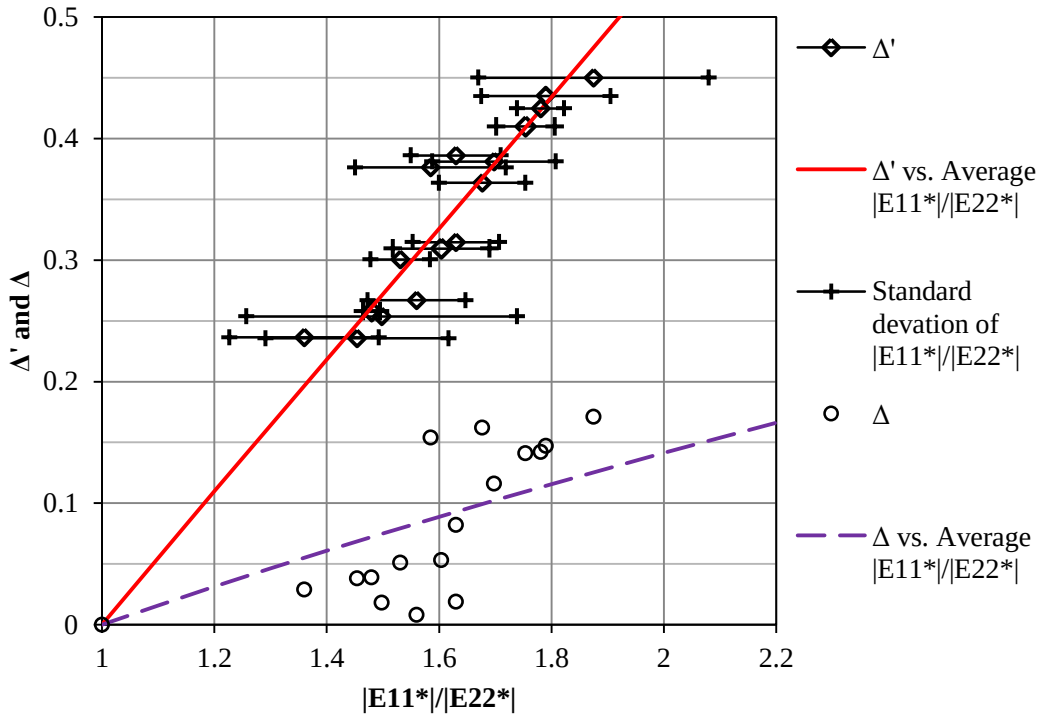

Figure 3-6 Relationship of vector magnitude with anisotropic modulus ratio

As can be seen from Figure 3-6, the average $\left|E_{11}^{*}\right| / \left|E_{22}^{*}\right|$ ranges from 1.2 to 2.0 with a corresponding Δ' ranging from 0.2 to 0.5. A higher value of the modified vector magnitude is associated with a larger modulus ratio, which indicates a stronger anisotropy of the specimen. The modulus ratio is found to depend solely on the modified vector magnitude that is a measure of the size, orientation and sphericity of the aggregate particles. These aggregate characteristics are the inherent properties of the asphalt mixture; they determine the level of the inherent anisotropy of the mixture. In contrast, the modulus ratio is independent of the type of the asphalt binder, air void content and mixture aging period.

The data of the modified vector magnitudes and the modulus ratios are fitted into Equation 3-26 using regression analysis and shown in Equation 3-27. The maximum modulus ratio (q) is determined to be 2.808 with an R-squared value of 0.9439. The reasonable value of the maximum modulus ratio and the high R-squared value demonstrate the goodness of this model. Equation 3-27 effectively establishes a bridge between the aggregate characteristics and the physical properties of the asphalt mixtures. This relationship promotes the understanding of the influence of the internal structure on the anisotropy of the asphalt mixture; it also brings convenience to the laboratory and field testing of asphalt mixtures. For example, when measuring the anisotropic properties of field pavement sections, the modified vector magnitude, vertical modulus and horizontal modulus can be measured on a number of field cores. Then the relationship between the modified vector magnitude and the modulus ratio can be developed using Equation 3-26. This relationship can be used together with the nondestructive testing data on the field pavement sections to predict the horizontal modulus of the field pavement in the entire project length.

$$\Delta' = \frac{3\left(\sqrt{\frac{|E_{11}^*|}{|E_{22}^*|}} - 1\right)}{4\left(\sqrt{2.808} - 1\right) - \left(\sqrt{\frac{|E_{11}^*|}{|E_{22}^*|}} - 1\right)} \qquad R^2 = 0.9439 \tag{3-27}$$

Regression analysis is also performed on the data of the original vector magnitude (Δ) that addresses only the inclination angle of the aggregates in the scanned image. When fitting the data of Δ into Equation 3-26, the model is shown in Equation 3-28 which indicates that the maximum modulus ratio is 10.9 that is impossible for an asphalt mixture and the R-squared value is only 0.4559. This fact demonstrates that the inclination angle of the aggregate alone is insufficient to appropriately quantify the inherent anisotropy of the asphalt mixtures and the original vector magnitude is not applicable for granular media having a non-uniform distribution of particle size and shape.

$$\Delta = \frac{3\left(\sqrt{\frac{|E_{11}^*|}{|E_{22}^*|}} - 1\right)}{4\left(\sqrt{10.9} - 1\right) - \left(\sqrt{\frac{|E_{11}^*|}{|E_{22}^*|}} - 1\right)} \qquad R^2 = 0.4559 \tag{3-28}$$

SUMMARIES AND CONCLUSIONS

Asphalt mixtures are demonstrated to be cross anisotropic materials in both laboratory and field tests. The anisotropy of the asphalt mixture is classified into inherent anisotropy and stress-induced anisotropy. The inherent anisotropy is investigated in this study based on the internal microstructure of the aggregates in the asphalt mixture and is represented by an aggregate-related geometric parameter, a modified vector magnitude. The original formulation of the vector magnitude, which addresses only the orientation of coarse aggregates, is modified to

take into account not only the coarse aggregate orientation, but also the size, orientation and sphericity of coarse and fine aggregates. This formulation is applied to 16 cylindrical LMLC asphalt mixture specimens varying in asphalt binder type, air void content and aging period. The lateral surface of each cylindrical specimen is scanned to measure the inclination angle, surface area and aspect ratio of the aggregates, which are then employed to calculate the modified vector magnitude. The calculation results indicate that the aggregates in an asphalt mixture indeed have a preferential orientation along the horizontal direction and two-thirds of the aggregates have an inclination angle between -45 °and 45 °. The modified vector magnitude of every specimen is found to be significantly larger than the original vector magnitude that addresses only the inclination angle. This fact indicates that the original vector magnitude substantially underestimates inherent anisotropy of the asphalt mixtures. The inclination angle itself is not sufficient to quantify the inherent anisotropy of the asphalt mixtures.

Three nondestructive tests, including the compressive creep test, tensile creep test and indirect tensile creep test, are performed on the same LMLC asphalt mixture specimens at three temperatures to measure the vertical modulus and the horizontal modulus. Master curves are constructed for the measured vertical and horizontal moduli. The vertical modulus is proved to be higher than the horizontal modulus at any specific frequency for all mixture types. The ratio of the vertical modulus to the horizontal modulus is then calculated and plotted against the corresponding modified vector magnitude. Among the various types of asphalt mixtures measured in this study, the modulus ratio ranges from 1.2 to 2.0 corresponding to a modified vector magnitude between 0.2 and 0.5.

A relationship between the modified vector magnitude and the modulus ratio is developed to quantify the influence of the inherent microstructure of the aggregates on the anisotropy of the mixtures. The R-squared value of this model has a high value of 0.9439. The

maximum modulus ratio is determined to be approximately 2.808. The modulus ratio solely depends on the aggregate characteristics including the inclination angle, size and sphericity, and it is independent of the asphalt binder type, air void content and aging period. This relationship successfully serves as a bridge between the physical properties and anisotropy of the asphalt mixtures.

CHAPTER IV

STRAIN DECOMPOSITION FOR PERMANENT DEFORMATION AND FRACTURE CHARACTERIZATIONS*

OVERVIEW

Permanent deformation and fracture may develop simultaneously when an asphalt mixture is subjected to a compressive load. The objective of this chapter is to separate the viscoplasticity and viscofracture from the viscoelasticity so that the permanent deformation and fracture of the asphalt mixtures can be individually and accurately characterized without the influence of the viscoelasticity. The undamaged properties of 16 asphalt mixtures that have two binder types, two air void contents and two aging periods are firstly obtained by conducting nondestructive creep tests and nondestructive dynamic modulus tests. Testing results are analyzed by using linear viscoelastic theory, in which creep compliance and relaxation modulus are modeled by the Prony model. The dynamic modulus and phase angle of the undamaged asphalt mixtures are found to remain constant with load cycle.

The undamaged asphalt mixtures are then used to perform destructive dynamic modulus tests, in which the dynamic modulus and phase angle of the damaged asphalt mixtures are found to vary with load cycle, which indicates the plastic evolution and the crack propagation. The growth of cracks is signaled principally by the increase of the phase angle, which occurs only in the tertiary stage. The measured total strain in the destructive dynamic modulus test is successfully decomposed into elastic strain, viscoelastic strain, plastic strain, viscoplastic strain

*Reprinted with permission from ASCE: "Characterizing Permanent Deformation and Fracture of Asphalt Mixtures using Compressive Dynamic Modulus Tests." by Yuqing Zhang, Rong Luo and Robert L. Lytton, 2012, *Journal of Materials in Civil Engineering*, 24(7), 898-906. Copyright [2012], ASCE.

and viscofracture strain by employing the pseudo strain concept and the extended elastic-viscoelastic correspondence principle. The separated viscoplastic strain is modeled with the Tseng-Lytton model to characterize the permanent deformation. The separated viscofracture strain is modeled by a fracture strain model to characterize the fracture of the asphalt mixtures, in which the flow number is determined and a crack speed index is proposed. Comparisons between the 16 samples show that the aged asphalt mixtures with lower air void content have a better performance resisting both permanent deformation and fracture.

INTRODUCTION

Permanent deformation (rutting) and fracture (cracking) are two major distresses of asphalt pavements. They may occur simultaneously under a compressive load and can significantly reduce the service life of the field asphalt pavements as described in Chapter I. The permanent deformation of asphalt mixtures primarily results from the irrecoverable viscoplastic deformation which has been investigated carefully using continuum mechanics. The cracks under compressive loads are randomly and widely distributed in the asphalt mixtures and they are normally characterized using an overall parameter such as damage density resulting from damage mechanics. The damage density is then embedded into the continuum mechanics to consider the evolution of viscofracture (time dependent fracture) and effect of the cracks on the viscoplastic deformation.

The continuum models for asphalt mixtures have an advantage in their computational simplicity, that is, the material responses such as permanent deformation can be easily estimated once the model parameters are provided. To accurately determine the model parameters for different material performances, the properties of viscoelasticity, viscoplasticity and viscofracture for the asphalt mixtures need be individually investigated and characterized.

However, the measured data in the tests are normally the total deformation or strain that represents the overall material properties of the asphalt mixtures. Thus, it is urgently necessary to conduct the strain decomposition on the testing results for the purpose of the accurate characterizations of the viscoplasticity and viscofracture.

The strain decomposition is usually accomplished by running the creep and recovery test in which repeated rest periods are provided during the creep test (Sides et al. 1985; Drescher et al. 1993; Uzan 1996; Masad et al. 2009; Darabi et al. 2011). Figure 4-1 shows a typical strain-versus-time curve in the creep and recovery test which has three distinctive strain stages:

1) Primary stage with a decreasing strain rate;
2) Secondary stage with a constant strain rate; and
3) Tertiary stage with an increasing strain rate.

The total strain is usually decomposed into four components:

1) Elastic strain that is recoverable and time-independent;
2) Viscoelastic strain that is recoverable and time-dependent;
3) Plastic strain that is irrecoverable and time-independent; and
4) Viscoplastic strain that is irrecoverable and time-dependent.

In the recovery period, the instantaneously recovered strain is the elastic strain and the retarded recovered strain is the viscoelastic strain. This currently used strain decomposition method assumes that the recovery time is sufficiently long so that the viscoelastic strain is fully recovered and that the remaining strain is the sum of the viscoplastic strain and the plastic strain. However, this strain decomposition method is associated with three problems:

1) It is impossible to directly separate the strain components in the creep process of the test, and the recovery loading time that is required will increase the testing time;

2) The accumulated strain at the end of each recovery period may include not only the plastic strain and the viscoplastic strain but also the viscoelastic strain that has not recovered yet due to the limited recovery time in the test; and
3) This method does not account for the viscofracture strain at all. In fact, when the total strain reaches the tertiary stage, the viscofracture strain develops due to the growth of cracks. Thus, the total strain should be decomposed into five components, including the viscofracture strain and the four aforementioned strain components.

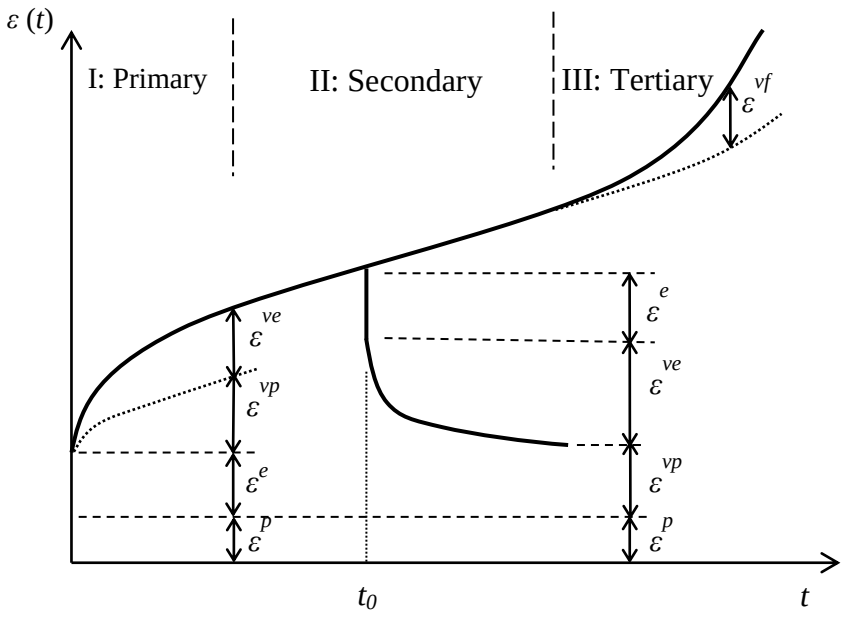

Figure 4-1 Schematic plot of the strain decomposition in a creep and recovery test

To address the above problems with the current strain decomposition method, this chapter aims at:

- Completely separate the viscoplastic strain and viscofracture strain from the other strain components when the asphalt mixtures are subjected to a compressive load; and

- Accurately characterize the permanent deformation and fracture of the asphalt mixtures, respectively, without influence of viscoelasticity.

In order to achieve these two objectives, this chapter proposes a new strain decomposition approach that decomposes the total strain of the material into five components, shown as follows:

$$\varepsilon^T = \varepsilon^e + \varepsilon^{ve} + \varepsilon^p + \varepsilon^{vp} + \varepsilon^{vf} \tag{4-1}$$

where ε^T = total strain; ε^e = elastic (instantaneous) strain; ε^{ve} = viscoelastic strain; ε^p = plastic strain; ε^{vp} = viscoplastic strain; and ε^{vf} = viscofracture strain. Since the strain caused by cracks has an increasing strain rate while the strain resulted from viscoplasticity has a decreasing strain rate, the increasing strain rate in the tertiary stage indicates that ε^{vf} develops only in the tertiary stage. Once the total strain is decomposed, the separated ε^{vp} and ε^{vf} are then used to characterize the permanent deformation and fracture of the asphalt mixtures, respectively.

This chapter is organized as follows. The next section discusses the proposed laboratory experiments for the purpose of strain decomposition, which is followed by a linear viscoelastic characterization of the undamaged asphalt mixtures. Then the strain decomposition is presented by employing the extended elastic-viscoelastic correspondence principle and the pseudo strain concept. The following section is the permanent deformation characterization using the separated viscoplastic strain curve and the fracture characterization based on the separated viscofracture strain data from destructive compressive dynamic modulus tests. The last section summarizes the major findings in this chapter.

LABORATORY EXPERIMENTS

Sixteen (16) lab-mixed-lab-compacted (LMLC) asphalt mixture specimens in addition to the samples used for viscoelasticity and inherent anisotropic characterization in Chapters II and III were fabricated with the following variables:

- Two types of asphalt binder: labeled by AAM and AAD in the Strategic Highway Research Program (SHRP) Materials Reference Library (MRL) (Jones 1993);
- Two air void contents: 4% and 7% (variation within ±0.5%); and
- Two aging periods: unaged and continuous 6-month 60 ℃ aged asphalt mixtures.

Two replicate specimens were made for each combination of the asphalt binder, air void content and aging period. The same materials and compaction processes were used in the sample fabrications as that in the viscoelastic characterization of Chapter II.

The testing protocol including the sequence of loading and testing methods was designed according to the mechanistic theories that were employed in the characterization of the viscoplasticity and viscofracture of the asphalt mixtures. In this chapter, the viscoplasticity and viscofracture were differentiated from the viscoelasticity by using a strain decomposition methodology, which yielded two principles for the selection of the loading sequence: 1) to quantify how far the damages including the viscoplasticity and viscofracture depart from the undamaged condition, the viscoelasticity that is the property of the undamaged material needs to be characterized firstly by using nondestructive tests; and 2) to introduce significant damage to the asphalt mixtures, the stress level needs to be increased in the destructive tests which will be continued until the material failed in the tertiary deformation stage.

Therefore, based on the aforementioned principles, an experimental protocol was developed that includes three tests: 1) a nondestructive compressive creep test to obtain the creep compliance and relaxation modulus of the undamaged asphalt mixtures, which have been

finished in Chapter II; 2) a nondestructive compressive dynamic modulus test to obtain the dynamic modulus and phase angle of the undamaged asphalt mixtures; and 3) a destructive compressive dynamic modulus test to obtain the dynamic modulus and phase angle of the damaged asphalt mixtures. The total strain measured in the destructive dynamic modulus test was used to conduct the strain decomposition. The three tests of the testing protocol had the same testing configurations as shown in Figure 4-2.

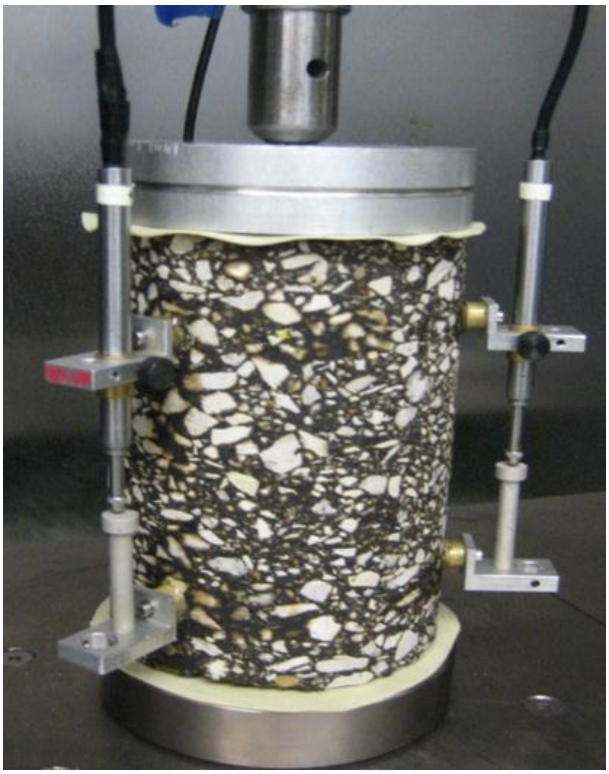

Figure 4-2 Configurations of creep test and dynamic modulus tests

In Figure 4-2, three vertical linear variable differential transformers (LVDTs) with a gauge length of 90 mm were mounted at 120 °from each other on the lateral surface of each asphalt mixture specimen. The specimens were stored in the environmental chamber of the Universal Testing Machine (UTM) with a temperature of 40 ℃ for at least 3 hours to reach the

equilibrium temperature. To reduce the lateral constraint due to the friction between specimen and the end caps, the following end treatments were employed: 1) two soft rubber membranes were put between the end caps and the specimens; and 2) a wax-based petroleum jelly was used between the rubber membranes and the end caps. With the help of the end treatments, the asphalt mixture specimens were found to be able to deform freely along the radial direction at the ends of the cylinder samples.

The loading sequence used in the experimental protocol was shown in Figure 4-3. The nondestructive creep test was firstly conducted using the UTM in which a constant compressive stress of 25 kPa was applied to the specimens for 120 sec. The total strain at the end of the creep test was controlled to less than 150 με which was believed to be the linear viscoelastic limit for the asphalt mixture in compression (Levenberg and Uzan 2004). Then the compressive load was removed and the specimen was at rest for 1 hour. After the 1-hour rest period, the nondestructive dynamic modulus test was performed on the same specimen, in which a compressive sinusoidal stress with a maximum stress value of 70 kPa was applied to the sample for 600 cycles at a frequency of 1 Hz. The measured dynamic modulus and phase angle remain constant, which indicates that no damage is introduced to the specimen. After another 1-hour rest period, the destructive dynamic modulus test was then performed on the same undamaged specimen, in which a sinusoidal compressive load with a minimum stress of 20 kPa and a maximum stress of 600 kPa was applied to the specimen at a frequency of 1 Hz. The total deformation was recorded with respect to time using the three LVDTs until the specimen fails in the tertiary deformation stage. It is noteworthy that the 1-hour rest period was used for the purposes of that: 1) the viscoelastic strains produced in the nondestructive tests were fully recovered and would not affect the results of the following tests; and 2) the 1-hour rest period was needed to compensate

the temperature loss due to the opening the door of the UTM chamber during the setup and operation of the tests.

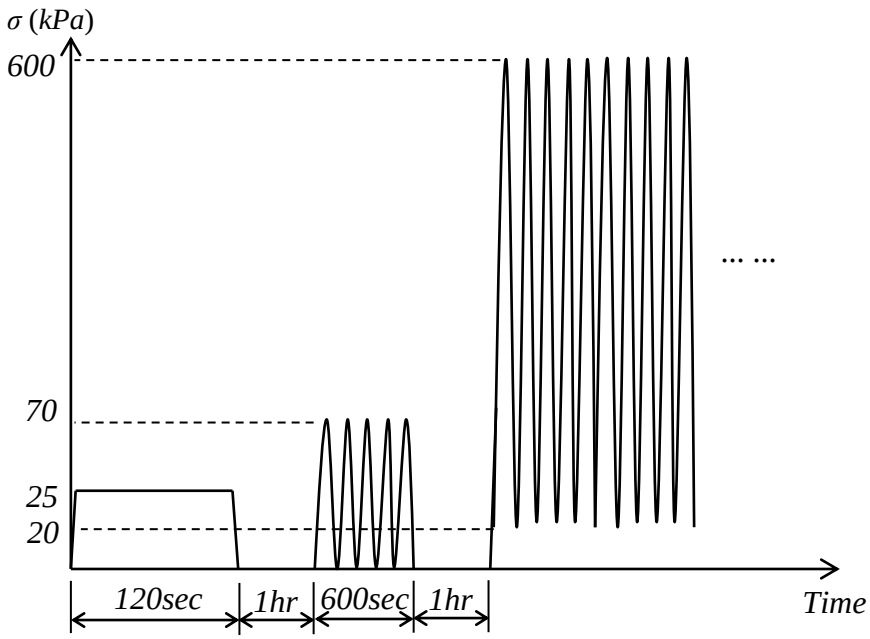

Figure 4-3 Schematic plot of loading sequences used in the tests (not scaled)

LINEAR VISCOELASTIC CHARACTERIZATION

The linear viscoelastic characterization of an undamaged asphalt mixture is conducted to provide a basis for quantifying how much the damage including viscoplasticity and fracture depart from the undamaged state. The asphalt mixture can be characterized as a linear viscoelastic material when the deformation is small, e.g. strains are controlled below 100 με in tension and 150 με in compression (Levenberg and Uzan 2004).

Creep Compliance and Relaxation Modulus

A Prony series model including multiple Kelvin elements and one spring in series is used in this study to represent the viscoelastic properties of the asphalt mixture and the creep compliance and the relaxation modulus for the Prony series model are shown as follows:

$$D(t) = D_0 + \sum_{i=1}^{M} D_i \left[1 - \exp\left(-\frac{t}{\tau_i} \right) \right] \tag{4-2}$$

$$E(t) = E_\infty + \sum_{j=1}^{M} E_j \exp\left(-\frac{t}{k_j} \right) \tag{4-3}$$

where $D(t)$ = creep compliance; D_0 = instantaneous compliance; D_i = components of creep compliance; τ_i = retardation time; $E(t)$ = relaxation modulus; E_∞ = long term equilibrium modulus ; E_j = components of relaxation modulus; k_j = relaxation time; and M = total number of Kelvin elements in the Prony series model. The creep compliance and relaxation modulus are related by the following equation (Findley et al. 1989):

$$\bar{E}(s)\bar{D}(s) = \frac{1}{s^2} \tag{4-4}$$

where $\bar{E}(s)$ and $\bar{D}(s)$ are respectively the Laplace transform of $E(t)$ and $D(t)$, and s = variable in the Laplace domain. By taking the inverse Laplace transform of Equation 4-4, it is possible to solve for the relaxation modulus or the creep compliance if the other material property is known.

In the nondestructive compressive creep test, the constant stress is $\sigma = 25\,kPa$ and the strain is calculated as the average value of the deformations measured from the three LVDTs divided by the gauge length of 90 mm. Then the creep compliance is directly calculated using $D(t) = \varepsilon(t)/\sigma$, which is perfectly fitted by Equation 4-2. The relaxation modulus is estimated

using Equation 4-4 and then fitted by Equation 4-3. Take the sample labeled as AAD14 (AAD binder, 7% air void content, Unaged) for example, $D(t)$ and $E(t)$ at 40 ℃ are shown in Figure 4-4 which indicates a good fitting between the Prony model and the measured data.

Young's modulus (E_Y) represents the instantaneous (elastic) response of a material and E_Y can be calculated using $E_Y = E(0) = 1/D(0)$ based on Equations 4-2, 4-3 and 4-4. The results of measured Young's moduli will be illustrated in the next section together with the dynamic moduli and phase angles for the undamaged 16 asphalt mixture specimens that vary in binder type, air void content and aging period.

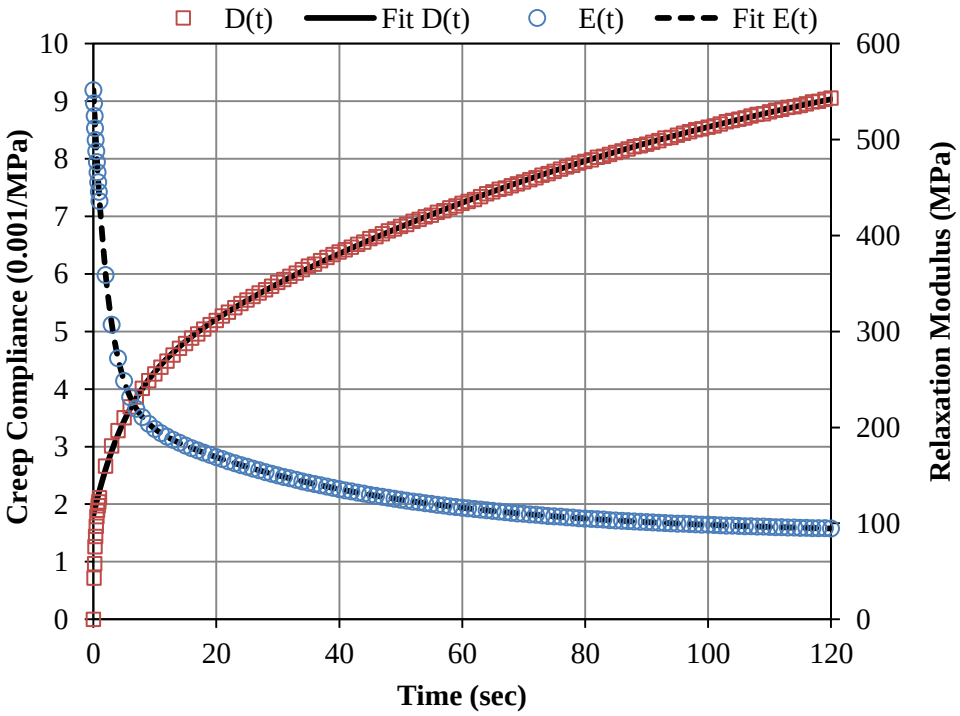

Figure 4-4 Creep compliance and relaxation modulus of an undamaged asphalt mixture (AAD binder, 7% air void, unaged) at 40 ℃

Dynamic Modulus and Phase Angle

In practice, the load applied to the asphalt pavement is not a static load but a dynamic load such as a moving traffic load that has a loading period of 0.1 sec corresponding to a vehicle speed of 64 km/h (Huang 2004). The measured strain data of the creep test in such a short loading period are not reliable due to the transient effect which may need several seconds to vanish. Therefore, the relaxation modulus and the creep compliance can only characterize the long-term viscoelastic properties of the material and a dynamic modulus test is needed to obtain the dynamic modulus and phase angle which can characterize the short-period properties of the viscoelastic material.

The dynamic modulus test employs an oscillatory stress loading that is:

$$\sigma(t) = \sigma_0 \cos(\omega t) \tag{4-5}$$

where σ_0 = stress amplitude which is 70 kPa in this study; and ω = angular frequency in rad/sec. When the initial transient effect vanish and the material system arrives at a steady state, the strain output due to the oscillatory stress in Equation 4-5 will be an oscillation function as shown in Equation 4-6 which has the same frequency as the stress but lags behind the stress by a phase angle of δ (Wineman and Rajagopal 2001).

$$\varepsilon(t) = \varepsilon_0 \cos(\omega t - \delta) \tag{4-6}$$

where ε_0 = strain amplitude which is constant if the specimen is not damaged. The dynamic modulus is calculated as:

$$\left|E^*\right| = \frac{\sigma_0}{\varepsilon_0} \tag{4-7}$$

By determining the time lag between the peak stress and peak strain within one load cycle, the phase angle can be calculated as:

$$\delta = \frac{180}{\pi}\frac{\Delta t}{T} \tag{4-8}$$

where Δt = time lag between peak stress and peak strain within one load cycle; and T = loading period that is 1 sec in this study. Figure 4-5 shows the dynamic moduli and phase angles at every 10 load cycles for the sample No. AAD14, in which the dynamic modulus and phase angle remain constant as the load cycle increase. The independence of the dynamic modulus and phase angle with time indicates that the sample is tested in a nondestructive condition.

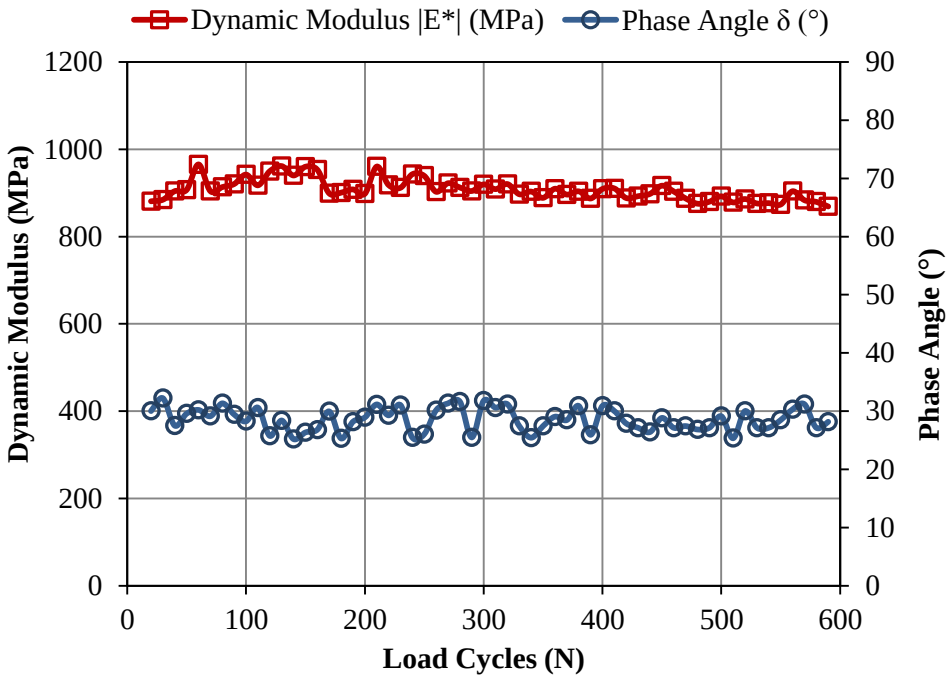

Figure 4-5 Dynamic modulus and phase angle of an undamaged asphalt mixture (AAD binder, 7% air void, unaged) at 40 ℃

The 16 samples are tested using a nondestructive compressive dynamic modulus test and the values of the dynamic modulus and phase angle are calculated for each sample. Figure 4-6 shows the dynamic moduli and phase angles measured in the nondestructive compressive

dynamic modulus test together with Young's moduli measured in the nondestructive compressive creep test for the 16 samples.

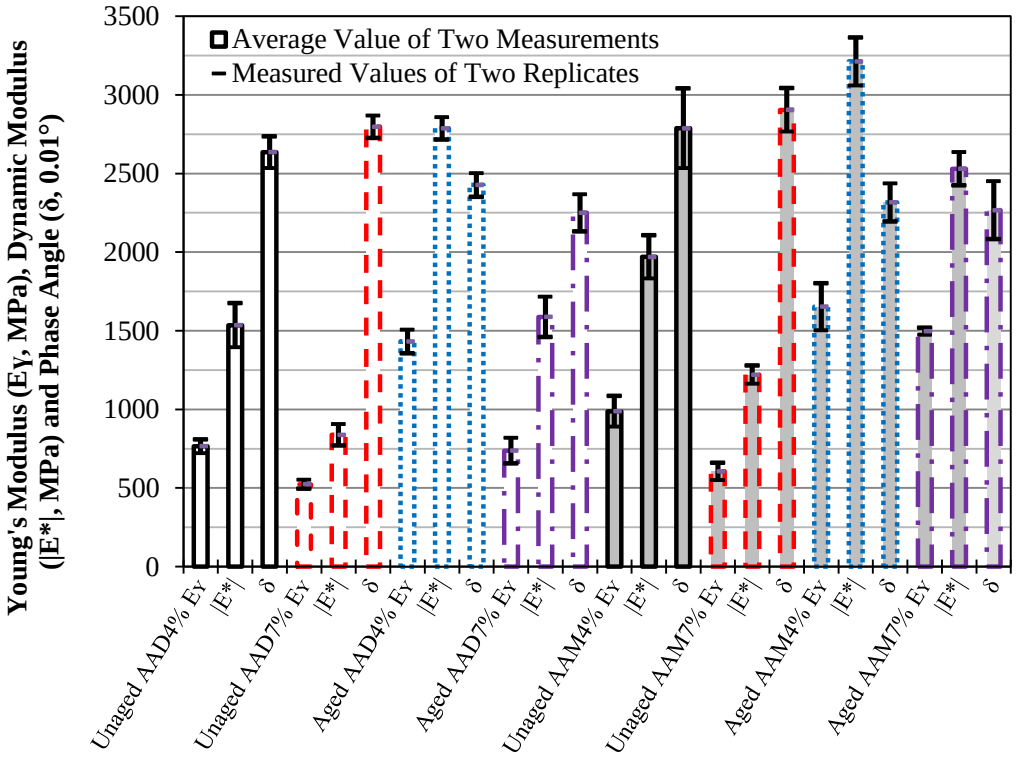

Figure 4-6 Young's modulus, dynamic modulus and phase angle for different asphalt mixtures at 40 ℃

It is found that the Young's modulus and the dynamic modulus both increase as the asphalt mixtures become stiffer due to aging or less air void content. The phase angle decreases as the asphalt mixture is aged which is reasonable because the asphalt mixture behaves more elastically when it is aged. No dependence is found of the phase angle on the air void content. However, aging reduces the phase angle more in the samples with the higher air void content which have more air available to oxidize the binder in the mix. All of the findings comply with the general understanding of the viscoelastic properties of asphalt mixtures. The measured

Young's modulus, dynamic modulus and phase angle of the undamaged asphalt mixtures will be used in the following calculation of the pseudo strain and the strain decomposition in the destructive dynamic modulus tests.

STRAIN DECOMPOSITION IN DESTRUCTIVE DYNAMIC MODULUS TEST

This section details the measurements of the dynamic moduli and phase angles of the damaged asphalt mixtures in the destructive dynamic modulus test and the strain decompositions by using the pseudo strain concept and the extended elastic-viscoelastic correspondence principle.

Destructive Dynamic Modulus Test

The function of the applied load in a destructive dynamic modulus test is:

$$\sigma(t) = \sigma_c - \sigma_d \cos(\omega t) \tag{4-9}$$

where σ_c = creep stress; and $\sigma_d \cos(\omega t)$ = dynamic cyclic stress. Based on the testing protocol, σ_c=310 kPa and $\sigma_d = 290\ kPa$. The strain outputs are:

$$\begin{cases} \varepsilon^T(t) = \varepsilon_c(t) - \varepsilon_d(t) \\ \varepsilon_c(t) = \varepsilon_0 + \sum_{i=1}^{L} \varepsilon_i \left[1 - \exp\left(-\dfrac{t}{\tau_i} \right) \right] \\ \varepsilon_d(t) = \varepsilon_N \cos(\omega t - \varphi_N) = \dfrac{\sigma_2}{\left| E_N^* \right|} \cos(\omega t - \varphi_N) \end{cases} \tag{4-10}$$

where ε^T = measured total strain; ε_c = creep strain due to the creep stress; $\varepsilon_0, \varepsilon_i, \tau_i$ = fitting parameters for the creep strain; L = total number of ε_i and τ_i; ε_d = dynamic cyclic strain due to

the dynamic cyclic stress; ε_N = amplitude of the cyclic strain at the N-th load cycle; $\left|E_N^*\right|$ = dynamic modulus of the damaged asphalt mixture at the N-th load cycle that is calculated using $\left|E_N^*\right| = \sigma_d / \varepsilon_N$; and φ_N = phase angle of the damaged asphalt mixture at the N-th load cycle. At least one $\varepsilon_i < 0$ and one $\tau_i < 0$ are required to fit the whole processes of the creep strain in the primary, secondary and tertiary stages. Figure 4-7 shows an example of the measured total strain, dynamic modulus and phase angle of the damaged asphalt mixture sample AAD14. Compared to the time-independent dynamic modulus and phase angle of the undamaged asphalt mixture shown in Figure 4-5, $\left|E_N^*\right|$ and φ_N of the damaged asphalt mixture are time (load cycle)-dependent at a constant loading frequency.

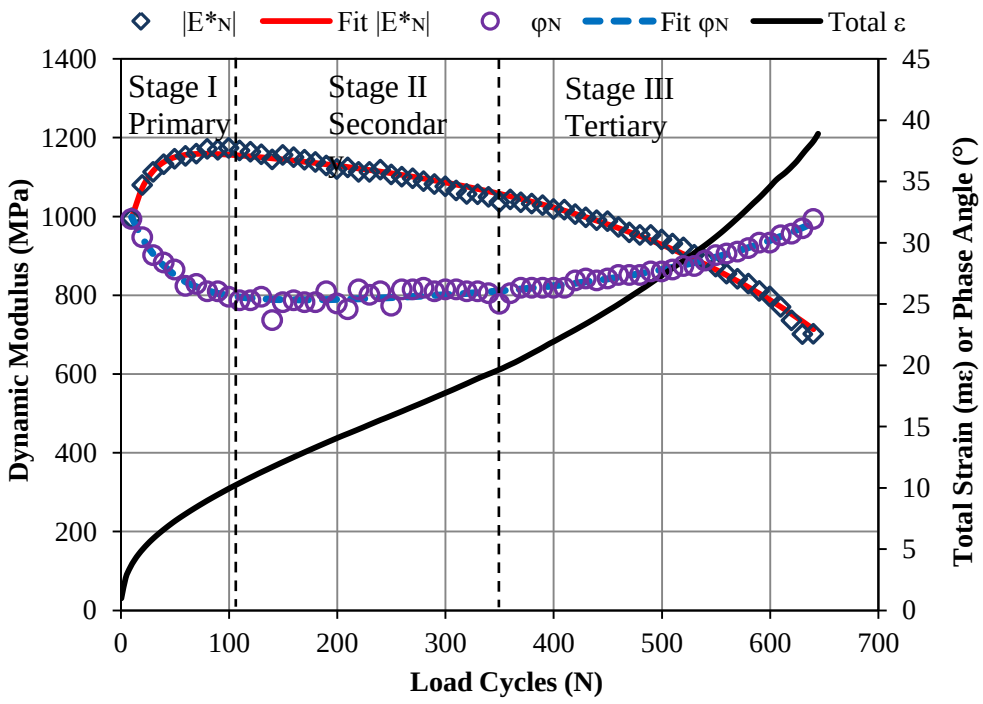

Figure 4-7 Total strain, dynamic modulus and phase angle of a damaged asphalt mixture (AAD binder, 7% air void, unaged) at 40 ℃

As indicated in Figure 4-7. In the primary stage, $\left|E_N^*\right|$ increases and φ_N decreases, which may have two causes: 1) the initial transient responses due to the dynamic loads need a period of time to disappear; and 2) the initial air voids in the asphalt mixture need a period of time to be compressed and closed. In the secondary stage, $\left|E_N^*\right|$ decreases slowly while φ_N remains constant, which are the results of the plastic flow of the material under the destructive compressive stress. In the tertiary stage, $\left|E_N^*\right|$ decreases rapidly and φ_N increases, which is because of the opening and propagation of cracks. The other 15 specimens are also found to have similar evolutions of $\left|E_N^*\right|$ and φ_N. One noteworthy point is that the constant phase angle in the secondary stage and the increasing phase angle in the tertiary stage indicate that the cracks under a compressive load will not develop until the tertiary stage and the growth of cracks is signaled principally by the increase of the phase angle. To consider the changes of the dynamic modulus and phase angle, $\left|E_N^*\right|$ and φ_N are modeled using Equations 4-11 and 4-12, respectively.

$$\left|E_N^*\right| = A_E\left(1-e^{-B_E\cdot N}\right)+C_E\left(1-e^{D_E\cdot N}\right)+E_E \tag{4-11}$$

$$\varphi_N = A_\varphi\left(e^{-B_\varphi\cdot N}-1\right)+C_\varphi\left(e^{D_\varphi\cdot N}-1\right)+E_\varphi \tag{4-12}$$

where A_E, B_E, C_E, D_E and E_E are positive fitting parameters for the model of $\left|E_N^*\right|$; and A_φ, B_φ, C_φ, D_φ and E_φ are positive fitting parameters for the model of φ_N. Figure 4-7 shows a good fitting between the models and the measured data.

Extended Elastic-Viscoelastic Correspondence Principle

Schapery (1984) proposed the extended elastic-viscoelastic correspondence principle which states that, if the actual stress or strain is replaced by the pseudo stress or pseudo strain,

the constitutive equation for the viscoelastic material is identical to that for the elastic case. The pseudo strain is defined as:

$$\varepsilon^R(t) = \frac{1}{E_R}\int_{0^-}^{t} E(t-\xi)\frac{d\varepsilon(\xi)}{d\xi}d\xi \tag{4-13}$$

where ε^R = pseudo strain; t = current time; ξ = previous time before t; $\varepsilon(\xi)$ = strain history measured in the test; $E(t)$ = relaxation modulus of the undamaged material; and E_R = reference modulus which is an arbitrary constant. Based on Equations 4-13, the physical stress and the pseudo strain have a relationship as:

$$\sigma(t) = E_R\varepsilon^R(t) \tag{4-14}$$

It is obvious that a correspondence can be found between Equation 4-14 and the elastic stress-strain relationship, e.g. the Hooke's law. The advantage of this extended correspondence principle is that the effect of time on the constitutive equation of the viscoelastic material is eliminated, which brings significant convenience to the damage analysis on the viscoelastic materials (Kim et al. 1995; Park et al. 1996; Si et al. 2002).

Equation 4-13 establishes a practical method to calculate the pseudo strain provided that the reference modulus is determined. Many researchers employ a unity for the reference modulus which has the same unit as stress (Lee and Kim 1998; Gibson et al. 2003; Kutay et al. 2008). However, the pseudo strain calculated using this method is only a relative strain with a maximum value of 1. This pseudo strain does not have a physical meaning and cannot be used in the strain decomposition. Thus, a reference modulus with a physical meaning is needed in the strain decomposition and the quantification of viscoplasticity and viscofracture.

The reference modulus can be determined by the extended correspondence principle which indicates that a viscoelastic problem is converted to an elastic problem when modeling

material constitutive relation using stress and pseudo strain, which further indicates that the pseudo strain removes the viscous effect on the total strain and pseudo strain becomes the remaining part of the total strain after subtracting the viscous strain. Thus, according to the strain components in Equation 4-1, we have:

$$\varepsilon^R = \varepsilon^T - \varepsilon^{ve} = \begin{cases} \varepsilon^e & \textit{Nondestructive Condition} \\ \varepsilon^e + \varepsilon^p + \varepsilon^{vp} + \varepsilon^{vf} & \textit{Destructive Condition} \end{cases} \tag{4-15}$$

Comparing Equation 4-14 with Hooke's law ($\sigma = E_Y \varepsilon^e$) and using Equation 4-15 in the nondestructive condition yields:

$$E_R = E_Y \tag{4-16}$$

where E_Y = Young's modulus. Two examples are provided here as proofs of Equation 4-16.

Taking the nondestructive creep test for the first example, the total strain in the creep test is expressed as $\varepsilon(t) = \sigma D(t)$ which is substituted in Equation 4-13 and yields:

$$\varepsilon^R(t) = \frac{\sigma}{E_R} \int_{0^-}^{t} E(t-\xi) \frac{dD(\xi)}{d\xi} d\xi = \frac{\sigma}{E_R} H(t) \tag{4-17}$$

where $H(t)$ is Heaviside step function; $H(t) = 0$ when $t < 0$ and $H(t) = 1$ when $t \geq 0$. Considering Hooke's law and $\varepsilon^R = \varepsilon^e$ in the undamaged condition, Equation 4-17 yields $E_R = E_Y$.

The second example is the nondestructive dynamic modulus test where the measured strain is expressed in Equation 4-6. The pseudo strain becomes:

$$\begin{aligned} \varepsilon^R(t) &= \frac{\varepsilon_0}{E_R} \int_{0^-}^{t} E(t-\xi) \frac{d\cos(\omega\xi - \delta)}{d\xi} d\xi \\ &= \frac{\varepsilon_0 |E^*|}{E_R} \cos(\omega t - \delta + \delta) = \frac{\sigma_0}{E_R} \cos(\omega t) \end{aligned} \tag{4-18}$$

where Equation 4-7 is used. The elastic strain under an oscillatory stress is $\varepsilon^e = \left[\sigma_0 \cos(\omega t)\right] / E_Y$. Comparing this with Equation 4-18 yields $E_R = E_Y$ by considering $\varepsilon^R = \varepsilon^e$ in the undamaged condition.

Calculation of Pseudo Strain and Strain Decomposition

Introducing the pseudo strain into the destructive test allows the separation of the components of the total strain. The pseudo strain for the destructive dynamic modulus test can be calculated by substituting the total strain modeled in Equation 4-10 and the relaxation modulus of the undamaged asphalt mixture in Equation 4-3 into the definition of the pseudo strain in Equation 4-13:

$$\begin{cases} \varepsilon^R(t) = \varepsilon_c^R(t) - \varepsilon_d^R(t) \\ \varepsilon_c^R(t) = \dfrac{1}{E_R}\left\{ E_\infty \varepsilon_c(t) + \varepsilon_0 \Delta E(t) + \sum_{i=1}^{L}\sum_{j=1}^{M} \dfrac{\varepsilon_i E_j}{\left(1-\tau_i/k_j\right)}\left[\exp\left(-\dfrac{t}{k_j}\right) - \exp\left(-\dfrac{t}{\tau_i}\right)\right]\right\} \\ \varepsilon_d^R(t) = \dfrac{\sigma_d}{E_R}\dfrac{\left|E^*\right|}{\left|E_N^*\right|}\cos\left(\omega t - \varphi_N + \delta\right) \end{cases} \tag{4-19}$$

where $E_R = E_Y$ based on Equation 4-16 and $\Delta E(t) = E(t) - E_\infty$ according to Equation 4-3. $\left|E^*\right|$ and δ are dynamic modulus and phase angle of the undamaged asphalt mixtures that are measured in the nondestructive dynamic modulus tests. $\left|E_N^*\right|$ and φ_N are the dynamic modulus and phase angle of the damaged asphalt mixtures that are measured in the destructive dynamic modulus tests and modeled by Equations 4-11 and 4-12, respectively.

The strain decomposition can be conducted once the pseudo strain is calculated. First, the elastic strain is always calculated by using the Hooke's law:

$$\varepsilon^{e} = \frac{\sigma(t)}{E_Y} \tag{4-20}$$

where $\sigma(t)$ is the controlled stress in the nondestructive dynamic modulus test. Second, the viscous strain is determined based on Equation 4-15 and is shown as:

$$\varepsilon^{ve} = \varepsilon^{T} - \varepsilon^{R} \tag{4-21}$$

Third, since the instantaneous viscoplastic stain and the instantaneous viscofracture strain are zero, that is, $\varepsilon^{vp}(0) = \varepsilon^{vf}(0) = 0$, Equation 4-15 yields the plastic strain as:

$$\varepsilon^{p} = \varepsilon^{R}(0) - \varepsilon^{e} \tag{4-22}$$

Fourth, the viscofracture strain will not develop until the tertiary stage because the viscofracture strain is caused by the initiation and propagation of the cracks that occur only in the tertiary stage. In other words, $\varepsilon^{vf}(I, II) = 0$. Thus the pseudo strain in the primary and secondary stages only includes the elastic strain, plastic strain and viscoplastic strain. As a result, the viscoplastic strain in the primary and secondary stage is:

$$\varepsilon^{vp}(I, II) = \varepsilon^{R}(I, II) - (\varepsilon^{e} + \varepsilon^{p}) \tag{4-23}$$

It is noteworthy that the Equation 4-23 theoretically remains true for the whole primary and secondary stages, however, since the flow number that is the separation point of secondary and tertiary stages has not been determined yet, the viscoplastic strain that is calculated by Equation 4-23 only includes the strain data at the whole primary stage and the first half of the secondary stage. To predict the viscoplastic strain during the entire deformation processes

including the primary, secondary and tertiary stages, the Tseng-Lytton model (Tseng and Lytton 1989) is employed to fit the viscoplastic strain data obtained by Equation 4-23 and gives:

$$\varepsilon^{vp} = \varepsilon_{\infty}^{vp} \exp\left[-\left(\rho/N\right)^{\lambda}\right] \tag{4-24}$$

where $\varepsilon_{\infty}^{vp}$ = saturated viscoplastic strain that is the viscoplastic strain when time goes to infinity; and ρ and λ are model coefficients. Fifth, the viscofracture strain (ε^{vf}) can be computed using Equation 4-1 and is given by:

$$\varepsilon^{vf} = \varepsilon^{R} - \varepsilon^{e} - \varepsilon^{p} - \varepsilon^{vp} \tag{4-25}$$

Finally, every component of the total strain is separated from each other and can be characterized individually. For example, Figure 4-8 shows the curves of all strain components of the asphalt mixture sample AAD14, in which the total strain is the only one that is measured in the destructive dynamic modulus tests and all other strain components are determined by conducting the strain decomposition to the measured total strain. It is found that elastic and plastic strain are time-independent and the viscoelastic strain shows three stage changes and occupies a large proportion of the total strain.

To clearly show the viscoplastic strain and viscofracture strain, Figure 4-8 is plotted in a smaller strain scale and is shown in Figure 4-9, which illustrates that the viscoplastic strain has a power curve that can be used to accurately determine the parameters of the viscoplastic constitutive model in the continuum mechanics analysis. Figure 4-9 also shows that the viscofracture strain declines very quickly to zero and remains at zero until the tertiary stage in which the viscofracture strain increases rapidly. The decline of the viscofracture strain in the first several load cycles is believed to be caused by the closure of the air voids in the asphalt mixture under a compressive load. The increasing viscofracture strain in the tertiary stage has an increasing strain rate, which is similar to a typical crack growth curve and can be implemented to

acquire the viscofracture properties of the asphalt mixture in compression. Another direct application of the viscofracture strain curve is to obtain the flow number that is the number of load cycles at which the viscofracture strain departs from zero and starts to grow, which is discussed in the next section.

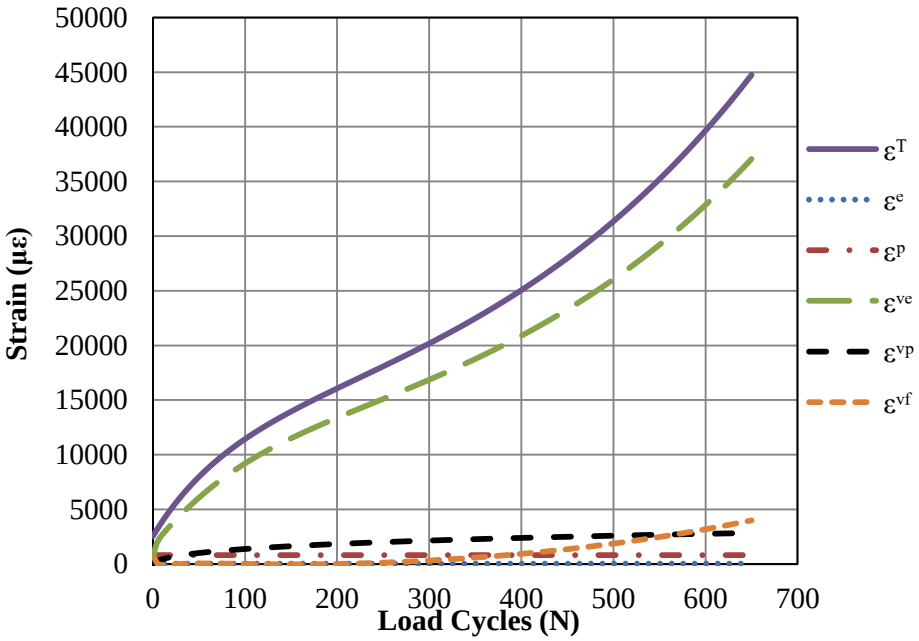

Figure 4-8 Strain decomposition in destructive dynamic modulus test for an asphalt mixture (AAD binder, 7% air void, unaged)

EMPIRICAL CHARACTERIZATION OF PERMANENT DEFORMATION AND FRACTURE

The strain decomposition technique proposed in the previous section provides an efficient method to simultaneously differentiate two distinctly different damage mechanisms, e.g. permanent deformation and fracture, which can be characterized by the separated viscoplastic strain and viscofracture strain, respectively.

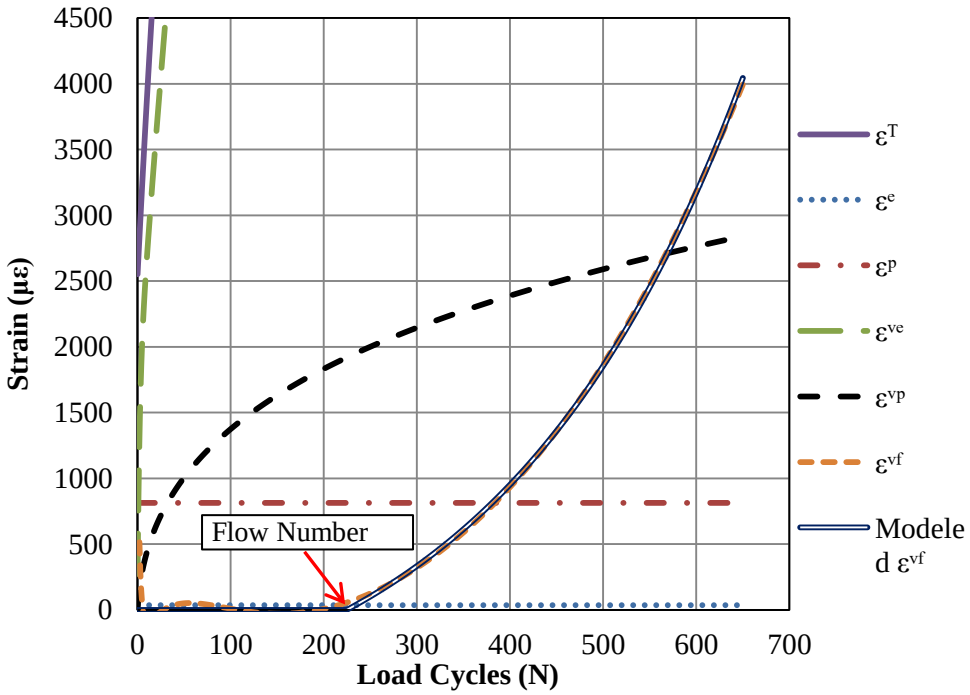

Figure 4-9 Strain decomposition on a smaller strain scale showing viscoplastic stain, viscofracture strain and modeled viscofracture strain

Firstly, the separated viscofracture strain is modeled using Equation 4-26 as follows:

$$\varepsilon^{vf} = \varepsilon_0^{vf}\left[e^{\theta_1\langle N-N_f\rangle} - 1\right] \tag{4-26}$$

where N_f = flow number that is the starting point of the tertiary stage; ε_0^{vf} and θ_1 = fitting parameters. $\langle N-N_f\rangle$ is a step function where $\langle N-N_f\rangle = N-N_f$ if $N-N_f \geq 0$ and $\langle N-N_f\rangle = 0$ if $N-N_f < 0$. Figure 4-9 shows that the viscofracture strain model in Equation 4-26 fits very well with the measured viscofracture strain data. By fitting Equation 4-26 to the separated viscofracture strain curve, the flow numbers (N_f) are determined for different asphalt mixtures and shown in Figure 4-10. Taking the first derivative of Equation 4-26 with respect to load cycles yields:

$$\frac{d\varepsilon^{vf}}{dN} = \left(\theta_1 \varepsilon_0^{vf}\right) e^{\theta_1 \langle N - N_f \rangle} = \eta e^{\theta_1 \langle N - N_f \rangle} \tag{4-27}$$

where $\eta = \theta_1 \varepsilon_0^{vf}$ in με/cycle. Since the increasing viscofracture strain results from the crack initiation and propagation, the derivative of viscofracture strain with respect to the load cycle in Equation 4-27 indicates the speed of crack growth. To compare the cracking speed of different asphalt mixtures, the parameter η is chosen as a crack speed index and a larger η means faster crack propagation. The values of η for different asphalt mixtures are shown in Figure 4-10.

Secondly, the separated viscoplastic strain is modeled using Equation 4-24. The model coefficients ρ and λ are also determined in the modeling process. The flow number (N_f) is then plugged into Equation 4-24 to calculate the viscoplastic strain at the flow number (i.e., $\varepsilon^{vp}(N_f)$) of each asphalt mixture specimen. The parameter $\varepsilon^{vp}(N_f)$ is regarded as the indicator of the permanent deformation of the asphalt mixtures, which is also plotted in Figure 4-10. Figure 4-10 shows that the flow number (N_f) increases while the viscoplastic strain at flow number ($\varepsilon^{vp}(N_f)$) and the crack speed index (η) decreases as the air void content decreases or the asphalt mixtures become aged, which means a smaller air void and a stiffer asphalt mixture due to aging can provide the material a better resistance to permanent deformation and fracture.

A further characterization of permanent deformation and fracture for the asphalt mixture will include the viscoplastic continuum mechanistic modeling of permanent deformation using the separated viscoplastic strain data to investigate the strain hardening effect during the plastic flow and the fracture mechanistic analysis on the cracking using the separated viscofracture strain data to estimate the evolution of the damage density as well as the J-integral Paris' law in the tertiary stage. Therefore, the viscoplastic strain and viscofracture strain obtained by using the

strain decomposition methodology proposed in this chapter will directly be used in the further mechanistic characterization of permanent deformation and fracture of the asphalt mixtures.

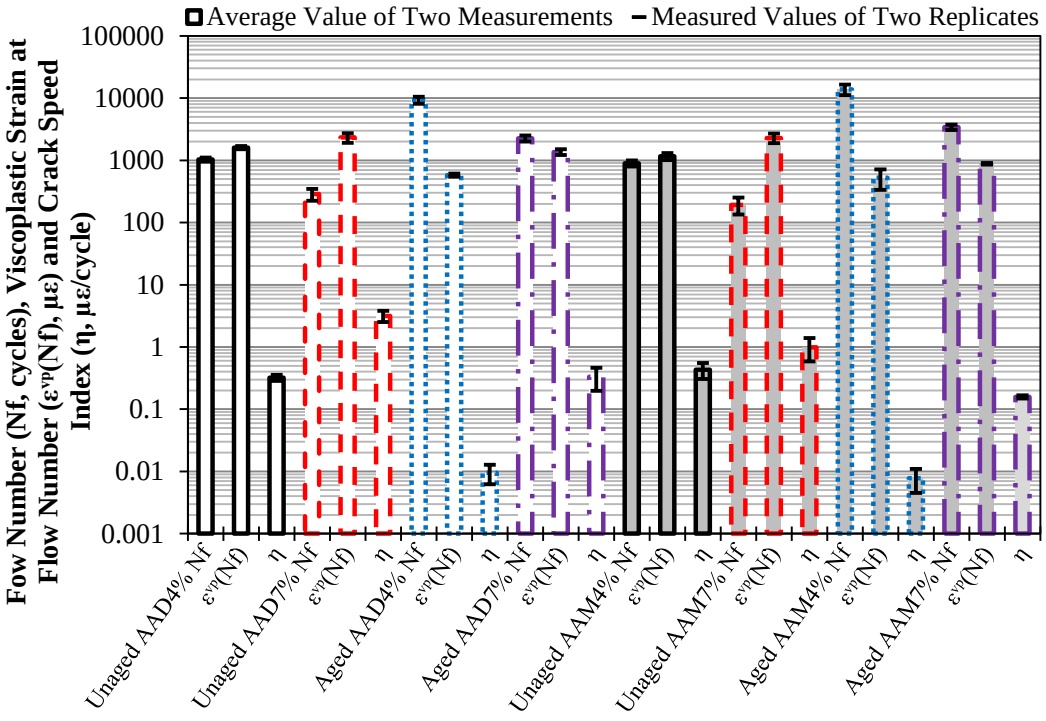

Figure 4-10 Flow number, viscoplastic strain at flow number and crack speed index for different asphalt mixtures at 40 ℃

SUMMARIES AND CONCLUSIONS

Asphalt mixtures in compression experience the primary, secondary and tertiary deformation stages. The viscoelastic and viscoplastic deformation of the asphalt mixture develop simultaneously during the three stages, while the cracks that lead to the viscofracture deformation initiate and propagate in the tertiary stage and yield the tertiary flow. The objective of this research is to separate the viscoelasticity, viscoplasticity and viscofracture in a destructive compressive dynamic modulus test so as to simultaneously characterize the permanent deformation and fracture of the asphalt mixtures.

The undamaged properties of 16 asphalt mixtures that have two binder types, two air void contents and two aging periods are firstly obtained by conducting nondestructive creep tests and nondestructive dynamic modulus tests. Testing results are analyzed by using linear viscoelastic theory, in which creep compliance and relaxation modulus are well modeled by the Prony model. The dynamic modulus and phase angle of the undamaged asphalt mixtures are found to remain constant with load cycle, which indicates that the samples are tested in nondestructive conditions. Then, the undamaged asphalt mixtures are used to perform destructive dynamic modulus tests, in which the dynamic modulus and phase angle of the damaged asphalt mixtures are found to vary with load cycle, which indicates the plastic evolution and the crack propagation. The growth of cracks is signaled principally by the increase of the phase angle, which occurs only in the tertiary stage.

The measured total strain in the destructive dynamic modulus test is successfully decomposed into elastic strain, viscoelastic strain, plastic strain, viscoplastic strain and viscofracture strain by employing the pseudo strain concept and the extended elastic-viscoelastic correspondence principle. The separated viscoplastic strain is modeled with the Tseng-Lytton model to characterize the permanent deformation and the separated viscofracture strain is modeled by a fracture strain model to characterize the fracture of the asphalt mixtures, in which the flow number is determined and a crack speed index is proposed. Comparisons between the 16 samples show that the aged asphalt mixtures with lower air void content have a better performance resisting both permanent deformation and fracture.

CHAPTER V

VISCOPLASTIC YIELD SURFACE OF ASPHALT MIXTURES

OVERVIEW

The existing yield surface models of asphalt mixture have failed in completely characterizing the important material properties of the asphalt mixture including: 1) distinctions between compression, extension and tension; 2) dilative volumetric change; 3) internal friction and cohesion; 4) rate and temperature dependence; 5) strain hardening; and 6) convexity and smoothness of the yield surface. Thus the objective of this chapter is to develop a comprehensive yield surface model for the asphalt mixture to consider all of the aforementioned material characteristics for the purpose of an accurate permanent deformation prediction.

The proposed ZLL (Zhang-Luo-Lytton) yield surface model coincides with the external apices of the Mohr-Coulomb yield surface to differentiate the distinctions between compression and extension but is still smooth and convex on both the meridian and the octahedral planes over the full possible range of the internal friction angle from 0 to 90 degrees. An Arrhenius temperature function and a power model are integrated into the ZLL model to include the temperature and strain rate dependence, respectively. A stress-pseudostrain strain decomposition method is proposed to accurately determine the initial yield strengths and the model parameters. Laboratory tests including compressive creep and uniaxial/triaxial strength tests are conducted on asphalt concrete mixtures that have two binders, two air void contents and three aging periods. More uniaxial strength tests are performed on two types of asphalt concrete at five temperatures and five strain rates.

The ZLL model parameters are determined and some significant conclusions are achieved: 1) The stress-pseudostrain curve in the strength tests can accurately (the stress-strain

curve cannot) determine the initial yield strength of the asphalt mixture because the pseudostrain removed the viscous effect on the material responses; 2) the ZLL model parameters representing the aggregate interlocks and cohesive properties of the asphalt mixture can be accurately predicted by the internal friction angle and cohesion; 3) the cohesion and strain hardening amplitude decline when temperature is increased or strain rate is decreased, which can be quantified by temperature and strain rate factors in the yield surface model; and 4) the cohesive parameters like cohesion, intercept of yield surface, strain hardening amplitude are greater for stiffer asphalt concretes which have stiffer binder, lower air voids, and longer aging periods. However, those properties do not affect the strength-related parameters like internal friction angle and slope of the yield surface which depend on aggregate contacts and interlocks.

INTRODUCTION

Viscoplastic mechanics are widely used in the constitutive modeling for the purpose of predicting the permanent deformation of asphalt mixtures. As the kernel of the viscoplastic theories, a yield surface model determines under what conditions the asphalt mixture begins to yield and how the yielding of the material evolves as the permanent deformation accumulates. Therefore, the yielding properties of the asphalt mixture should be characterized accurately and comprehensively by using an appropriate yield surface model. As a viscoelastoplastic material, the asphalt mixture has the following complicated material properties associated with the yielding of the material:

1) Material properties of the asphalt mixture show significant distinctions in compression, tension and extension. For instance, the yield strength in extension is less than the yield strength in compression. The tensile phase angle is greater than the compressive phase angle as discussed in Chapter II. Since the rutting primarily depends on the compressive

and extensive material properties, this chapter does not include the characterization of the tensile material properties;

2) Asphalt mixture is a frictional material with cohesion. Thus the asphalt mixture will dilate under a deviatoric shear stress (Bahuguna et al. 2006) and the yield strength will increase with an increasing confining pressure (Sousa and Weissman 1994);
3) Asphalt mixture shows a viscoplastic strain hardening (i.e., before the ultimate yield strength, the yield surface of the asphalt mixture expands as the accumulation of the viscoplastic deformation); and
4) Material behaviors of the asphalt mixture are rate and temperature dependent (e.g., the cohesion and strain hardening of the yield surface depends on loading rate and temperature).

In addition to the above inherent material properties of the asphalt mixture, the yield surface model also needs to satisfy the following two mathematical criteria:

1) Convexity. The work-hardening materials (e.g., soils, sands, and asphalt mixtures) need to comply with Drucker's Postulate (Drucker 1959), which indicates that the work done during an incremental load is positive and the work done in a loading-unloading cycle is nonnegative. As a consequence, the yield surface of asphalt mixture must be convex in stress space. In addition, the convexity of yield surfaces is practically demonstrated by the experiments in all materials and had become a fundamental property of plasticity (Jiang and Pietruszczak 1988; Bigoni and Piccolroaz 2004).
2) Smoothness. A non-smooth yield surface (e.g., Mohr-Coulomb criterion which represents an irregular hexagon on the octahedral plane) is not very convenient for finite element analysis since the corners conflict with convergence of numerical computation

(Lin and Bazant 1986). Thus the yield surface of the asphalt mixture must be smooth in stress space.

To accurately predict rutting in the field asphalt pavement, it is crucial to propose a comprehensive yield surface model to account for all of the aforementioned critical material characteristics and the mathematical requirements. The existing yield surface models for asphalt mixture are discussed in detail in the next section. One can conclude that the existing yield surface models are not able to completely characterize the yielding properties of the asphalt mixture and simultaneously satisfy the mathematical requirements.

The objective of this chapter is to develop a convex and smooth yield surface model to comprehensively and accurately characterize the yielding properties of the asphalt mixture. The next section discusses the advantages and disadvantages of the currently existing yield surface models for asphalt mixture, which is followed by a derivation of a comprehensive yield surface model for asphalt mixture. Then the laboratory experiments are presented in detail. The following section presents an analytical method to accurately determine the initial yield strength for a viscoelastic material, e.g., asphalt mixture. After this, the yield surface model parameters are determined and analyzed based on testing results. The last section summarizes the major findings of this chapter.

EXISTING YIELD SURFACE MODELS FOR ASPHALT MIXTURE

Many yield surface models have been proposed in the literature to characterize the yielding properties of an asphalt mixture. The most widely used yield surface models for asphalt mixture include the Mohr-Coulomb model, Drucker-Prager model, Extended Drucker-Prager model, Matsuoka-Nakai model, Hierarchical Single-Surface model, etc. The typical functions and problems associated with these yield surface models are presented as follows.

Mohr-Coulomb (M-C) Model

The function of Mohr-Coulomb yield surface model is shown as follows (Fwa et al. 2004):

$$\tau - \sigma \tan\phi - C = 0 \tag{5-1}$$

where τ is the yield shear stress; σ is the normal stress; C and ϕ are cohesion and internal friction angle of the asphalt mixture, respectively. Researchers (Tan et al. 1994) found that ϕ was primarily a function of aggregate contacts and interlocks, which were insensitive to temperature and strain rates, whereas C depended on testing temperature, strain rate, and properties of binder and fine aggregates. Figure 5-1 showed an example of a Mohr-Coulomb yield surface which is an irregular hexagon on the octahedral plane.

Drucker-Prager (D-P) Model

Drucker-Prager yield surface model is expressed as (Tan et al. 1994; Seibi et al. 2001; Park et al. 2005):

$$\sqrt{J_2} - \alpha I_1 - \kappa_0 = 0 \tag{5-2}$$

where $J_2 (= \frac{1}{2} S_{ij} S_{ji})$ is the second invariant of the deviatoric stress tensor , $S_{ij} (= \sigma_{ij} - \frac{1}{3}\delta_{ij} I_1)$; δ_{ij} is Kronecker delta; $I_1 (= \sigma_{kk})$ is the first invariant of the stress tensor (σ_{ij}). α and κ_0 are material properties, which can be determined by the cohesion and internal friction angle. By matching the Drucker-Prager yield surface with the external apices of the Mohr-Coulomb criterion (as shown in Figure 5-1), the following relationships are obtained (Chen and Mizuno 1990; Tashman et al. 2004):

$$\alpha = \frac{2\sin\phi}{\sqrt{3}(3 - \sin\phi)} \tag{5-3}$$

$$\kappa_0 = \frac{6C\cos\phi}{\sqrt{3}(3-\sin\phi)} \tag{5-4}$$

Extended Drucker-Prager (ED-P) Model

Extended Drucker-Prager yield surface model is expressed as (Argyris et al. 1974; Dessouky and Masad 2006; Saadeh et al. 2007; Darabi et al. 2011):

$$\frac{\sqrt{J_2}}{2}\left[1+\frac{1}{d}+\left(1-\frac{1}{d}\right)\frac{3\sqrt{3}J_3}{2(J_2)^{3/2}}\right]-\alpha I_1-\kappa=0 \tag{5-5}$$

where $J_3\,(=\det(S_{ij}))$ is the third invariant of the deviatoric stress tensor; κ is the strain hardening parameter; d is an extension ratio that is the ratio of yield strength in extension to that in compression, which is the length ratio of segment OB to segment OA in Figure 5-1. d is related to the internal friction angle of geomaterials as follows (Bardet 1990; Maiolino and Luong 2009):

$$d = \frac{3-\sin\phi}{3+\sin\phi} \tag{5-6}$$

The value of d ranges from 1 to 0.5 which corresponds to the internal friction angle from 0 to 90 degrees. A d value less than 1 indicates that the yield strength in extension is lower than that in compression, which is true for asphalt mixture. When $d=1$, the extended Drucker-Prager model reduces to the Drucker-Prager model. To ensure convexity of the extended Drucker-Prager yield surface, d is limited to between 1 and 0.778 (Lin and Bazant 1986; Maiolino 2005; Masad et al. 2007; ABAQUS 2010), which corresponds to the internal friction angle from 0 to 22 degrees based on Equation 5-6. Examples in Figure 5-1 show that the extended Drucker-Prager is convex when $\phi=15^\circ$ whereas concave when $\phi=35^\circ$. It had been

indicated by some studies (Fwa et al. 1997; Birgisson et al. 2003) that the asphalt mixtures commonly have a larger internal friction angle than 22 degrees. Thus, even though the extended Drucker-Prager is widely employed in the viscoplastic modeling of the asphalt mixture, a new convex yield surface model is still needed to account for a full range of the internal friction angle from 0 to 90 degree for the asphalt mixture.

To consider the strain hardening and temperature effect on the yield surface, κ can be written as (Abu Al-Rub et al. 2010):

$$\kappa = \left\{ \kappa_0 + \kappa_1 \left[1 - \exp\left(-\kappa_2 \varepsilon_e^{vp} \right) \right] \right\} \exp\left[-\delta \left(1 - \frac{T}{T_0} \right) \right] \tag{5-7}$$

in which κ_0, κ_1 and κ_2 are material parameters identified at the reference temperature T_0; κ_0 defines the initial yield strength; κ_1 determines the amplitude of the strain hardening; κ_2 is the strain hardening rate; δ is an experimentally determined parameter; and ε_e^{vp} is effective viscoplastic strain, the rate of which is expressed as follows (Dessouky 2005; Huang et al. 2011):

$$\dot{\varepsilon}_e^{vp} = \left[1 + 2 \left(\frac{0.5 + \beta/3}{1 - \beta/3} \right)^2 \right]^{-\frac{1}{2}} \sqrt{\dot{\varepsilon}_{ij}^{vp} \dot{\varepsilon}_{ij}^{vp}} \tag{5-8}$$

where β is the slope of the viscoplastic potential and $\dot{\varepsilon}_{ij}^{vp}$ is the rate of viscoplastic strain tensor.

In addition to the above three well-known yield surface models, pavement researchers also introduced yield surface models of geomaterials into the viscoplastic modeling of asphalt mixture, which are briefly discussed as follows.

Extended Matsuoka-Nakai (EM-N) Model

Bahuguna et al. (2006) extended Matsuoka-Nakai model (Matsuoka and Nakai 1974; 1985) and proposed the following yield surface equation:

$$I_1 I_2 + \alpha I_3 - Hk = 0 \tag{5-9}$$

where $I_1 (= \sigma_{kk})$, $I_2 (= \frac{1}{2}\left(\sigma_{ii}\sigma_{jj} - \sigma_{ij}\sigma_{ji}\right))$and $I_3 (= \det\left(\sigma_{ij}\right))$ are first, second and third invariants of the stress tensor; H is an isotropic hardening parameter; and k is a friction dependent parameter. Matsuoka-Nakai model is an excellent yield surface model for cohesionless geomaterials (e.g., sands) and it is inherently smooth and convex (Haythornthwaite 1985; Mortara 2008). However, Equation 5-9 cannot address the effect of the rate and temperature dependent cohesion and strain hardening on the yielding properties of the asphalt mixture. In addition, Equation 5-9 is a function with the third order of the stress and the differential of the yield surface is a function with the second order of the stress, which will bring difficulties during numerical simulations.

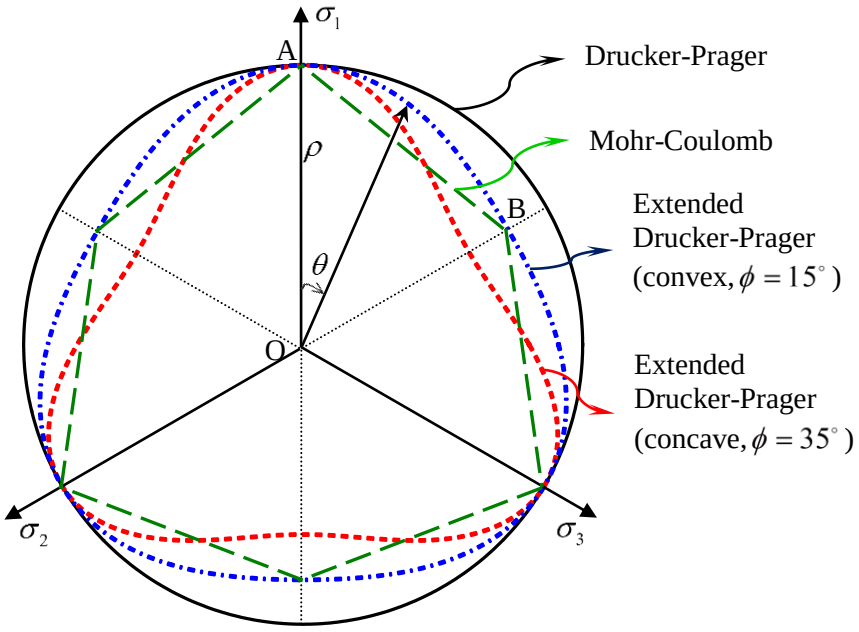

Figure 5-1 Yield surfaces of Mohr-coulomb, Drucker-Prager and extended Drucker-Prager models on octahedral plane

Di Benedetto (DBN) Model

Di Benedetto et al. (2007b) proposed a yield surface based on the Lode angle and a hardening variable. The yield surface is expressed as:

$$\sqrt{J_2}\cos\left(\frac{\pi}{3}-\theta\right)-R\frac{I_1+3S_0}{\sqrt{3}}=0 \tag{5-10}$$

where R is a scalar hardening variable; S_0 is a parameter; and θ is the Lode angle which is defined as:

$$\theta=\frac{1}{3}\arccos\left[\frac{3\sqrt{3}}{2}\frac{J_3}{\left(J_2\right)^{3/2}}\right] \qquad \in \left[0,\ \frac{\pi}{3}\right] \tag{5-11}$$

The value of θ, as shown in Figure 5-1, is zero in extension and $\pi/3$ in compression. The yield surface derived by Equation 5-10 is an equilateral triangle on the octahedral plane. Thus the yield strength ratio of extension to compression is always 0.5 (i.e., $d=0.5,\ \phi=90^\circ$), which is not reasonable for the asphalt mixture.

Desai's Hierarchical Single-Surface (HISS) Model

Desai et al. (1986) proposed a hierarchical single-surface model (HISS) to constitutively model geologic materials and the yield surface function has a form as follows:

$$J_2\left[1-B\cos\left(3\theta\right)\right]^m-\left[\gamma\left(I_1+S\right)^2-\alpha\left(I_1+S\right)^n\right]=0 \tag{5-12}$$

where γ is a softening parameter; α is a hardening parameter, S is a cohesion related parameter; n is a parameter determining shape of the yield surface in the deviatoric-hydrostatic stress ($\sqrt{J_2}\sim I_1$) plane (or meridian plane); B and m are parameters determining the shape of the yield surface on the octahedral plane. Pavement researchers used Desai's HISS model to

model asphalt mixtures by setting m as 0.5 (Muraya et al. 2009) and sand/aggregate base by setting m as 1 (Bonaquist and Witczak 1996). Several problems exists in Desai's HISS model when applied to model asphalt mixture: 1) to ensure a convex yield surface for the full range of the internal friction angle from 0 to 90 degrees, the value of m must be 0.229 (Van Eekelen 1980); 2) Desai's HISS model exhibits a spindle shape and the yield surface becomes nonlinear at relatively high confining pressures, which are normally used to characterize the nonlinear softening of soils or granular base. In contrast, the confinement in an asphalt layer cannot reach a very high level and the yield surface remains linear on the meridian plane for the asphalt mixture; 3) too many fitting parameters in the HISS model require complicated laboratory experiments for the determination of the model parameters; and 4) the rate and temperature dependent strain hardening is not accounted for in Desai's HISS model.

Table 5-1 summarizes the properties of the existing yield surface models used for asphalt mixtures. Based on the discussions in this section as well as Table 5-1, one may conclude that the currently existing yield surface models are not capable of completely characterizing the yielding properties of asphalt mixtures and a comprehensive yield surface model of the asphalt mixture is needed for the purpose of an accurate rutting prediction.

A NEW YIELD SURFACE (ZLL) MODEL FOR ASPHALT MIXTURE

This section derives a comprehensive yield surface model to account for all of the aforementioned yielding properties of the asphalt mixture.

Development of the Yield Surface Model

By evaluating the existing yield surface models as discussed in the previous section, a general yield surface function for an asphalt mixture is written as:

$$\sqrt{J_2}\rho(\theta)-\alpha I_1-\kappa a_T a_{\dot{\varepsilon}}=0 \tag{5-13}$$

where J_2, I_1, and α are defined in Equation 5-2. θ is the Lode angle that is defined in Equation 5-11. $\rho(\theta)$ is a function that defines the yield surface shape on the octahedral plane and determines the convexity of yield surface. κ is a strain hardening function which will be discussed later. a_T and $a_{\dot{\varepsilon}}$ are temperature and strain rate effect factors, respectively. The term $\kappa a_T a_{\dot{\varepsilon}}$ represents the temperature and strain rate dependent cohesion and strain hardening for an asphalt mixture, which will be discussed in detail after the derivation of $\rho(\theta)$.

Table 5-1 Yield Surface Models for Asphalt Mixture in the Literature

Yield Surface Model	Smooth?	Convex?	Consider Distinctions between Compression and Extension?	Consider Friction and Cohesion?	Consider Strain Hardening?	Consider Temperature and Rate Dependence?
Mohr-Coulomb	**No**	Yes	Yes	Yes	**No**	**No**
Drucker-Prager	Yes	Yes	**No**	Yes	**No**	**No**
Extended Drucker-Prager	Yes	**No**	Yes	Yes	Yes	Temperature: Yes Rate: No
Extended M-N	Yes	Yes	Yes	Friction: Yes Cohesion: **No**	Yes	**No**
Di Benedetto DBN	**No**	Yes	Strength ratio is always 0.5	Yes	Yes	**No**
Desai's HISS	Yes	**No**	Yes	Yes	Yes	**No**

As an inherently smooth and convex yield surface, Matsuoka-Nakai model is used and transformed to an expression with the first order of the stress so as to determine the function of $\rho(\theta)$. The Matsuoka-Nakai model is expressed as:

$$\frac{I_1 I_2}{I_3} = k \tag{5-14}$$

where $I_1 (= \sigma_{kk})$, $I_2 (= \frac{1}{2}\left(\sigma_{ii}\sigma_{jj} - \sigma_{ij}\sigma_{ji}\right))$and $I_3 (= \det\left(\sigma_{ij}\right))$ are first, second and third invariants of the stress tensor; k is a friction dependent parameter. Matsuoka-Nakai model is commonly used for cohesionless materials such as sands and the parameter k can be expressed in terms of the material internal friction angle (or the extension ratio d based on Equation 5-6) (Bardet 1990):

$$k = \frac{9 - \sin^2\phi}{1 - \sin^2\phi} = \frac{9d}{(2d-1)(2-d)} \tag{5-15}$$

In addition, I_2 and I_3 can be written as:

$$I_2 = \frac{1}{3} I_1^2 - J_2 \tag{5-16}$$

$$I_3 = J_3 - \frac{1}{3} I_1 J_2 + \frac{1}{27} I_1^3 \tag{5-17}$$

Substituting Equations 5-15, 5-16, and 5-17 into Equation 5-14 obtains:

$$2(d-1)^2 I_1^3 - 6\left(d^2 - d + 1\right) I_1 J_2 + 27 d J_3 = 0 \tag{5-18}$$

Equations 5-3 and 5-6 relate α with d as follows:

$$\alpha = \frac{1-d}{\sqrt{3}d} \tag{5-19}$$

Employing Equations 5-19 and 5-11 in Equation 5-18 gives:

$$d^2\left(\alpha I_1\right)^3-\left(d^2-d+1\right)J_2\left(\alpha I_1\right)+\left(1-d\right)\left(J_2\right)^{3/2}\cos\left(3\theta\right)=0 \tag{5-20}$$

Equation 5-20 is a transformed expression for the Matsuoka-Nakai model and still does not account for the temperature and rate dependent cohesion and strain hardening. To consider these material properties of the asphalt mixture, the term $\kappa a_T a_{\dot{\varepsilon}}$ is added to the hydrostatic stress and Equation 5-20 becomes:

$$d^2\left(\alpha I_1+\kappa a_T a_{\dot{\varepsilon}}\right)^3-\left(d^2-d+1\right)J_2\left(\alpha I_1+\kappa a_T a_{\dot{\varepsilon}}\right)+\left(1-d\right)\left(J_2\right)^{3/2}\cos\left(3\theta\right)=0 \tag{5-21}$$

To acquire an expression with the first order of stress, Equation 5-21 is regarded as a cubic equation which has a variable of $\alpha I_1+\kappa a_T a_{\dot{\varepsilon}}$. Solving this cubic equation gives a new yield surface function for the asphalt mixture:

$$\sqrt{J_2}\mu\cos\left[\frac{1}{3}\arccos\left(\gamma\cos 3\theta\right)\right]-\alpha I_1-\kappa a_T a_{\dot{\varepsilon}}=0 \tag{5-22}$$

The yield surface model in Equation 5-22 is named as ZLL (Zhang-Luo-Lytton) yield surface model, where $\rho\left(\theta\right)=\mu\cos\left[\frac{1}{3}\arccos\left(\gamma\cos 3\theta\right)\right]$, and parameters μ and γ depend on internal friction angle and can be calculated using d (i.e., Equation 5-6) as follows:

$$\begin{cases}\mu=\dfrac{2\sqrt{1-d+d^2}}{\sqrt{3}d}\\ \gamma=-\dfrac{3\sqrt{3}}{2}\dfrac{\left(1-d\right)d}{\left(1-d+d^2\right)^{3/2}}\end{cases} \tag{5-23}$$

It is further proved that μ and γ have the following relations:

$$\begin{cases}\rho\left(\theta=0\right)=\mu\cos\left[\dfrac{1}{3}\arccos\left(\gamma\right)\right]=1\\ \rho\left(\theta=\dfrac{\pi}{3}\right)=\mu\cos\left[\dfrac{1}{3}\arccos\left(-\gamma\right)\right]=\dfrac{1}{d}\end{cases} \tag{5-24}$$

The ZLL yield surface model as shown in Equation 5-22 is derived by combining the Matsuoka-Nakai model with the Drucker-Prager model and incorporating the temperature and rate dependent strain hardening function. When the differences between extension and compression are neglected (i.e., $d=1$), the ZLL model is reduced to the Drucker-Prager model; while the cohesion is neglected (i.e., $\kappa=0$), the ZLL model becomes the Matsuoka-Nakai model. In addition, the ZLL model also satisfies the three requirements of Lode dependence for pressure-sensitive materials (Bardet 1990): 1) extension ratio (i.e., $\rho(0)/\rho\left(\frac{\pi}{3}\right)=d$); 2) smoothness (i.e., the first derivative of the function $\rho(\theta)$ with respective to θ are zero, that is $\rho'(0)=\rho'\left(\frac{\pi}{3}\right)=0$); and 3) convexity that is inherited form Matsuoka-Nakai model. Figure 5-2 plots three dimensional examples of the ZLL yield surface and Figure 5-3 shows the yield surfaces of the ZLL model on the octahedral plane with different internal friction angles. One can find that the ZLL model provides a smooth and convex yield surface when the internal friction angle changes from 0 to 90 degrees and the extensive yield strength is less than compressive yield strength which is quantified by parameter d (or parameters μ and γ). The ZLL yield surface also characterizes the increasing yield strength with an increasing confinement (i.e., I_1 is included in the model). The temperature and strain rate dependent cohesion and strain hardening is represented by term $\kappa a_T a_{\dot{\varepsilon}}$ which is modeled in the next section.

Strain Hardening Model

In the derived ZLL yield surface model shown as Equation 5-22, $\kappa a_T a_{\dot{\varepsilon}}$ is used to consider the temperature and strain rate dependent strain hardening of the asphalt mixture. κ is

a strain hardening function at a reference temperature and a reference strain rate. κ is modeled by an exponential function as follows:

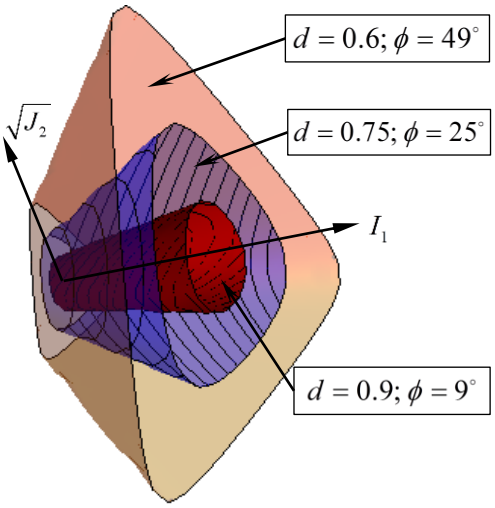

Figure 5-2 Three dimensional plot of the proposed ZLL yield surfaces

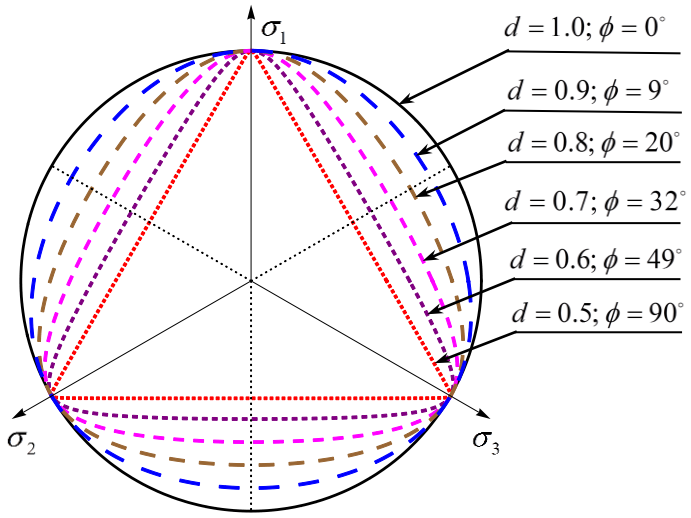

Figure 5-3 The ZLL yield surfaces on the octahedral plane with different internal friction angles

$$\kappa = \kappa_0 + \kappa_1\left[1-\exp\left(-\kappa_2\varepsilon_e^{vp}\right)\right] \tag{5-25}$$

where κ_0, κ_1 and κ_2 are material parameters identified at the reference temperature (T_0) and the reference strain rate ($\dot{\varepsilon}_0$); and ε_e^{vp} is the effective viscoplastic strain which will be discussed in the next sub-section.

The effect of temperature on the cohesion and strain hardening is accounted for by a temperature effect factor that is formulated by an Arrhenius temperature function as follows:

$$a_T = \exp\left[\frac{\Delta E_T}{R}\left(\frac{1}{T}-\frac{1}{T_0}\right)\right] \tag{5-26}$$

where ΔE_T is the activation energy of the temperature effect on the strain hardening, J/mol; R is the universal gas constant, 8.314 J/mol K; T is the temperature of interest, K; and T_0 is the reference temperature, K, at which κ_0, κ_1 and κ_2 are determined. ΔE_T is determined by performing uniaxial strength tests at different temperatures. It must be emphasized that a_T is totally different from the time-temperature shift factor (i.e., α_T in Chapter II) used in the construction of the master curve for the thermorheologically simple materials. The Arrhenius temperature function a_T quantifies the effect of the temperature on the yield strength during the strain hardening process while the time-temperature shift factor α_T evaluates the equivalent effects of the time and temperature on the responses of the viscoelastic materials. Equation 5-26 indicates that the cohesion and strain hardening amplitude will decrease as temperature increases, which will be verified by the experimental results in this chapter.

The effect of strain rate on the cohesion and strain hardening is evaluated by a strain rate effect factor ($a_{\dot{\varepsilon}}$) which is modeled by a power function as follows:

$$a_{\dot{\varepsilon}} = \left(\frac{\dot{\varepsilon}}{\dot{\varepsilon}_0} \right)^{\kappa_3} \tag{5-27}$$

where $\dot{\varepsilon}$ is the strain rate of interest, 1/sec; $\dot{\varepsilon}_0$ is the reference strain rate, 1/ sec; and κ_3 is a material property that can be determined by performing uniaxial strength tests on asphalt mixtures at different loading (strain) rates. For asphalt mixtures, it is satisfied that $0 < \kappa_3 < 1$. Equation 5-27 shows that the cohesion and strain hardening amplitude will increase as the strain rate increases, which will also be verified by the experimental results in this chapter.

Effective Viscoplastic Strain

In plastic analysis, the deformation of a strain hardening material under multiaxial loading is commonly correlated by a single uniaxial stress-strain curve which can be related to the multiaxial experimental results. To accomplish this correlation, the effective plastic strain (or, effective viscoplastic strain for an asphalt mixture) is employed to establish a correspondence between a material deforming under multiaxial loading and the same material deforming under uniaxial loading. The hardening behavior of the yield surface is normally controlled by the effective plastic strain, which is usually expressed in an incremental form such as (Khan and Huang 1995):

$$d\varepsilon_e^p = \sqrt{\frac{2}{3} d\varepsilon_{ij}^p d\varepsilon_{ij}^p} \tag{5-28}$$

where $d\varepsilon_{ij}^p$ is the incremental plastic strain tensor. The definition of the effective plastic strain in Equation 5-28 can only be applied to the materials that employ the von Mises yield surface and the associated flow rule (plastic potential is the same as yield surface). When the material is

assumed incompressible (i.e., Poisson's ratio is 0.5), Equation 5-28 gives $d\varepsilon_e^p = d\varepsilon_{11}^p$ which is the axial plastic strain increment in a uniaxial test.

For an asphalt mixture, Equation 5-8 has been widely used to calculate the effective viscoplastic strain rate; however, it is proved that Equation 5-8 employed the following assumptions: 1) associated flow rule which overestimates the dilation of the asphalt mixture (Masad et al. 2007); 2) Drucker-Prager yield surface which neglects the differences between extension and compression for an asphalt mixture; and 3) an asphalt mixture is assumed as an isotropic material. Thus, a new expression for the effective viscoplastic strain rate is derived to remove these assumptions. The derivation of the effective viscoplastic strain rate is presented in Chapter VI and the final expression is written as:

$$\dot{\varepsilon}_e^{vp} = \left[\left(\frac{1-\sqrt{3}\beta}{1-\sqrt{3}\alpha} \right)^2 + (n'-1)\left(\frac{1-\Delta'}{1+\Delta'} \right)^2 \left(\frac{0.5+\sqrt{3}\beta}{1-\sqrt{3}\alpha} \right)^2 \right]^{-\frac{1}{2}} \sqrt{\dot{\varepsilon}_{ij}^{vp}\dot{\varepsilon}_{ij}^{vp}} \tag{5-29}$$

where $n'=1$ in a uniaxial condition and $n'=3$ in a triaxial condition; Δ' is the modified vector magnitude defined in Equation 3-10; and β is the slope of the viscoplastic potential that reflects the dilative potential of the material. The theoretical relationship between β and Δ' is derived as an implicit expression (i.e., Equation 6-36) in Chapter VI. For practical use, the implicit theoretical relationship is converted to a linear explicit relation as follows:

$$\beta = 0.5889\Delta' - 0.0122 \ \left(R^2 = 0.9988\right) \tag{5-30}$$

Equation 5-29 is a very general definition for the effective viscoplastic strain rate which considers anisotropy ($\Delta' > 0$) and employs the ZLL yield surface model with a nonassociated flow rule ($\alpha > \beta$). Some studies have indicated that the viscoplastic deformation of the asphalt mixture is nonassociated (Florea 1994b; Masad et al. 2005). If using an associated viscoplastic flow rule ($\alpha = \beta$) and considering isotropy ($\Delta' = 0$), Equation 5-29 is reduced to Equation 5-8

that is used for asphalt mixtures in the literature. If further assuming $\alpha = \beta = 0$ (using von Mises yield criterion), Equation 5-29 is reduced to Equation 5-28 that has been widely used in plasticity theory.

LABORATORY TESTING AND MATERIALS

To obtain the model parameters and verify the temperature and strain rate effects on the yield surface, laboratory tests were performed on lab-mixed-lab-compacted (LMLC) asphalt mixture specimens that were fabricated with two types of asphalt binder (Valero asphalt (PG64-16) and NuStar asphalt (PG67-22)), two air void contents (4% and 7%) and three aging periods (0, 3, and 6-month continuous aging at 60 ℃). Two replicate specimens were fabricated for each combination of the asphalt binder, air void content and aging period. The testing protocol (including test method, loading mode, and temperature), tested materials and corresponding material properties are summarized in Table 5-2.

The lateral surface scanning test in Table 5-2 is described in Chapter III. Each cylinder specimen was laid horizontally on an automatic rotator which rotated the sample at a constant speed. The lateral surface of the sample was scanned by a portal scanner to obtain a lateral surface image, which was then analyzed to determine the aggregates' properties including the inclination angle, area of the cutting surface, and the aspect ratio. These measurements were used to calculate the modified vector magnitude by Equation 3-10. The UCC test (see Table 5-2) employed a constant stress and the axial strain was recorded to calculate the creep compliance. By using a Prony model (i.e., Equation 4-3), the relaxation modulus ($E(t)$) was determined based on the creep compliance (i.e., Equation 4-2) and was employed to calculate pseudostrain and determine the initial yield strength for the asphalt mixture.

Table 5-2 Testing Protocol, Materials and Parameters Determination for the Verification of the ZLL Yield Surface

<table>
<tr><th colspan="3">Testing Protocol</th><th rowspan="2">Materials Tested</th><th rowspan="2">Material Properties Obtained</th></tr>
<tr><th>Tests</th><th>Loading</th><th>Temperature</th></tr>
<tr><td>Lateral Surface Scanning Test</td><td>N/A</td><td>Room temperature</td><td rowspan="4">VHL and NHL mixtures:

<u>Binder:</u>
Valero (PG64-16)
NuStar (PG67-22)
<u>Air Void:</u>
4%
7%
<u>Periods of Aging at 60 ℃:</u>
0 month
3 months
6 months</td><td>Δ', β</td></tr>
<tr><td>Uniaxial Compressive Creep (UCC) Test</td><td>Remain constant at 40kPa</td><td>40 ℃</td><td>$E(t)$</td></tr>
<tr><td>Uniaxial Compressive Strength (UCS) Test</td><td>311με/sec</td><td>40 ℃</td><td rowspan="2">C, ϕ
α, κ_0
κ_1, κ_2</td></tr>
<tr><td>Triaxial Compressive Strength (TCS) Test</td><td>311με/sec
Confining pressures:
103kPa (15psi)
207kPa (30psi)</td><td>40 ℃</td></tr>
<tr><td>UCS at Different Strain Rate</td><td>18 με/sec
65 με/sec
311 με/sec
622 με/sec
1074 με/sec</td><td>40 ℃</td><td>NHL mixtures:
Binder: NuStar
Air Void: 7%
Aging: 6 months</td><td>κ_3</td></tr>
<tr><td>Uniaxial Compressive Creep (UCC) Test</td><td>40 kPa (at 40 ℃)
30 kPa (at 45 ℃)
25 kPa (at 50 ℃)
20 kPa (at 55 ℃)
15 kPa (at 60 ℃)</td><td rowspan="2">40 ℃
45 ℃
50 ℃
55 ℃
60 ℃</td><td rowspan="2">NHL mixtures:
Binder: NuStar
Air Void: 4%
Aging: 6 months</td><td>$E(t)$</td></tr>
<tr><td>UCS at Different Temperature</td><td>311με/sec</td><td>ΔE_T</td></tr>
</table>

The strength tests (e.g., UCS and TCS as shown in Table 5-2) employed a constant crosshead strain rate control mode, in which the specimens were compressed at a constant crosshead strain rate until failure occurred or the limits of the linear variable differential transducers (LVDTs) were reached. Figure 5-4 shows the typical stress responses, crosshead strains and on-specimen strains in a TCS test. Both the strain and strain rate of the on-specimen measurements were less than the crosshead strain and strain rate due to the machine compliance

that consumed part of the crosshead deformation, which was also observed in the literature (Zhao and Kim 2003). The strain rates mentioned in Table 5-2 are all referred to the strain rate measured by the on-specimens' LVDTs.

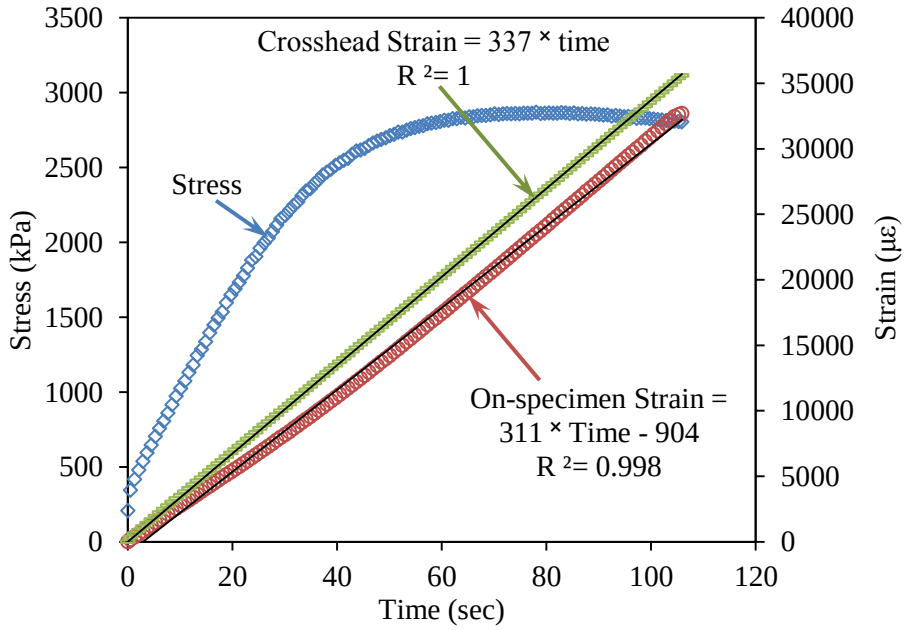

Figure 5-4 Stress, crosshead strains and on-specimen strains in a triaxial compressive strength test of an asphalt mixture

As for the materials used in the tests, a commonly-used Texas Hanson limestone shipped from New Braunfels, Texas, was selected in this study and the gradation for the aggregates was determined based on a Type C (coarse surface) dense gradation specified by the Texas Department of Transportation (TxDOT) (2004). The optimum asphalt content was calculated based on the TxDOT test procedure (TxDOT 2008) and was determined as 4.4% for the two binders (i.e., NuStar and Valero). The asphalt mixtures VHL and NHL stand for Valero binder with Hanson Limestone and NuStar binder with Hanson Limestone, respectively. The asphalt mixtures were compacted using the Superpave gyratory compactor to a cylindrical sample with

150 mm in diameter and 175 mm in height. Then the asphalt mixture samples were cored to 100 mm in diameter and were cut to 150 mm in height. The specimens were stored in an environmental chamber at the testing temperature for at least 3 hours to reach the equilibrium temperature and then tested using Universal Testing Machine (UTM) and Rapid Triaxial Test (RaTT) cell.

The testing configuration of the uniaxial tests such as UCC tests and UCS tests remain the same as the tests in Chapter IV (see Figure 4-2). The triaxial compressive strength (TCS) tests require a confining pressure, which is accomplished by the rapid triaxial testing (RaTT) cell of the UTM that is shown in Figure 5-5. In the RaTT cell, the confining pressure is provided by compressed air and the asphalt mixture specimen is wrapped by a cylindrical rubber. Two vertical LVDTs and two radial LVDTs are used to record the vertical and horizontal deformation of the samples.

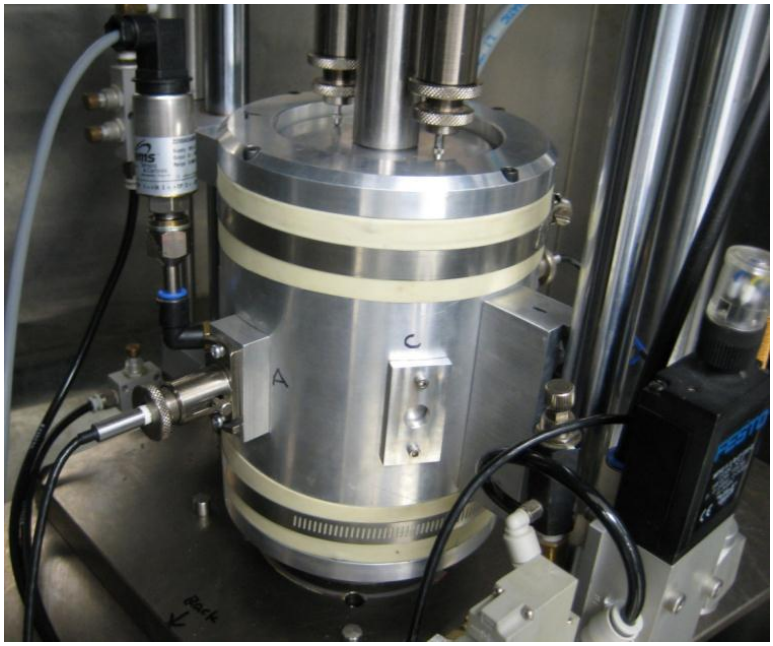

Figure 5-5 Testing configuration of rapid triaxial test (RaTT) cell

DETERMINATION OF INITIAL YIELD STRENGTH AND STRAIN DECOMPOSITION IN STRENGTH TESTS

To obtain material properties such as C, ϕ, α and κ_0, the initial yield strength (σ_y) should be firstly determined. The initial yield strength is defined as the stress at which the plastic (or viscoplastic) deformation occurs. For the elastoplastic material (e.g., metal), the initial yield strength is determined as the separation point at which the stress-strain curve of a strength test transits from the linear part (elastic domain) to the nonlinear part (plastic domain). However, for a viscoplastic material like an asphalt mixture, no linear part is observed on the stress-strain curve measured in the strength test. As shown in Figure 5-6, the stress-strain curve illustrates a nonlinear relationship even at a very small load level and no obvious separation point is observed on the stress-strain curve. Based on this observation, some researchers (Drescher et al. 1993; Lu and Wright 1998) concluded that no yielding threshold (i.e., initial yield strength) existed for the asphalt mixture, which is proved to be an incorrect conclusion based on the following analysis.

In fact, the nonlinearity of the stress-strain curve is caused by the relaxation of the viscoelastic material, which can be explained by a simple mechanistic analysis: if the input of the strength test is a controlled strain: $\varepsilon = ct$ where c is the constant strain rate, the output stress in the viscoelastic domain (before the yielding threshold) is theoretically calculated as $\sigma = c\int_0^t E(s)\,ds$. One can find that the strain is linear with time while the stress is nonlinear with time, thus the stress is nonlinearly related to the strain and the stress-strain curve becomes nonlinear even in the viscoelastic domain. Because of the nonlinearity of the stress-strain curve, the traditional approach of determining the initial yield strength by using the separation point of the linear and the nonlinear curves does not apply to the asphalt mixture.

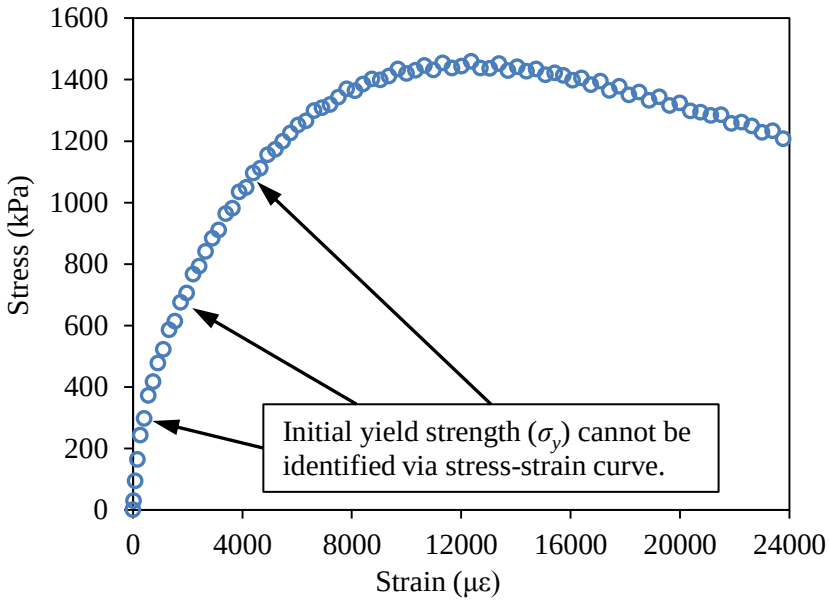

Figure 5-6 Typical stress-strain curve in a uniaxial compressive strength test of an asphalt mixture

However, the asphalt mixture does have a yielding threshold that separates the viscoelastic part from the viscoplastic part of the stress-strain curve. An analytical method using pseudostrain concept is proposed in this chapter to effectively and accurately determine the initial yield strength of the asphalt mixture, which is illustrated by the following steps.

First, the relaxation modulus of the undamaged asphalt mixture is determined from the uniaxial compressive creep tests and modeled by Prony series in Equation 4-3. Details about the model can be found in Chapter IV.

Second, the pseudostrain in a strength test with a constant strain rate is calculated based on the definition of pseudostrain (i.e., Equation 4-13) and shown as:

$$\varepsilon^R(t) = \frac{c}{E_R}\left[E_\infty t + \sum_{j=1}^{M} E_j k_j \left(1 - e^{-\frac{t}{k_j}}\right)\right] \tag{5-31}$$

where c is the constant strain rate used in the strength test; E_R is reference modulus which is assigned equal to the Young's modulus of the asphalt mixture ($E_Y = E\left(t=0\right)$).

Third, the measured stress is plotted against the pseudostrain, as shown in Figure 5-7 which has a linear portion ($R^2 = 0.9989$) with a slope of Young's modulus. It is noted that the initial several data (before the linear portion) in Figure 5-7 showing nonlinearity is caused by the machine compliance. The initial yield strength (σ_y) is determined as the stress at the end of the linear portion of the stress-pseudostrain curve. The initial yield strengths determined from uniaxial and triaxial strength tests are employed to calculate the material properties such as C, ϕ, α, and κ_0.

The reason for using the pseudostrain rather than total strain is that, when E_R equals to the Young's modulus, the pseudostrain is demonstrated to be equal to the remaining strain after subtracting the viscous strain from the total strain (Zhang et al. 2012b). In other words, the pseudostrain is the strain component after removing the viscous effect on the material responses. Before yielding occurs (viscoelastic zone), the pseudostrain shows a linear relation with the stress since it is equivalent to the elastic strain (ε^e). As the viscoplastic deformation occurs, the pseudostrain equals to the sum of ε^e and viscoplastic strain (ε^{vp}). After the peak stress, the viscofracture strain (ε^{vf}) also contribute to the pseudostrain. Thus the pseudostrain in a strength test is physically decomposed as:

$$\varepsilon^R = \begin{cases} \varepsilon^e & \textit{Viscoelastic Undamaged Zone} \\ \varepsilon^e + \varepsilon^{vp} & \textit{Viscoplastic Hardening Zone} \\ \varepsilon^e + \varepsilon^{vp} + \varepsilon^{vf} & \textit{Viscofracture Softening Zone} \end{cases} \tag{5-32a}$$

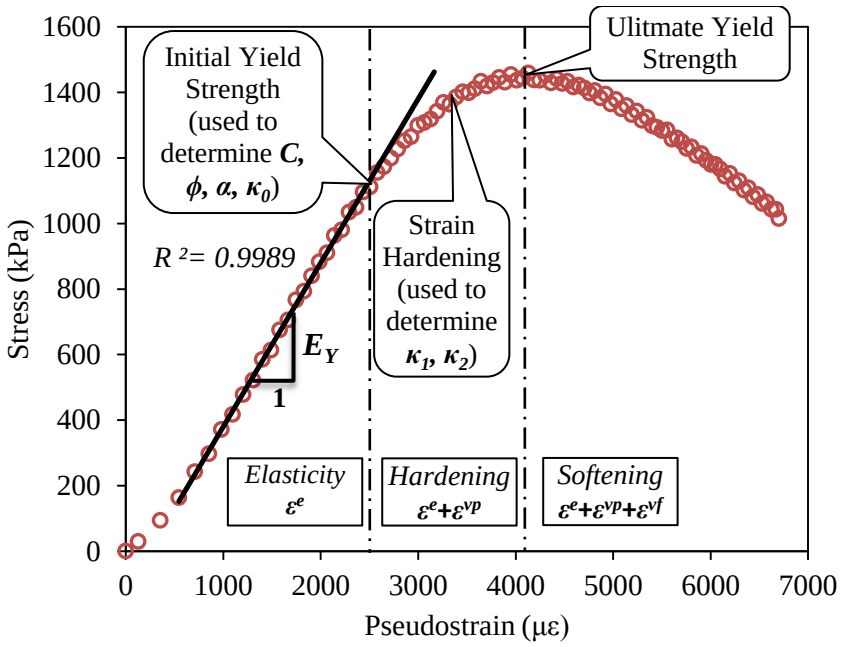

Figure 5-7 Stress versus pseudostrain in a uniaxial compressive strength test of an asphalt mixture

The stress-pseudostrain curve from the initial yield strength (σ_y) to the ultimate yield strength (peak stress, σ_u) shows a nonlinear relation as shown in Figure 5-7, which actually is the strain hardening process. The determinations of the hardening parameters (i.e., κ_1 and κ_2) are based on this portion of the curve. According to the above analysis and Equation 5-32a, a strain decomposition can be performed on the total strain (ε^T) before σ_u in the strength test:

$$\begin{cases} \varepsilon^e = \sigma / E_Y \\ \varepsilon^{vi} = \varepsilon^T - \varepsilon^R \\ \varepsilon^{vp} = \varepsilon^R - \varepsilon^e \end{cases} \tag{5-32b}$$

After the peak stress, the asphalt mixture is in a strain softening process due to the initiation and propagation of cracks, and the viscofracture strain (ε^{vf}) that is caused by the

opening of cracks will be introduced into the material. The viscofracture will be characterized using fracture and damage mechanics in Chapter VII.

TESTING RESULTS AND PARAMETRIC ANALYSIS

This section presents data analysis methods, testing results and parametric analysis. The effects of the temperature and strain rate on the yielding properties of the asphalt mixture are discussed based on the testing results.

Yielding Strength Parametric Analysis

The yielding strength properties are firstly presented in this subsection including determination of the initial yield strength, slope and intercept of the ZLL yield surface, cohesion and internal friction angle of the asphalt mixture.

Based on the pseudostrain method proposed in the last section, the Young's moduli (E_Y) and the initial yield strengths (σ_y) for different asphalt mixtures were obtained. Figure 5-8 shows the measured Young's moduli and the initial yield strengths in the UCS test for different asphalt mixtures at 40 ℃. It is found that both E_Y and σ_y increase as the air void content decreases or the aging period increases. No significant differences are found between the asphalt mixtures with the Valero binder (PG64-16) and the asphalt mixtures with the NuStar binder (PG67-22) since the two binders have very close Superpave performance grading (PG) at the high temperature. A relationship was obtained as shown in Equation 5-33 between the initial yield strength and the Young's modulus with an acceptable coefficient of determination (R^2).

$$\sigma_y\left(kPa\right)=0.8782\times E_Y\left(MPa\right)+64.32 \qquad R^2=0.8306 \tag{5-33}$$

Equation 5-33 indicates a stiffer asphalt mixture tends to have a higher initial yield strength. It must be emphasized that the relationship between E_Y and σ_y can be affected by loading rate, confinement and temperature.

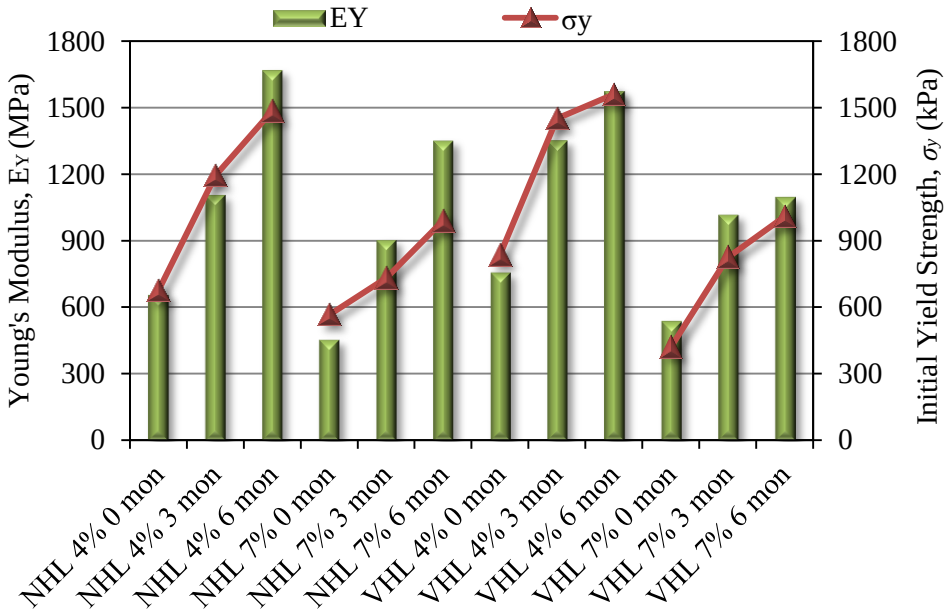

Figure 5-8 Young's modulus and initial yield strength in uniaxial compressive strength test for different asphalt mixtures at 40 ℃

The slope (α) and intercept (κ_0) of the proposed ZLL yield surface model (i.e., Equation 5-22) were determined based on the initial yield strengths in the UCS and TCS tests. At the reference temperature and strain rate, the ZLL model in Equation 5-22 gives the initial yield surface function at triaxial compressive condition as follows:

$$\frac{\sigma_y - p}{\sqrt{3}} - \alpha\left(\sigma_y + 2p\right) - \kappa_0 = 0 \tag{5-34}$$

where σ_y is the initial yield strength and p is the confining pressure. The slope (α) and intercept (κ_0) of the yield surface were determined for varieties of asphalt mixtures and shown in Figure 5-9.

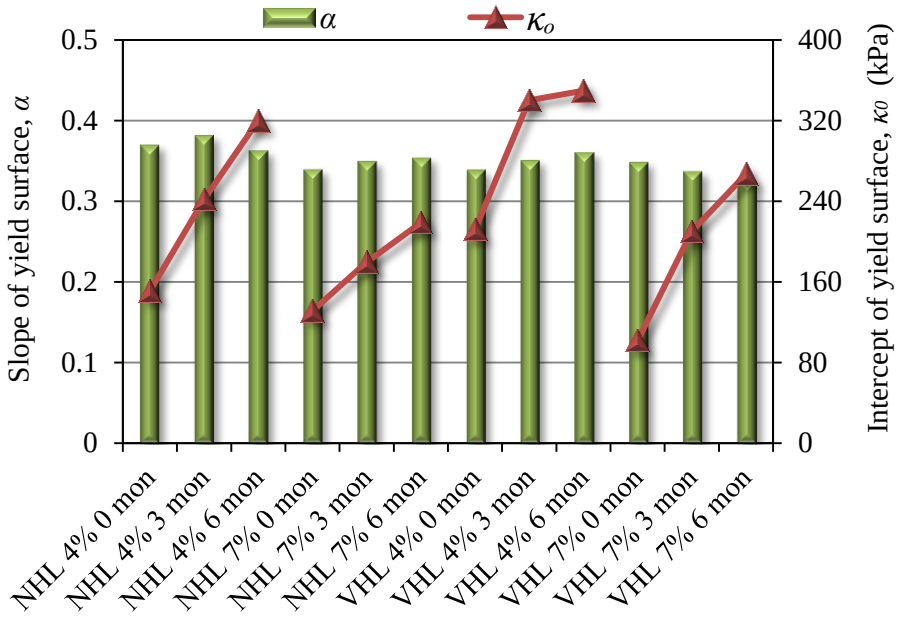

Figure 5-9 Slope and intercept of the ZLL yield surface on meridian plane for different asphalt mixtures

The cohesion (C) and internal friction angle (ϕ) for the asphalt mixture were also determined based on the UCS and TCS testing data. The Mohr-Coulomb initial yield surface function is written as follows:

$$\frac{\sigma_y - p}{2} = \frac{\sigma_y + p}{2}\sin\phi - C\cdot\cos\phi \tag{5-35}$$

Employing the initial yield strengths (σ_y) at three different confining pressures (p = 0, 103, 207 kPa) in Equation 5-35, the cohesion (C) and internal friction angle (ϕ) of the asphalt mixtures were determined and shown in Figure 5-10.

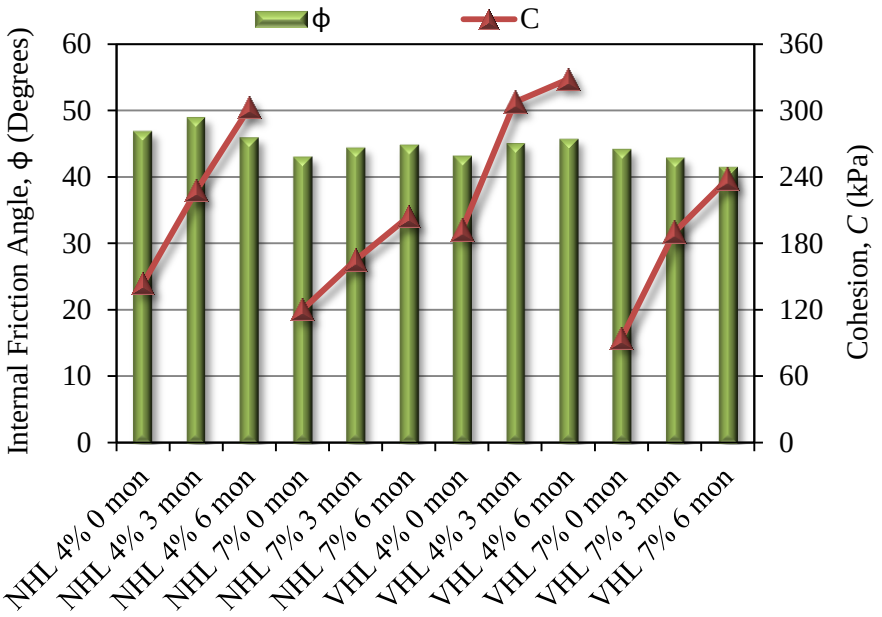

Figure 5-10 Cohesion and internal friction angle for different asphalt mixtures at 40 ℃

It is found from Figure 5-9 and Figure 5-10 that the slope of the ZLL yield surface (α) has an average value of 0.352 with a standard deviation of 0.016 and the internal friction angle (ϕ) has an average value of 45 degrees with a standard deviation of 2 degrees. Both α and ϕ have limited variations for the tested asphalt mixture specimens, thus one can conclude that α and ϕ are not affected by the binder type, air void content and aging period. This is reasonable since ϕ relies on the aggregate contacts and interlocks which depend on the aggregate gradation of the asphalt mixture specimen. Since all of the tested asphalt mixture specimens have an identical gradation, it makes sense that ϕ remains similar for different asphalt mixture specimens that were tested in this study. α represents the internal friction angle according to Equation 5-3; thus α also stays close even though the asphalt mixture specimens have different binders, air void contents and aging periods. In fact, since the proposed ZLL yield surface coincides with the external apices of the Mohr-Coulomb yield surface, the relationship between

α and ϕ in Equation 5-3 also applies to the ZLL yield surface. Using the measured ϕ, α is predicted by Equation 5-3 and compared with the measured α. A good agreement is found in Figure 5-11 between the measured α and the predicted α.

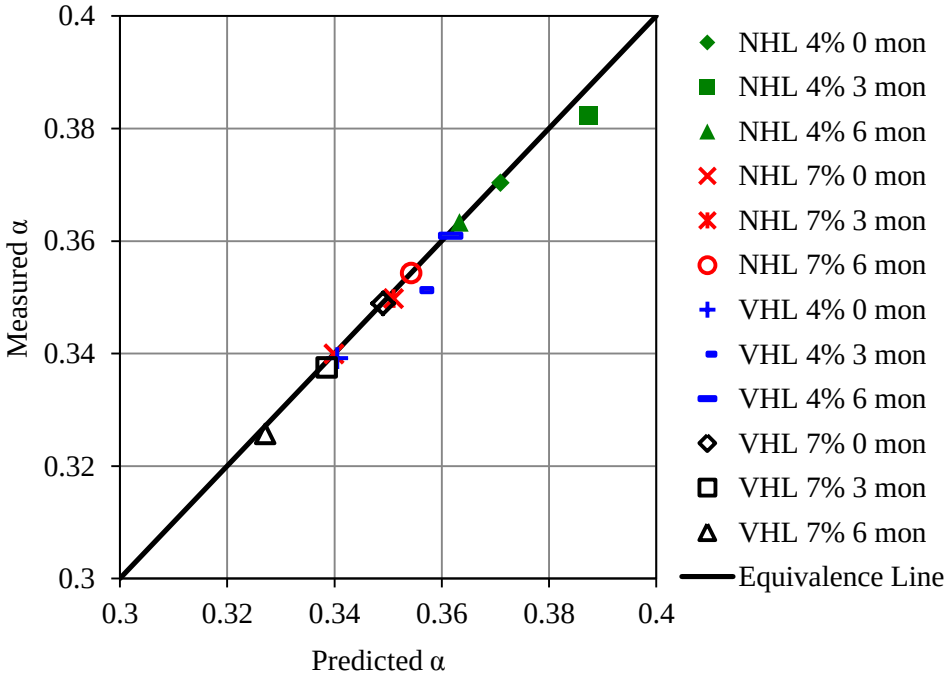

Figure 5-11 Comparisons between measured α from tests and predicted α based on ϕ for different asphalt mixtures

Figure 5-9 and Figure 5-10 also indicate that the intercept of the ZLL yield surface (κ_0) and cohesion (C) increase as the aging period increases or the air void content decreases. κ_0 and C of the asphalt mixture with Valero binder are a little greater than the asphalt mixture with NuStar binder. Actually, κ_0 and C quantify the cohesive properties of the concrete. A stiffer asphalt mixture (e.g., due to stiffer binder, low air voids, longer aging periods) tends to have a greater cohesive strength. With using the measured C and ϕ, κ_0 is predicted by Equation 5-4

and compared with the measured κ_0. A good agreement is shown in Figure 5-12 between the measured κ_0 and the predicted κ_0, which demonstrates that the relationship between C, ϕ and κ_0 in Equation 5-4 also applies to the proposed ZLL yield surface.

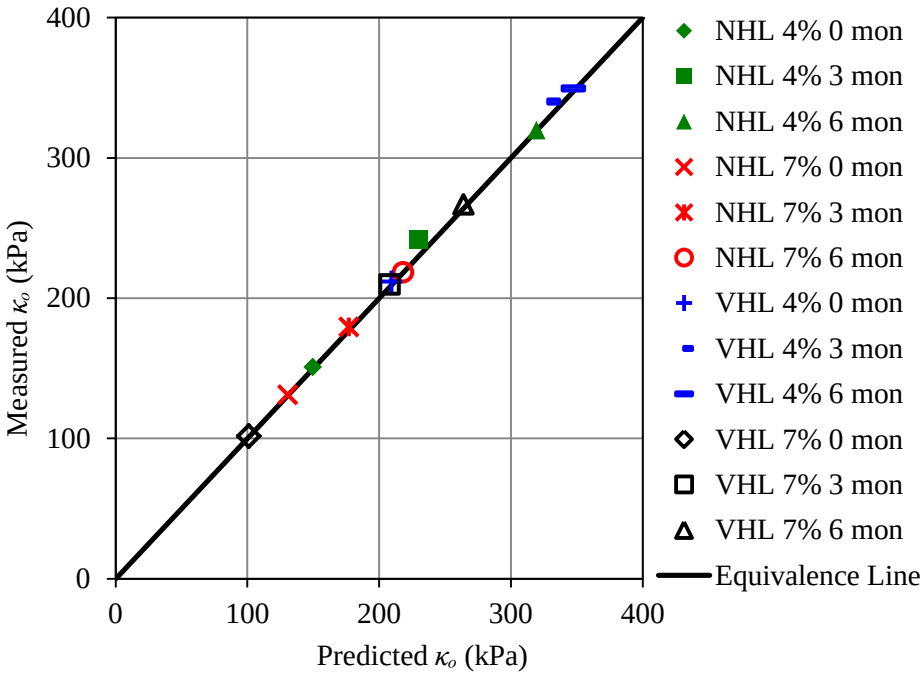

Figure 5-12 Comparisons between measured κ_0 from tests and predicted κ_0 based on C and ϕ for different asphalt mixtures at 40 ℃

Based on the testing results, two relations between κ_0, C and σ_y in the uniaxial compressive strength tests are regressed as follows:

$$C = 0.1973 \times \sigma_y + 16.22 \qquad R^2 = 0.9734 \tag{5-36}$$

$$\kappa_0 = 0.2102 \times \sigma_y + 20.93 \qquad R^2 = 0.9536 \tag{5-37}$$

Equations 5-36 and 5-37 demonstrate that κ_0 and C are highly related to the initial yield strength in the uniaxial compressive strength test. By considering Equation 5-33 with

Equations 5-36 and 5-37, one may conclude that a stiffer asphalt mixture tends to have a higher values for κ_0 and C.

The relationships between α, κ_0 and C, ϕ in Equations 5-3 and 5-4 are verified by Figure 5-11 and Figure 5-12. This finding can be used to simplify the testing protocols that are used to determine the model parameters. The TCS tests in Table 5-2 are employed to perform strength tests at different confining pressures and determine the strength parameters such as α, κ_0 and C, ϕ. However, the TCS tests require testing equipment which can provide a confinement during the tests, such as RaTT cell used in this study or triaxial cell used in material testing system (MTS) machine. The equipment might not be accessible since they are relatively expensive and the operations are also more complicated compared to the uniaxial tests. To avoid those problems, the users can employ the indirect tensile strength (IDT) test as an alternative test for the TCS test. In fact, some studies (Christensen et al. 2004; Pellinen et al. 2005) showed that the Mohr-Coulomb strength parameters (C and ϕ) could be determined by performing UCS and IDT strength test . Once, C and ϕ are determined, the model parameters α and κ_0 can be directly calculated by Equations 5-3 and 5-4.

Strain Hardening Parametric Analysis

This subsection presents the determination of hardening parameters κ_1 and κ_2 in the strain hardening function (i.e., Equation 5-25) based on the strength testing data. At the reference temperature and strain rate, the ZLL model in Equation 5-22 gives the hardening yielding surface function in uniaxial ($p = 0$) or triaxial ($p > 0$) compressive condition as follows:

$$\frac{\sigma_1 - p}{\sqrt{3}} - \alpha\left(\sigma_1 + 2p\right) - \kappa_0 = \kappa_1\left[1 - \exp\left(-\kappa_2 \varepsilon_e^{vp}\right)\right] \tag{5-38}$$

where σ_1 is the measured stress during strain hardening process that is between the initial yield strength and the ultimate yield strength. ε_e^{vp} is the effective viscoplastic strain that is defined by Equation 5-29. In the uniaxial compressive condition, ε_e^{vp} is obtained by integrating Equation 5-29 over time and becomes:

$$\varepsilon_e^{vp} = \frac{1-\sqrt{3}\alpha}{1-\sqrt{3}\beta}\varepsilon_1^{vp} = \frac{1-\sqrt{3}\alpha}{1-\sqrt{3}\beta}\left(\varepsilon^R - \frac{\sigma_1}{E_Y}\right) \tag{5-39}$$

where ε_1^{vp} is the viscoplastic strain in the axial direction of the UCS test that can be calculated by subtracting the elastic strain ($\varepsilon^e = \sigma_1 / E_Y$ based on Hooke's law) from the pseudostrain (i.e. ε^R in Equation 5-31) . β is determined by Equation 5-30 in which the modified vector magnitude is measured by the lateral surface scanning test.

Figure 5-13 shows an example for the measured stress (σ_1) versus the effective viscoplastic strain (ε_e^{vp}). It is found that the effective viscoplastic strains do not occur before the initial yield strength and the stresses show a power curve with the effective viscoplastic strains during the strain hardening process. The measured $\sigma_1 \sim \varepsilon_e^{vp}$ data during the strain hardening process were modeled by the exponential function shown in Equation 5-25. The modeled stresses were plotted as the solid line in Figure 5-13 and the hardening parameters κ_1 and κ_2 were determined by fitting Equation 5-25 to the $\sigma_1 \sim \varepsilon_e^{vp}$ data.

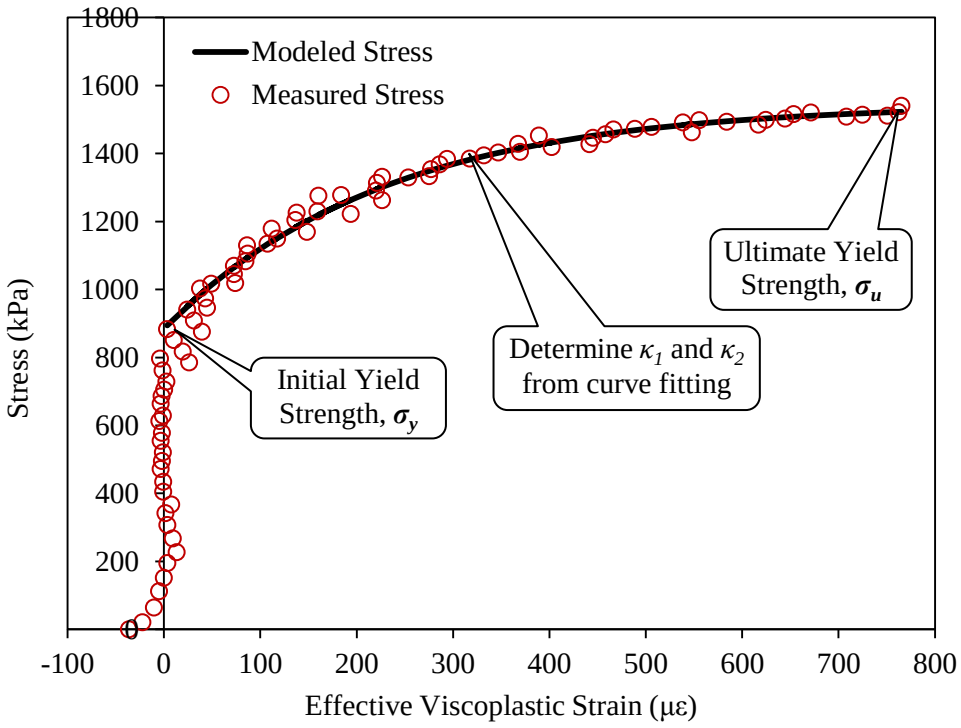

Figure 5-13 Stress versus effective viscoplastic strain in a uniaxial compressive strength test of an asphalt mixture at 40 ℃

One can conclude from Figure 5-13 that the strain hardening model using an exponential function can perfectly model the measured stresses during the strain hardening process in the strength tests. The same data analyses were performed on all of the tested asphalt mixtures and Figure 5-14 shows the measured values of the hardening parameters κ_1 and κ_2 for different asphalt mixtures. In general, κ_1 determines the amplitude of the strain hardening and it increases as the air void content decreases or the aging period increases. In fact, κ_1, similar to κ_0, represents the cohesive properties of the asphalt mixture and a stiffer asphalt mixture tends to have a greater κ_1. κ_2 determines the rate of the strain hardening for the asphalt mixture in compression. Testing results in Figure 5-14 do not show obvious differences for κ_2 when asphalt mixtures have different binders, air void contents, and aging periods.

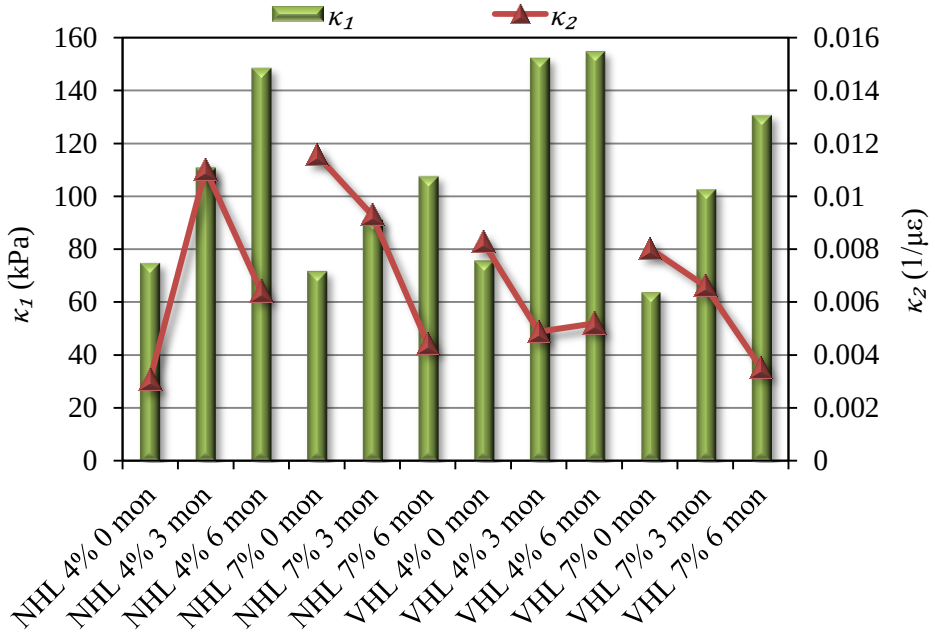

Figure 5-14 Calculated κ_1 and κ_2 for different asphalt mixtures at 40 ℃

Effect of Temperature on the Yielding of Asphalt Mixture

This subsection determines the temperature effect factor (a_T) and discusses the effect of temperature on the yielding properties of the asphalt mixture.

The uniaxial compressive strength tests were performed on the NHL asphalt mixtures (NuStar binder, 4% air void, 6-month aging) at five different temperatures (40 ℃, 45 ℃, 50 ℃, 55 ℃, and 60 ℃). Figure 5-15 shows the stress-strain curves at the five temperatures. Each curve is an average of the testing data from two replicate specimens. One can find that the yield strength decreases as the temperature increases, which is due to the lower cohesion of the asphalt mixture at a higher temperature. From Figure 5-15, it is very easy to determine the ultimate yield strength (σ_u) which is the peak stress on the stress-strain curve.

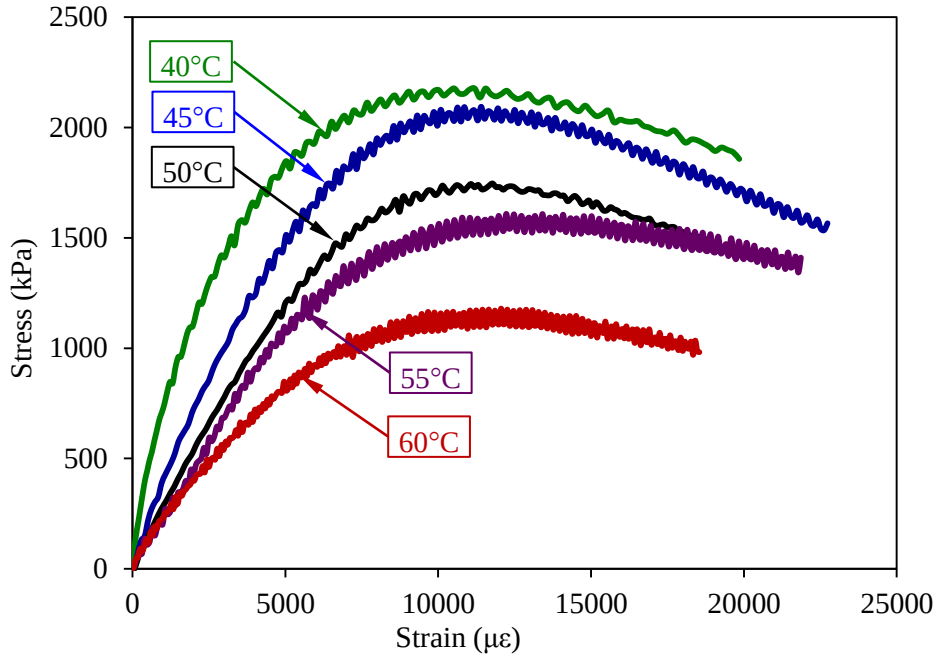

Figure 5-15 Measure stress versus strain in uniaxial compressive strength tests of asphalt mixtures at different temperatures

The ultimate yield strengths at the five different temperatures (in Kelvin: K=273.15+ ℃) are shown in Figure 5-16 and found to decline with the increasing testing temperature. The ultimate yield strengths were employed to determine the temperature effect factor. The asphalt mixture starts to yield at the initial yield strength and the yield surface expands due to strain hardening until the stress arrives at the ultimate yield strength. At the moment of the ultimate yield strength, the strain hardening becomes saturated and the ZLL yield surface function in the uniaxial condition is:

$$\frac{\sigma_u}{\sqrt{3}} - \alpha\sigma_u = \left(\kappa_0 + \kappa_1\right) a_T \tag{5-40}$$

where σ_u is the ultimate yield strength that is determined from the stress-strain curve of the UCS test; a_T is the temperature effect factor. α, κ_0 and κ_1 are yielding parameters determined

at the reference temperature (i.e., 40 ℃ in this study). Thus the values of a_T were solved based on Equation 5-40 and shown in Figure 5-16.

The relationship between a_T and temperature (in Kelvin) was modeled by the Arrhenius temperature function shown in Equation 5-26. Using the measured data of a_T, the activation energy for the temperature effect (ΔE_T) was determined to be 21020 J/mol for this asphalt mixture (NHL: NuStar binder, 4% air void, 6-month aging). Figure 5-16 also shows the modeled a_T by the Arrhenius temperature model, which is demonstrated to be approximate to the calculated a_T. The decreasing a_T with temperature quantifies the loss of the cohesion and strain hardening amplitude due to an increasing temperature.

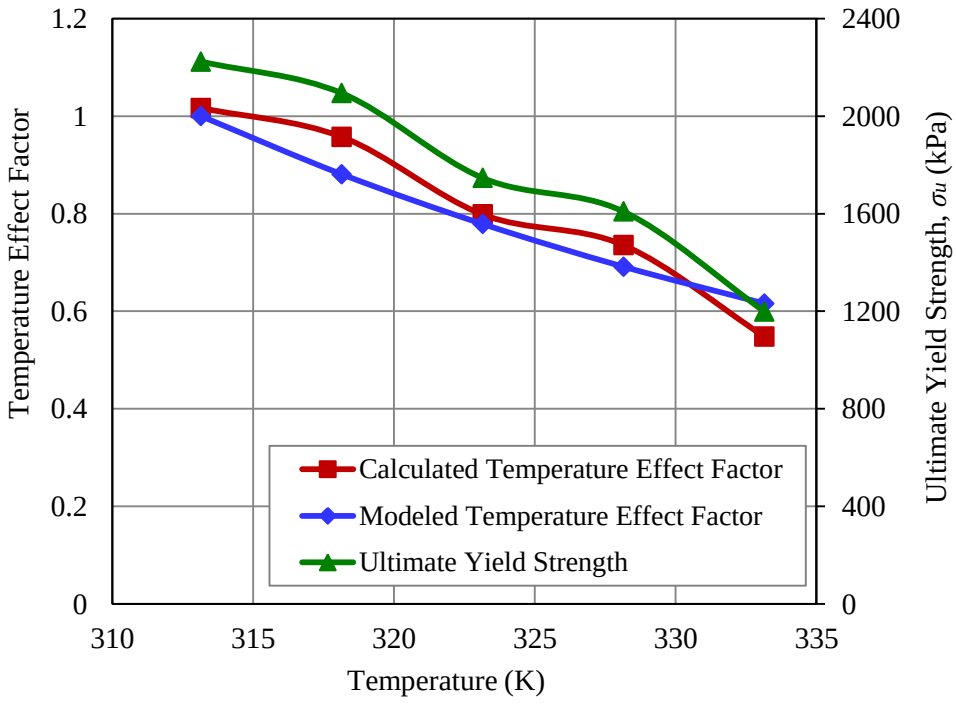

Figure 5-16 Ultimate yield strengths (σ_u) of asphalt mixtures at different temperatures and comparisons between the calculated and the predicted temperature effect factors (a_T)

From the above determining method, one can find that a_T or ΔE_T can be solely determined by the ultimate yield strength (σ_u). However, it must be verified that the calculated a_T based on the ultimate yield strength can successfully predict the yield stresses during the entire strain hardening process that are the stresses between the initial yield strength and the ultimate yield strength. Thus, the calculated values of a_T solely based on σ_u were employed to predict the yield stresses during the strain hardening as follows:

$$\frac{\sigma_1}{\sqrt{3}} - \alpha\sigma_1 = \left\{\kappa_0 + \kappa_1\left[1 - \exp\left(-\kappa_2 \varepsilon_e^{vp}\right)\right]\right\} a_T \tag{5-41}$$

where σ_1 is the yield stresses during strain hardening and ε_e^{vp} is the effective viscoplastic strain that is computed by Equation 5-39. On the one hand, the yield stresses were predicted by Equation 5-41 using the parameters α, κ_0, κ_1 and κ_2 at the reference temperature and a_T calculated based on the ultimate yield strengths at different temperatures. On the other hand, the yield stresses were directly measured in the uniaxial compressive strength tests at the five temperatures. Figure 5-17 compares the measured yield stresses and the predicted yield stresses at 40 ℃, 45 ℃, 50 ℃, 55 ℃, and 60 ℃, respectively.

It can be found from Figure 5-17 that the predicted stresses are comparable with the measured stresses for the asphalt mixtures at each of the temperatures. Thus one can conclude that it is reliable and feasible to calculate the temperature effect factor (a_T) solely based on the ultimate yield strengths which can be easily obtained from the stress-strain curves of the asphalt mixture. In addition, Figure 5-17 also indicates that the asphalt mixture requires a lower yield stress to achieve the same viscoplastic strain when the temperature increases, which means a_T is a decreasing function of the temperature; however, the rate of the strain hardening (κ_2) does not change significantly at different temperatures.

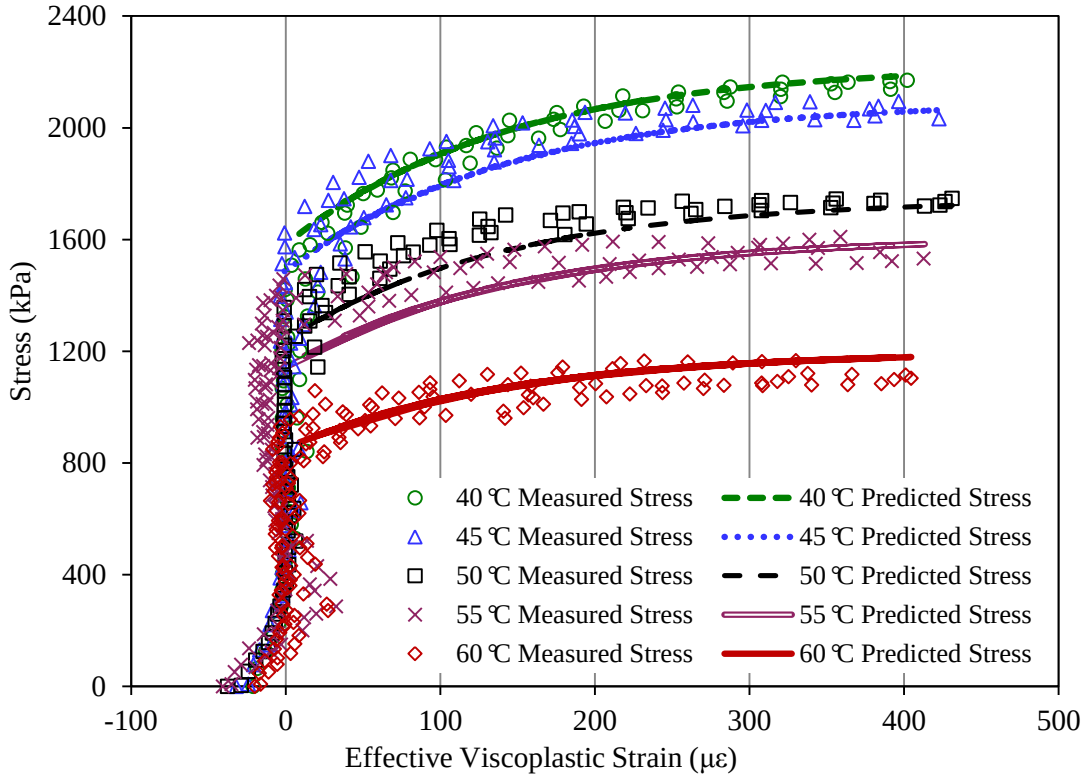

Figure 5-17 Comparisons between the measured stresses and the predicted stresses during strain hardening process of the asphalt mixtures at different temperatures

Effect of Strain Rate on the Yielding of Asphalt Mixture

This subsection determines the strain rate effect factor ($a_{\dot{\varepsilon}}$) and discusses the effect of strain rate on the yielding properties of the asphalt mixture.

The uniaxial compressive strength tests were performed on the NHL asphalt mixtures (NuStar binder, 7% air void, 6-month aging) at 40 ℃ using five different strain rates (i.e., 18 με/sec, 65 με/sec, 311 με/sec, 622 με/sec and 1074 με/sec). Figure 5-18 illustrates the stress-strain curves in the uniaxial compressive strength tests of asphalt mixtures at the five strain rates. Each curve is an average of the testing data from two replicate specimens. It is found from Figure 5-18 that the yield stress increases with an increasing strain rate, which indicates that a larger cohesive strength and the amplitude of the strain hardening are obtained for the asphalt

mixture tested at a higher strain rate. The strain rate effect factor ($a_{\dot{\varepsilon}}$) in Equation 5-27 was employed to account for the effect of strain rate on the cohesion and strain hardening. To determine $a_{\dot{\varepsilon}}$, the ultimate yield strengths (σ_u) were acquired from the stress-strain curves. Figure 5-19 shows σ_u at different strain rates and σ_u increases and follows a power curve as the strain rate increases.

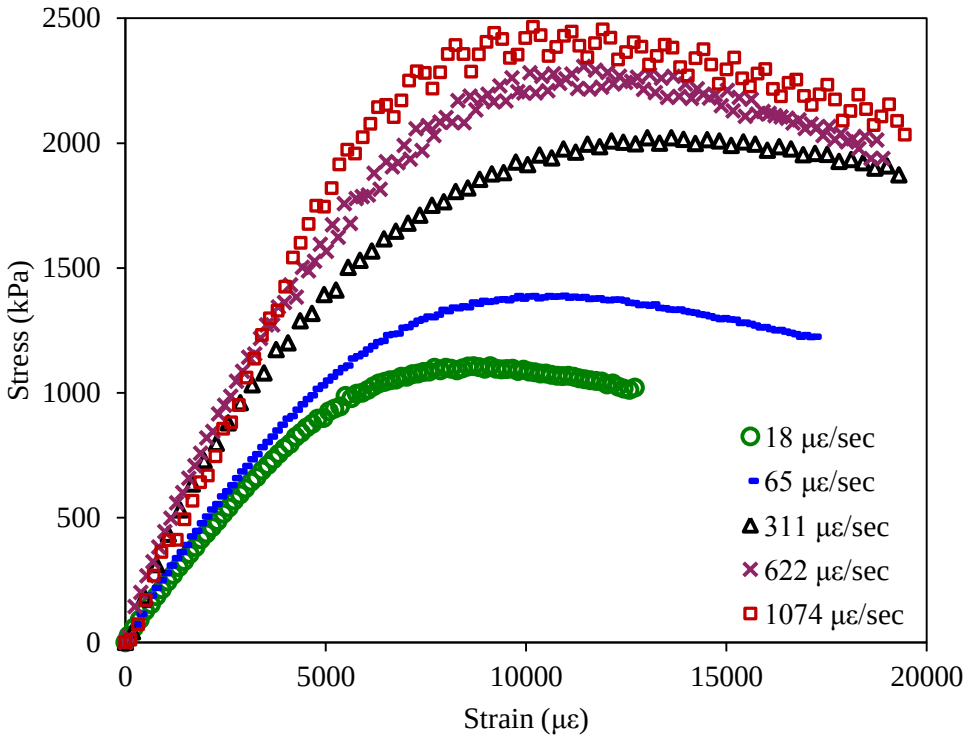

Figure 5-18 Measure stress versus strain in uniaxial compressive strength tests of asphalt mixtures at different strain rates and 40 ℃

At a constant temperature, $a_T = 1$ and the ZLL yield surface function at the ultimate yield strength of the uniaxial compressive strength (UCS) test becomes:

$$\frac{\sigma_u}{\sqrt{3}} - \alpha\sigma_u = \left(\kappa_0 + \kappa_1\right) a_{\dot{\varepsilon}} \tag{5-42}$$

where σ_u is the ultimate yield strength that is determined from the stress-strain curve of the UCS test; $a_{\dot{\varepsilon}}$ is the strain rate effect factor. α, κ_0 and κ_1 are yielding parameters determined at the reference strain rate (i.e., 311 με/sec in this study). By substituting the ultimate yield strengths in Equation 5-42, the values of $a_{\dot{\varepsilon}}$ were resolved at the five different strain rates which are shown as the calculated $a_{\dot{\varepsilon}}$ in Figure 5-19. The calculated $a_{\dot{\varepsilon}}$ were modeled by a power function in Equation 5-27 in which the power coefficient κ_3 was resolved as 0.196 for this NHL asphalt mixture (NuStar binder, 7% air void, 6-month aging). The increasing $a_{\dot{\varepsilon}}$ following a power function with strain rates quantifies the effect of strain rate on the material cohesion and strain hardening during the viscoplastic deformation of the asphalt mixture.

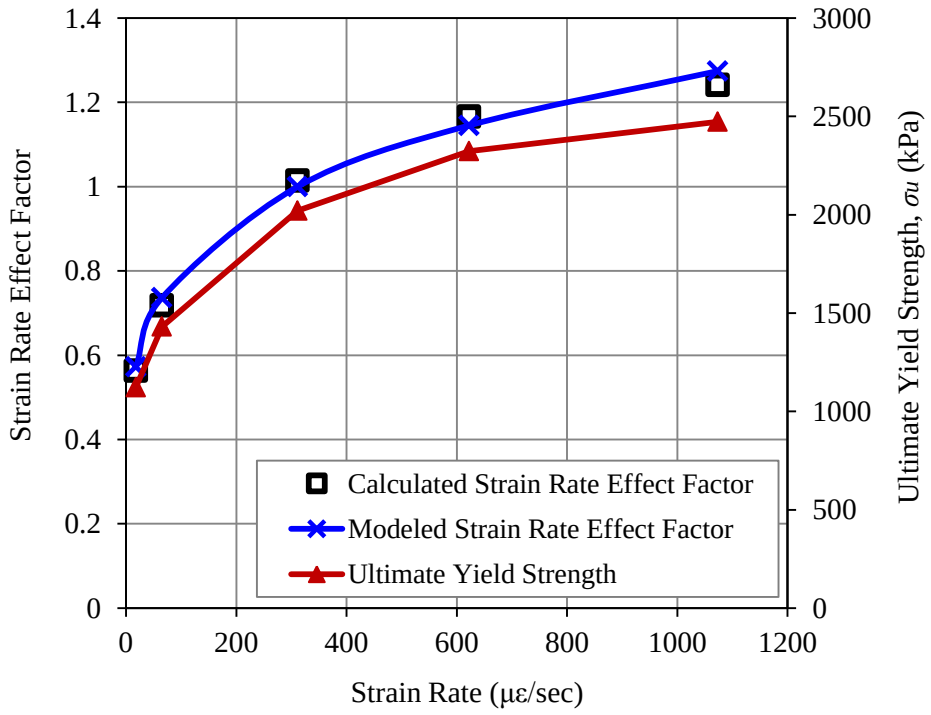

Figure 5-19 Ultimate yield strengths (σ_u) of asphalt mixtures at different strain rates and comparisons between the calculated and the predicted strain rate effect factors ($a_{\dot{\varepsilon}}$)

Similar to the verification process of a_T, the verification of $a_{\dot{\varepsilon}}$ was performed on the entire strain hardening process. The values of $a_{\dot{\varepsilon}}$ calculated solely based on the ultimate yield strengths were employed to predict the yield stresses during the whole strain hardening process. The yield stresses predicting function is as follows:

$$\frac{\sigma_1}{\sqrt{3}} - \alpha\sigma_1 = \left\{\kappa_0 + \kappa_1\left[1 - \exp\left(-\kappa_2 \varepsilon_e^{vp}\right)\right]\right\} a_{\dot{\varepsilon}} \tag{5-43}$$

where σ_1 is the yield stresses during strain hardening and ε_e^{vp} is the effective viscoplastic strain that is computed by Equation 5-39. α, κ_0, κ_1 and κ_2 are parameters determined at the reference strain rate and $a_{\dot{\varepsilon}}$ is strain rate effect factor calculated based on the ultimate yield strengths at different strain rates. Figure 5-20 compares the measured yield stresses with the predicted yield stresses at 40 ℃ using strain rates of 18 με/sec, 65 με/sec, 311 με/sec, 622 με/sec and 1074 με/sec, respectively. One can find that the predicted stresses match well with the measured stresses during the entire strain hardening process for all of the strain rates used in the tests. Thus, the same as with the temperature effect factor, it is also reliable and feasible to calculate the strain rate effect factor solely based on the ultimate yield strengths of the asphalt mixture. In addition, Figure 5-20 also indicates that the asphalt mixture requires a higher yield stress to achieve the same viscoplastic strain when the strain rate increases, which means $a_{\dot{\varepsilon}}$ is an increasing function of the strain rate; however, the rate of the strain hardening (κ_2) remains almost unchanged at different strain rates.

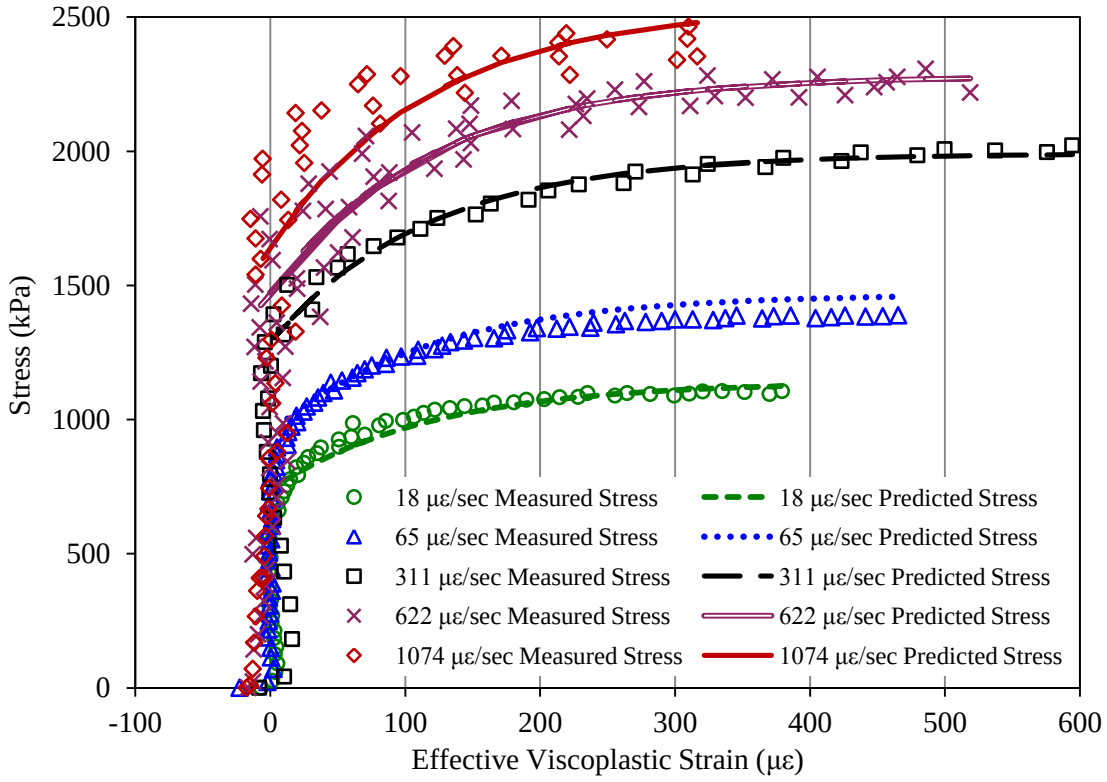

Figure 5-20 Comparisons between the measured stresses and the predicted stresses during strain hardening process of the asphalt mixtures at different strain rates

The findings of the temperature and strain rate dependent yield surface reveal the viscoplastic mechanisms of the accumulating permanent deformation of the field asphalt pavement under repeated traffic loads. The yield driving stress ($\sqrt{J_2}\rho(d,\theta)-\alpha I_1$) remains unchanged if the traffic load is simulated as a repeated load in a stress-controlled test applied to the asphalt concrete. The hardening stress (κ) functions as a resistance to the viscoplastic deformation and it increases as the viscoplastic deformation accumulates due to the strain hardening effect. However, the strain rate decreases under the repeated load. Thus, the increase of κ is reduced by a factor of $a_{\dot{\varepsilon}}$ due to the decrease of the strain rate. The temperature also has an effect on the increase of κ: if the temperature increases or decreases, the increase of κ is

reduced or magnified by a factor of a_T, respectively. As long as the yield function, $f = \sqrt{J_2}\rho(d,\theta) - \alpha I_1 - \kappa a_T a_{\dot{\varepsilon}} > 0$, the viscoplastic deformation will keep accumulating. It is noteworthy that the strain rate declines only in the primary and secondary stages, whereas it increases in the tertiary stage due to the viscofracture development which also contributes to the permanent deformation.

SUMMARIES AND CONCLUSIONS

This chapter presents the development of a comprehensive yield surface model to characterize the complicated yielding properties of an asphalt mixture for the purpose of the accurate permanent deformation prediction. The vital and essential material properties of an asphalt mixture that must be considered in the yield surface model includes: 1) distinctions between compression and extension; 2) dilative volumetric change; 3) internal friction and cohesion; 4) rate and temperature dependence; 5) strain hardening; and 6) convexity and smoothness of the yield surface. Based on the mechanistic analysis and the laboratory testing on the asphalt mixtures with two binders, two air void contents and three aging periods, the following conclusions are made:

1) The existing yield surface models in the literature cannot completely characterize the aforementioned yielding properties of the asphalt mixture. The proposed ZLL (Zhang-Luo-Lytton) model is a comprehensive and general yield surface model for the asphalt mixture. The Drucker-Prager model and the Matsuoka-Nakai model are special cases of the ZLL model. The ZLL yield surface coincides with the external apices of the Mohr-Coulomb yield surface but is still smooth and convex over the full possible range of the internal friction angle from 0 to 90 degrees.

2) A stress-pseudostrain method was proposed to accurately determine the initial yield strength of the asphalt mixtures. The yielding strength analysis indicates that the internal friction angle (ϕ) only depends on the aggregate contacts and interlocks while the cohesion (C) depends on cohesive properties of the mixtures which can be affected by binder properties, air void content, aging periods, temperature, and strain rate. A stiffer asphalt mixture (e.g., due to stiffer binder, low air voids, longer aging period) tends to have a greater cohesion. The model parameters (slope α and intercept κ_0) of the ZLL model were determined based on strength testing results. It was found that α and κ_0 could be accurately predicted with using C and ϕ.

3) A temperature and strain rate dependent strain hardening function was developed and embedded in the ZLL yield surface model. Testing results demonstrated that the cohesion and the amplitude of the strain hardening declined when temperature increased or the strain rate decreased. The temperature effect factor was modeled using an Arrhenius temperature function and the strain rate effect factor was modeled by a power function. Both effect factors can be determined solely based on the ultimate yield strength in the uniaxial compressive strength tests at different temperatures or strain rates. The determined effect factors are reliable since they can be employed to accurately predict the stresses during the entire strain hardening process. The rate of strain hardening does not change significantly with temperature or strain rate.

CHAPTER VI

ANISOTROPIC VISCOPLASTICITY OF DAMAGED ASPHALT MIXTURES

OVERVIEW

The mechanisms of permanent deformation (rutting) in asphalt pavements have not been well addressed due to the complexities of asphalt concrete. In this chapter, the permanent deformation in asphalt mixture is comprehensively characterized by modeling the anisotropic viscoplasticity of the damaged asphalt mixture. An extended Perzyna's anisotropic viscoplastic model is employed for asphalt mixture, which incorporated 1) modified effective stresses in the formulation of the models to account for the inherent and the stress-induced anisotropy; 2) an extended ZLL yield surface to provide a smooth and convex yield surface and address the cohesion and internal friction; 3) a non-associated flow rule to address the volumetric dilation; and 4) a temperature and strain rate dependent strain hardening function.

The parameters of the viscoplastic yield surface and potential function are related to fundamental material properties such as cohesion, internal friction angle and inherent anisotropy of the asphalt mixtures. Using the decomposed viscoplastic strain in the destructive dynamic modulus tests, the Perzyna's viscoplastic coefficients are determined and the viscosity related coefficient Γ is found to decrease as the aging period increases or the air void content decreases; while the rate dependent parameters N and κ_3 have limited variations for the asphalt mixtures having different binder, air voids and aging periods. The effect of the inherent anisotropy on the viscoplastic yielding is that the yield strengths of the asphalt mixture modeled by isotropic viscoplastic models are greater in the triaxial compressive condition while less in the triaxial

extensive condition than the yield strengths of the asphalt mixture modeled as an anisotropic material. Thus the predicted permanent deformation of the asphalt pavement is underestimated without considering the inherent anisotropy. Using the modified stresses in the viscoplastic models provide a straight forward method to account for the inherent anisotropy of the asphalt mixture during the modeling of the viscoplastic deformation.

INTRODUCTION

The permanent deformation (i.e., rutting) has been one of the major distresses in asphalt pavements since the asphaltic materials are widely used in the pavement constructions. The rutting can bring severe damages to the pavement structures which lead to significant waste of the natural resources such as asphalt and aggregates. Rutting can also result in safety problems especially after raining because the rutting can trap water and cause unstable control of vehicles. Thus many research efforts were focused on the investigations of the fundamental mechanisms of the rutting. Some phenomenological methods (Mahboub 1990; Qi and Witczak 1998; Zhou et al. 2004; Li et al. 2011) and mechanistic models (Drescher et al. 1993; Collop et al. 2003; Hajj et al. 2007) were proposed to characterize the development of the rutting and used to predict the permanent deformation of the asphalt pavements using finite element modeling techniques.

Extensive studies indicate that one of the main resources for rutting is the permanent deformation developed in the asphalt mixture layers, which are primarily attributed to the irrecoverable shear deformation under heavy truck loads and a high environmental temperature (Sousa and Weissman 1994). To accurately model and predict the permanent deformation occurring in the asphalt mixture layers, a variety of mechanistic models based on viscoplasticity theories have been proposed and widely employed as constitutive relations in the continuum mechanistic modeling (Florea 1994a; 1994b; Lu and Wright 1998; Huang et al. 2001; Bahuguna

et al. 2006; Di Benedetto et al. 2007b; Yun and Kim 2011). The continuum mechanistic models for asphalt mixtures have an advantage in their computational simplicity, that is, the material responses such as permanent deformation can be easily predicted once the model parameters are provided. However, some problems exist in those models which impede the wide applications of the mechanistic models. Several significant problems of the existing viscoplastic models for asphalt mixtures are presented as follows.

First, the inherent anisotropy of asphalt mixtures has not been well addressed in the constitutive modeling. Asphalt mixture is an inherently anisotropic viscoelastic material according to the discussions in Chapter II. Studies (Pickering 1970; Tobita and Yanagisawa 1992) on geomaterials indicated that, without consideration of inherent anisotropy caused by the preferentially oriented granular particles (e.g., soils, sands, and aggregates) in the constitutive formulation, some important material properties such as non-coaxial and dilatant behaviors would not be properly accounted for.

Second, in addition to considering the inherent anisotropy, the stress-induced anisotropy should also be taken into account in the constitutive models of the asphalt mixture. In fact, the anisotropic cracks dominate the evolution of the permanent deformation when the material has encountered the peak of the stress-strain curves, high stress levels and long loading periods. For instance, the anisotropic viscofracture controls the properties of the asphalt mixture in the softening stage after the peak stress in a strength test or the tertiary flow stage in a repeated destructive stress test.

Third, a non-associated viscoplastic flow rule must be used in the viscoplastic model of the asphalt mixture. The non-associated flow rule indicates that the direction of the incremental viscoplastic strain is not parallel to the direction of the incremental stress. Many studies (Oda and Nakayama 1989; Florea 1994b; Masad et al. 2005) have indicated that the viscoplastic

deformation of asphalt mixtures and granular materials in general is nonassociated and an associated flow rule (directions are the same for incremental strain and stress) overestimates the dilation of the asphalt mixture (Masad et al. 2007). Thus, it would be very important to accurately determine the viscoplastic potential that has a different parameter than the viscoplastic yield surface based on a non-associated flow rule.

Fourth, the temperature and rate dependence needs to be addressed in the viscoplastic constitutive models. A new viscoplastic yield surface (i.e., ZLL model) has been proposed in Chapter V, in which the temperature and strain rate dependent cohesion and strain hardening had been embedded in the yield surface. The temperature and strain rate dependence should be further included in the viscoplastic constitutive model when the new ZLL yield surface model and the non-associated flow rule are used.

To address the aforementioned problems, a modified effective stress method is proposed to integrate both the inherent anisotropy and the stress-induced anisotropy in the viscoplastic constitutive models, which is presented in the next section. Then, an extended Perzyna-type viscoplastic constitutive model is developed to incorporate the ZLL yield surface and the non-associated flow rule, in which the general expressions for the effective viscoplastic strain and the slope of the viscoplastic potential are derived. The following section presents the laboratory experiments that are used to determine the model parameters. In the succeeding section, the viscoplastic properties of the asphalt mixtures are analyzed based on the constitutive models and testing results. The last section summarizes the major findings of this chapter.

INTEGRATION OF ANISOTROPY IN CONSTITUTIVE MODELING

A modified effective stress is proposed in this section to account for the inherent anisotropy and the stress-induced anisotropy of the asphalt mixture. The modified effective

stress is used to formulate the viscoplastic yield surface function, viscoplastic potential function, and viscoplastic constitutive models of the asphalt mixture.

Modified Stress for Characterization of Inherent Anisotropy

To consider the inherent anisotropy of the asphalt mixture, one can use different material properties (e.g., modulus and Poisson's ratio) in different directions and formulate an anisotropic constitutive model. However, this method introduces many unknown material properties that need to be determined by performing more experiments on the materials. For example, an isotropic material has two independent material parameters whereas a cross-anisotropic material has five independent material parameters. An alternative way to address the inherent anisotropy that is caused by the preferential particle orientation is to formulate the constitutive equation based on the modified stresses (instead of the nominal stress) that are obtained by modifying the nominal stress using a microstructural fabric tensor. Literature studies (Oda and Nakayama 1989; Tobita 1989; Li 2002) had successfully captured the material inherent anisotropy of the granular materials by using the modified stresses. It was also suggested that the isotropic yield condition in terms of the modified stresses could lead to an anisotropic yielding and hardening nature of the granular materials with less mathematical complexities (Tobita and Yanagisawa 1988; Yang et al. 2008).

As a granular material, the asphalt mixture exhibits the inherent anisotropy due to preferred aggregates' orientation along the horizontal direction that is perpendicular to the load direction. Pavement researchers (Masad et al. 1998; Tashman et al. 2002) adopted the same fabric tensor concept to account for the anisotropy during the viscoplastic constitutive modeling of an asphalt mixture. In Chapter III, the microstructural parameter characterizing the inherent anisotropy was improved as a modified vector magnitude (Δ') which considered not only the

aggregate orientation, but the size and shape of both the coarse and fine aggregates. A high correlation is also obtained between Δ' and the anisotropic modulus ratio of asphalt mixture. Based on the modified vector magnitude, a modified fabric tensor is formulated in Chapter III (i.e., Equation 3-11) which is repeated as:

$$\left[F'_{ij}\right]=\frac{1}{3+\Delta'}\begin{bmatrix}1-\Delta' & 0 & 0\\ 0 & 1+\Delta' & 0\\ 0 & 0 & 1+\Delta'\end{bmatrix} \tag{6-1}$$

where Δ' is the modified vector magnitude that is reprinted from Equation 3-10 as:

$$\Delta'=\frac{1}{A_0}\sqrt{\left(\sum_{k=1}^{M}\rho^{(k)}\lambda^{(k)}\sin 2\theta_k\right)^2+\left(\sum_{k=1}^{M}\rho^{(k)}\lambda^{(k)}\cos 2\theta_k\right)^2} \tag{6-2}$$

The modified stress tensor is determined by modifying the nominal stress tensor using the fabric tensor (Tobita and Yanagisawa 1988; Oda 1993; Yang et al. 2008):

$$\bar{\sigma}_{ij}=\frac{1}{6}\left(\sigma_{in}F'^{-1}_{nj}+F'^{-1}_{in}\sigma_{nj}\right) \tag{6-3}$$

where, $\bar{\sigma}_{ij}$ is the modified stress tensor; σ_{ij} is the nominal stress tensor. F'^{-1}_{ij} is the inverse of the modified fabric tensor. If a fourth-order fabric tensor is defined as:

$$F_{imnj}=\frac{1}{6}\left(\delta_{im}F'^{-1}_{nj}+F'^{-1}_{im}\delta_{nj}\right) \tag{6-4}$$

where, δ_{ij} is Kronecker delta tensor; the modified stress tensor becomes:

$$\bar{\sigma}_{ij}=F_{imnj}\sigma_{mn}=\frac{1}{6}\left(\sigma_{im}F'^{-1}_{nj}+F'^{-1}_{im}\sigma_{nj}\right) \tag{6-5}$$

In this dissertation, a variable with a superimposed bar indicates that the variable is modified by the fabric tensor and the modified variables are used in the viscoplastic modeling to account for the inherent anisotropy of the asphalt mixture.

Effective Stress for Characterization of Stress-induced Anisotropy

Once a material is damaged, the load is transferred or carried out by the remaining undamaged (effective or intact) material. The cracked (lost) area cannot be used to transfer load inside of the material. Thus the viscoplastic constitutive equations cannot be formulated in terms of the nominal (apparent) stress that is calculated by using the total material area which includes both the intact area and the lost area. Instead, the effective (true) stress should be employed to express the viscoplastic models. The effective stress concept was introduced (Kachanov 1986; Lemaitre and Desmorat 2005) to capture the overall fracture properties of the hundreds of microcracks and macrocracks that are randomly dispersed in the damaged materials. The damage density is physically defined as (Rabotnov 1969; Lemaitre and Desmorat 2005; Sullivan 2008):

$$\xi = \frac{A^c}{A^T} \tag{6-6}$$

where, ξ is the damage density that can be explained as a lost area ratio and $0 \le \xi \le 1$; $\xi = 0$ when there is no damage and $\xi = 1$ when the material is completely damaged. A^c is the lost area due to damages such as voids, flaws and cracks and A^T is the total cross-sectional area of the material.

Based on the continuum damage mechanics (CDM) (Chaboche 1987; Lemaitre and Desmorat 2005), a force balance equation exists between the nominal (apparent) configuration and the effective (true) configuration as follows:

$$\sigma A^T = \sigma^e \left(A^T - A^c \right) \tag{6-7}$$

where, σ is the nominal stress that is defined in the apparent configuration; σ^e is the effective stress that considers the damages in the material and defined in the true configuration. Substituting Equation 6-6 into Equation 6-7 yields the effective stress as:

$$\sigma^e = \frac{\sigma}{1-\xi} \tag{6-8}$$

Equation 6-8 gives an isotropic effective stress which assumes that the damages of the material are identical in all directions. However, the damages such as cracks may have different propagation and evolution speed at different directions. Thus the projected lost areas differ in different directions, which indicate that the damage density can be an anisotropic parameter. Thus an anisotropic damage density is proposed as follows:

$$\xi_{ij} = \frac{A_{ij}^c}{A_{ij}^T} \qquad \text{(no sum on sub-indices)} \tag{6-9}$$

where, ξ_{ij} is the anisotropic damage density that can be explained as a lost area ratio on a specific cross section. A_{ij}^c is the lost area and A_{ij}^T is the total area of the specific cross section. In order to formulate the effective stress based on the anisotropic damage density, a fourth-order damage tensor is developed as follows:

$$M_{imnj} = \frac{1}{2}\left[\delta_{im}\left(\delta_{nj}-\xi_{nj}\right)^{-1} + \left(\delta_{im}-\xi_{im}\right)^{-1}\delta_{nj}\right] \tag{6-10}$$

where M_{imnj} is the fourth-order damage density tensor; δ_{ij} is the Kronecker delta tensor. Then the effective stress becomes:

$$\sigma_{ij}^e = M_{imnj}\sigma_{mn} = \frac{1}{2}\left[\sigma_{in}\left(\delta_{nj}-\xi_{nj}\right)^{-1} + \left(\delta_{im}-\xi_{im}\right)^{-1}\sigma_{mj}\right] \tag{6-11}$$

where σ_{mn} is the nominal stress tensor. In this dissertation, a variable with a superscript *(e)* indicates that the variable has been modified by the anisotropic damage density and has become an effective variable. The effective variable is used in the viscoplastic modeling to account for the stress-induced anisotropy of the asphalt mixture. If the inherent and stress-induced

anisotropy needs to be accounted for simultaneously in the constitutive modeling, Equations 6-5 and 6-11 are combined to compute a modified effective stress that is expressed as:

$$\bar{\sigma}_{ij}^{e} = M_{imnj} F_{mabn} \sigma_{ab} \tag{6-12}$$

ANISOTROPIC VISCOPLASTIC MODEL FOR ASPHALT MIXTURE

To account for the inherent anisotropy and the stress-induced anisotropy, the modified effective stress in Equation 6-12 is employed in the following derivation of the viscoplastic modeling of the asphalt mixture.

Perzyna's Viscoplastic Flow Rule

The deformation response of an asphalt mixture under a destructive load can be decomposed into recoverable and irrecoverable components. The recoverable components include the elastic and viscoelastic strains while the irrecoverable components consist of the plastic, viscoplastic and viscofracture strains. This chapter is focused on the mechanistic modeling of the anisotropic viscoplastic strains.

The viscoplastic strain is associated with the permanent deformation of the asphalt mixture and the rate of the viscoplastic strain can be defined by a Perzyna-type viscoplasticity theory as (Perzyna 1971):

$$\dot{\varepsilon}_{ij}^{vp} = \Gamma \left\langle \Phi\left(f \right) \right\rangle^{N} \frac{\partial g}{\partial \sigma_{ij}^{e}} \tag{6-13}$$

where $\dot{\varepsilon}_{ij}^{vp}$ represents the rate of the viscoplastic strain with respect to time; Γ is the viscosity related parameter and $1/\Gamma$ is proportional to the viscosity of the asphalt mixture and $1/\Gamma$ also represents the viscoplastic relaxation time. Thus Γ is a temperature dependent parameter. N is

the viscoplastic rate dependent exponent. Both Γ and N are experimentally determined and 0 $N>1$ for the asphalt mixtures. Φ is the overstress function which is expressed in terms of the yield surface function, f . σ_{ij}^{e} is the effective stress tensor and is defined in Equation 6-11. *g* is the anisotropic viscoplastic plastic potential function. The non-associated flow rule applies when $g \neq f$, which is appropriate for the asphalt mixture. It must be noted that the function of f and g are formulated by the modified effective stress $\bar{\sigma}_{ij}^{e}$, while the effective stress σ_{ij}^{e} (neither the modified effective stress $\bar{\sigma}_{ij}^{e}$ nor the nominal stress σ_{ij}) is utilized in the term of $\partial g / \partial \sigma_{ij}^{e}$ of the viscoplastic model. This is because that it is the effective stress σ_{ij}^{e} that acting on the intact material area drives the viscoplastic deformation of the material. The McCauley brackets in Equation 6-13 imply that:

$$\left\langle \Phi(f) \right\rangle = \begin{cases} 0, & \Phi(f) \le 0 \\ \dfrac{f}{Pa}, & \Phi(f) > 0 \end{cases} \tag{6-14}$$

Equations 6-13 and 6-14 indicate that the viscoplastic strain occurs only when the overstress function Φ is greater than zero. The Perzyna-type viscoplastic model as shown in Equations 6-13 and 6-14 has been used to describe the viscoplastic evolution of the asphalt mixture for decades (Abdulshafi and Majidzadeh 1984; Tan et al. 1994; Seibi et al. 2001; Tashman et al. 2005a; Masad et al. 2007; Abu Al-Rub et al. 2012). However, most of the yield surface functions used in the literature studies are Drucker-Prager (D-P) or extended Drucker-Prager (ED-P) models. As discussed in Chapter V, the D-P and ED-P yield surface models have some significant limitations such as non-convexity when the internal frictional angle is greater than 22 degrees. Thus the new yield surface model (i.e., ZLL model) developed in Chapter V is expressed in terms of the modified effective stresses and used in this chapter.

Extended ZLL Viscoplastic Yield Surface

To account for the inherent and stress-induced anisotropy, the ZLL yield surface model developed in Chapter V is extended by formulating the yield surface model using modified effective stresses. The extended ZLL yield surface model is formulated as:

$$f = \sqrt{\bar{J}_2^e}\,\rho(\theta') - \alpha \bar{I}_1^e - \kappa a_T a_{\dot{\varepsilon}} \tag{6-15}$$

where $\bar{J}_2^e$ ($= \frac{1}{2}\bar{S}_{ij}^e \bar{S}_{ji}^e$) is the second invariant of the modified effective deviatoric stress tensor $\bar{S}_{ij}^e$ ($= \bar{\sigma}_{ij}^e - \frac{1}{3}\delta_{ij}\bar{I}_1^e$); $\bar{I}_1^e$ ($= \bar{\sigma}_{kk}^e$) is the first invariant of the modified effective stress tensor ($\bar{\sigma}_{ij}^e$) that is defined in Equation 6-12. Schematic plots of the ZLL yield surface on the meridian plane and in the modified effective principal stress space are shown in Figure 6-1 and Figure 6-2, respectively. The two Figures indicate that the viscoplastic deformation does not occur when the stress of the material is located on and within the yield surface locus. θ' is the Lode angle that has the same formulation as Equation 5-11 but is expressed using invariants of the modified effective stress as follows:

$$\theta' = \frac{1}{3}\arccos\left[\frac{3\sqrt{3}}{2}\frac{\bar{J}_3^e}{\left(\bar{J}_2^e\right)^{3/2}}\right] \qquad \in \left[0,\ \frac{\pi}{3}\right] \tag{6-16}$$

where $\bar{J}_2^e$ and $\bar{J}_3^e = \det\left(\bar{S}_{ij}^e\right)$ are the second and third invariants of the modified effective deviatoric stress tensor. θ' is zero in compression (direction OA in Figure 6-2) and θ' is $\pi/3$ in extension (direction OB in Figure 6-2). $\rho(\theta')$ is a function that defines the yield surface shape on the octahedral plane and determines the convexity of the yield surface. Based on Equation 5-22, $\rho(\theta')$ is expressed as:

$$\rho(\theta') = \mu \cos\left[\frac{1}{3}\arccos(\gamma \cos 3\theta')\right] \tag{6-17}$$

where μ and γ are dependent on the extension ratio according Equation 5-23, and:

$$\begin{cases} \mu = \dfrac{2\sqrt{1-d+d^2}}{\sqrt{3}d} \\ \gamma = -\dfrac{3\sqrt{3}}{2}\dfrac{(1-d)d}{(1-d+d^2)^{3/2}} \\ d = \dfrac{3-\sin\phi}{3+\sin\phi} \end{cases} \tag{6-18}$$

where d is the extension ratio that is the ratio of the yield strength in extension to that in compression. In Figure 6-2, d is explained as the segment length ratio of OB to OA. ϕ is the internal friction angle of the asphalt mixture. The formula of $\rho(\theta')$ in Equation 6-17 ensures that the yield surface of the asphalt mixture is smooth and convex on both the meridian plane as shown in Figure 6-1and the octahedral plane as shown in Figure 6-2.

Viscoplastic Strain Hardening Function

The term $\kappa a_T a_{\dot{\varepsilon}}$ in the extended ZLL yield surface represents the temperature and strain rate dependent cohesion and strain hardening for an asphalt mixture. κ is a strain hardening function that is defined by Equation 5-25. a_T and $a_{\dot{\varepsilon}}$ are temperature and strain rate effect factors which are defined by Equations 5-26 and 5-27, respectively. To have a complete description of the viscoplastic model, the functions of κ, a_T and $a_{\dot{\varepsilon}}$ are repeated as follows:

$$\kappa = \kappa_0 + \kappa_1\left[1-\exp\left(-\kappa_2 \varepsilon_e^{vp}\right)\right] \tag{6-19}$$

$$a_T = \exp\left[\frac{\Delta E_T}{R}\left(\frac{1}{T}-\frac{1}{T_0}\right)\right] \tag{6-20}$$

$$a_{\dot{\varepsilon}} = \left(\frac{\dot{\varepsilon}}{\dot{\varepsilon}_0}\right)^{\kappa_3} \tag{6-21}$$

where κ_0, κ_1 and κ_2 are material parameters identified at the reference temperature (T_0) and the reference strain rate ($\dot{\varepsilon}_0$); ε_e^{vp} is the effective viscoplastic strain which is derived in the following sub-section. ΔE_T is the activation energy of the temperature effect, J/mol; R is the universal gas constant, 8.314 J/mol·K; T is the temperature of interest, K; $\dot{\varepsilon}$ is the strain rate of interest, and κ_3 is a material property that is determined by experiments.

The yield surface of the asphalt mixture expands with the increase of the effective viscoplastic strain. The dashed straight lines in Figure 6-1 illustrate the expanded yield surfaces of the asphalt mixture during the strain hardening process. In addition, the relationships between α, κ_0 and C and ϕ in Equations 5-3 and 5-4 still apply to the extended ZLL viscoplastic yield surface models and the relationships are repeated as follows:

$$\alpha = \frac{2\sin\phi}{\sqrt{3}(3-\sin\phi)} \tag{6-22}$$

$$\kappa_0 = \frac{6C\cos\phi}{\sqrt{3}(3-\sin\phi)} \tag{6-23}$$

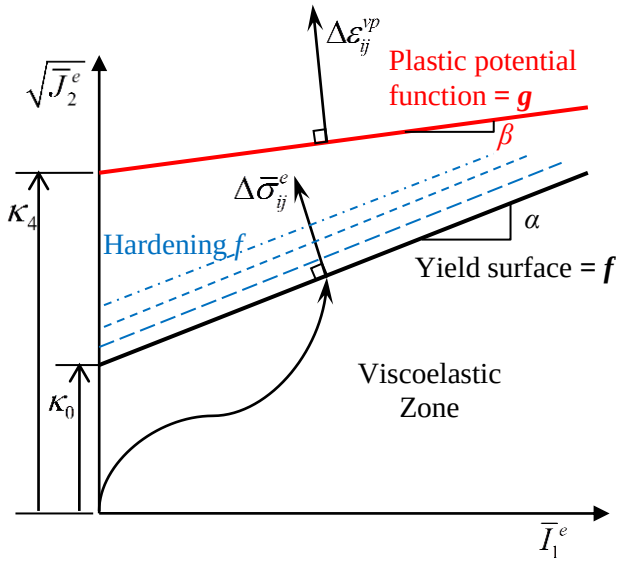

Figure 6-1 Schematic plot of the viscoplastic yield surface and potential surface on the meridian plane

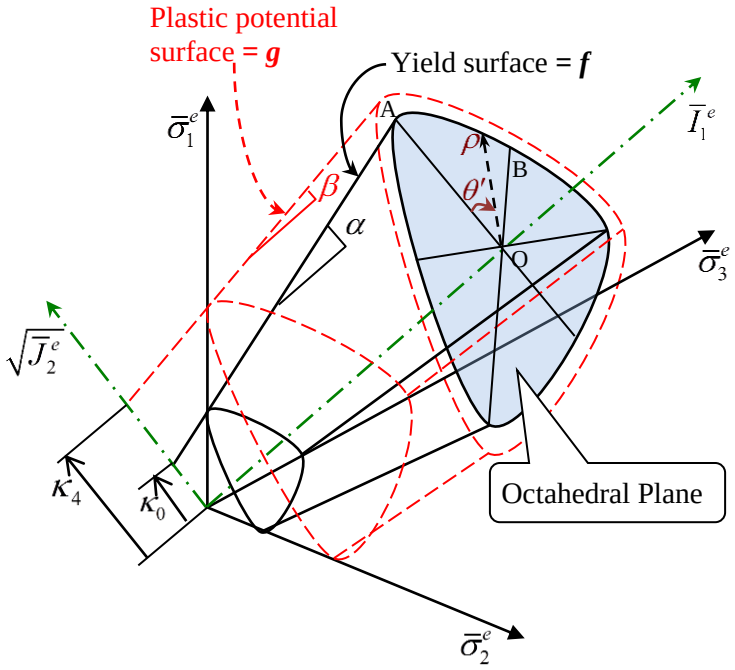

Figure 6-2 Schematic plot of the viscoplastic yield surface and potential surface on the modified effective principal stresses space

Viscoplastic Potential Function

The viscoplastic model in Equation 6-13 uses a non-associated viscoplastic flow rule for the asphalt mixture, which is reasonable because i) the associated flow rule would overestimate the amount of viscoplastic dilation of materials and ii) the direction of the viscoplastic strain increment is not perpendicular to the yield surface, but to the viscoplastic potential surface, as shown in Figure 6-1. It is assumed that the viscoplastic potential surface has the same linear form as the yield surface but with a smaller slope which affects the volumetric dilation of the material. Thus the viscoplastic potential is expressed as:

$$g = \sqrt{\bar{J}_2^e}\,\rho(\theta') - \beta \bar{I}_1^e - \kappa_4 \tag{6-24}$$

where β is the slope of the viscoplastic potential surface and $\beta \neq \alpha$. κ_4 is the incept of the viscoplastic potential surface which vanishes during the calculation of $\partial g / \partial \sigma_{ij}^e$. A number of studies have indicated that the value of β is less than the value of α for geomaterials such as soils, sands, and asphalt mixtures (Oda and Nakayama 1989; Tashman et al. 2005a). Figure 6-1 and Figure 6-2 illustrate the viscoplastic potential surface on the meridian plane and in the modified effective principal stress space, respectively.

The gradient operator of $\partial g / \partial \sigma_{ij}^e$ determines the directions of the viscoplastic strain increment, which can be calculated by performing the first derivative of Equation 6-24 with respect to the effective stress components as follows:

$$\frac{\partial g}{\partial \sigma_{ij}^e} = \frac{\partial g}{\partial \bar{\sigma}_{mn}^e}\frac{\partial \bar{\sigma}_{mn}^e}{\partial \sigma_{ij}^e} = \left(\frac{\partial g}{\partial \sqrt{\bar{J}_2^e}}\frac{\partial \sqrt{\bar{J}_2^e}}{\partial \bar{\sigma}_{mn}^e} + \frac{\partial g}{\partial \bar{I}_1^e}\frac{\partial \bar{I}_1^e}{\partial \bar{\sigma}_{mn}^e} + \frac{\partial g}{\partial \theta'}\frac{\partial \theta'}{\partial \bar{\sigma}_{mn}^e} \right)\frac{\partial \bar{\sigma}_{mn}^e}{\partial \sigma_{ij}^e} \tag{6-25}$$

where

$$\begin{cases} \dfrac{\partial \bar{I}_1^e}{\partial \bar{\sigma}_{mn}^e} = \delta_{mn} \\ \dfrac{\partial \sqrt{\bar{J}_2^e}}{\partial \bar{\sigma}_{mn}^e} = \dfrac{\bar{S}_{mn}^e}{2\sqrt{\bar{J}_2^e}} \\ \dfrac{\partial \theta'}{\partial \bar{\sigma}_{mn}^e} = -\dfrac{\sqrt{3}}{2\left(\bar{J}_2^e\right)^{\frac{3}{2}} \sin 3\theta}\left(\bar{S}_{mk}^e \bar{S}_{kn}^e - \dfrac{2}{3}\bar{J}_2^e \delta_{mn} - \sqrt{\dfrac{\bar{J}_2^e}{3}}\bar{S}_{mn}^e \cos 3\theta \right) \end{cases} \tag{6-26}$$

where $\bar{S}_{mn}^e$ is the modified effective deviatoric stress tensor ($\bar{S}_{ij}^e = \bar{\sigma}_{ij}^e - \frac{1}{3}\delta_{ij}\bar{I}_1^e$). Equations 6-5 indicates

$$\frac{\partial \bar{\sigma}_{mn}^e}{\partial \sigma_{ij}^e} = F_{mijn} = \frac{1}{3}\begin{bmatrix} \dfrac{3+\Delta'}{1-\Delta'} & 0 & 0 \\ 0 & \dfrac{3+\Delta'}{1+\Delta'} & 0 \\ 0 & 0 & \dfrac{3+\Delta'}{1+\Delta'} \end{bmatrix} \tag{6-27}$$

Substituting Equations 6-26 and 6-27 into Equation 6-25 gives

$$\frac{\partial g}{\partial \sigma_{ij}^e} = F_{mijn}\left\{ \begin{array}{l} \dfrac{\mu \cos\left[\frac{1}{3}\arccos\left(\gamma \cos 3\theta'\right)\right]}{2\sqrt{\bar{J}_2^e}}\bar{S}_{mn}^e - \beta\delta_{mn} \\ + \dfrac{\sqrt{3}\mu\gamma \sin\left[\frac{1}{3}\arccos\left(\gamma \cos 3\theta'\right)\right]}{2\bar{J}_2^e\sqrt{1-\gamma^2\cos^2 3\theta'}}\left(\bar{S}_{mk}^e \bar{S}_{kn}^e - \dfrac{2}{3}\bar{J}_2^e\delta_{mn} - \sqrt{\dfrac{\bar{J}_2^e}{3}}\bar{S}_{mn}^e \cos 3\theta \right) \end{array} \right\} \tag{6-28}$$

The slope of the viscoplastic potential is a material property which can be derived based on the viscoplastic model proposed in this section. Employing Equation 6-28 in the Perzyna's viscoplastic model of Equation 6-13, the viscoplastic strain rate (or increment) in the triaxial compressive condition ($\bar{\sigma}_1^e \geq \bar{\sigma}_2^e = \bar{\sigma}_3^e$, $\theta' = 0$) is expressed as:

$$\dot{\varepsilon}_{ij}^{vp} = \Gamma \left\langle \phi(f) \right\rangle^n \begin{bmatrix} Xa & 0 & 0 \\ 0 & Yb & 0 \\ 0 & 0 & Yb \end{bmatrix} \tag{6-29}$$

where

$$\begin{cases} a = \dfrac{3+\Delta'}{3(1-\Delta')} \\ b = \dfrac{3+\Delta'}{3(1+\Delta')} \\ X = \dfrac{\sqrt{3}}{3} - \beta \\ Y = -\dfrac{\sqrt{3}}{6} - \beta \end{cases} \tag{6-30}$$

Thus the first invariant of the viscoplastic strain increment is expressed as:

$$I_1^{\varepsilon} = \Gamma \left\langle \phi(f) \right\rangle^n (Xa + 2Yb) \tag{6-31}$$

The deviatoric viscoplastic strain increment is defined as:

$$\dot{e}_{ij}^{vp} = \dot{\varepsilon}_{ij}^{vp} - \frac{1}{3} I_1^{\varepsilon} \delta_{ij} \tag{6-32}$$

Then the second invariant of the deviatoric viscoplastic strain increment is computed as:

$$J_2^{\varepsilon} = \frac{1}{2} e_{ij}^{vp} e_{ji}^{vp} = \frac{1}{3} \left[\Gamma \left\langle \phi(f) \right\rangle^n \right]^2 (Xa - Yb)^2 \tag{6-33}$$

The slope of the viscoplastic strain increments plotted in the meridian viscoplastic strain increment ($\sqrt{J_2^{\varepsilon}} \sim I_1^{\varepsilon}$) plane becomes:

$$m_{\varepsilon} = \frac{\sqrt{J_2^{\varepsilon}}}{I_1^{\varepsilon}} = \frac{Xa - Yb}{\sqrt{3}(Xa + 2Yb)} \tag{6-34}$$

A normality condition must be satisfied that the viscoplastic stain increment is normal to the viscoplastic potential surface, as shown in Figure 6-1. The Equation 6-24 indicates that the slope of the viscoplastic potential function is β, thus one can have the following relation:

$$m_{\varepsilon} \cdot \beta = -1 \tag{6-35}$$

Considering Equations 6-30, 6-34 and 6-35 solves β as:

$$\beta = \frac{\sqrt{3}\left(Xa + 2Yb\right)}{Yb - Xa} = \frac{2\Delta' - 3\sqrt{3}\beta + \sqrt{3}\beta\Delta'}{-\frac{\sqrt{3}}{2} - \frac{\sqrt{3}}{6}\Delta' + 2\beta\Delta'} \tag{6-36}$$

It can be found that Equation 6-36 is an implicit solution for β. Thus, for practical use, the values of β are resolved over the entire theoretical range of Δ' from 0 to 1. Then a linear relationship is regressed with a high coefficient of determination (R^2) as follows:

$$\beta = 0.5889\Delta' - 0.0122 \ \left(R^2 = 0.9988\right) \tag{6-37}$$

For the asphalt mixture, Δ' normally ranges from 0.2 to 0.5 based on the conclusions in Chapter III. Thus β changes from 0.1 to 0.28 according to Equation 6-37. As we know, an asphalt mixture normally has an internal friction angle between 20 and 60 degrees, thus α ranges from 0.15 to 0.47 according to Equation 6-22. Thus the value of α is always greater than the value of β for an asphalt mixture, which means that a non-associated flow rule is applied to the asphalt mixture. Equation 6-37 has been employed as Equation 5-30 in Chapter V.

Determination of Effective Viscoplastic Strain

As discussed in Chapter V, the effective viscoplastic strain is normally used to correlate the stress-strain relation of a material under multiaxial loading to that of the same material under uniaxial loading. The hardening behaviors of the material are evaluated by the effective viscoplastic strain. This sub-section presents the derivation of a general form of the effective

viscoplastic strain based on the Perzyna's viscoplastic flow rule in Equation 6-13, the extended ZLL yield surface in Equation 6-15 and the viscoplastic potential function in Equation 6-24.

The effective viscoplastic strain is determined based on an viscoplastic work equivalence principle (Chen and Han 1988), which states that the viscoplastic work increment ($\dot{W}_{vp}$) of a material under multiaxial loading that is expressed by the stress and strain measured on the material is equivalent to the viscoplastic work increment of the same material under uniaxial loading that is expressed by the effective viscoplastic stress (σ_e^{vp}) and the effective viscoplastic strain (ε_e^{vp}). It is noted that σ_e^{vp} is different from the effective stress (σ_{ij}^e) defined in Equation 6-11. Thus the viscoplastic work increment equivalence is formulated as

$$\dot{W}_{vp} = \bar{\sigma}_{ij}^e \dot{\varepsilon}_{ij}^e = \sigma_e^{vp} \dot{\varepsilon}_e^{vp} \tag{6-38}$$

Rewrite the yield surface function in Equation 6-15 as:

$$f = F\left(\sigma_{ij}\right) - \kappa a_T a_{\dot{\varepsilon}} \tag{6-39}$$

where $F\left(\sigma_{ij}\right) = \sqrt{\bar{J}_2^e}\,\rho\left(\theta'\right) - \alpha \bar{I}_1^e$ which is a driving force of the viscoplastic strain. Chen and Han (1988) demonstrated that $F\left(\sigma_{ij}\right)$ was defined as a power function of the effective viscoplastic stress as follows:

$$F\left(\sigma_{ij}\right) = \sqrt{\bar{J}_2^e}\,\rho\left(\theta'\right) - \alpha \bar{I}_1^e = K\left(\sigma_e^{vp}\right)^m \tag{6-40}$$

where K and m are constant coefficients. Equation 6-40 applies to the material under both the uniaxial and multiaxial loading conditions. Thus, when a uniaxial compressive load is applied on the material, Equation 6-40 becomes

$$F\left(\sigma_{ij}\right) = \frac{3+\Delta'}{3\left(1-\Delta'\right)} \frac{1}{\left(1-\xi_{11}\right)} \left[\frac{\sigma_e^{vp}}{\sqrt{3}} - \alpha \sigma_e^{vp} \right] = K\left(\sigma_e^{vp}\right)^m \tag{6-41}$$

One can solve for the constants as follows:

$$\begin{cases} K = \dfrac{3+\Delta'}{3(1-\Delta')}\dfrac{1}{(1-\xi_{11})}\left(\dfrac{1}{\sqrt{3}}-\alpha\right) \\ m = 1 \end{cases} \tag{6-42}$$

Substituting Equation 6-42 into 6-40 yields the effective viscoplastic stress as:

$$\sigma_e^{vp} = \frac{F(\sigma_{ij})}{K} = \frac{3(1-\Delta')}{(3+\Delta')}\frac{3(1-\xi_{11})}{\left(\sqrt{3}-3\alpha\right)}\left[\sqrt{\bar{J}_2^e}\rho(\theta') - \alpha\bar{I}_1^e\right] \tag{6-43}$$

It is also demonstrated that $F(\sigma_{ij})$ is homogenous of degree m of the stress (Chen and Han 1988; Tashman et al. 2005b) and the viscoplastic work increment can be expressed as:

$$\dot{W}_{vp} = \bar{\sigma}_{ij}^e \dot{\varepsilon}_{ij}^e = \Gamma\left\langle\Phi(f)\right\rangle^N \bar{\sigma}_{ij}^e \frac{\partial g}{\partial \sigma_{ij}^e} = \Gamma\left\langle\Phi(f)\right\rangle^N mF(\sigma_{ij}) \tag{6-44}$$

Equation 6-13 yields

$$\Gamma\left\langle\Phi(f)\right\rangle^N = \frac{\sqrt{\dot{\varepsilon}_{ij}^{vp}\dot{\varepsilon}_{ij}^{vp}}}{\sqrt{\dfrac{\partial g}{\partial \sigma_{ij}^e}\dfrac{\partial g}{\partial \sigma_{ij}^e}}} \tag{6-45}$$

Substituting Equations 6-43, 6-44 and 6-45 into Equation 6-38 gives a general expression for the effective viscoplastic strain rate:

$$\dot{\varepsilon}_e^{vp} = \frac{3+\Delta'}{3(1-\Delta')}\frac{\left(\sqrt{3}-3\alpha\right)}{3(1-\xi_{11})}\frac{\sqrt{\dot{\varepsilon}_{ij}^{vp}\dot{\varepsilon}_{ij}^{vp}}}{\sqrt{\dfrac{\partial g}{\partial \sigma_{ij}^e}\dfrac{\partial g}{\partial \sigma_{ij}^e}}} \tag{6-46}$$

In a uniaxial compressive condition, Equation 6-28 gives:

$$\begin{cases} \dfrac{\partial g}{\partial \sigma_{11}^e} = \left(\dfrac{\sqrt{3}}{3}-\beta\right)\dfrac{3+\Delta'}{3(1-\Delta')(1-\xi_{11})} \\ \dfrac{\partial g}{\partial \sigma_{22}^e} = \dfrac{\partial g}{\partial \sigma_{33}^e} = \dfrac{\partial g}{\partial \sigma_{12}^e} = \dfrac{\partial g}{\partial \sigma_{23}^e} = \dfrac{\partial g}{\partial \sigma_{31}^e} = 0 \end{cases} \tag{6-47}$$

Then the effective viscoplastic strain rate in uniaxial compression becomes

$$\dot{\varepsilon}_e^{vp} = \frac{\left(1-\sqrt{3}\alpha\right)}{\left(1-\sqrt{3}\beta\right)}\sqrt{\dot{\varepsilon}_{ij}^{vp}\dot{\varepsilon}_{ij}^{vp}} \tag{6-48}$$

In a triaxial compressive condition, Equation 6-28 gives:

$$\begin{cases} \dfrac{\partial g}{\partial \sigma_{11}^e} = \left(\dfrac{\sqrt{3}}{3}-\beta\right)\dfrac{3+\Delta'}{3\left(1-\Delta'\right)\left(1-\xi_{11}\right)} \\ \dfrac{\partial g}{\partial \sigma_{22}^e} = \dfrac{\partial g}{\partial \sigma_{33}^e} = \left(-\dfrac{\sqrt{3}}{6}-\beta\right)\dfrac{3+\Delta'}{3\left(1+\Delta'\right)\left(1-\xi_{22}\right)} \\ \dfrac{\partial g}{\partial \sigma_{12}^e} = \dfrac{\partial g}{\partial \sigma_{23}^e} = \dfrac{\partial g}{\partial \sigma_{31}^e} = 0 \end{cases} \tag{6-49}$$

In compression, the cracks do not grow until a fracture threshold such as the peak stress in a strength test or the flow number in a repeated destructive test is reached. Thus the damage densities in different directions are assumed to be very small and identical value before the viscofracture strains that are caused by the cracks occur (i.e., $\xi_{ij} = constant \approx 0$). Thus the effective viscoplastic strain rate in triaxial compression can be written as:

$$\dot{\varepsilon}_e^{vp} = \left[\left(\frac{1-\sqrt{3}\beta}{1-\sqrt{3}\alpha}\right)^2 + 2\left(\frac{1-\Delta'}{1+\Delta'}\right)^2\left(\frac{0.5+\sqrt{3}\beta}{1-\sqrt{3}\alpha}\right)^2\right]^{-\frac{1}{2}}\sqrt{\dot{\varepsilon}_{ij}^{vp}\dot{\varepsilon}_{ij}^{vp}} \tag{6-50}$$

Generalizing Equations 6-48 and 6-50 gives:

$$\dot{\varepsilon}_e^{vp} = \left[\left(\frac{1-\sqrt{3}\beta}{1-\sqrt{3}\alpha}\right)^2 + \left(n'-1\right)\left(\frac{1-\Delta'}{1+\Delta'}\right)^2\left(\frac{0.5+\sqrt{3}\beta}{1-\sqrt{3}\alpha}\right)^2\right]^{-\frac{1}{2}}\sqrt{\dot{\varepsilon}_{ij}^{vp}\dot{\varepsilon}_{ij}^{vp}} \tag{6-51}$$

where $n'=1$ in a uniaxial condition and $n'=3$ in a triaxial condition; Integrating Equation 6-51 over time can give the effective viscoplastic strain. It is noteworthy that Equation 6-51 has been used as Equation 5-29 in Chapter V.

LABORATORY EXPERIMENTS

In this chapter, both the nondestructive dynamic modulus (NDM) tests and the destructive dynamic modulus (DDM) tests that are employed in Chapter IV (i.e., Figure 4-3) are performed on more asphalt mixture specimens. The measured axial total strains are decomposed based on the strain decomposition developed in Chapter IV and obtain the viscoplastic strains which are implemented in the characterization of the viscoplasticity of the asphalt mixtures.

The asphalt mixtures used in the NDM and the DDM tests were the same types of asphalt mixtures that had been used in Chapter V (i.e., Table 5-2). The VHL and NHL asphalt mixtures were fabricated by mixing Texas Hanson limestone with two types of asphalt binder (Valero asphalt (PG64-16) and NuStar asphalt (PG67-22)), respectively. The VHL and NHL asphalt mixture specimens are varied by two air void contents (4% and 7%) and three aging periods (0, 3, and 6-month continuous aging at 60 ℃). Two replicate specimens were fabricated for each combination of the asphalt binder, air void content and aging condition.

The NDM and the DDM tests employed the same testing configurations of the NDM and DDM tests used in Chapter IV (i.e., Figure 4-3). In the NDM test, a compressive sinusoidal stress with a maximum stress value of 70 kPa was applied to the sample for 600 cycles at a frequency of 1 Hz and at a temperature of 40 ℃. Stresses and strains were recorded by three LVDTs to calculate the dynamic moduli and phase angles of undamaged asphalt mixtures. In the DDM test, a compressive sinusoidal load with a minimum stress of 20 kPa and a maximum stress of 600 kPa was applied to the asphalt mixture specimen at the frequency of 1 Hz and at the temperature of 40 ℃. The total deformation was recorded with respect to time using the three LVDTs until the specimen fails in the tertiary deformation stage.

The total strains measured from the DDM tests on different asphalt mixtures are decomposed by using the strain decomposition method proposed in Chapter IV. The separated

viscoplastic strains are employed to determine the Perzyna's viscoplastic parameters, Γ and N, which is presented in this chapter. The separated viscofracture strains will be implemented in Chapter VII to determine anisotropic damage densities and the parameters of the viscofracture evolution.

ANALYSIS OF VISCOPLASTIC PROPERTIES OF ASPHALT MIXTURES

In Chapter V, the strength tests at different confining pressures, temperatures and strain rates have been performed to determine the following viscoplastic material properties of asphalt mixtures: 1) strength-related parameters: α, ϕ, κ_0, C and d in the ZLL yield surface; 2) strain hardening parameters: κ_1 and κ_2; and 3) temperature and strain rate dependent parameters: a_T, ΔE_T and $a_{\dot{\varepsilon}}$, κ_3. In this section, the Perzyna's viscoplastic parameters, Γ and N are determined and analyzed when the asphalt mixtures have different binders, air voids and aging periods.

In addition, the slope of the viscoplastic potential function, β, is also calculated for the asphalt mixtures based on the measured modified vector magnitudes in Chapter V. The effects of the inherent anisotropy of the asphalt mixtures on the viscoplastic yielding are analyzed based on the extended ZLL yield surface model and the viscoplastic testing data.

Determination of Perzyna's Viscoplastic Properties

Based on the Perzyna's viscoplastic flow rule and the extended ZLL yield surface model, the axial viscoplastic strain rate of a DDM test can be theoretically expressed as:

$$\dot{\varepsilon}_{11}^{vp} = \Gamma\left[\sqrt{\bar{J}_2^e}\rho(\theta') - \alpha\bar{I}_1^e - \kappa a_T a_{\dot{\varepsilon}}\right]^N \frac{\partial g}{\partial \sigma_{11}^e} \tag{6-52}$$

The DDM test is a uniaxial compressive test conducted at a constant temperature, thus $\theta' = 0$, $\rho(\theta') = 1$, $a_T = 1$. Using Equations 6-19, 6-20, 6-47, 6-48 in Equation 6-52 and assuming the axial damage density (ξ_{11}) before viscofracture occurs is zero give:

$$\dot{\varepsilon}_{11}^{vp} = \Gamma \left\{ \left(\frac{\sqrt{3}}{3} - \alpha \right) \bar{\sigma}_1^e - \left\{ \kappa_0 + \kappa_1 \left[1 - \exp\left(-\kappa_2 \frac{\left(1 - \sqrt{3}\alpha\right)}{\left(1 - \sqrt{3}\beta\right)} \varepsilon_{11}^{vp} \right) \right] \right\} \left(\frac{\dot{\varepsilon}}{\dot{\varepsilon}_0} \right)^{\kappa_3} \right\}^N \left(\frac{\sqrt{3}}{3} - \beta \right) \frac{3 + \Delta'}{3\left(1 - \Delta'\right)} \tag{6-53}$$

It is noted that the assumption that $\xi_{11} \approx 0$ is believed reasonable because 1) the initial air voids of the asphalt mixture are squeezed under a compressive load and becomes a very small value (normally less than half of the initial air void content) and 2) the cracks will not grow in the viscoplastic deformation stage, thus the axial damage density will not be increased due to the crack growth before the viscofracture occurs (e.g., peak stress of a strength test or the flow number of a repeated destructive load test).

In Equation 6-53, the parameters α, κ_0, κ_1, κ_2 and κ_3 have been determined using UCS and TCS tests at the reference strain rate, $\dot{\varepsilon}_0$. $\dot{\varepsilon}$ is the total strain rates of the DMM test and it keeps decreasing as the total strain increases. The value of β is also calculated by Equation 6-36 or Equation 6-37 based on the modified vector magnitude, Δ', which has been determined using the lateral surface scanning test proposed in Chapter III. The only unknown parameters in Equation 6-53 are the Perzyna's viscoplastic coefficients, Γ and N. However, the strain rate dependent parameter, κ_3, is also treated as an unknown parameter in this study. This is because 1) the total strain rates of the DDM test are not constants but keep decreasing during the primary and secondary deformation stages; 2) κ_3 is a strain rate dependent parameter, which can be inherently characterized by the DDM test that has varying strain rates during the tests;

and 3) by doing so, the UCS tests at different strain rates shown in Table 5-2 can be avoided and the total experimental work is minimized.

It must be noted that the modified effective stress, $\bar{\sigma}_1^e$ in Equation 6-53, should be assigned as the measured stresses in the lab tests. This is because the measured stresses are directly determined on the real asphalt mixture specimens which are anisotropic materials. Thus the measured stresses have already characterized the inherent anisotropy of the asphalt mixture. They do not need the modifications of the fabric tensor and the measured stresses are equivalent to the modified effective variables. In contrast, if a stress is calculated or predicted (e.g., by employing the finite element program) on an inherently anisotropic material such as the asphalt mixture which, however, is characterized by an isotropic model (e.g., use an identical modulus and Poisson's ratio in all directions of the finite element models of the asphalt mixture), then this stress does not include the anisotropic properties of the material and needs to be modified by the fabric tensor to account for the inherent anisotropy. Without considering the inherent anisotropy of the material will introduce a possibly very large systematic error in the performance prediction of the material, which will be illustrated in the next sub-section.

The axial viscoplastic strains are obtained by performing the strain decomposition proposed in Chapter IV on the measured total strain of the DDM test. Then the axial viscoplastic strain rates with respective to time are calculated and implemented in Equation 6-53, and the Perzyna's viscoplastic coefficients (Γ, N) and the strain rate dependent parameter (κ_3) can be determined. Figure 6-3 shows an example of the viscoplastic strain and the axial viscoplastic strain rate of an asphalt mixture measured in the primary and secondary stages. The axial viscoplastic strain rate is fitted by Equation 6-53. It is found that the viscoplastic strain increases while the viscoplastic strain rate decreases with load cycles. The Equation 6-53 can be used to predict the viscoplastic strain rate in the DDM test.

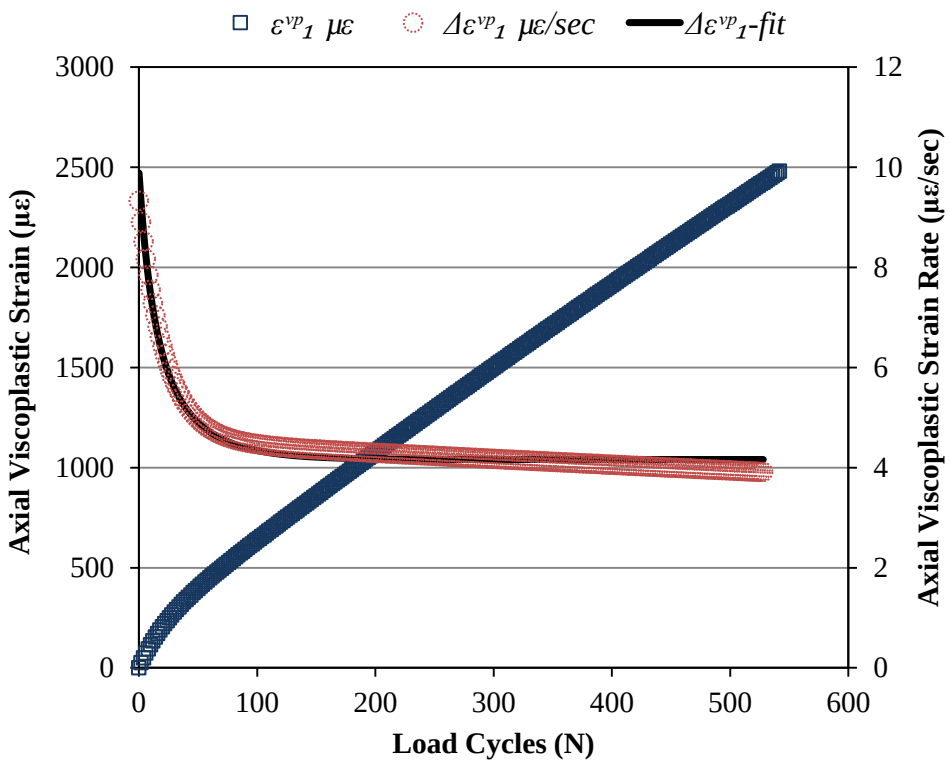

Figure 6-3 Viscoplastic strain and viscoplastic strain rate in primary and secondary stages of an asphalt mixture (VHL-22, 4%, 0-month aged)

The aforementioned analysis method is applied to all of the tested asphalt mixtures that have different binders, air voids and aging periods. Figure 6-4 shows the measured Perzyna's viscoplastic coefficients (Γ, N) and strain rate dependent parameters (κ_3) of the asphalt mixtures. It can be found that Γ decreases as the aging period increases or the air void content decreases. The values of Γ for the mixtures using Valero binder (PG64-16) are a little greater than that of using NuStar binder (PG67-16). These findings make sense because Γ is inversely proportional to the viscosity of the material. A stiffer asphalt mixture that is caused by a stiffer binder, lower air void and longer aging period normally has a higher viscosity, which results in a

lower value of Γ. It is also must be noted that the value of Γ might also be affected by other factors such as temperatures.

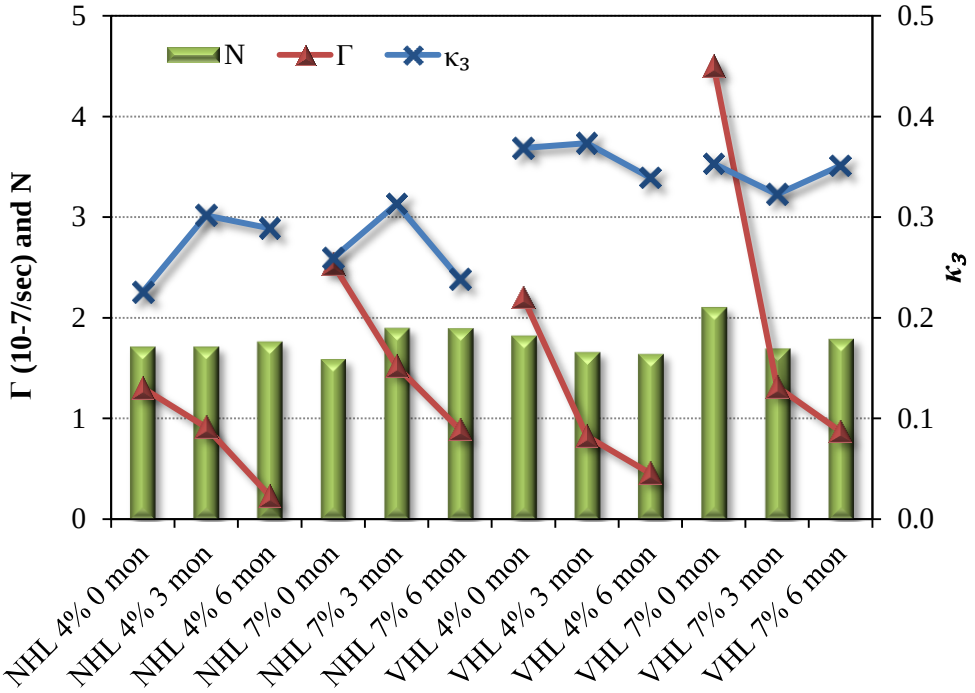

Figure 6-4 Measured Perzyna's viscoplastic coefficients (Γ, N) and strain rate dependent parameters (κ_3) of asphalt mixtures

The testing results in Figure 6-4 do not show obvious trends for the rate dependent parameters including N and κ_3 when the asphalt mixtures have different binders, air void contents and aging periods. For all the tested asphalt mixtures, N has an average value of 1.77 with a standard deviation of 0.141 while κ_3 has an average value of 0.31 with a standard deviation of 0.050. Thus, based on the limited testing data, it might be appropriate to conclude that the viscoplastic rate dependent parameters (N and κ_3) of the asphalt mixtures have limited

variation and might be assumed as constants when the asphalt mixtures have different binders, air void contents and aging periods.

Effect of Inherent Anisotropy on Viscoplastic Yielding

This subsection presents the results of the inherent anisotropy of asphalt mixture due to the preferentially oriented aggregates and its effect on the yield surfaces and the viscoplastic deformation.

The inherent anisotropy of the asphalt mixture is quantified by a modified vector magnitude (Δ') which is measured by the lateral surface scanning tests in Chapter III. As mentioned previously, $\Delta' = 0$ indicates an isotropic condition and $\Delta' = 1$ implies a fully cross anisotropic condition. As shown in Table 5-2, the lateral surface scanning tests are performed for all the asphalt mixture specimens which employ one aggregate gradation and have two binders, two air void contents and three aging periods. According to Equation 6-36 or 6-37, the slopes of the viscoplastic potential (β) are calculated based on the values of Δ'. Figure 6-5 shows that the measured Δ' and β for the tested specimens. On can find that the values of Δ' vary from 0.2 to 0.5, which are consistent with the measurements in Chapter III. The corresponding values of β range from 0.1 to 0.28. No obvious relations are found between Δ' or β and the binder type and air void content. In fact, according to the analysis in Chapter III, Δ' solely depends on the aggregate properties including aggregate inclination angle relative to the horizontal direction, aggregate size and aggregate shape, all of which are related to the aggregate gradation used for the asphalt mixture and the compaction effort during the specimen fabrication.

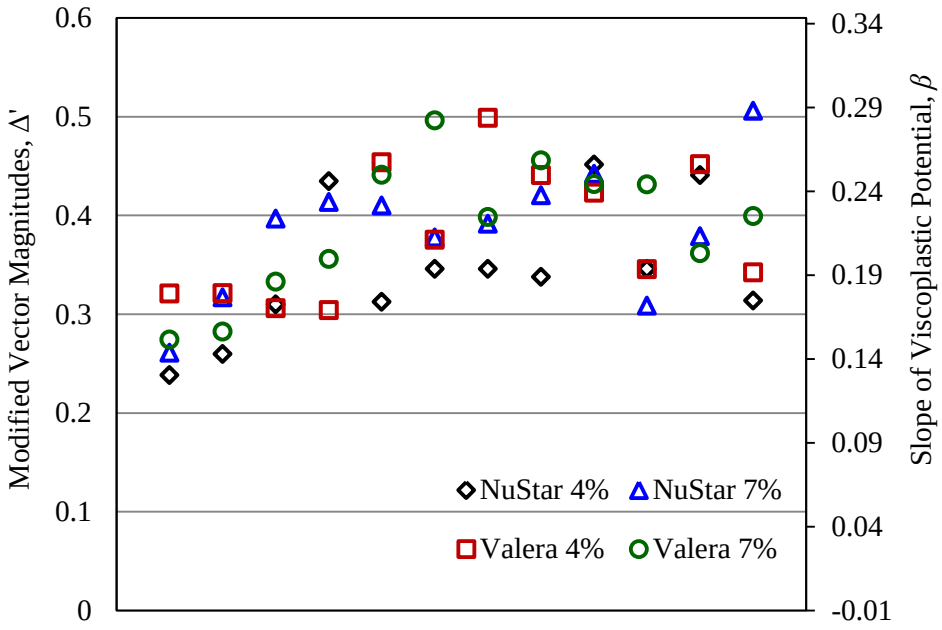

Figure 6-5 Modified vector magnitudes and slope of the viscoplastic potential of asphalt mixtures

Two typical values of Δ' ($\Delta' = 0.25$ and $\Delta' = 0.5$) are selected to quantify the effect of the inherent anisotropy on the viscoplastic yielding properties of the asphalt mixture. Based on the measurements of the yielding properties in this study, the following material parameters were implemented in the plot of yield surface examples: $C = 209kPa$ and $\phi = 45^\circ$ which correspond to $\alpha = 0.352$, $\kappa_0 = 224kPa$, and $d = 0.62$. The initial yield surfaces (before hardening) for the asphalt mixture considering isotropy ($\Delta' = 0$), low anisotropy ($\Delta' = 0.25$) and high anisotropy ($\Delta' = 0.5$) are plotted in Figure 6-6, in which σ_1, σ_2 and σ_3 are nominal principal stresses. Figure 6-6 demonstrates that, when the asphalt mixture is modeled as an isotropic material, the yield strength is greater in the triaxial compressive condition while less in the triaxial extensive condition than the yield strengths of the asphalt mixture when modeled as an anisotropic material. Thus, if using an isotropic yield surface model for the asphalt mixture,

the predicted viscoplastic deformation in the vertical direction (along the direction of tire pressure) will be underestimated in the triaxial compressive condition and overestimated in the triaxial extensive condition compared to the viscoplastic deformation which occurs in the asphalt mixture of the field pavement which is an inherently anisotropic material.

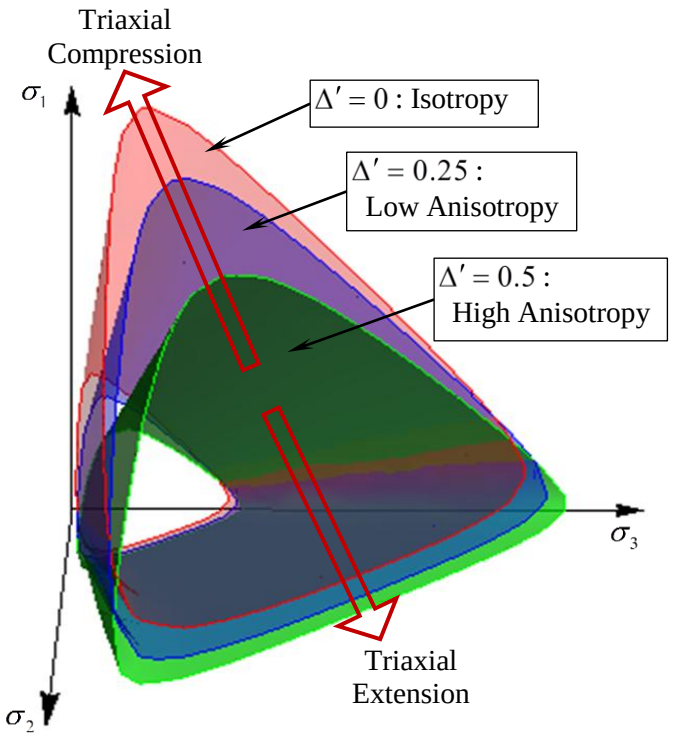

Figure 6-6 Yield surfaces of asphalt mixture (with an internal friction angle of 45 degrees) at different levels of anisotropy ($\Delta' = 0$: Isotropy; $\Delta' = 0.25$: Low anisotropy, $\Delta' = 0.5$: High anisotropy)

As we know, the asphalt mixtures beneath the tire load is subjected to triaxial compressive stresses (compression zone $\sigma_x < \sigma_y$ in Figure 6-7) which lead to the development of the vertical viscoplastic deformation. The asphalt mixtures away from the tire load (including the asphalt mixtures along the wheel paths which are ahead of and behind the vehicle tire) are

subjected to triaxial extensive stresses (extension zone $\sigma_x < \sigma_y$ in Figure 6-7) which cause the reversal of the vertical viscoplastic deformation. When using an isotropic yield surface model to model the asphalt mixture, the development of the vertical viscoplastic deformation is underestimated and the reversal of the vertical viscoplastic deformation is overestimated, both of which result in the underestimation of the permanent deformation in the asphalt pavements.

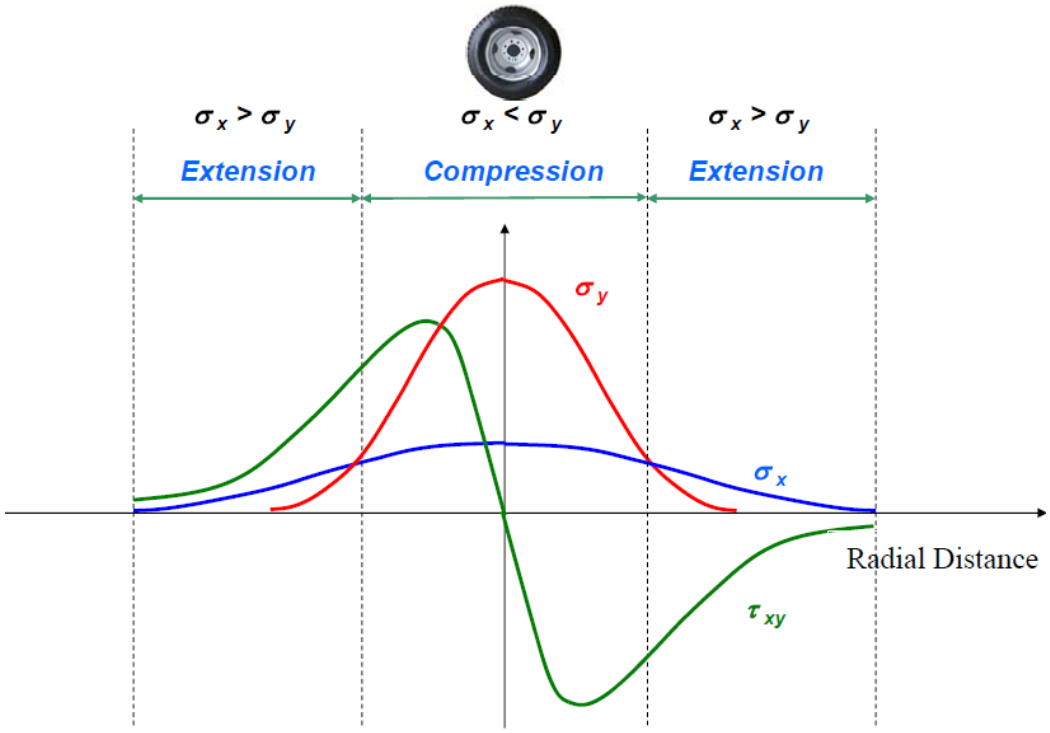

Figure 6-7 Schematic representations of stresses induced by wheel load in asphalt pavements (σ_x is horizontal stress and σ_y is vertical stress) (Ashtiani 2009)

It was also found in the literature (Wang et al. 2005; Oh et al. 2006) that, using anisotropic moduli in the finite element modeling of the asphalt pavement, larger tensile and shear stresses were obtained than those modeled by isotropic moduli. The predicted rutting of pavements with anisotropic modeling of the asphalt mixture matched well with the measured

pavement rutting, which exceeded the rutting predicted by the isotropic moduli. The study in this chapter explains the fundamental mechanisms of these calculated results based on the effect of the inherent anisotropy on the viscoplastic yield surface of the asphalt mixture. Therefore, a yield surface considering the anisotropy of the asphalt mixture is more appropriate to be used in the constitutive modeling when making the rutting predictions of asphalt pavements. This study provides a straight forward method of using the modified stresses in the viscoplastic yield surface and viscoplastic potential functions to account for the inherent anisotropy of the asphalt mixture.

SUMMARIES AND CONCLUSIONS

The mechanisms of permanent deformation (rutting) in asphalt pavements have not been well addressed due to the complexities of asphalt concrete. In this chapter, the permanent deformation in an asphalt mixture is comprehensively characterized by modeling the anisotropic viscoplasticity of the damaged asphalt mixture. An extended Perzyna's anisotropic viscoplastic model is employed for the asphalt mixture, which incorporates: 1) a modified effective stress in the formulation of the models to account for both the inherent anisotropy due to the aggregates' orientation and the stress-induced anisotropy caused by the crack growth; 2) an extended ZLL yield surface developed in Chapter V to provide a smooth, convex, hydrostatic pressure dependent yield surface function; 3) a non-associated flow rule to address the volumetric dilation; and 4) a temperature and strain rate dependent strain hardening function.

The parameters of the viscoplastic yield surface models are related to fundamental material properties such as cohesion and internal friction angle of the asphalt mixtures. A general expression is derived for the effective viscoplastic strain of the asphalt mixture based on the proposed viscoplastic models. The slope of the viscoplastic potential surface is found to be

solely dependent on the modified vector magnitude which was used to quantify the inherent anisotropy of the asphalt mixtures. Using the decomposed viscoplastic strain measured in the destructive dynamic modulus tests, the Perzyna's viscoplastic coefficients are determined for different asphalt mixtures. It is found that the viscosity related coefficient Γ decreases as the aging period increases or the air void content decreases; while the rate dependent parameters N and κ_3 do not change very much when the asphalt mixtures have different binders, air void contents and aging periods.

The inherent anisotropy is quantified by a modified vector magnitude (Δ') which is demonstrated to be independent of binder, air void content and aging periods. The systematic error when using isotropic model in the viscoplastic characterization is that the yield strength of the asphalt mixture is greater in the triaxial compressive condition while less in the triaxial extensive condition than the yield strengths of the asphalt mixture modeled as an anisotropic material. Thus the predicted permanent deformation of the asphalt pavement will be underestimated without considering the inherent anisotropy. Using the modified effective stresses in the viscoplastic models provides a straight forward method to account for the inherent anisotropy of the asphalt mixture in the modeling of the viscoplastic deformation.

CHAPTER VII

ANISOTROPIC VISCOFRACTURE OF DAMAGED ASPHALT MIXTURES*

OVERVIEW

When an asphalt mixture is subjected to a destructive compressive load, it experiences a sequence of three deformation stages: the primary, secondary and tertiary stages. Most of the research in the literature focused on the plastic deformation in the primary and secondary stages, or the prediction of the flow number which, in fact, is the initiation of the tertiary stage. However, little research effort has been reported on the mechanistic modeling of the damage that occurs in the tertiary stage. The main objectives of this chapter are to provide a mechanistic characterization method for the damage modeling of the asphalt mixtures in the tertiary stage and to provide a method to determine the anisotropic damage densities used in the effective stress during the anisotropic viscoplastic modeling of the asphalt mixture.

The strain caused by the growth of cracks is the viscofracture strain which is an anisotropic variable. The axial viscofracture strain is obtained by conducting the strain decomposition of the measured total axial strain in the destructive compressive test, which has been presented in Chapter IV. The radial strain decomposition is proposed in this chapter based on a generalized elastic-viscoelastic correspondence principle. The testing results of the destructive tests illustrate that the deformation during the tertiary flow of the asphalt mixtures is principally caused by the formation and propagation of cracks which is signaled by the increase

*Part of this chapter is reprinted with permission from ASCE: "Mechanistic Modeling of Fracture in Asphalt Mixtures under Compressive Loading." by Yuqing Zhang, Rong Luo and Robert L. Lytton, 2012, *Journal of Materials in Civil Engineering*, In Press, Copyright [2012] by ASCE.

of the phase angle in the tertiary phase. The decomposed axial and radial viscofracture strains are employed to mechanistically characterize the viscofracture of asphalt mixtures in compression, which are represented by the anisotropic damage densities and true stress.

The axial damage density and true stress are determined by using the dissipated pseudo strain energy (DPSE) balance principle, and the radial damage density is determined based on a geometric analysis of the cracking mode in compression. Both damage densities and true stress are demonstrated to increase with load cycle in the tertiary stage. The increased true stress yields extra viscoplastic strain, which is the reason why the permanent deformation is accelerated by the occurrence of the cracks. To characterize the evolution of the anisotropic viscofracture in the asphalt mixtures in compression, an anisotropic pseudo J-integral Paris' law in terms of damage densities is proposed and the material constants in the Paris' law are determined, which are temperature independent and can be employed to predict the time-dependent fracture of asphalt mixtures in compression.

INTRODUCTION

When a paving asphalt mixture is subjected to a destructive compressive load, it experiences a sequence of three deformation stages: the primary stage, secondary stage and tertiary stage. During the primary and secondary stages, permanent deformation (rutting) accumulates based on a strain (or work) hardening mechanism. The work done by the repeated load accumulates energy in the asphalt mixture which yields a stiffer material. The asphalt mixture reaches a point at which it is so stiff that the microcracks and voids start to grow and propagate to macrocracks in the tertiary stage (Lytton 2000; Zhou and Scullion 2002). This point is actually the initiation of the tertiary stage and is defined as the flow number in the repeated load test or the flow time in the static creep test (Witczak et al. 2002). The increase of the crack

size leads to the loss of the area of the intact material, which is the major reason for the degradation of the modulus. The cracks that appear in the tertiary stage in turn accelerate the development of permanent deformation and eventually reduce the service life of pavements. In order to accurately predict the field performance of asphalt pavements, there is an imperative need to perform the fundamentally mechanistic modeling and laboratory evaluation on the fracture that occurs in the tertiary stage of asphalt mixtures.

However, little effort has been made on the investigation of the fracture properties of the asphalt mixtures during the tertiary deformation stage. Most of the research efforts documented in the literature (Kvasnak et al. 2007; Goh and You 2009; Bausano and Williams 2010; Rodezno et al. 2010) focused on the prediction of the flow number or flow time which was the starting point of the tertiary stage. Bausano and Williams (2010) used an energy-based approach to predict the flow number while Kvasnak et al. (2007) and Rodezno et al. (2010) employed statistical models to relate the flow number with the material properties. A number of researchers (Kaloush and Witczak 2002; Zhou et al. 2004; Biligiri et al. 2007) modeled the evolution of the plastic strain with load cycle in the tertiary stage by using empirical fitting functions. Nevertheless, the fundamental mechanisms for the tertiary flow were not clearly discovered. Lytton (2000) emphasized that "*what has been called 'tertiary creep' is in fact not creep at all but an increase of permanent strain due to the formation and growth of microcracks*". Some other researchers (Ramsamooj and Ramadan 1999; Zhou and Scullion 2002) also reported that the cracks were observed during the tertiary deformation stage of asphalt mixtures. Therefore, further mechanistic characterizations based on fracture mechanics and damage mechanics should be performed to reveal the fundamental mechanisms of the time dependent fracture (viscofracture) in the tertiary phase of the asphalt mixtures in compression, which is also the objective of this study.

The fracture of an asphalt mixture in compression develops with viscoplasticity simultaneously in the tertiary stage when the asphalt mixtures are subjected to a destructive compressive load. Chapter IV proposes a strain decomposition to differentiate viscoplasticity and viscofracture from the viscoelasticity of the asphalt mixtures. The modulus and phase angle data in Chapter IV indicate that the cracking mode in compression differs significantly from that in tension of the asphalt mixture. The studies in the literature have not presented any in-depth investigations on the cracking of the asphalt mixture in compression.

This chapter presents more fundamental studies on the viscofracture properties of the asphalt mixtures in compression and provides the determination of the anisotropic damage densities (defined in Equations 6-9 and 6-11) used in viscoplastic modeling. The contents are organized as follows. The next section introduces the observation of the cracks of the asphalt mixture in compression. Then laboratory experiments and testing results are presented. The following section presents a brief description of the axial strain decomposition proposed in Chapter IV and further develops a radial strain decomposition technique. Then the mechanistic modeling of the anisotropic viscofracture in the tertiary stage is presented in detail. After this, the evolution of the anisotropic viscofracture of the asphalt mixtures under repeated compressive loads is characterized by an anisotropic pseudo J-integral Paris' law. The last section summarizes the major findings in this chapter.

CRACKING MODE OF ASPHALT MIXTURE IN COMPRESSION

An asphalt mixture has a different cracking model in compression and in tension. It is well known that the cracks grow in the direction that is perpendicular to the direction of stress in tension. To demonstrate the cracking mode of the asphalt mixture in compression, some of the asphalt mixture specimens were painted on the lateral surface by white plaster before the

destructive tests, as shown in Figure 7-1. It is noted that the top and bottom plaster caps on the specimens were employed to ensure that the top surface is parallel to the bottom surface and that the three LVDTs deformed uniformly. Figure 7-2 shows the asphalt mixture specimen after the destructive test. It can be seen from the figure that some of the cracks were illustrated as splitting cracking which grow along the vertical direction that is the direction of the stresses, while some of the cracks are shown as diagonal cracking which propagate in the diagonal directions.

Figure 7-1 An asphalt mixture specimen painted by white plaster on surfaces before destructive test

The studies on the crack development in compression have been intensively performed on some civil materials such as glass, casting resin, cement, mortar and rocks (Hoek and Bieniawski 1965; Reys 1991; Eberhardt et al. 1999; Dyskin et al. 2003). Figure 7-3 shows the

two dimensional (left figure) plot and three dimensional (right image) photos of the cracks in compression. It can be seen that the cracks can initiate at the pre-existing defects such as voids, flaws of the materials and the cracks incline to propagate along the compression axis.

The asphalt mixture fractures in the tertiary stage when it is subjected to a compressive load. The literature studies on compressive cracking of civil materials provide an approach to understand the phenomena of the cracks of the asphalt mixtures in compression. However, a systematic mechanistic characterization of the cracking mode in the asphalt mixture is urgently needed and will be addressed in this chapter.

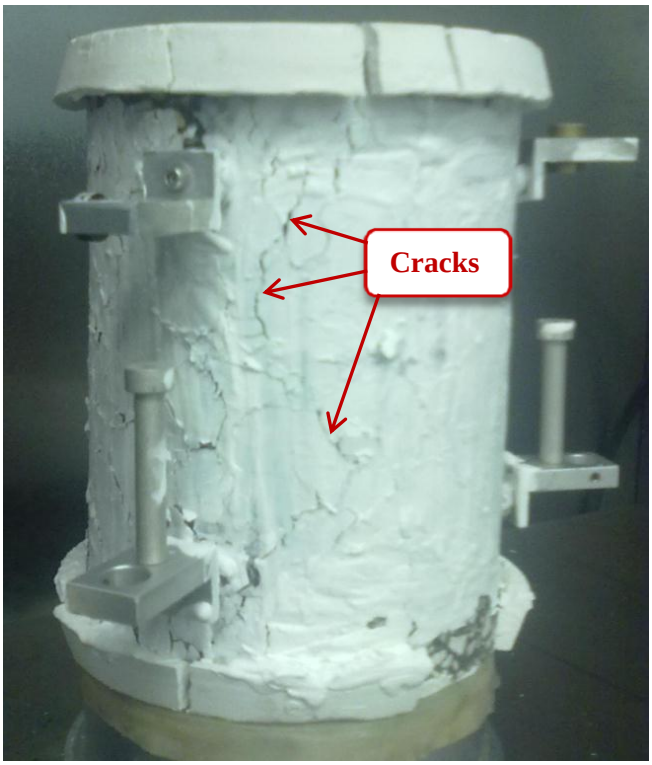

Figure 7-2 An asphalt mixture specimen painted by white plaster on surfaces after destructive test

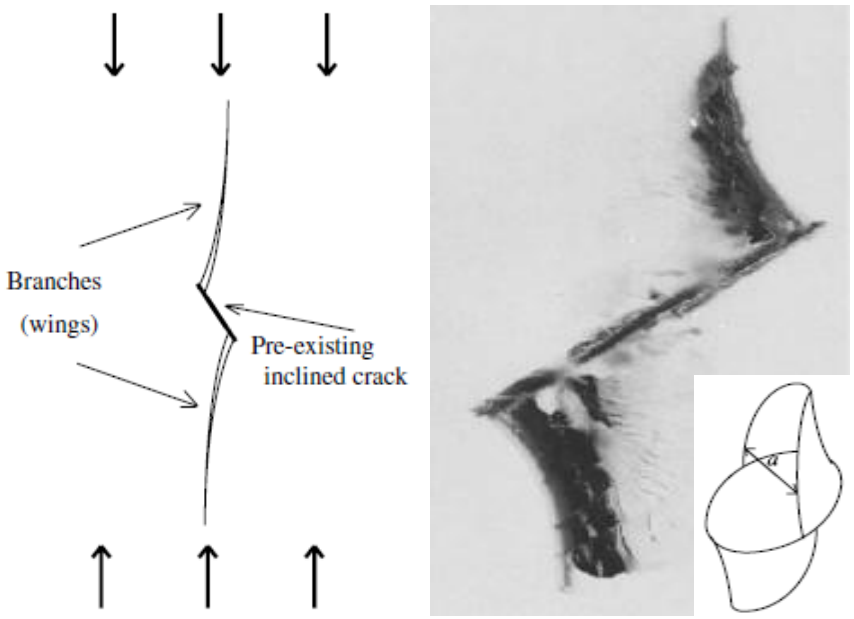

Figure 7-3 Crack propagation in uniaxial compression plotted in 2-D (left figure) and imaged in 3-D (right photo) (Dyskin et al. 2003)

LABORATORY EXPERIMENTS AND MATERIALS

The anisotropic damage densities (defined in Equations 6-9 and 6-11) including the axial damage density and the radial damage density are employed to characterize anisotropic viscofracture and used in the anisotropic viscoplastic modeling of the asphalt mixture. The data that are needed to determine the anisotropic damage densities are the decomposed viscofracture strains including the axial viscofracture strains and the radial viscofracture strains in the tertiary stage of the destructive dynamic modulus (DDM) test, which can be provided by the tests performed in Chapter VI. Thus no new tests are needed to perform in this chapter. A brief summary for the testing protocol and materials used in Chapter VI is provided as follows: the testing protocol includes a series of three laboratory tests: 1) uniaxial compressive creep (UCC) test; 2) nondestructive dynamic modulus (NDM) test; and 3) destructive dynamic modulus (DDM) test. The three tests were conducted on the asphalt mixtures that were fabricated by

mixing Texas Hanson limestone with two types of asphalt binder (Valero asphalt (PG64-16) and NuStar asphalt (PG67-22)), respectively. The VHL and NHL asphalt mixture specimens are varied by two air void contents (4% and 7%) and three aging periods (0, 3, and 6-month continuous aging at 60 ℃). Two replicate specimens were fabricated for each combination of the asphalt binder, air void content and aging period.

To obtain the radial strains, a radial LVDT is mounted on a bracelet which surrounds the specimen to record the deformation of the specimen's circumference during the tests, as shown in Figure 7-4. The radial strain is calculated as the ratio of the circumferential deformation to the specimen's circumference (314 mm). The same technique is used in Chapter II (see Figure 2-3).

Figure 7-4 Testing configurations of the UCC, NDM, DDM tests including axial and radial LVDTs.

The measured total axial strain and the total radial strain in the DDM tests need to be decomposed to obtain the axial and radial viscofracture strains. Chapter IV has presented a strain decomposition method to acquire the axial viscofracture strain in the tertiary stage. This chapter is about to provide a similar strain decomposition based on a generalized elastic-viscoelastic correspondence principle to obtain the radial viscofracture strain from the data of the DDM tests.

AXIAL AND RADIAL STRAIN DECOMPOSITIONS

In this section, a brief summary is presented for the axial strain decomposition. Then a generalized elastic-viscoelastic correspondence principle is proposed, based on which the radial strain decomposition is accomplished. In the end, both the axial and the radial viscofracture strain are obtained based on the measured axial and radial total strains in the DDM tests and will be employed in the anisotropic viscofracture characterization of the next section.

Axial Strain Decomposition

The total axial strain measured in the destructive dynamic modulus test is decomposed into five components (see Equation 7-1) using the materials properties of the undamaged asphalt mixtures, including $E(t)$, $|E^*|$, δ, and E_Y as discussed in Chapter IV

$$\varepsilon_1^T = \varepsilon_1^e + \varepsilon_1^{ve} + \varepsilon_1^p + \varepsilon_1^{vp} + \varepsilon_1^{vf} \tag{7-1}$$

where ε_1^T is axial total strain; ε_1^e is axial elastic strain; ε_1^{ve} is axial viscoelastic strain; ε_1^p is axial plastic strain; ε_1^{vp} is axial viscoplastic strain; and ε_1^{vf} is axial viscofracture strain.

The axial strain decomposition is conducted by employing the extended elastic-viscoelastic correspondence principle and the pseudo strain concept (Schapery 1984). It is proved in Chapter IV that, when the Young's modulus is assigned as the reference modulus, the

pseudo strain equals the remaining strain after subtracting the viscous strain from the total strain. Therefore, once the pseudo strain ($\varepsilon_1^R(t)$) is calculated based on its definition (i.e., Equation 7-9), the strain decomposition can be accomplished by the following steps:

1) elastic strain is always calculated by the Hooke's law as follows:

$$\varepsilon_1^e = \sigma(t)/E_Y \tag{7-2}$$

2) viscoelastic strain is computed by subtracting the pseudo strain from the measured total strain as follows:

$$\varepsilon_1^{ve} = \varepsilon_1^T - \varepsilon_1^R \tag{7-3}$$

3) plastic strain is the difference between the instantaneous pseudo strain ($\varepsilon_1^R(t=0)$) and the elastic strain as shown below:

$$\varepsilon_1^p = \varepsilon_1^R(t=0) - \varepsilon_1^e \tag{7-4}$$

4) viscoplastic strains in the primary and secondary stages are calculated by subtracting the elastic strain and the plastic strain from the pseudo strain as shown in Equation 7-5. Then the viscoplastic strain in the tertiary stage was predicted by using the Tseng-Lytton model (Tseng and Lytton 1989) as shown in Equation 7-6;

$$\varepsilon_1^{vp}(I,II) = \varepsilon_1^R(I,II) - \left(\varepsilon_1^e + \varepsilon_1^p\right) \tag{7-5}$$

$$\varepsilon_1^{vp} = \varepsilon_{1\infty}^{vp} \exp\left[-\left(\rho_1/N\right)^{\lambda_1}\right] \tag{7-6}$$

5) viscofracture strain was calculated by subtracting all of the other strain components from the measured total strain as shown in Equation 7-7.

$$\varepsilon_1^{vf} = \varepsilon_1^R - \left(\varepsilon_1^e + \varepsilon_1^p\right) - \varepsilon_1^{vp} \tag{7-7}$$

Details of the axial strain decomposition can be found in Chapter IV.

Generalized Elastic-Viscoelastic Correspondence Principle

In the extended elastic-viscoelastic correspondence principle, Schapery (1984) formulated a linear constitutive law for the viscoelastic material as follows:

$$\sigma(t) = E_R \varepsilon_1^R(t) \tag{7-8}$$

where E_R is the reference modulus and $\varepsilon_1^R(t)$ is the axial pseudo strain that is expressed as:

$$\varepsilon_1^R(t) = \frac{1}{E_R}\int_{0^-}^{t} E(t-\xi)\frac{d\varepsilon_1^T(\xi)}{d\xi}d\xi \tag{7-9}$$

where $\varepsilon_1^T(\xi)$ is the axial total strain measured in the test and $E(t)$ is the relaxation modulus of the undamaged asphalt mixture. It is proved in Chapter IV that, if the reference modulus is assigned as Young's modulus, $\varepsilon_1^R(t)$ is capable of eliminating the viscous effect on the axial total strain and mathematically equals $\varepsilon_1^R(t) = \varepsilon_1^T(t) - \varepsilon_1^{ve}(t)$ where $\varepsilon_1^{ve}(t)$ is the axial viscoelastic strain.

Inspired by Equation 7-8 and 7-9, another corresponding law is formulated for the viscoelastic material to relate the axial strain to the radial strain as follows:

$$\varepsilon_1(t) = -\frac{1}{\upsilon_{12}^R}\varepsilon_2^R(t) \tag{7-10}$$

where υ_{12}^R is the reference Poisson's ratio that is assigned as the elastic Poisson's ratio. $\varepsilon_2^R(t)$ is the radial pseudo strain that can be calculated by:

$$\varepsilon_2^R(t) = -\upsilon_{12}^R\left[-\int_{0^-}^{t}\pi_{12}(t-\xi)\frac{d\varepsilon_2^T(\xi)}{d\xi}d\xi\right] \tag{7-11}$$

where $\varepsilon_2^T(\xi)$ is the radial total strain that is measured in the test and $\pi_{12}(t)$ is named as inverse viscoelastic Poisson's ratio of the undamaged viscoelastic material. Similar to the axial pseudo

strain, the radial pseudo strain is capable of removing the viscous effect on the material responses and mathematically, $\varepsilon_2^R = \varepsilon_2^T - \varepsilon_2^{ve}$ where ε_2^{ve} is radial viscoelastic strain.

$\pi_{12}(t)$ is a newly proposed viscoelastic variable that is used to determine the axial strain provided that the radial strain is given and can be defined through:

$$\varepsilon_1(t) = -\int_{0^-}^{t} \pi_{12}(t-s)\, d\varepsilon_2(s) \tag{7-12}$$

If the axial strain ($\varepsilon_1(t)$) and the radial strain ($\varepsilon_2(t)$) are measured in a nondestructive creep test, $\pi_{12}(t)$ can be determined by taking Laplace transform to Equation 7-12 and yields:

$$\pi_{12}(t) = \mathcal{L}^{-1}\left\{-\frac{\bar{\varepsilon}_1(s)}{s\bar{\varepsilon}_2(s)}\right\} \tag{7-13}$$

where $\bar{\varepsilon}_1(s)$ and $\bar{\varepsilon}_2(s)$ are the Laplace transform of the axial strain and radial strain, respectively. s is the variable in the Laplace domain. It is known that the viscoelastic Poisson's ratio can be defined through Equation 7-14 and determined by Equation 7-15 based on the measured axial and redial strains.

$$\varepsilon_2(t) = -\int_{0^-}^{t} \upsilon_{12}(t-s)\, d\varepsilon_1(s) \tag{7-14}$$

$$\upsilon_{12}(t) = \mathcal{L}^{-1}\left\{-\frac{\bar{\varepsilon}_2(s)}{s\bar{\varepsilon}_1(s)}\right\} \tag{7-15}$$

Equations 7-13 and 7-15 indicate that, in the Laplace domain, we have:

$$s\bar{\pi}_{12}(s) = \frac{1}{s\bar{\upsilon}_{12}(s)} \tag{7-16}$$

Equation 7-16 is a companion formula to the relationship between the creep compliance and the relaxation modulus as shown in Equation 4-4. Figure 7-5 shows an example of $\pi_{12}(t)$ and

$\upsilon_{12}(t)$ that are determined by conducting a UCC test on an asphalt mixture. It is found that the viscoelastic Poisson's ratio is an increasing power curve and can be greater than 0.5 for an anisotropic viscoelastic material. The inverse viscoelastic Poisson's ratio is a decreasing curve and always greater than 1.

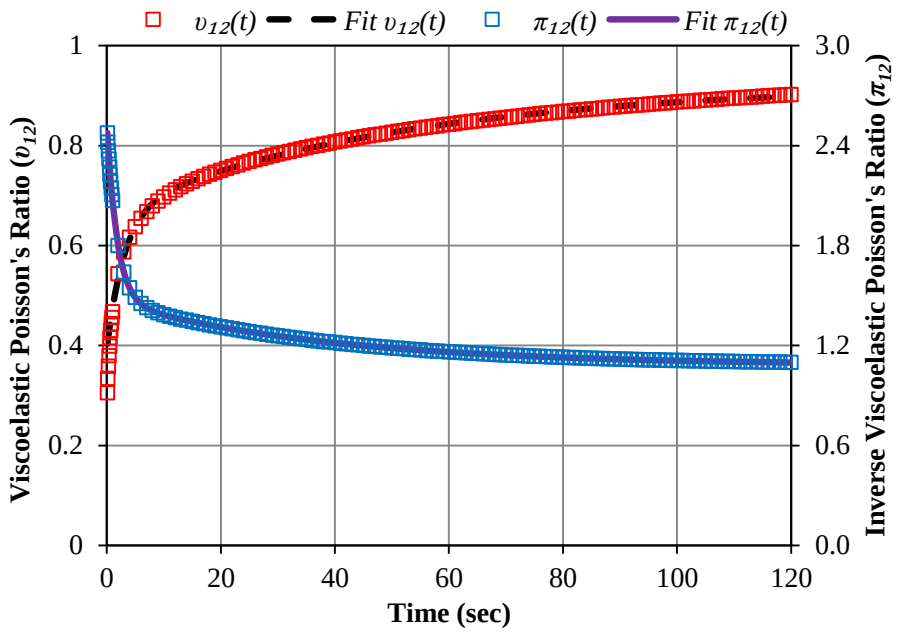

Figure 7-5 Viscoelastic Poisson's ratio and inverse viscoelastic Poisson's ratio for an asphalt mixture

Figure 7-5 also demonstrates that the measured $\pi_{12}(t)$ and $\upsilon_{12}(t)$ can be perfectly fitted by the Prony series models that are shown in Equations 7-16 and 7-17, respectively.

$$\upsilon_{12}(t) = \upsilon_0 + \sum_{i=1}^{M} \upsilon_i \left[1 - \exp\left(-\frac{t}{r_i} \right) \right] \tag{7-16}$$

$$\pi_{12}(t) = \pi_\infty + \sum_{j=1}^{M} \pi_j \exp\left(-\frac{t}{z_j} \right) \tag{7-17}$$

where M is the total number of the Kelvin elements in the Prony series model; υ_0, υ_i, r_i, π_∞, π_j and z_j are fitting parameters. υ_0 is used as the elastic Poisson's ratio, i.e., $\upsilon_{12}^R = \upsilon_0$.

Radial Strain Decomposition

In order to perform the radial strain decomposition, the radial pseudo strain needs to be firstly calculated based on Equation 7-11, in which $\varepsilon_2^T(t)$ is the measured radial total strain of the DDM tests. Similar to the model for the axial total strain in Equation 4-10, $\varepsilon_2^T(t)$ can be modeled as:

$$\begin{cases} \varepsilon_2^T(t) = \varepsilon_{2c}(t) - \varepsilon_{2d}(t) \\ \varepsilon_{2c}(t) = \varepsilon_{20} + \sum_{i=1}^{L} \varepsilon_{2i}\left[1 - \exp\left(-\dfrac{t}{\tau_{2i}}\right)\right] \\ \varepsilon_{2d}(t) = \varepsilon_{2N}\cos(\omega t - \varphi_{2N}) = \dfrac{\sigma_2}{\left|E_{2N}^*\right|}\cos(\omega t - \varphi_{2N}) \end{cases} \tag{7-18}$$

where ε_2^T is measured radial total strain; ε_{2c} is radial creep strain due to the creep stress; $\varepsilon_{20}, \varepsilon_{2i}, \tau_{2i}$ are fitting parameters for the radial creep strain; L is total number of ε_{2i} and τ_{2i}; ε_{2d} is radial dynamic cyclic strain due to the dynamic cyclic stress; ε_{2N} is amplitude of the radial dynamic strain at the N-th load cycle; $\left|E_{2N}^*\right|$ is the magnitude of the radial dynamic modulus (E_{2N}^*) of the damaged asphalt mixture at the N-th load cycle that is calculated using $\left|E_{2N}^*\right| = \sigma_d / \varepsilon_{2N}$; and φ_{2N} is phase angle of E_{2N}^*, which equals the lag angle between the radial total strain and the stress at the N-th load cycle.

Employing Equations 7-17 and 7-18 in Equation 7-11 gives the radial pseudo strain as:

$$\begin{cases} \varepsilon_2^R(t) = \varepsilon_{2c}^R(t) - \varepsilon_{2d}^R(t) \\ \varepsilon_{2c}^R(t) = \upsilon_{12}^R \left\{ \pi_\infty \varepsilon_{2c}(t) + \varepsilon_{20} \Delta\pi_{12}(t) + \sum_{i=1}^{L} \sum_{j=1}^{M} \frac{\varepsilon_{2i}\pi_j}{\left(1-\tau_i/z_j\right)} \left[\exp\left(-\frac{t}{z_j}\right) - \exp\left(-\frac{t}{\tau_{2i}}\right) \right] \right\} \\ \varepsilon_{2d}^R(t) = \frac{\upsilon_{12}^R}{\left|\upsilon_{12}^*\right|} \frac{\sigma_d}{\left|E_{2N}^*\right|} \cos\left(\omega t - \varphi_{2N} + \delta'\right) \end{cases} \tag{7-19}$$

where $\upsilon_{12}^R = \upsilon_0$ that is the elastic Poisson's ratio and $\Delta\pi(t) = \pi(t) - \pi_\infty$ according to Equation 7-17. $\left|\upsilon_{12}^*\right|$ and δ' are the magnitude and phase angle of the complex Poisson's ratio of the undamaged asphalt mixtures that are measured in the NDM tests. Figure 7-6 illustrates an example of $\left|\upsilon_{12}^*\right|$ and δ' of an undamaged asphalt mixture. It is found that both $\left|\upsilon_{12}^*\right|$ and δ' remain unchanged with load cycles in the NDM test.

Similar to the axial strain decomposition, the total radial strain is also decomposed into five components as follows:

$$\varepsilon_2^T = \varepsilon_2^e + \varepsilon_2^p + \varepsilon_2^{ve} + \varepsilon_2^{vp} + \varepsilon_2^{vf} \tag{7-20}$$

where ε_2^T is radial total strain; ε_2^e is radial elastic strain; ε_2^{ve} is radial viscoelastic strain; ε_2^p is radial plastic strain; ε_2^{vp} is radial viscoplastic strain; ε_2^{vf} is radial viscofracture strain. By inputting the measured total radial strain into Equation 7-11, the radial pseudo strain is calculated by Equation 7-19. Based on the generalized elastic-viscoelastic correspondence principle the radial pseudo strain is the remaining strain by subtracting the radial viscoelastic strain from the total radial strain. Thus:

$$\varepsilon_2^R = \varepsilon_2^T - \varepsilon_2^{ve} = \varepsilon_2^e + \varepsilon_2^p + \varepsilon_2^{vp} + \varepsilon_2^{vf} \tag{7-21}$$

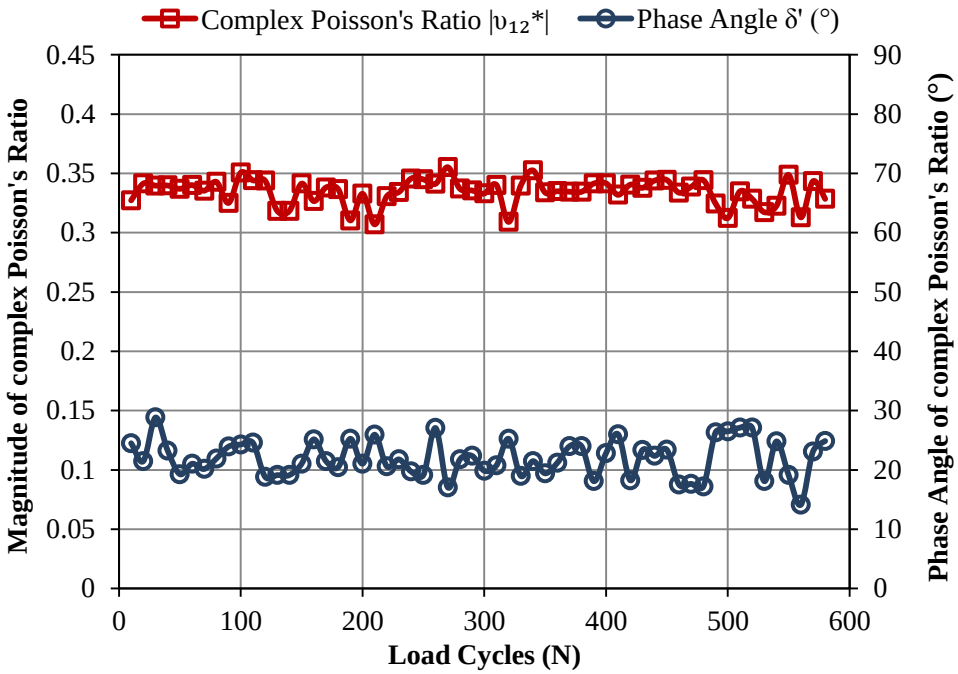

Figure 7-6 Magnitude and phase angle of complex Poisson's ratio for asphalt mixture

The radial strain decomposition is performed as follows:

1) the radial elastic strain is calculated using axial elastic strain multiplied by the reference Poisson's ratio that is elastic Poisson's ratio, which is shown as

$$\varepsilon_2^e = -\upsilon_{12}^R \varepsilon_1^e = -\upsilon_0 \frac{\sigma(t)}{E_Y} \tag{7-22}$$

2) the radial viscoelastic strain is obtained by subtracting the radial pseudo strain from the radial total strain:

$$\varepsilon_2^{ve} = \varepsilon_2^T - \varepsilon_2^R \tag{7-23}$$

3) since $\varepsilon_2^{vp}(t=0) = \varepsilon_2^{vf}(t=0) = 0$, the radial plastic strain is determined as:

$$\varepsilon_2^p = \varepsilon_2^R(t=0) - \varepsilon_2^e \tag{7-24}$$

4) since the viscofracture strain due to the growth of cracks does not occur until the tertiary stage (Part III), the radial pseudo strain in the primary and secondary stages ($\varepsilon_2^R\left(I,II\right)$) only includes the radial elastic strain, radial plastic strain and radial viscoplastic strain. As a result, the radial viscoplastic strain in the primary and secondary stage ($\varepsilon_2^{vp}\left(I,II\right)$) can be calculated using Equation 7-25. Then the Tseng-Lytton model in Equation 7-26 is employed to fit $\varepsilon_2^{vp}\left(I,II\right)$ and predict the radial viscoplastic strain during the entire deformation process including the primary, secondary and tertiary stages;

$$\varepsilon_2^{vp}\left(I,II\right)=\varepsilon_2^R\left(I,II\right)-\left(\varepsilon_2^e+\varepsilon_2^p\right) \tag{7-25}$$

$$\varepsilon_2^{vp}=\varepsilon_{2\infty}^{vp}\exp\left[-\left(\rho_2/N\right)^{\lambda_2}\right] \tag{7-26}$$

5) the radial viscofracture strain can be computed by subtracting all other components from the total radial strain:

$$\varepsilon_2^{vf}=\varepsilon_2^R-\left(\varepsilon_2^e+\varepsilon_2^p\right)-\varepsilon_2^{vp} \tag{7-27}$$

Thus the radial strain decomposition is accomplished by a complete separation of each strain component in the DDM test. An example is given in Figure 7-7 to show the radial strain decomposition for an asphalt mixture in the DDM test. It is found that radial elastic and plastic strain are time-independent and the radial viscoelastic strain shows three stage changes and occupies a large proportion of the radial total strain. The radial viscoplastic strain shows a power curve and the viscofracture strain increases with load cycles at an increasing strain rate in the tertiary stage.

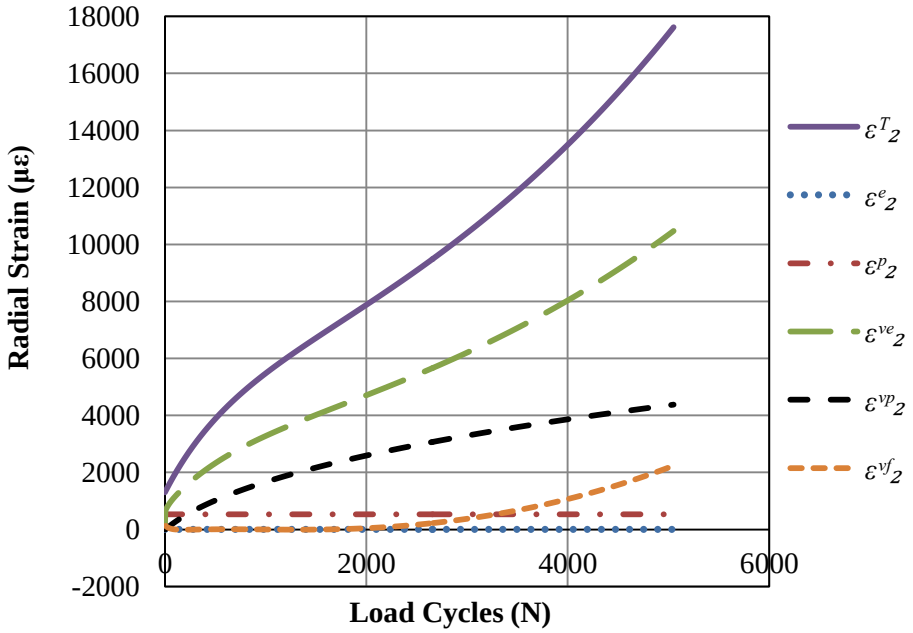

Figure 7-7 Radial strain decomposition for an asphalt mixture

MECHANISTIC MODELING OF VISCOFRACTURE IN TERTIARY FLOW

By using the decomposed axial and radial viscofracture strains, this section presents the determination of the axial and radial damage densities which are employed in the effective stress as shown in Equation 6-11. Since the cracks grow only in the tertiary stage of the destructive tests in compression, the damage densities are calculated only for the tertiary stage.

To determine the axial damage density, a balance principle of the incremental dissipated pseudo fracture strain energy ($\Delta DPFSE$) is implemented between the apparent configuration and the true configuration of the material. This principle states that the apparent dissipated pseudo strain energy ($DPSE$) that is consumed in developing the viscofracture strain within each load cycle in the apparent configuration equals the true $DPSE$ that is dissipated for the fracture of the intact material within the same load cycle in the true configuration.

The reason for using $DPSE$ to formulate the energy balance is that $DPSE$ is the irrecoverable energy that is dissipated during the evolution of the different types of damage such as viscoplasticity and fracture. Actually, the $DPSE$ has already been widely and successfully used in characterizing the damages including fatigue cracking and permanent deformation in viscoelastic materials such as asphalt binders and asphalt mixtures (Gibson et al. 2003; Walubita et al. 2006; Wen and Bahia 2009). If the $DPSE$ used for viscoplasticity is denoted as $DPPSE$ and the $DPSE$ used for fracture is denoted as $DPFSE$, then $DPSE = DPPSE + DPFSE$. The $\Delta DPFSE$ equivalence equation is formulated step by step as follows.

Step 1: Calculate the Apparent Incremental Dissipated Pseudo Fracture Strain Energy

First, the apparent $DPFSE$, denoted as $DPFSE^A$, is calculated by integrating the apparent stress with the viscofracture strain that is obtained using strain decomposition, as shown in Equation 7-28:

$$DPFSE^A = \int_{\frac{2\pi}{\omega}N_f}^{\frac{2\pi}{\omega}N} \sigma^A(t) \frac{d\varepsilon_1^{vf}(t)}{dt} dt \tag{7-28}$$

where $\sigma^A(t) = \sigma_0^A\left[1-\cos(\omega t)\right]$ is the apparent stress in kPa, which is equal to the applied load divided by the entire cross-sectional area (including the crack opening areas); σ_0^A is the amplitude of the stress and $\sigma_0^A = 0.5\times(\sigma_c + \sigma_d) = 300\ kPa$ according to Equation 4-9; ω is the load frequency, rad/sec; $N = \frac{\omega}{2\pi}t$ is the number of load cycles; N_f is the flow number; and $\varepsilon_1^{vf}(t)$ is the axial viscofracture strain that is modeled using Equation 4-26, which is repeated as $\varepsilon_1^{vf} = \varepsilon_0^{vf}\left[e^{\theta_1(N-N_f)}-1\right]$ where N_f is flow number that is the starting point of the tertiary stage.

Figure 7-8 illustrates that the flow number is greater for an asphalt mixture that has a lower air void content or a longer aging period. ε_0^{vf} and θ_1 are fitting parameters. Substituting ε_1^{vf} function into Equation 7-28 and conducting the integration yields $DPFSE^A$ to be:

$$DPFSE^A = \varepsilon_0^{vf}\left[\sigma_0^A - \frac{\sigma_0^A}{1+\left(2\pi/\theta_1\right)^2}\right]\left[e^{\theta_1\langle N-N_f\rangle}-1\right] \tag{7-29}$$

The exponent of the viscofracture strain, θ_1, is always less than 0.1 in its magnitude, as shown in Figure 7-8. As a result, the calculating error caused by ignoring the term $\frac{\sigma_0^A}{1+\left(2\pi/\theta_1\right)^2}$ in Equation 7-29 is less than 0.025%. Therefore, Equation 7-29 is abbreviated to:

$$DPFSE^A = \sigma_0^A\varepsilon_0^{vf}\left[e^{\theta_1\langle N-N_f\rangle}-1\right] = \sigma_0^A\varepsilon_1^{vf}\left(N\right) \tag{7-30}$$

Then the apparent incremental $DPFSE$ is:

$$\Delta DPFSE^A\left(N\right) = \sigma_0^A\Delta\varepsilon_1^{vf}\left(N\right) = \sigma_0^A\left[\varepsilon_1^{vf}\left(N+1\right)-\varepsilon_1^{vf}\left(N\right)\right] \tag{7-31}$$

Equation 7-31 indicates that only the axial viscofracture strain (ε_1^{vf}) component of the total strain is involved in the calculation of $\Delta DPFSE^A$. Consequently $\Delta DPFSE^A$ is the energy dissipated to drive the propagation of the cracks in one load cycle.

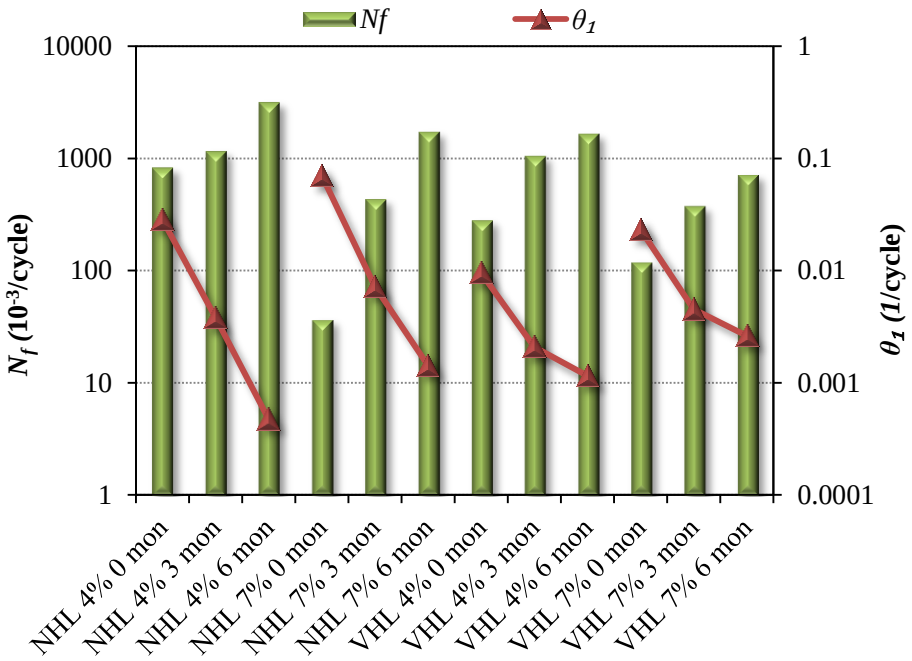

Figure 7-8 Flow number (N_f) and exponent of viscofracture strain (θ_1) of asphalt mixture

Step 2: Calculate the True Incremental Dissipated Pseudo Fracture Strain Energy

The true incremental dissipated pseudo fracture strain energy ($\Delta DPFSE^T$) is obtained by performing an energy analysis in the intact materials that are in the true configuration of the material. The total energy that results from the work done by an external load is dissipated by both the material relaxation due to the viscoelasticity of the asphalt mixtures and the damages including plasticity and fracture in the tertiary phase of the asphalt mixtures. Since the constitutive equation based on pseudo strain is capable of eliminating the viscous effect on the material responses (Kim et al. 1995; Park et al. 1996; Si et al. 2002), the dissipated pseudo strain energy (DPSE) does not include the energy dissipated for the material viscoelastic relaxation. The DPSE only accounts for the energy dissipated in generating the damages including viscoplasticity and viscofracture in the asphalt mixture, which means:

$$\Delta DPSE^T = \Delta DPPSE^T + \Delta DPFSE^T \tag{7-32}$$

Thus $\Delta DPFSE^T$ can be determined by subtracting the true incremental dissipated pseudo plastic strain energy ($\Delta DPPSE^T$) from the true incremental dissipated pseudo strain energy ($\Delta DPSE^T$). The following derivations show the calculations of $\Delta DPSE^T$ and $\Delta DPPSE^T$.

In the true configuration, the true stress acts on the intact material. Under cyclic loading, the true stress varies with time as:

$$\sigma^T(t) = \sigma_N^T\left[1-\cos(\omega t)\right] \tag{7-33}$$

where σ_N^T is the amplitude of the true stress at the load cycle, N, the true strain responding to the true stress includes the following two parts (Findley et al. 1989):

1) True creep strain, which is caused by the true creep stress (σ_N^T) and is determined as $\sigma_N^T D(t)$, where $D(t)$ is the creep compliance of the undamaged asphalt mixtures; and
2) True oscillatory strain, which is caused by the true oscillatory stress ($-\sigma_N^T\cos(\omega t)$) and is determined as $\left[-\frac{\sigma_N^T}{|E^*|}\cos(\omega t-\delta)\right]$, where $|E^*|$ and δ are the magnitude and phase angle of the complex modulus for the undamaged asphalt mixtures, respectively.

The amplitude of the true stress (σ_N^T), which increases with load cycle due to the growth of cracks, is assumed to remain constant within one load cycle. Thus the true stain caused by the true stress becomes:

$$\varepsilon^T(t) = \sigma_N^T D(t) - \frac{\sigma_N^T}{|E^*|}\cos(\omega t - \delta) \tag{7-34}$$

In the calculation of the dissipated energy for damage, the pseudo strain concept is employed to eliminate the viscous effect on the material responses. By definition, the true pseudo strain corresponding to the true strain can be determined as (Schapery 1984):

$$\varepsilon^{TR}(t) = \frac{1}{E_R}\int_{0^-}^{t} E(t-\xi)\frac{d\varepsilon^T(\xi)}{d\xi}d\xi \tag{7-35}$$

where ε^{TR} is true pseudo strain, t is the current time, ξ is the previous time before t, $E(t)$ is relaxation modulus of the undamaged material, and E_R is the reference modulus which is determined as the Young's modulus according to the study in Chapter IV. Based on Equations 7-34 and 7-35, the true pseudo strain is written as:

$$\varepsilon^{TR}(t) = \varepsilon_c^{TR}(t) - \varepsilon_d^{TR}(t) \tag{7-36}$$

where $\varepsilon_c^{TR}(t)$ is the creep part of the true pseudo strain and $\varepsilon_d^{TR}(t)$ is the dynamic part of the true pseudo strain. Thus $\varepsilon_c^{TR}(t)$ is calculated as follows:

$$\varepsilon_c^{TR}(t) = \frac{\sigma_N^T}{E_R}\int_{0^-}^{t} E(t-\xi)\frac{dD(\xi)}{d\xi}d\xi = \frac{\sigma_N^T}{E_R} \tag{7-37}$$

$\varepsilon_d^{TR}(t)$ is determined as:

$$\varepsilon_d^{TR}(t) = \frac{\sigma_N^T}{E_R}\frac{1}{|E^*|}\int_{0^-}^{t} E(t-\xi)\frac{d\cos(\omega\xi-\delta)}{d\xi}d\xi \tag{7-38}$$

Substituting $s = t - \xi$ in Equation 7-38 yields:

$$\varepsilon_d^{TR}(t) = \frac{\sigma_N^T}{E_R}\frac{1}{|E^*|}\int_{0^-}^{t} E(s)\frac{d\cos[\omega(t-s)-\delta]}{d(t-s)}ds \tag{7-39}$$

Let $E(t)=E(\infty)+\Delta E(t)$ where $E(\infty)$ is the asymptotic value when time approaches infinity and $\Delta E(t)$ is the difference between $E(t)$ and $E(\infty)$, which decreases with time for a viscoelastic solid, then Equation 7-39 becomes:

$$\begin{aligned}\varepsilon_d^{TR}(t)&=\frac{\sigma_N^T}{E_R}\frac{1}{|E^*|}\left\{E(t)\cos(\delta)+\int_0^t E(s)\frac{d\cos\left[\omega(t-s)-\delta\right]}{d(t-s)}ds\right\}\\&=\frac{\sigma_N^T}{E_R}\frac{1}{|E^*|}\left\{\Delta E(t)\cos(\delta)+\left[E(\infty)+\omega\int_0^t\Delta E(s)\sin(\omega s)ds\right]\cos(\omega t-\delta)\right.\\&\qquad\left.-\left[\omega\int_0^t\Delta E(s)\cos(\omega s)ds\right]\sin(\omega t-\delta)\right\}\end{aligned} \tag{7-40}$$

After sufficient load cycles, the initial transient response vanishes and the material undergoes a steady oscillation, which can be explained mathematically that, when $t\to\infty$, $\Delta E(\infty)\to 0$ and both $\int_0^{t\to\infty}\Delta E(s)\sin(\omega s)ds$ and $\int_0^{t\to\infty}\Delta E(s)\cos(\omega s)ds$ approach a well-defined limit. For an asphalt mixture that is subjected to a destructive compressive sinusoidal loading, the initial transient mainly occurs and vanishes within the primary deformation stage and the steady oscillation state is approached in the secondary deformation stage. Based on viscoelastic theory (Wineman and Rajagopal 2001), one can have:

$$E_{II}'=E(\infty)+\omega\int_0^{t\to\infty}\Delta E(s)\sin(\omega s)ds \tag{7-41}$$

$$E_{II}''=\omega\int_0^{t\to\infty}\Delta E(s)\cos(\omega s)ds \tag{7-42}$$

where E_{II}' and E_{II}'' are the real and imaginary parts of the complex modulus in the secondary deformation stage (E_{II}^*). Based on the results of the destructive dynamic modulus tests, the magnitude of E_{II}^* is the dynamic modulus ($|E_{II}^*|$), which is a variable that is dependent on the

load cycle, and the phase angle of E_{II}^{*} is φ_{II}, which was demonstrated to be a constant for a specific asphalt mixture. Substituting Equations 7-41 and 7-42 as well as $E_{II}' = \left|E_{II}^{*}\right|\cos\varphi_{II}$ and $E_{II}'' = \left|E_{II}^{*}\right|\sin\varphi_{II}$ into Equation 7-40 gives:

$$\varepsilon_d^{TR}(t) = \frac{\sigma_N^T}{E_R}\frac{\left|E_{II}^{*}\right|}{\left|E^{*}\right|}\cos\left(\omega t - \delta + \varphi_{II}\right) \tag{7-43}$$

The material properties in the secondary deformation stage are determined as the reference properties in the true configuration because of the following two reasons:

1) The secondary stage is in a steady oscillatory phase and the initial transient response has disappeared; and
2) The fracture starts to grow in the tertiary stage when it departs from the steady state in the secondary stage.

As a result, the reference modulus in Equations 7-37 and 7-43 is determined as the Young's modulus of the asphalt mixtures in the secondary stage (E_{YII}). Substituting Equations 7-37 and 7-43 into Equation 7-36 and using $E_R = E_{YII}$ yields the true pseudo strain:

$$\varepsilon^{TR}(t) = \frac{\sigma_N^T}{E_{YII}}\left[1 - \frac{\left|E_{II}^{*}\right|}{\left|E^{*}\right|}\cos\left(\omega t - \delta + \varphi_{II}\right)\right] \tag{7-44}$$

$\Delta DPSE^T$ can be computed by integrating the true stress in Equation 7-33 with the true pseudo strain in Equation 7-44 within one load cycle, which is:

$$\Delta DPSE^T(N) = \int_{N\frac{2\pi}{\omega}}^{(N+1)\frac{2\pi}{\omega}} \sigma^T(t)\frac{d\varepsilon^{TR}(t)}{dt}dt = \frac{\left(\sigma_N^T\right)^2}{E_{YII}}\frac{\left|E_{II}^{*}\right|}{\left|E^{*}\right|}\pi\sin\left(\delta - \varphi_{II}\right) \tag{7-45}$$

Assuming that the ratio of the Young's modulus to the dynamic modulus in the undamaged condition remains the same as that in the secondary deformation stage for each asphalt mixture, that is,

$$\frac{E_Y}{\left|E^*\right|} = \frac{E_{YII}}{\left|E_{II}^*\right|} \tag{7-46}$$

where E_Y is the Young's modulus of the undamaged asphalt mixture, and the values of with asphalt mixtures with different binders, air void contents and aging periods have been shown in Figure 5-8. Substituting Equation 7-46 into 7-45 gives:

$$\Delta DPSE^T\left(N\right) = \frac{\left(\sigma_N^T\right)^2}{E_Y}\pi\sin\left(\delta - \varphi_{II}\right) \tag{7-47}$$

In the tertiary stage, $\Delta DPSE^T$ is the pseudo strain energy dissipated by both viscoplasticity and viscofracture. In contrast, in the secondary stage, $\Delta DPSE^T$ is the pseudo strain energy dissipated only by viscoplasticity since no viscofracture occurs in this stage. Thus $\Delta DPSE^T$ is equal to $\Delta DPPSE^T$ in the secondary stage. Actually, in the primary stage, the air voids of the asphalt mixture are squeezed due to the compressive load, which is indicated by a deceasing phase angle. Thus the lost area keeps decreasing which results in a decreasing damage density in this stage. While in the secondary stage, the phase angle remains unchanged which demonstrates that the decrease of air voids have ceased and a steady stage is reached. Thus the damage density at the flow number (i.e., the end of the secondary stage) is the minimum damage density after the compression during the primary and secondary stages. Therefore the true stress at the flow number is $\sigma_{N_f}^T = \sigma_0^A / \left(1 - \xi_{01}\right)$ where ξ_{01} is the axial damage density at the flow number. Thus $\Delta DPPSE^T$ at the flow number load cycle is determined as:

$$\Delta DPPSE^T\left(N_f\right)=\left(\frac{\sigma_0^A}{1-\xi_{01}}\right)^2\frac{\pi\sin\left(\delta-\varphi_{II}\right)}{E_Y} \tag{7-48}$$

It is assumed that the $\Delta DPPSE^T\left(N\right)$ in the tertiary stage remains unchanged from $\Delta DPPSE^T\left(N_f\right)$ that is in the flow number load cycle. This assumption is reasonable because:

1) In the tertiary stage the apparent stress remains unchanged, however, the true stress continues to increase;
2) An asphalt mixture follows a work hardening rule and the incremental viscoplastic strain (i.e., viscoplastic strain rate) continues to decrease with load cycles; thus
3) Because of the reasons (1) and (2), the integral of the product of the true stress and the incremental viscoplastic strain within each load cycle in the tertiary stage remains unchanged from that at the flow number load cycle.

Substituting Equations 7-47 and 7-48 into Equation 7-32 gives:

$$\Delta DPFSE^T\left(N\right)=\left[\left(\sigma_N^T\right)^2-\left(\frac{\sigma_0^A}{1-\xi_{01}}\right)^2\right]\frac{\pi\sin\left(\delta-\varphi_{II}\right)}{E_Y} \tag{7-49}$$

If defining $K=\dfrac{E_Y}{\pi\sin\left(\delta-\varphi_{II}\right)}$ as the compressive viscofracture modulus, the incremental dissipated pseudo fracture strain energy is expressed as:

$$\Delta DPFSE^T\left(N\right)=\left[\left(\sigma_N^T\right)^2-\left(\frac{\sigma_0^A}{1-\xi_{01}}\right)^2\right]\frac{1}{K} \tag{7-50}$$

For a specific asphalt mixture, test observations have shown that δ, φ_{II} and E_Y remain unchanged with load cycles even in a destructive test. Thus the compressive viscofracture modulus (K) also remains unchanged with load cycles and can be recognized as a material property which characterizes the viscofracture of the asphalt mixture in compression. Figure 7-9

shows δ and φ_{II} for the asphalt mixtures with different binders, air void contents and aging periods.

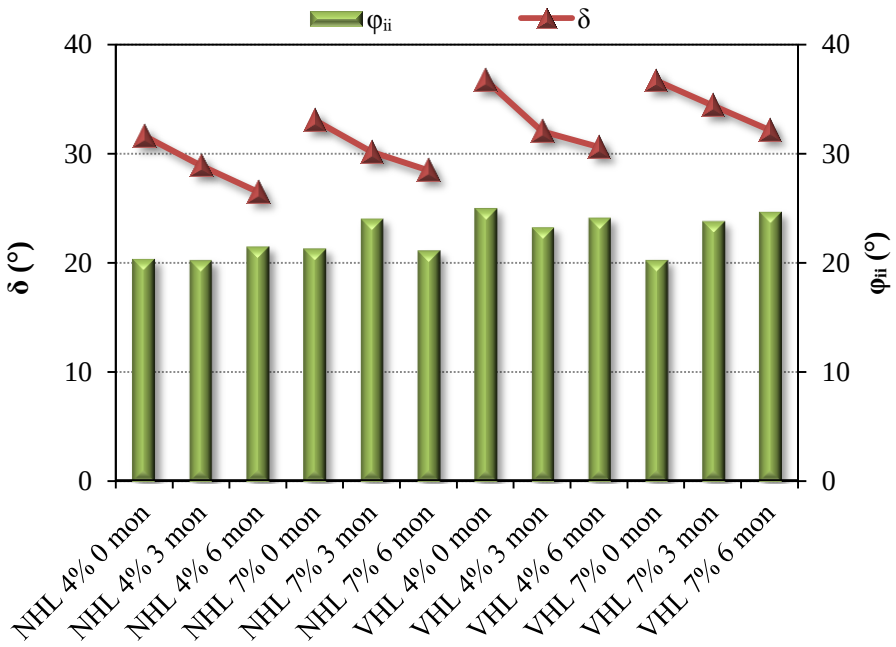

Figure 7-9 Phase angle of undamaged asphalt mixture (δ) and phase angle of damaged asphalt mixture in the secondary deformation stage (φ_{II})

It is found from Figure 7-9 that $\delta > \varphi_{II}$ applies to all asphalt mixtures. This is because the phase angle δ is the phase angle of the asphalt mixture before applying destructive compressive loads and φ_{II} is the phase angle of the asphalt mixtures in the secondary phase after such loads are applied. The asphalt mixture is compressed in the primary stage and the air voids are squeezed during compression, which yields a stiffer asphalt mixture because of less air voids and more intact material. A stiffer viscoelastic material normally has a lower phase angle, which indicates $\delta > \varphi_{II}$. For different asphalt mixtures, δ decreases as the asphalt mixtures are

aged or have a low air void content while φ_{II} does not have a significant change when the asphalt mixtures use different binder, air void content and aging period.

Step 3: Calculate True Stress and Axial Damage Density

Let $\Delta DPFSE^A(N) = \Delta DPFSE^T(N)$ according to the $\Delta DPFSE$ balance principle, the amplitude of the true stress is solved to be:

$$\sigma_N^T = \sqrt{\left(\frac{\sigma_0^A}{1-\xi_{01}}\right)^2 + \sigma_0^A K \Delta\varepsilon_1^{vf}(N)} \tag{7-51}$$

Based on Equations 6-8 and 7-51, the axial damage density is determined as:

$$\xi_1(N) = 1 - \left[\left(\frac{1}{1-\xi_{01}}\right)^2 + \frac{K\Delta\varepsilon_1^{vf}(N)}{\sigma_0^A}\right]^{-\frac{1}{2}} \tag{7-52}$$

At the flow number load cycle ($N = N_f$), the viscofracture strain still remains zero, that is $\Delta\varepsilon_1^{vf}(N_f) = 0$. Thus, based on Equations 7-51 and 7-52, one has $\sigma_{N_f}^T = \sigma_0^A / (1-\xi_{01})$ and $\xi_1(N_f) = \xi_{01}$, which indicates that Equations 7-51 and 7-52 satisfy their boundary conditions implicitly.

To determine the true stress amplitude in Equation 7-51 and the damage density in Equation 7-52, the measured average K and $\Delta\varepsilon_1^{vf}$ based on the testing results of the two replicates are used in the calculations of true stress and damage density. However, ξ_{01} is still an unknown parameter. Thus a trial and error method is employed as follows:

1) An initial value is assigned to ξ_{01}, such as half of the air void content, in the first trial calculation of σ_N^T and $\xi_1(N)$;

2) The calculated $\xi_1(N)$ is fitted by a damage density prediction model in Equation 7-61 that is derived in the next section, where ξ_{01}, C_1 and D_1 are fitting parameters;

3) Minimize the error between the assumed ξ_{01} and the fitted ξ_{01} and determine the optimum ξ_{01} using the Solver function in the Excel processor.

Figure 7-10 shows the calculated true stress and axial damage density for an asphalt mixture, which indicates that both the true stress and the axial damage density increases in the tertiary stage. This is because the area of the intact material decreases and the lost area increases due to the growth of cracks in this stage. Since the true stress acts on the intact material, more viscoplastic strain is produced due to the increase of the true stress, which is the reason why the cracks in the tertiary stage accelerate the evolution of the permanent deformation. To take into consideration the accelerating effect of the cracks on the plastic deformation, the true stress, instead of the apparent (nominal) stress, should be used in the prediction of the permanent deformation for the asphalt mixtures. In addition, Figure 7-10 indicates that the air void content of the specimen is 0.51% at the flow number load cycle. This demonstrates that the air voids are significantly compressed during the primary stages, which leads to a dramatic decrease of the air void content (from the original air void 7% to 0.51% at the flow number).

Step 4: Calculate Radial Damage Density Based on Geometry of Cracks

Damage density is employed in this study to characterize the viscofracture of the asphalt mixture in compression and it is defined as a ratio of the lost area due to cracks to the total area of a cross section in a specific direction. Since the projections of the cracks differ in different directions, the damage density is an anisotropic parameter. The axial damage density (ξ_1) has been determined in step 3 by employing the incremental dissipated pseudo fracture strain energy

balance principle. To determine the radial damage density (ξ_2), a geometrical method is proposed in this study as follows:

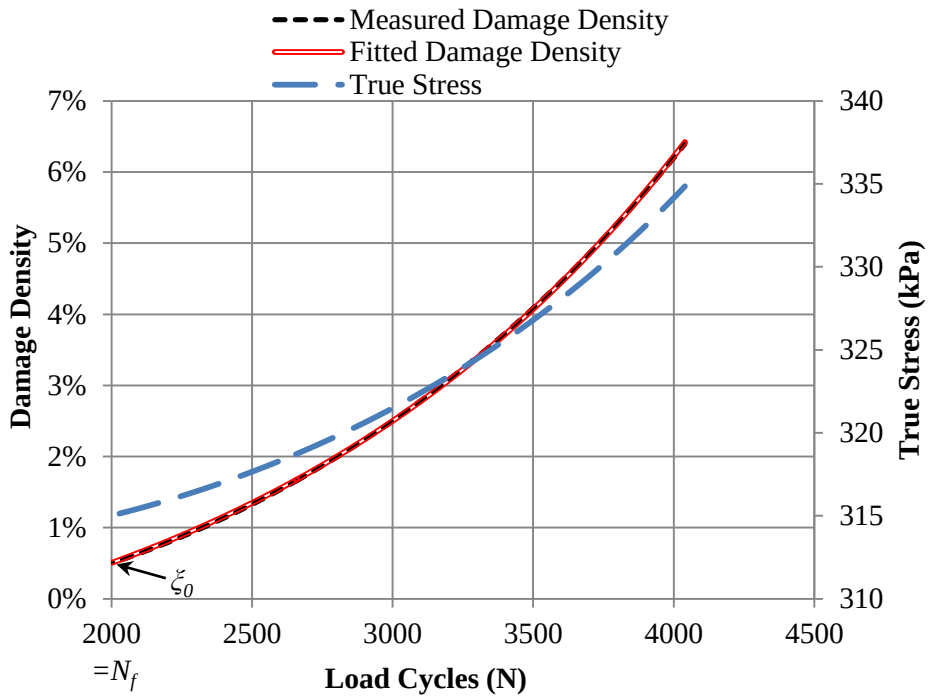

Figure 7-10 True stress and axial damage density of an asphalt mixture in tertiary stage

First, the axial viscofracture strain (ε_1^{vf}) and radial viscofracture strain (ε_2^{vf}) are obtained by strain decompositions, which have been presented in the last section. Figure 7-11 plots a geometric illustration of cracks in a cylindrical asphalt mixture specimen under a compressive load. The cylindrical specimen has a height of *H* and a radius of *R*. Under a compressive load, the height of the specimen is decreased and the radius of the specimen is increased. As we know, the deformation of the specimen can be caused by viscoelasticity, viscoplasticity or viscofracture of the asphalt mixture. It is assumed that the decrease of the specimen's height and the increase of the specimen's radius, which are the viscofracture

deformations and purely caused by the growth of cracks, are denoted as ΔH and ΔR, respectively.

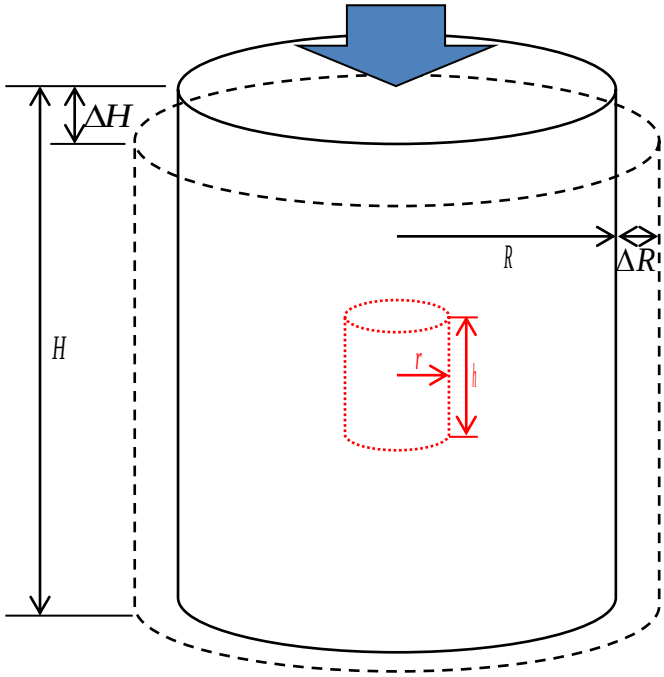

Figure 7-11 Geometric illustration of cracks in a cylindrical specimen under a compressive load

Since the axial viscofracture strain (ε_1^{vf}) and radial viscofracture strain (ε_2^{vf}) characterize the viscofracture deformation of the asphalt mixture that are caused by cracks. Then we have:

$$\begin{cases} \varepsilon_1^{vf} = \dfrac{\Delta H}{H} \\ \varepsilon_2^{vf} = \dfrac{\Delta R}{R} \end{cases} \tag{7-53}$$

Second, the cracks disperse randomly in the asphalt mixture. If assuming that all cracks are collected in a cylinder whose height and radius are *r* and *h*, respectively; then the damage densities can be calculated based on their definitions in Equation 6-9 and one has:

$$\begin{cases} \xi_1 = \dfrac{\pi r^2}{\pi R^2} \\ \xi_2 = \dfrac{2\pi r \cdot h}{2\pi R \cdot H} \end{cases} \tag{7-54}$$

Third, since ΔH and ΔR are purely caused by the cracks, the increased volume of the cylindrical asphalt mixture specimen should equal to the volume of cracks, that is:

$$\pi\left(R+\Delta R\right)^2\left(H-\Delta H\right)-\pi R^2 H=\pi r^2 h \tag{7-55}$$

Finally, Equations 7-53, 7-54 and 7-55 yield an expression to determine the radial damage density based on the axial and radial viscofracture strains as well as the axial damage density, which is shown as follows:

$$\xi_2 = \frac{\left(1+\varepsilon_2^{vf}\right)^2\left(1-\varepsilon_1^{vf}\right)-1}{\sqrt{\xi_1}} \tag{7-56}$$

Figure 7-12 shows the axial and radial damage densities for an asphalt mixture with a 4% air void content and Figure 7-13 shows the axial and radial damage densities for an asphalt mixture with a 7% air void content. It can be concluded that the asphalt mixture with 4% air void content has a higher radial damage density and a lower axial damage density while the asphalt mixture with 7% air void content has a lower radial damage density and a higher axial damage density. The same conclusion is found for all of the tested asphalt mixtures that vary by two binders (Valero, NuStar), two air void contents (4%, 7%) and three aging periods (0, 3, 6-month 60 ℃ aged).

In fact, the asphalt mixture with the 4% air void content is stiffer than the asphalt mixture with the 7% air void content and has more axial cracks during fracture, which is called brittle fracture and has a splitting cracking mode. The axial cracks have a larger projection area on the circumferential surface, which yields a higher radial damage density. In contrast, the asphalt mixture with the 7% air void content is relatively soft and tends to have a ductile fracture and has a diagonal cracking mode. The cracks grow along the diagonal plane that is the plane of the maximum shear stress, which yields a larger projection area on the horizontal cross section and eventually causes a higher axial damage density.

Based on the axial and radial damage density curves, the evolution of the viscofracture in compression for different asphalt mixtures can be characterized by using a pseudo J-integral Paris' law in terms of damage density, which is illustrated in the next section.

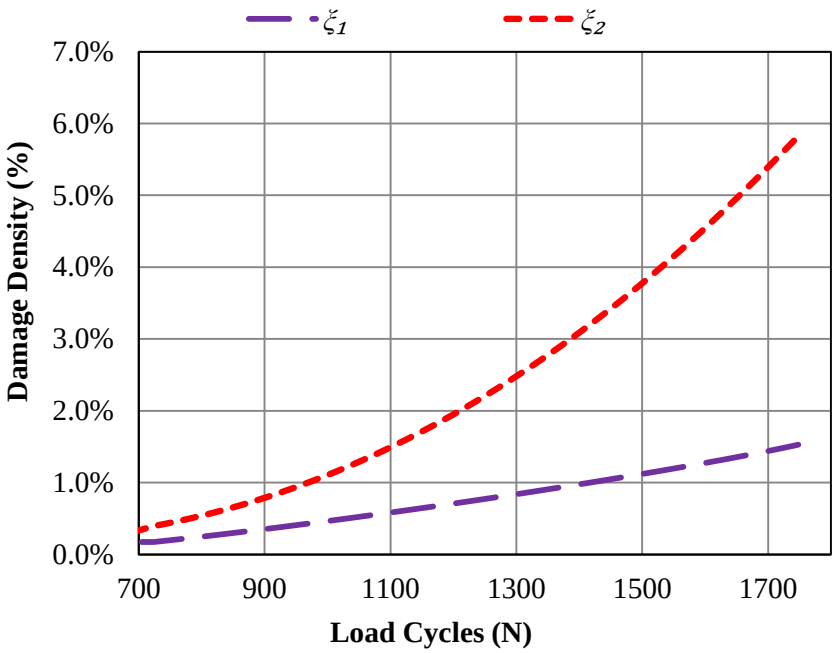

Figure 7-12 Damage densities for an asphalt mixture with 4% air void

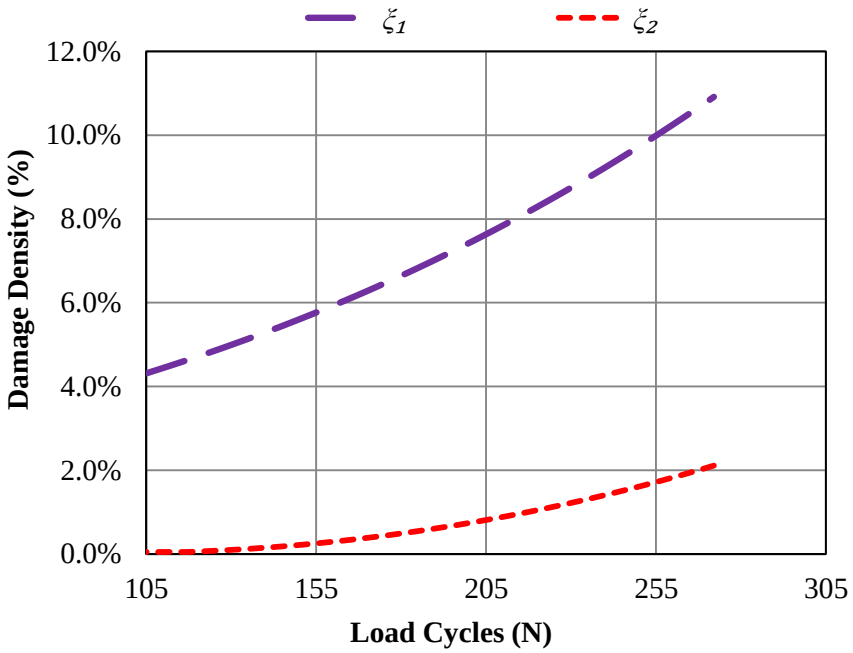

Figure 7-13 Damage densities for an asphalt mixture with 7% air void

ANISOTROPIC PSEUDO J-INTEGRAL PARIS' LAW

The pseudo J-integral Paris' law had been widely employed to characterize the fatigue damage and moisture damage of the asphalt mixtures and was proved to be capable of capturing the fracture properties of the materials (Si et al. 2002; Cleveland et al. 2003; Arambula et al. 2007; Castelo Branco et al. 2008; Masad et al. 2008a). The pseudo J-integral Paris' law is also used in this chapter to model the viscofracture evolution of the asphalt mixtures under a repeated compressive load during the tertiary stage.

The reason for using the pseudo J-integral Paris' law is firstly discussed as follows. As we know, the conventional Paris' law is expressed as (Paris and Erdogan 1963):

$$\frac{dc}{dt} = A\left(\Delta K\right)^n \tag{7-57}$$

where c is the crack size; t is time; ΔK is the amplitude of the stress intensity factor under a repeated load; A and n are parameters determined by experiments. The conventional Paris' law is normally employed in the characterization of the fatigue and fracture of the metallic materials (Beden et al. 2009). To characterize crack propagation of the ductile and viscoelastic materials, the pseudo J-integral is used to replace the stress intensity factor in the function, where the pseudo J-integral is defined as (Schapery 1984; Kuai et al. 2009):

$$J_R = \int_0^t D(t-s)\frac{\partial K^2}{\partial s} ds \tag{7-58}$$

where $D(t)$ is the creep compliance, s is the current time before time t. J_R is temperature dependent because of the temperature dependence of the creep compliance. To account for the temperature effect, a reduced time ($\psi(t) = \int_0^t \frac{ds}{a_T}$) can be employed in Equation 7-58, in which a_T is the time-temperature shift factor. The advantage of using the pseudo J-integral is that the temperature effect on the fracture development can be taken into account by the pseudo J-integral. Then the model coefficients A and n are independent of the testing temperature and become the material constants. Thus one testing temperature is sufficient to determine the two material properties in the pseudo J-integral Paris' law.

Under a destructive compressive load, it is common that hundreds and thousands of microcracks and macrocracks are widely and randomly distributed in the asphalt mixture. Thus it is neither convenient nor reasonable to use one single crack size in the formulation of the pseudo J-integral Paris' law. Instead of using crack size as in the conventional Paris' law, the damage density which represents the overall viscofracture property of the asphalt mixture is implemented in the pseudo J-integral Paris' law. The model is expressed as:

$$\frac{d\xi_i}{dN} = A_i \left(J_{Ri} \right)^{n_i} \qquad i = 1, 2 \tag{7-59}$$

where ξ_i is the anisotropic damage density; A_i and n_i are coefficients of Paris' law that are material constants, where A_i indicates the initial evolution speed of the viscofracture in terms of damage density and n_i indicates the changing rate of the damage density evolution speed. J_{Ri} is the pseudo J-integral that can be calculated as:

$$J_{Ri} = \frac{\partial DPFSE^A}{\partial \left(c.s.a. \right)_i} = \frac{\partial DPFSE^A / \partial N}{\partial \left(c.s.a. \right)_i / \partial N} = \frac{\partial \left[\sigma_0^A \varepsilon_1^{vf} \left(N \right) \right] / \partial N}{\partial \left[2 A_i^T \xi_i \left(N \right) \right] / \partial N} \tag{7-60}$$

where Equations 6-9 and 7-30 are used. $\left(c.s.a. \right)_i$ is the crack surface area projected on a specific direction and $\left(c.s.a. \right)_i$ is determined as two times the lost area projection on the specific direction within the asphalt mixture. A_i^T is the total (apparent) area of the cross section in the specific direction. Substituting Equation 7-60 into Equation 7-59 and then integrating both sides of Equation 7-59 yields:

$$\xi_i \left(N \right) = \xi_{0i} + C_i \left[e^{D_i \left(N - N_f \right)} - 1 \right] \tag{7-61}$$

where ξ_{0i} is the damage density at the flow number in the specific direction and C_i and D_i are model parameters that can be expressed as:

$$\begin{cases} C_i = A_i^{\frac{1}{1+n_i}} \left(\dfrac{\theta_1 \sigma_0^A \varepsilon_0^{vf}}{2 A_i^T} \right)^{\frac{n_i}{1+n_i}} \left(\dfrac{1+n_i}{\theta_1 n_i} \right) \\ D_i = \dfrac{\theta_1 n_i}{1+n_i} \end{cases} \tag{7-62}$$

The damage density predicted using Equation 7-61 is also shown in Figure 7-10, which indicates that the Equation 7-61 predicts perfectly the damaged density that is calculated using

Equation 7-52 with a R^2 of 0.9997. Once the model parameters (C_i and D_i) are determined, the material constants in Paris' law can be determined as follows:

$$\begin{cases} A_i = \left(\dfrac{2A_0^T}{\theta_1 \sigma_0^A \varepsilon_0^{vf}} \right)^{n_i} \left(C_i D_i \right)^{1+n_i} \\ n_i = \dfrac{D_i}{\theta_1 - D_i} \end{cases} \tag{7-63}$$

By applying the above pseudo J-integral Paris' law to the separated viscofracture strain of the asphalt mixtures with different binder, air void content and aging periods, the damage density curves are obtained and the material constants in the pseudo J-integral Paris' law are determined. Figure 7-14 and Figure 7-15 show the viscofracture coefficients (A_i and n_i) of the axial and radial pseudo J-integral Paris' law for different asphalt mixtures, respectively.

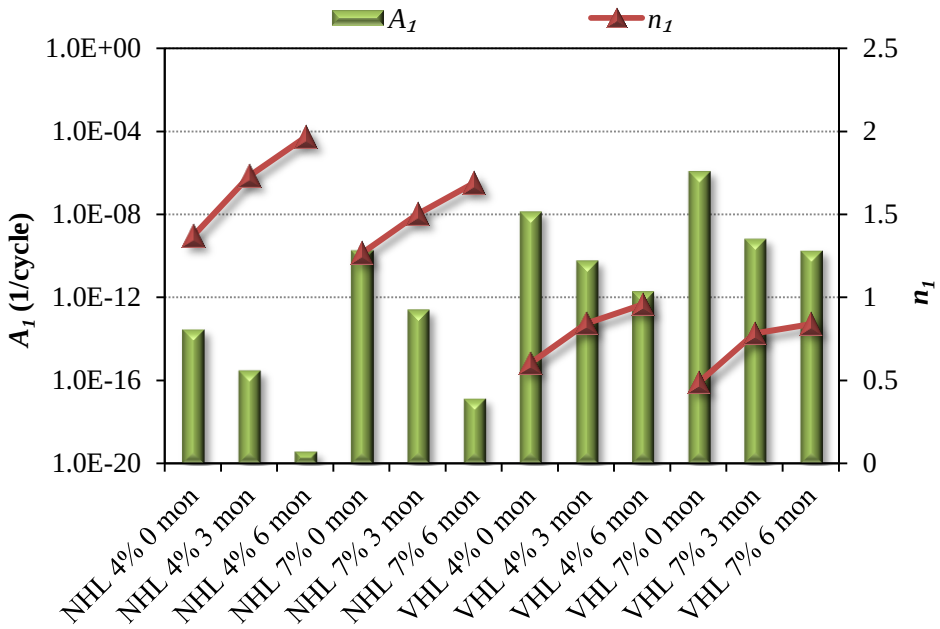

Figure 7-14 Viscofracture coefficients of axial pseudo J-integral Paris' law for different asphalt mixtures

It is found from Figure 7-14 that A_1 decreases and n_1 increases when the asphalt mixture become stiffer which might be caused by a stiffer binder, a lower air void content and a longer aging period. This observation complies with Schapery's viscoelastic fracture theory (Schapery 1975). Based on Schapery's theory, n_1 is inversely proportional to the slope of creep compliance, e.g. $n_1 = 1 + 1/m$, where m is slope of the creep compliance that is modeled by $D(t) = D_0 + D_2 t^m$. It is known that a stiffer asphalt mixture normally has a smaller value of m than the softer asphalt mixture. Thus a stiffer asphalt mixture has a relatively larger n_1 value, which is verified by the testing results of this study.

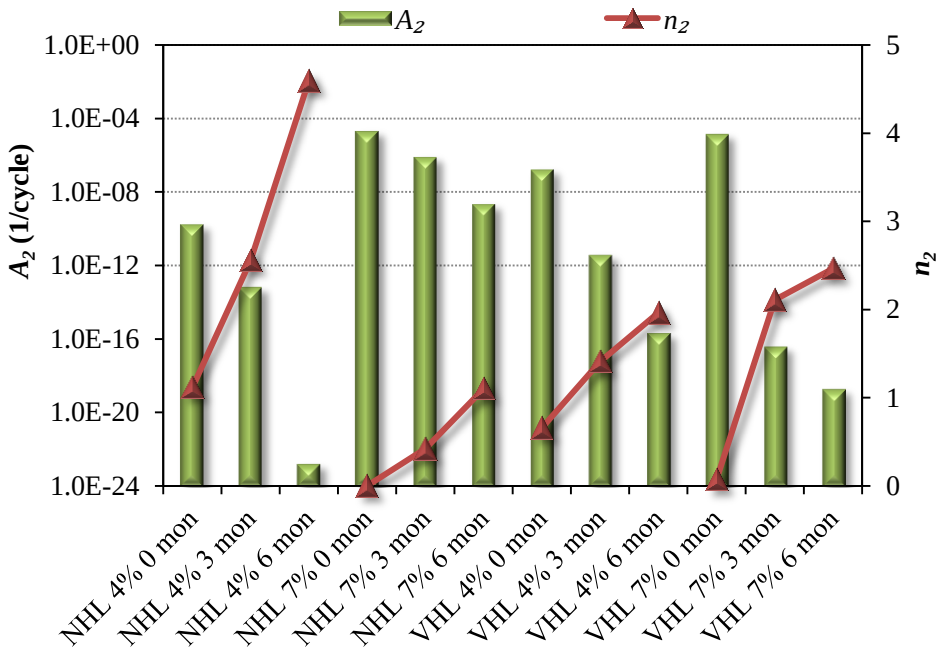

Figure 7-15 Viscofracture coefficients of radial pseudo J-integral Paris' law for different asphalt mixtures

It is found from Figure 7-15 that A_2 decreases and n_2 increases when the asphalt mixture become stiffer which is due to a longer aging period. However, the changes of A_2 and n_2 do not show a consistent laws (e.g., A_2 decreases and n_2 increases) when the asphalt mixture has a lower air void contents or uses a stiffer binder. More theoretical analysis and laboratory tests might be needed to investigate the factors that affect the values of A_2 and n_2 of the asphalt mixtures. In addition, Equation 7-63 indicates that A_i is strongly related to n_i. Based on the testing data in Figure 7-14 and Figure 7-15, relationships are found between $\log(A_i)$ and n_i with high values of coefficients of determination (R^2), which are shown in Figure 7-16.

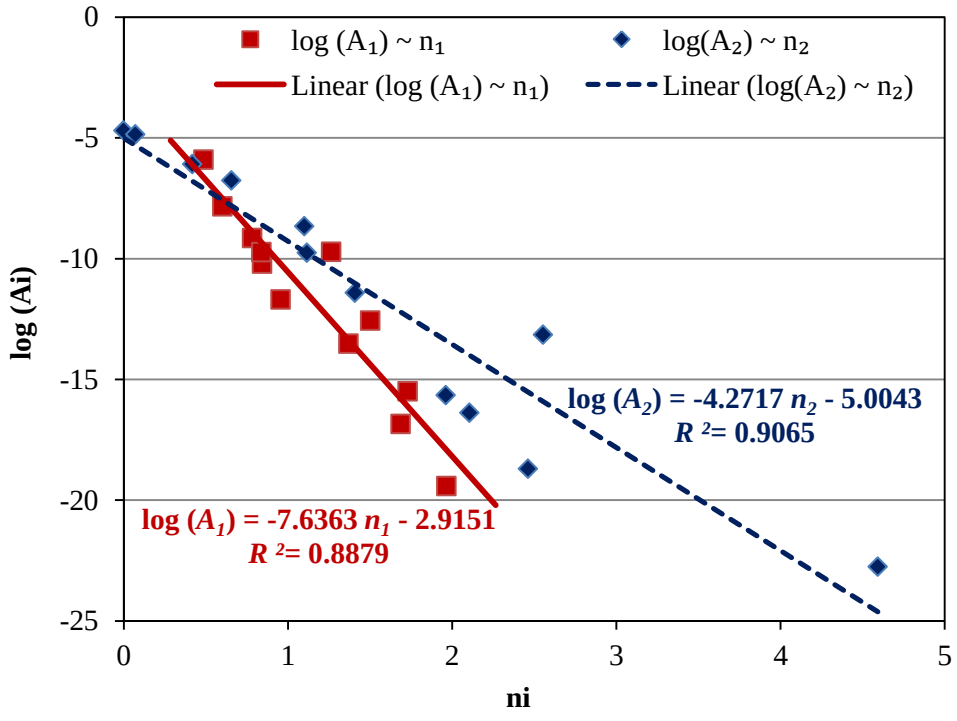

Figure 7-16 Relationships between A_i and n_i of pseudo J-integral Paris' law for asphalt mixtures

Once the material constants (A_i and n_i) are determined, the evolution of the damage densities due to a variety of apparent stress histories can be predicted by inputting the pseudo J-integral that is calculated based on the apparent stress history into the pseudo J-integral Paris' law. Then the evolution of the effective (true) stress corresponding to this apparent stress history can be determined using Equation 6-11. Finally, the viscofracture strain that is caused by this specific apparent stress history can be estimated by the constitutive relationship between the true stress and viscofracture strain, e.g. Equation 7-51. To calibrate the mechanistic model for the viscofracture characterization of the asphalt mixtures in compression, the destructive compressive tests using a variety of the forms of the load need to be performed on the asphalt mixtures and then the measured viscofracture strain is compared with the predicted value using the pseudo J-integral Paris law and the viscofracture constitutive relationship.

SUMMARIES AND CONCLUSIONS

The objectives of this chapter are to provide a mechanistic characterization method for the damage modeling of the asphalt mixtures in the tertiary stage and to provide a method to determine the anisotropic damage densities used in the effective stress during the viscoplastic modeling of the asphalt mixture. Based on the mechanistic analysis and the laboratory testing on the fracture properties of asphalt mixtures in compression, the following summaries and conclusions can be achieved:

1) The asphalt mixture does fracture in the tertiary stage under a destructive compressive load. The deformation caused by the formation and propagation of the cracks is viscofracture strain, which is signaled by the increase of the phase angle in the tertiary phase. The moment at which the cracks are initiated is recognized as the flow number or flow time that is the starting point of the tertiary stage.

2) Viscofracture strain is an anisotropic variable, in which the axial viscofracture strain can be obtained by conducting the strain decomposition of the total measured axial strain based on extended elastic-viscoelastic correspondence principle, which has been presented in Chapter IV. The radial strain decomposition is proposed in this chapter based on a generalized elastic-viscoelastic correspondence principle. The axial and radial strain decompositions demonstrate that the viscoplastic strains increase with a decreasing strain rate while the viscofracture strains increase with load cycles at an increasing strain rate, which implies that the viscofracture deformation contributes significantly to the permanent deformation in the tertiary stage.
3) The asphalt mixture with 4% air void content has more axial cracks during viscofracture, which is brittle fracture and has a splitting cracking mode. The axial cracks have a larger projection area on the circumferential surface, which yields a higher radial damage density. In contrast, the asphalt mixture with 7% air void content is relatively soft and tends to have a ductile fracture and a diagonal cracking mode. The cracks grow along a diagonal plane that is the plane of the maximum shear stress, which yields a larger projection area on the horizontal plane and eventually causes a higher axial damage density.
4) The viscofracture properties of an asphalt mixture in compression are characterized by the anisotropic damage densities and true stress. The axial damaged density and true stress are determined by employing the dissipated pseudo strain energy balance principle. The radial damage density is determined based on a geometric analysis of the cracking mode in compression. Both damage densities and true stress increase with load cycles, which indicates that the extra plastic strain is produced by the increase of true

stress. Therefore the permanent deformation is accelerated by the occurrence of cracks in the tertiary stage.

5) Anisotropic Pseudo J-integral Paris' laws in terms of damage densities are employed to accurately characterize the evolution of the viscofracture of the asphalt mixtures in compression. The material constants in the Paris' law are determined, which are temperature independent and can be employed to predict the fracture properties of the asphalt mixtures in compression.

CHAPTER VIII

SUMMARIES, CONCLUSIONS AND RECOMMENDATIONS

Permanent deformation (or rutting) is one of the major distresses on asphalt pavements and it not only increases the road roughness but traps water and leads to wet-weather accidents due to loss of tire-pavement friction and hydroplaning. However, the mechanisms of rutting have not been well addressed due to the complexity of the asphalt concrete which behaves significantly differently under a compressive load than under a tensile load. Thus, to demonstrate the mechanisms of rutting, it is crucial to investigate the fundamental material behaviors of the asphalt concrete in compression.

SUMMARIES AND CONCLUSIONS

This study addresses the characterization of the fundamental mechanisms of the permanent deformation of an asphalt mixture when it is subjected to a compressive load. The criteria that are followed during the characterization include:

1) Comprehensive and complete characterization of the material properties of the asphalt mixture including anisotropy, viscoelasticity, viscoplasticity and viscofracture.
2) Fundamental mechanistic characterization models and data analysis methods.
3) Relating model coefficients to understandable engineering parameters with physical meaning.
4) Simple, fast and accurate testing protocol design based on affordable and accessible testing equipment.

The comprehensive characterization of asphalt concrete in compression was accomplished by constitutively modeling the anisotropy and viscoelasticity of the undamaged asphalt mixture, and the viscoplasticity and viscofracture of the damaged asphalt mixture.

Chapter II presented the characterization of the anisotropic viscoelasticity of the undamaged asphalt mixture based on anisotropic linear viscoelastic theory. Three simple nondestructive creep tests were developed and master curve models were proposed to determine the magnitudes and phase angles of the anisotropic complex moduli and complex Poisson's ratio. The test results indicate that asphalt mixtures have significantly different tensile properties from compressive properties. The vertical modulus of the undamaged asphalt mixtures is 1.2 to 2 times as large as the horizontal modulus, which demonstrates distinctively the inherent anisotropy of the asphalt mixture in compression.

In Chapter III, the inherent anisotropy was characterized based on the microstructure of the asphalt mixture. The inherent anisotropy was indicated to be caused by the preferentially oriented aggregates and was characterized by a microstructural parameter, the modified vector magnitude. A lateral surface scanning test was designed to obtain the microstructural properties including orientation, size and shape of the fine and coarse aggregates which can be used to calculate the modified vector magnitude. A relationship was derived to physically relate the modified vector magnitude to the macroscopic material properties, i.e. anisotropic modulus ratio, of the asphalt mixture.

In Chapter IV, an effective and efficient strain decomposition technique was developed by employing the pseudostrain concept and the extended elastic-viscoelastic correspondence principle. The viscoplasticity and viscofracture were separated from the viscoelasticity so that the permanent deformation and fracture of the asphalt mixtures in compression can be individually and accurately characterized without the influence of the viscoelastic responses. The

viscoplasticity developed in the primary, secondary and tertiary deformation stage of the asphalt mixture, whereas the viscofracture of the mixture occurred only in the tertiary stage and was demonstrated to be caused by the growth of cracks which is signaled principally by the increase of the phase angle.

Chapter V presented the development of a comprehensive viscoplastic yield surface model (the ZLL yield surface) which was capable of completely characterizing the fundamental material properties of the asphalt mixture including: 1) distinctions between compression, extension and tension; 2) dilative volumetric change; 3) internal friction and cohesion; 4) rate and temperature dependence; 5) strain hardening; and 6) convexity and smoothness of the yield surface. A stress-pseudostrain method was proposed to accurately determine the yield surface model parameters which were also related to the engineering material properties such as cohesion and internal friction angle.

In Chapter VI, the permanent deformation (rutting) of the asphalt concrete was intensively characterized by an extended Perzyna's anisotropic viscoplastic model which incorporated 1) a modified effective stress in the formulation of the models to account for both the inherent anisotropy due to the aggregates' orientation and the stress-induced anisotropy caused by the crack growth; 2) an extended ZLL yield surface to provide a smooth and convex yield surface and to address the cohesion and internal friction of the material; 3) a non-associated flow rule for the viscoplastic potential to address the volumetric dilation of the asphalt mixture; and 4) a temperature and strain rate dependent strain hardening function. The slope of the viscoplastic potential surface was found to be solely dependent on the inherent anisotropy of the asphalt mixtures. The permanent deformation of the asphalt pavement would be underestimated if the inherent anisotropy was not included in the viscoplastic modeling of the asphalt mixture.

Chapter VII provided a mechanistic characterization method for the anisotropic viscofracture of the asphalt mixtures in the tertiary stage and determined the anisotropic damage densities. Axial and radial strain decompositions were conducted by proposing a generalized elastic-viscoelastic correspondence principle. Then the separated axial and radial viscofracture strains were employed to achieve the anisotropic damage densities based on dissipated pseudo strain energy balance principle and the geometric analysis of the cracks in compression. The evolutions of the anisotropic viscofracture were modeled by the Pseudo J-integral Paris' laws in terms of damage densities. Testing results indicated that the viscofracture deformation contributed significantly to the permanent deformation in the tertiary stage and the viscoplastic deformation was also accelerated by the occurrence of cracks in the tertiary stage. The asphalt mixture with a low air void (i.e., 4%) has a brittle-like fracture which is a splitting cracking mode; whereas, the asphalt mixture a high air void (i.e., 7%) has a ductile-like fracture which is a diagonal cracking mode.

In order to describe a complete and clear map for the characterization of the asphalt mixture in compression, Table 8-1 summarizes the material properties, model parameters, testing protocols, testing measurements and contents in corresponding chapters of this study. The measured results for the material properties and model parameters of the VHL and NHL asphalt mixtures at two different air void contents and three aging periods are collected from the individual chapter and summarized in Table 8-2 and Table 8-3. The Table 8-2 shows the measured results of the inherent anisotropy, viscoelasticity and viscofracture properties of the asphalt mixtures while the Table 8-3 shows the measured results of the viscoplasticity properties of the asphalt mixtures.

Table 8-1 Summary of Material Properties, Parameters, Testing Protocols and Chapter Contents in the Characterization of Asphalt Mixtures in Compression

Material Properties		Material Parameters		Testing Protocols	Data for Parameter Determination	Chapters
		Symbol	Physical Meaning			
Nondestructive Properties	Viscoelasticity	$E(t)$ E_Y	Relaxation and Young's Modulus	Uniaxial Compressive Creep Tests (UCC)	Creep Strain	Chapters II and IV
		α_T	Time-Temperature Shift Factor			
		$\lvert E^* \rvert$	Magnitude of Dynamic Modulus	Nondestructive Dynamic Modulus Test (NDM)	Dynamic Strain and Stress	
		δ, φ_{II}	Phase Angle of Dynamic Modulus			
	Inherent Anisotropy	Δ'	Modified Vector Magnitude	Lateral Surface Scanning Tests	Aggregate Size, Area, Aspect Ratio	Chapter III
Destructive Properties	Viscoplastic Yield Surface	α , ϕ	Slope, Internal Friction Angle	Uniaxial/Triaxial Compressive Strength Tests (UCS/TCS)	Initial yield Strength	Chapter V
		κ_0 , C	Intercept, Cohesion			
		d	Yield Extension Ratio			
	Strain Hardening Function	κ_1	Strain Hardening Amplitude		Yield Stresses during Strain Hardening	
		κ_2	Strain Hardening Rate			
	Temperature and Strain Rate Dependence	a_T , ΔE_T	Temperature Effect Factor	UCS at Different Temperatures	Ultimate Yield Strength	
		$a_{\dot{\varepsilon}}$, κ_3	Strain Rate Effect Factor	UCS at Different Strain Rates or DDM tests	Ultimate Yield Strength or Viscoplastic Strain	
	Viscoplastic Potential Function	β	Slope of Viscoplastic Potential	N/A	Δ'	Chapters V and VI
	Perzyna's Viscoplasticity	Γ	Viscosity Parameter	Destructive Dynamic Modulus Tests (DDM)	Separated Viscoplastic Strain	Chapters IV and VI
		N	Rate Parameter			
	Viscofracture Damage Density Function	ξ_{ij}	Anisotropic Damage Density		Separated Viscofracture Strain (in Tertiary Stage)	Chapters IV and VII
		A_i, n_i	Coefficients in Paris' Law			
		N_f, η	Flow Number, Crack Speed Index			

Table 8-2 Measured Results of the Inherent Anisotropy, Viscoelasticity and Viscofracture Properties for the VHL and NHL Asphalt Mixtures

Material Properties			Inherent Anisotropy	Viscoelasticity				Viscofracture					
Physical Meaning			Modified Vector Magnitude	Young's Modulus	Dynamic Moudlus	Phase Angle	Phase Angle in Phase II	Flow Number	Crack Speed Index	Paris' Law's Coefficients for Axial Damage Density		Paris' Law's Coefficients for Radial Damage Density	
Asphalt Mixtures			Δ'	E_Y	$\|E^*\|$	δ	φ_{II}	Nf	η	A_1	n_1	A_2	n_2
Binder	Air Void	Aging Months	N/A	MPa	MPa	degrees	degrees	cycles	με/cycle	1/cycle	N/A	1/cycle	N/A
NHL PG64-16	4%	0	0.3106	656	1513	31.7	20.4	824	0.580	3.04E-14	1.369	1.75E-10	1.115
		3	0.3354	1108	2015	28.9	20.3	1153	0.036	3.19E-16	1.731	7.05E-14	2.555
		6	0.3880	1670	3435	26.5	21.6	3156	0.012	3.79E-20	1.965	1.75E-23	4.593
	7%	0	0.3471	455	502	33.1	21.4	37	21.231	1.90E-10	1.265	2.02E-05	0.000
		3	0.3998	906	1438	30.2	24.1	435	0.919	2.71E-13	1.502	8.12E-07	0.419
		6	0.4088	1352	2072	28.5	21.2	1718	0.045	1.42E-17	1.688	2.21E-09	1.100
VHL PG67-22	4%	0	0.3131	759	1531	36.8	25.1	282	0.625	1.44E-08	0.602	1.71E-07	0.657
		3	0.4422	1354	3093	32.1	23.3	1050	0.156	6.18E-11	0.843	3.88E-12	1.409
		6	0.3907	1575	3268	30.6	24.2	1650	0.046	2.02E-12	0.956	2.22E-16	1.963
	7%	0	0.3114	540	998	36.7	20.3	119	2.169	1.23E-06	0.486	1.39E-05	0.071
		3	0.4478	1019	2181	34.4	23.9	375	0.664	6.99E-10	0.782	4.10E-17	2.107
		6	0.4060	1099	2407	32.2	24.7	713	0.517	1.87E-10	0.839	2.01E-19	2.464

Table 8-3 Measured Results of Viscoplasticity Properties for the VHL and NHL Asphalt Mixtures

Material Properties			Viscoplasticity											
Physical Meaning			Perzyna's Coefficients		Initial Yield Strength	Cohesion	Internal Friction Angle	Slope of Yield Surface	Intercept of Yield Surface	Coefficients of Strain Hardening		Rate Coefficient	Extension Ratio	Slope of Plastic Potential
Asphalt Mixtures			Γ	N	σ_Y	C	φ	α	κ_0	κ_1	κ_2	κ_3	d	β
Binder	Air Void	Aging Months	1/sec	N/A	kPa	kPa	Degrees	N/A	kPa	kPa	1/με	N/A	N/A	N/A
NHL PG64-16	4%	0	1.30E-07	1.71	675.3	143.6	46.8	0.370	150.8	75.0	0.0031	0.23	0.61	0.17
		3	9.12E-08	1.71	1194.4	227.3	48.9	0.382	241.5	111.0	0.0110	0.30	0.60	0.19
		6	2.31E-08	1.77	1486.9	302.5	45.9	0.363	319.6	148.6	0.0064	0.29	0.61	0.22
	7%	0	2.53E-07	1.59	566.0	119.8	43.0	0.340	131.0	72.0	0.0116	0.26	0.63	0.19
		3	1.52E-07	1.90	731.6	164.8	44.4	0.350	179.4	91.4	0.0093	0.31	0.62	0.22
		6	8.90E-08	1.90	990.1	203.9	44.8	0.354	218.4	107.8	0.0044	0.24	0.62	0.23
VHL PG67-22	4%	0	2.20E-07	1.82	835.3	191.9	43.1	0.339	211.7	75.9	0.0083	0.37	0.63	0.17
		3	8.23E-08	1.66	1451.2	307.6	45.0	0.351	339.9	152.5	0.0049	0.37	0.62	0.25
		6	4.55E-08	1.64	1560.6	328.1	45.7	0.361	349.4	154.9	0.0052	0.34	0.61	0.22
	7%	0	4.50E-07	2.10	419.1	93.9	44.1	0.349	101.5	63.9	0.0080	0.35	0.62	0.17
		3	1.32E-07	1.69	824.3	190.0	42.9	0.338	209.7	102.8	0.0066	0.32	0.63	0.25
		6	8.70E-08	1.79	1009.8	238.0	41.5	0.326	266.7	130.9	0.0035	0.35	0.64	0.23

The testing methods proposed in study (see Table 8-1) are very effective and efficient for the determination of the model parameters and material properties. A brief review of the efficiency of each characterizing test is shown as follows:

1) Inherent Anisotropy: the lateral surface scanning tests utilizes a portable scanner and a rotating device to obtain the image of the aggregates with a high resolution and can be finished within 5 minutes;
2) Viscoelasticity: nondestructive uniaxial compressive creep (UCC) tests can be accomplished in any common material testing machine that can provide a constant axial load and record the axial deformation. This test can also be finished within 5 minutes;
3) Viscoplasticity (Yielding and strain hardening): the UCS test is performed on the same machine as the UCC test with the same testing configuration. TCS needs a triaxial cell or RaTT cell; however, as discussed in Chapter V, the TCS test can be replaced by the indirect tensile strength test which only requires the same testing machine as the UCC test. Each of the strength tests can be finished within 5 minutes.
4) Viscoplasticity (Perzyna's viscosity) and Viscofracture: the NDM and DDM tests are uniaxial tests and they can be performed on any common material testing machine that can provide a sinusoidal repeated axial load and record the axial and radial deformation. The NDM tests need about 15 minutes and the DDM can be finished within 2 hours for most of the asphalt mixtures at relatively high temperature (e.g., $\geq$40°C).

To account for the temperature effect on the material properties, the aforementioned tests such as the UCC tests, UCS tests and DDM tests might need to be performed at several different temperatures. To reach the equilibrium temperature, it is common to take two or three hours to change from one temperature to another. In summary, by using the mechanistic models and testing protocol proposed in this study, it is possible to characterize one type of the asphalt

mixture in compression and obtain all the material properties and model parameters within one day. The constitutive models developed for the characterization of asphalt concrete in compression can be effectively implemented for the rutting prediction of the asphalt pavements under a variety of traffic, structural, and environmental conditions.

RECOMMENDATIONS

This study is focused on the fundamentally mechanistic modeling of the asphalt mixture in compression. Some characterization models and testing protocols were proposed and the critical material properties associated with permanent deformation were obtained for limited asphalt mixture specimens. The work done in this study is a first and basic step to a successful prediction of the field performance of the asphalt pavements. More studies are recommended as continuations of this study:

First, the mechanistic models proposed in this study are in an urgent need to be implemented in the performance prediction of the asphalt pavements. A necessary step toward performance prediction is to formulate the evolutionary rules which are used in the numerical finite and boundary element predictions of pavement distresses. This can be done by using the material characteristics and constitutive models for permanent deformation and fracture that have been developed in this dissertation. Thus, more work can be done in the prediction of the field performance of the asphalt pavements at different traffic loads, environmental conditions and pavement structures. Comparisons between the predictions and field measurements are also very necessary to evaluate the accuracy of the constitutive models.

Second, the yield criterion on the octahedral plane of the newly developed ZLL yield surface model in this study was derived based on the model and testing data of geomaterials. Even though the asphalt mixture is one of the geomaterials, the validation of the ZLL yield

surface on the octahedral plane still need to be performed on the asphalt mixtures by conducting the yield strength tests at different octahedral shear stress paths.

Third, a microstructural study by using more advanced techniques such as X-ray CT might be performed on the investigations of the initiation of the microcracks and the propagation of the macrocracks of the asphalt mixtures when it is subjected to a destructive compressive load. The direct observation of the cracks in compression can be utilized to validate the theoretical viscofracture characterization results in this study.

Fourth, because these test protocols produce measured material properties, a systematic program of measuring and cataloging the properties of the most commonly used mixture properties can now be initiated. Once it is developed and available to the pavement designers, this catalog will make the process of mixture design and performance prediction much more efficient.

Fifth, these testing protocols being simple, rapid and efficient can now be used to measure the effects of moisture vapor, healing, additives and modifiers on the properties of commonly used asphalt mixtures. The characteristics of the warm mix asphalt mixture can now be compared objectively with the same properties of the hot mix asphalt mixtures.

Sixth, a large number of replicate samples needs to be tested in order to determine precision, bias and variances of the test results. These individual test results may then be used to predict pavement life cycles to determine their expected values and variances. This is an essential step toward using these fundamental test methods in design. Furthermore, these test protocols and analysis methods can be the basis of test process specifications that will eventually be adopted by American Association of State Highway and Transportation Officials (AASHTO) and American Society for Testing and Materials (ASTM). This is a lengthy process but one that can and need to be initiated.

REFERENCES

ABAQUS (2010). *User's and theory manuals*, Hibbit, Karlsson & Sorensen Inc., Pawtucket, Rhode Island.

Abdulshafi, A., and Majidzadeh, K. (1984). "Combo viscoelastic-pastic modeling and rutting of asphalt mixtures." *Transportation Research Record: Journal of the Transportation Research Board*, No. 968, Transportation Research Board of the National Academies, Washington, D.C., 19-31.

Abu Al-Rub, R. K., Darabi, M. K., Huang, C.-W., Masad, E. A., and Little, D. N. (2012). "Comparing finite element and constitutive modelling techniques for predicting rutting of asphalt pavements." *International Journal of Pavement Engineering*, 13(4), 322-338.

Abu Al-Rub, R. K., Darabi, M. K., Little, D. N., and Masad, E. A. (2010). "A micro-damage healing model that improves prediction of fatigue life in asphalt mixes." *International Journal of Engineering Science*, 48(11), 966-990.

Adu-Osei, A. (2000). "Characterization of unbound granular layers in flexible pavements." Ph.D. Dissertation, Texas A&M University, College Station, Texas.

Arambula, E., Masad, E., and Martin, A. (2007). "Moisture susceptibility of asphalt mixtures with known field performance: Evaluated with dynamic analysis and crack growth model." *Transportation Research Record: Journal of the Transportation Research Board*, No. 2001, Transportation Research Board of the National Academies, Washington, DC., 20-28.

Argyris, J. H., Faust, G., Szimmat, J., Warnke, E. P., and Willam, K. J. (1974). "Recent developments in the finite element analysis of prestressed concrete reactor vessels." *Nuclear Engineering and Design*, 28(1), 42-75.

Ashtiani, R. S. (2009). "Anisotropic characterization and performance prediction of chemically and hydraulically bounded pavement foundations." Ph.D. Dissertation, Texas A&M University, College Station, Texas.

Bahia, H. U., Hason, D. I., Zeng, M., Zhai, H., HKhatri, M. A., and Anderson, R. M. (2001). "Characterization of modified asphalt binders in suprepave mix design, report 459." National Cooperative Highway Research Program (NCHRP), Transportation Research Board of the National Academies, Washington, D.C.

Bahuguna, S., Panoskaltsis, V. P., and Papoulia, K. D. (2006). "Identification and modeling of permanent deformations of asphalt concrete." *Journal of Engineering Mechanics*, 132(3), 231-239.

Bardet, J. P. (1990). "Lode dependences for isotropic pressure-sensitive elastoplastic materials." *Journal of Applied Mechanics*, 57(3), 498-506.

Bausano, J., and Williams, R. C. (2010). "Energy-based approach for determining flow number." *Journal of Testing and Evaluation*, 38(1), 1-8.

Beden, S. M., Abdullah, S., and Ariffin, A. K. (2009). "Review of fatigue crack propagation models for metallic components." *European Journal of Scientific Research*, 28(3), 364-397.

Bigoni, D., and Piccolroaz, A. (2004). "Yield criteria for quasibrittle and frictional materials." *International Journal of Solids and Structures*, 41(11), 2855-2878.

Biligiri, K. P., Kaloush, K., and Uzan, J. (2010). "Evaluation of asphalt mixtures' viscoelastic properties using phase angle relationships." *International Journal of Pavement Engineering*, 11(2), 143-152.

Biligiri, K. P., Kaloush, K. E., Mamlouk, M. S., and Witczak, M. W. (2007). "Rational modeling of tertiary flow for asphalt mixtures." *Transportation Research Record: Journal of the Transportation Research Board*, No. 2001, Transportation Research Board of the National Academies, Washington, DC, 63-72.

Birgisson, B., Soranakom, C., Napier, J., and Roque, R. (2003). "Simulation of fracture initiation in hot-mix asphalt mixtures." *Transportation Research Record: Journal of the Transportation Research Board*, No. 1849, Transportation Research Board of the National Academies, Washington, DC., 183-190.

Bonaquist, R., and Witczak, M. (1996). "Plasticity modeling applied to the permanent deformation response of granular materials in flexible pavement systems." *Transportation Research Record: Journal of the Transportation Research Board*, No. 1540, Transportation Research Board of the National Academies, Washington, D.C., 7-14.

Castelo Branco, V., Masad, E., Bhasin, A., and Little, D. (2008). "Fatigue analysis of asphalt mixtures independent of mode of loading." *Transportation Research Record: Journal of the Transportation Research Board*, No. 2057, Transportation Research Board of the National Academies, Washington, DC., 149-156.

Chaboche, J. L. (1987). "Continuum damage mechanics: Present state and future trends." *Nuclear Engineering and Design*, 105(1), 19-33.

Chehab, G. R., Kim, Y. R., Schapery, R. A., Witczak, M. W., and Bonquist, R. (2003). "Characterization of asphalt concrete in uniaxial tension using a

viscoelastoplastic continuum damage model." *Journal of the Association of Asphalt Paving Technologists*, 72, 315-355.

Chen, W. F., and Han, D. J. (1988). *Plasticity for structural engineers*, Springer, New York.

Chen, W. F., and Mizuno, E. (1990). *Nonlinear analysis in soil mechanics, theory and implementation*, Elsevier Science Ltd., Amsterdam, The Netherlands.

Christensen, D. W., Bonaquist, R., Anderson, D. A., and Gokhale, S. (2004). "Indirect tension strength as a simple performance test." *New Simple Performance Tests for Asphalt Mixes*, E-Circular, Transportation Research Board of The National Academies, Washington, DC, 44-57.

Christensen, R. M. (2003). *Theory of viscoelasticity*, Dover Publications, Inc., Mineola, New York.

Christensen, R. M. (2005). *Mechanics of composite materials*, Dover Publications, Inc., Mineola, New York.

Cleveland, G., Lytton, R., and Button, J. (2003). "Using pseudostrain damage theory to characterize reinforcing benefits of geosynthetic materials in asphalt concrete overlays." *Transportation Research Record: Journal of the Transportation Research Board*, No. 1849, Transportation Research Board of the National Academies, Washington, DC., 202-211.

Collop, A. C., Scarpas, A., Kasbergen, C., and De Bondt, A. (2003). "Development and finite element implementation of stress-dependent elastoviscoplastic constitutive model with damage for asphalt." *Transportation Research Record: Journal of the Transportation Research Board*, No. 1832, Transportation Research Board of the National Academies, Washington, D.C., 96-104.

Cowin, S. C. (1985). "The relationship between the elasticity tensor and the fabric tensor." *Mechanics of Materials*, 4(2), 137-147.

Curray, J. R. (1956). "Analysis of two-dimensional orientation data." *Journal of Geology*, 64(2), 117-131.

Dafalias, Y. F., Papadimitriou, A. G., and Li, X. S. (2004). "Sand plasticity model accounting for inherent fabric anisotropy." *Journal of Engineering Mechanics*, 130(11), 1319-1333.

Darabi, M. K., Abu Al-Rub, R. K., Masad, E. A., Huang, C.-W., and Little, D. N. (2011). "A thermo-viscoelastic-viscoplastic-viscodamage constitutive model for

asphaltic materials." *International Journal of Solids and Structures*, 48(1), 191-207.

Desai, C. S., Somasundaram, S., and Frantziskonis, G. (1986). "A hierarchical approach for constitutive modelling of geologic materials." *International Journal for Numerical and Analytical Methods in Geomechanics*, 10(3), 225-257.

Dessouky, S., Masad, E., and Little, D. (2006). "Mechanistic modeling of permanent deformation in asphalt mixes with the effect of aggregate characteristics." *Journal of the Association of Asphalt Paving Technologists*, 75, 535-576.

Dessouky, S. H. (2005). "Multiscale approach for modeling hot mix asphalt." Ph.D. Dissertation, Texas A&M University, College Station, Texas.

Dessouky, S. H., and Masad, E. A. (2006). "The development of a microstructural-based continuum model for hot mix asphalt." *Proc. of Asphalt Concrete: Simulation, Modeling, and Experimental Characterization*, Baton Rouge, LA, United States, 44-52.

Di Benedetto, H., Delaporte, B., and Sauzeat, C. (2007a). "Three-dimensional linear behavior of bituminous materials: Experiments and modeling." *International Journal of Geomechanics*, 7(2), 149-157.

Di Benedetto, H., Mondher, N., Sauzéat, C., and Olard, F. (2007b). "Three-dimensional thermo-viscoplastic behaviour of bituminous materials: The DBN model." *Road Materials and Pavement Design*, 8(2), 285-315.

Ding, H., Chen, W., and Zhang, L. (2006). *Elasticity of transversely isotropic materials*, Springer, Dordrecht, The Netherlands.

Drescher, A., Kim, J. R., and Newcomb, D. E. (1993). "Permanent deformation in asphalt concrete." *Journal of Materials in Civil Engineering*, 5(1), 112-128.

Drucker, D. C. (1959). "A definition of stable inelastic material." *Journal of Applied Mechanics*, 26(3), 101-106.

Dyskin, A. V., Sahouryeh, E., Jewell, R. J., Joer, H., and Ustinov, K. B. (2003). "Influence of shape and locations of initial 3-d cracks on their growth in uniaxial compression." *Engineering Fracture Mechanics*, 70(15), 2115-2136.

Eberhardt, E., Stead, D., and Stimpson, B. (1999). "Quantifying progressive pre-peak brittle fracture damage in rock during uniaxial compression." *International Journal of Rock Mechanics and Mining Sciences*, 36(3), 361-380.

Findley, W. N., Lai, J. S., and Onaran, K. (1989). *Creep and relaxation of nonlinear viscoelastic materials with an introduction to linear viscoelasticity*, Dover Publication, Inc., Mineola, New York.

Florea, D. (1994a). "Associated elastic/viscoplastic model for bituminous concrete." *International Journal of Engineering Science*, 32(1), 79-86.

Florea, D. (1994b). "Nonassociated elastic viscopastic model for bituminous concrete." *International Journal of Engineering Science*, 32(1), 87-93.

Fwa, T. F., Tan, S. A., and Low, B. H. (1997). "Relating triaxial test properties of asphalt mixtures to mix parameters determined by marshall stability test." *Journal of Testing and Evaluation*, 25(5), 471-478.

Fwa, T. F., Tan, S. A., and Zhu, L. Y. (2004). "Rutting prediction of asphalt pavement layer using c-phi model." *Journal of Transportation Engineering*, 130(5), 675-683.

Gibson, N. H., Schwartz, C. W., Schapery, R. A., and Witczak, M. W. (2003). "Viscoelastic, viscoplastic, and damage modeling of asphalt concrete in unconfined compression." *Transportation Research Record: Journal of the Transportation Research Board*, No. 1860, Transportation Research Board of the National Academies, Washington, DC., 3-15.

Goh, S. W., and You, Z. (2009). "A simple stepwise method to determine and evaluate the initiation of tertiary flow for asphalt mixtures under dynamic creep test." *Construction and Building Materials*, 23(11), 3398-3405.

Hajj, E. Y., Siddharthan, R. V., Sebaaly, P. E., and Weitzel, D. (2007). "Laboratory-based unified permanent deformation model for hot-mix asphalt mixtures." *Journal of Testing and Evaluation*, 35(3), 272-280.

Haythornthwaite, R. M. (1985). "A family of smooth yield surfaces." *Mechanics Research Communications*, 12(2), 87-91.

Hoek, E., and Bieniawski, Z. T. (1965). "Brittle fracture propagation in rock under compression." *International Journal of Fracture Mechanics*, 1(3), 137-155.

Houque, E., and Tatsuoka, F. (1998). "Anisotropy in elastic deformation of granular materials." *Journal of the Japanese Geotechnical Society: Soils and Foundation*, 38(1), 163-179.

Huang, B., Mohammad, L., and Rasoulian, M. (2001). "Three-dimensional numerical simulation of asphalt pavement at Louisiana accelerated loading facility." *Transportation Research Record: Journal of the Transportation Research Board*,

No. 1764, Transportation Research Board of the National Academies, Washington, D.C., 44-58.

Huang, C.-W., Masad, E., Muliana, A. H., and Bahia, H. (2007). "Analysis of nonlinear viscoelastic properties of asphalt mixtures." *Symposium on Mechanics of Flexible Pavements at the 15th U.S. National Congress of Theoretical and Applied Mechanics*, American Society of Civil Engineers, Boulder, CO, United States, 64-72.

Huang, C. W., Abu Al-Rub, R. K., Masad, E. A., and Little, D. N. (2011). "Three-dimensional simulations of asphalt pavement permanent deformation using a nonlinear viscoelastic and viscoplastic model." *Journal of Materials in Civil Engineering*, 23(1), 56-68.

Huang, Y. H. (2004). *Pavement analysis and design*, Pearson Education, Inc., Upper Saddle River, New Jersey.

Jiang, J., and Pietruszczak, S. (1988). "Convexity of yield loci for pressure sensitive materials." *Computers and Geotechnics*, 5(1), 51-63.

Jones, R. D. (1993). "SHRP materials reference library: Asphalt cements: A concise data compilation." Strategic Highway Research Program, SHRP-A-645, National Research Council, Washington, D.C.

Kachanov, L. M. (1986). *Introduction to continuum damage mechanics*, Springer, LLC, New York, NY.

Kaloush, K. E., and Witczak, M. W. (2002). "Tertiary flow characteristics of asphalt mixtures." *Journal of the Association of Asphalt Paving Technologists*, 71, 248-280.

Khan, A. S., and Huang, S. (1995). *Continuum theory of plasiticity*, John Wiley & Sons, Inc., New York, NY.

Kim, S. H., Little, D., and Masad, E. (2005). "Simple methods to estimate inherent and stress-induced anisotropy of aggregate base." *Transportation Research Record: Journal of the Transportation Research Board*, No. 1913, Transportation Research Board of the National Academies, Washington, D.C., 24-31.

Kim, Y. R., Lee, Y. C., and Lee, H. J. (1995). "Correspondence principle for characterization of asphalt concrete." *Journal of Materials in Civil Engineering*, 7(1), 59-68.

Kim, Y. R., Seo, Y., King, M., and Momen, M. (2004). "Dynamic modulus testing of asphalt concrete in indirect tension mode." *Transportation Research Record:*

Journal of the Transportation Research Board, No. 1891, Transportation Research Board of the National Academies, Washington, D.C., 163-173.

Kuai, H., Lee, H., Zi, G., and Mun, S. (2009). "Application of generalized j-integral to crack propagation modeling of asphalt concrete under repeated loading." *Transportation Research Record: Journal of the Transportation Research Board*, No. 2127, Transportation Research Board of the National Academies, Washington, DC., 72-81.

Kutay, M. E., Gibson, N. H., and Youtcheff, J. (2008). "Use of pseudostress and pseudostrain concepts for characterization of asphalt fatigue tests." *Proc. of Pavement Cracking: Mechanisms, Modeling, Detection, Testing and Case Histories*, Chicago, IL, 305-314.

Kvasnak, A., Robinette, C. J., and Williams, R. C. (2007). "Statistical development of a flow number predictive equation for the mechanistic-empirical pavement design guide." *Transportation Research Board 86th Annual Meeting*, Transportation Research Board, National Research Council, Washington, D.C., Paper No. 07-1000.

Lakes, R., and Wineman, A. (2006). "On poisson's ratio in linearly viscoelastic solids." *Journal of Elasticity*, 85(1), 45-63.

Lashkari, A., and Latifi, M. (2007). "A simple plasticity model for prediction of non-coaxial flow of sand." *Mechanics Research Communications*, 34(2), 191-200.

Lee, H.-J., and Kim, Y. R. (1998). "Viscoelastic constitutive model for asphalt concrete under cyclic loading." *Journal of Engineering Mechanics*, 124(1), 32-40.

Lemaitre, J., and Desmorat, R. (2005). *Engineering damage mechanics: Ductile, creep, fatigue and brittle failures*, Springer, LLC, New York, NY.

Levenberg, E., and Shah, A. (2008). "Interpretation of complex modulus test results for asphalt-aggregate mixes." *Journal of Testing and Evaluation*, 36(4), 326-334.

Levenberg, E., and Uzan, J. (2004). "Triaxial small-strain viscoelastic-viscoplastic modeling of asphalt aggregate mixes." *Mechanics of Time-Dependent Materials*, 8(4), 365-384.

Li, Q., Lee, H. J., and Lee, S. Y. (2011). "Permanent deformation model based on shear properties of asphalt mixtures: Development and calibration." *Transportation Research Record: Journal of the Transportation Research Board*, No. 2210, Transportation Research Board of the National Academies, Washington, DC., 81-89.

Li, X., and Dafalias, Y. F. (2002). "Constitutive modeling of inherently anisotropic sand behavior." *Journal of Geotechnical and Geoenvironmental Engineering*, 128(10), 868-880.

Li, X. S. (2002). "A constitutive platform for sand modeling." *15th ASCE Engineering Mechanics Conference*, Columbia University, New York, NY, 47-54.

Lin, F.-B., and Bazant, Z. P. (1986). "Convexity of smooth yield surface of frictional material." *Journal of Engineering Mechanics*, 112(11), 1259-1262.

Loukidis, D., and Salgado, R. (2009). "Modeling sand response using two-surface plasticity." *Computers and Geotechnics*, 36(1-2), 166-186.

Lu, Y., and Wright, P. J. (1998). "Numerical approach of visco-elastoplastic analysis for asphalt mixtures." *Computers & Structures*, 69(2), 139-147.

Luo, R., and Lytton, R. L. (2010). "Characterization of the tensile viscoelastic properties of an undamaged asphalt mixture." *Journal of Transportation Engineering*, 136(3), 173-180.

Lytton, R. L. (2000). "Characterizing asphalt pavements for performance." *Transportation Research Record: Journal of the Transportation Research Board*, No. 1723, Transportation Research Board of the National Academies, Washington, DC., 5-16.

Lytton, R. L., Uzan, J., Fernando, E. G., Roque, R., Hiltunen, D., and Stoffels, S. (1993). "Development and validation of performance prediction models and specifications for asphalt binders and paving mixes." The Strategic Highway Research Program Report No. SHRP-A-357, National Research Council, Washington, DC.

Mahboub, K. (1990). "Asphalt concrete creep as related to rutting." *Journal of Materials in Civil Engineering*, 2(3), 147-163.

Maiolino, S. (2005). "Proposition of a general yield function in geomechanics." *Comptes Rendus Mecanique*, 333(3), 279-284.

Maiolino, S., and Luong, M. P. (2009). "Measuring discrepancies between coulomb and other geotechnical criteria : Drucker-prager and matsuoka-nakai." *Proc. of 7th Euromech Solid Mechanics Conference*, Lisbon, Portugal, 1-12.

Mamlouk, M. S., Witczak, M. W., Kaloush, K. E., and Ho, Y. S. (2002). "Effect of anisotropy on compressive and tensile properties of asphalt mixtures." *Journal of Testing and Evaluation*, 30(5), 432-438.

Marasteanu, M. O., and Anderson, D. A. (1999). "Improved model for bitumen rheological characterization." *Eurobitume Workshop on Performance Related Properties for Bituminous Binders*, Luxembourg, Paper No. 133.

Masad, E., and Button, J. W. (2004). "Implications of experimental measurements and analyses of the internal structure of hot-mix asphalt." *Transportation Research Record: Journal of the Transportation Research Board*, No. 1891, Transportation Research Board of the National Academies, Washington, DC., 212-220.

Masad, E., Castelo Branco, V. T. F., Little, D. N., and Lytton, R. (2008a). "A unified method for the analysis of controlled-strain and controlled-stress fatigue testing." *International Journal of Pavement Engineering*, 9(4), 233-246.

Masad, E., Dessouky, S., and Little, D. (2007). "Development of an elastoviscoplastic microstructural-based continuum model to predict permanent deformation in hot mix asphalt." *International Journal of Geomechanics*, 7(2), 119-130.

Masad, E., Huang, C.-W., Airey, G., and Muliana, A. (2008b). "Nonlinear viscoelastic analysis of unaged and aged asphalt binders." *Construction and Building Materials*, 22(11), 2170-2179.

Masad, E., Huang, C.-W., D'Angelo, J., and Little, D. (2009). "Characterization of asphalt binder resistance to permanent deformation based on nonlinear viscoelastic analysis of multiple stress creep recovery (mscr) test." *Journal of the Association of Asphalt Paving Technologists*, 78, 535-562.

Masad, E., Muhunthan, B., Shashidhar, N., and Harman, T. (1998). "Aggregate orientation and segregation in asphalt concrete." *Application of geotechnical principles in pavement engineering*, A. T. Papagiannakis, and C. W. Schwartz, Boston, MA, USA, 69-80.

Masad, E., Tashman, L., Little, D., and Zbib, H. (2005). "Viscoplastic modeling of asphalt mixes with the effects of anisotropy, damage and aggregate characteristics." *Mechanics of Materials*, 37(12), 1242-1256.

Masad, E., Tashman, L., Somedavan, N., and Little, D. (2002). "Micromechanics-based analysis of stiffness anisotropy in asphalt mixtures." *Journal of Materials in Civil Engineering*, 14(5), 374-383.

Matsuoka, H., and Nakai, T. (1974). "Stress-deformation and strength characteristics of soil under three different principal stresses." *Proc. of Japan Society of Civil Engineers*, 59-70.

Matsuoka, H., and Nakai, T. (1985). "Relationship among tresca, mises, mohr-coulomb and matsuoka-nakai failure criteria." *Soils and Foundations*, 25(4), 123-128.

MediaCybernetics (2000). "Image-pro plus." Media Cybernetics, Rockville, Maryland.

Mirza, M., Graul, R., Groeger, J., and Lopez, A. (1997). "Theoretical evaluation of poisson's ratio and elastic modulus using indirect tensile test with emphasis on bituminous mixtures." *Transportation Research Record: Journal of the Transportation Research Board*, No. 1590, Transportation Research Board of the National Academies, Washington, D.C., 34-44.

Mortara, G. (2008). "A new yield and failure criterion for geomaterials." *Geotechnique*, 58(2), 125-132.

Motola, Y., and Uzan, J. (2007). "Anisotropy of field-compacted asphalt concrete material." *Journal of Testing and Evaluation*, 35(1), 103-105.

Muraya, P. M., Molenaar, A. A. A., and van de Ven, M. F. C. (2009). "Contribution of asphalt mix components to permanent deformation resistance." *Proc. of 8th International Conference on the Bearing Capacity of Roads, Railways and Airfields*, Champaign, IL, 259-268.

Nguyen, D. T., Nedjar, B., and Tamagny, P. (2007). "Cyclic elasto-viscoplastic model for asphalt concrete materials." *Road Materials and Pavement Design*, 8(2), 239-255.

Oda, M. (1993). "Inherent and induced anisotropy in plasticity theory of granular soils." *Mechanics of Materials*, 16(1-2), 35-45.

Oda, M., and Nakayama, H. (1989). "Yield function for soil with anisotropic fabric." *Journal of Engineering Mechanics*, 115(1), 89-104.

Oh, J., Lytton, R. L., and Fernando, E. G. (2006). "Modeling of pavement response using nonlinear cross-anisotropy approach." *Journal of Transportation Engineering*, 132(6), 458-468.

Paris, P. C., and Erdogan, F. (1963). "A critical analysis of crack propagation laws." *Journal of Basic Engineering*, Transaction, American Society of Mechanical Engineers, Series D, (85), 528-534.

Park, D., Martin, A., Lee, H., and Masad, E. (2005). "Characterization of permanent deformation of an asphalt mixture using a mechanistic approach." *KSCE Journal of Civil Engineering*, 9(3), 213-218.

Park, S. W., Kim, Y. R., and Schapery, R. A. (1996). "Viscoelastic continuum damage model and its application to uniaxial behavior of asphalt concrete." *Mechanics of Materials*, 24(4), 241-255.

Park, S. W., and Schapery, R. A. (1999). "Methods of interconversion between linear viscoelastic material functions. Part i - a numerical method based on prony series." *International Journal of Solids and Structures*, 36(11), 1653-1675.

Pellinen, T. K., Xiao, S., Carpenter, S., Masad, E., Di Benedetto, H., and Roque, R. (2005). "Relationship between triaxial shear strength and indirect tensile strength of hot mix asphalt." *Journal of the Association of Asphalt Paving Technologists*, 74, 347-379.

Perl, M., Uzan, J., and Sides, A. (1983). "Visco-elasto-plastic consititutive law for a bituminous mixture under repeated loading." *Transportation Research Record: Journal of the Transportation Research Board*, No. 911, Transportation Research Board of the National Academies, Washington, DC., 20-27.

Perzyna, P. (1971). "Thermodynamic theory of viscoplastcity." *Advances in Applied Mechanics*, 11, 313-354.

Pickering, D. J. (1970). "Anisotropic elastic parameters for soil." *Geotechnique*, 20(3), 271-276.

Qi, X., and Witczak, M. W. (1998). "Time-dependent permanent deformation models for asphaltic mixtures." *Transportation Research Record*, No. 1639, Transportation Research Board of the National Academies, Washington, DC., 83-93.

Rabotnov, Y. N. (1969). *Creep problems in structural members*, North-Holland, Amsterdam, The Netherlands.

Ramos-Aparicio, S. I. (2004). "Study of the asphalt pavement damage through nondestructive testing on overweight truck routes." M.Sc. Dissertation, Texas A&M University, College Station, Texas.

Ramsamooj, D. V., and Ramadan, J. (1999). "Prediction of permanent deformation of asphalt concrete in cyclic and monotonic loading." *Journal of Testing and Evaluation*, 27(5), 320-326.

Reys, O. M. (1991). "Experimental study and analytical modeling of compressive fracture in brittle materials." Ph.D. Dissertation, Massachusetts Institute of Technology, Cambridge, MA.

Rodezno, M. C., Kaloush, K. E., and Corrigan, M. R. (2010). "Development of a flow number predictive model." *Transportation Research Record: Journal of the*

Transportation Research Board, No. 2181, Transportation Research Board of the National Academies, Washington, DC, 79-87.

Saadeh, S., Masad, E., and Little, D. (2007). "Characterization of asphalt mix response under repeated loading using anisotropic nonlinear viscoelastic-viscoplastic model." *Journal of Materials in Civil Engineering*, 19(10), 912-924.

Schapery, R. A. (1965). "A method of viscoelastic stress analysis using elasitic solutions." *Journal of the Franklin Institute-Engineering and Applied Mathematics*, 279(4), 268-289.

Schapery, R. A. (1969). "On the characterization of nonlinear viscoelastic materials." *Polymer Engineering & Science*, 9(4), 295-310.

Schapery, R. A. (1975). "Theory of crack initiation and growth in viscoelastic media - II. Approximate methods of analysis." *International Journal of Fracture*, 11(3), 369-388.

Schapery, R. A. (1984). "Correspondence principles and a generalized J-integral for large deformation and fracture analysis of viscoelastic media." *International Journal of Fracture*, 25(3), 195-223.

Schapery, R. A. (1997). "Nonlinear viscoelastic and viscoplastic constitutive equations based on thermodynamics." *Mechanics of Time-Dependent Materials*, 1(2), 209-240.

Schapery, R. A. (1999). "Nonlinear viscoelastic and viscoplastic constitutive equations with growing damage." *International Journal of Fracture*, 97(1-4), 33-66.

Schapery, R. A., and Park, S. W. (1999). "Methods of interconversion between linear viscoelastic material functions. Part II - an approximate analytical method." *International Journal of Solids and Structures*, 36(11), 1677-1699.

Schwartz, C. W., Gibson, N. H., Schapery, R. A., and Witczak, M. W. (2004). "Viscoplasticity modeling of asphalt concrete behavior." *Proc. of Recent Advances in Materials Characterization and Modeling of Pavement Systems*, New York, NY., United states, 144-159.

Seibi, A., Sharma, M., Ali, G., and Kenis, W. (2001). "Constitutive relations for asphalt concrete under high rates of loading." *Transportation Research Record: Journal of the Transportation Research Board*, No. 1767, Transportation Research Board of the National Academies, Washington, D.C., 111-119.

Si, Z., Little, D. N., and Lytton, R. L. (2002). "Characterization of microdamage and healing of asphalt concrete mixtures." *Journal of Materials in Civil Engineering*, 14(6), 461-470.

Sides, A., Uzan, J., and Perl, M. (1985). "A comprehensive visco-elastoplastic characterization of sand-asphalt under compression and tension cyclic loading." *Journal of Testing and Evaluation*, 13(1), 49-59.

Sousa, J., Weissman, S. L., Sackman, J. L., and Monismith, C. L. (1993). "A nonlinear elastic viscous with damage model to predict permanent deformation of asphalt concrete mixtures." *Transportation Research Record: Journal of the Transportation Research Board*, No. 1384, Transportation Research Board of the National Academies, Washington, D.C., 80-93.

Sousa, J. B., and Weissman, S. L. (1994). "Modeling permanent deformation of asphalt-aggregate mixes." *Journal of Association of Asphalt Paving Technologists*, 63, 224-224.

Sullivan, R. (2008). "Development of a viscoelastic continuum damage model for cyclic loading." *Mechanics of Time-Dependent Materials*, 12(4), 329-342.

Tan, S.-A., Low, B.-H., and Fwa, T.-F. (1994). "Behavior of asphalt concrete mixtures in triaxial compression." *Journal of Testing and Evaluation*, 22(3), 195-203.

Tashman, L., Masad, E., Little, D., and Zbib, H. (2005a). "A microstructure-based viscoplastic model for asphalt concrete." *International Journal of Plasticity*, 21(9), 1659-1685.

Tashman, L., Masad, E., Peterson, B., and Saleh, H. (2002). "Internal structure analysis of asphalt mixes to improve the simulation of superpave gyratory compaction to field conditions." *Journal of Association of Asphalt Paving Technologists*, 70, 605-645.

Tashman, L., Masad, E., Zbib, H., Little, D., and Kaloush, K. (2004). "Anisotropic viscoplastic continuum damage model for asphalt mixes." *Proc. of Recent Advances in Materials Characterization and Modeling of Pavement Systems in the 15th Engineering Mechanics Division Conference*, New York, NY, 111-125.

Tashman, L., Masad, E., Zbib, H., Little, D., and Kaloush, K. (2005b). "Microstructural viscoplastic continuum model for permanent deformation in asphalt pavements." *Journal of Engineering Mechanics*, 131(1), 48-57.

Tobita, Y. (1989). "Fabric tensors in constitutive equations for granular materials." *Soils and Foundations*, 29(4), 91-104.

Tobita, Y., and Yanagisawa, E. (1988). "Contact tensor in constitutive model for granular materials." *Micromechanics of Granular Materials*, 263-270.

Tobita, Y., and Yanagisawa, E. (1992). "Modified stress tensors for anisotropic behavior of granular materials." *Soils and Foundations*, 32(1), 85-99.

Tschoegl, N. W., Knauss, W. G., and Emri, I. (2002). "Poisson's ratio in linear viscoelasticity - a critical review." *Mechanics of Time-Dependent Materials*, 6(1), 3-51.

Tseng, K. H., and Lytton, R. L. (1989). "Prediction of permanent deformation in flexible pavement materials." *Implication of aggregates in the design, construction, and performance of flexible pavements*, H. G. Schreuders, and C. R. Marek, American Society for Testing and Materials (ASTM), Philadelphia, 154-172.

TxDOT (2004). "Standard specifications for construction and maintenance of highways, streets, and bridges." Texas Department of Transportation, Austin, TX.

TxDOT (2008). "Test procedure for design of bituminous mixtures." TxDOT designation: Tex-204-F, Texas Department of Transportation, Austin, TX.

Underwood, S., Heidari, A., Guddati, M., and Kim, Y. (2005). "Experimental investigation of anisotropy in asphalt concrete." *Transportation Research Record: Journal of the Transportation Research Board*, No. 1929, Transportation Research Board of the National Academies, Washington, D.C., 238-247.

Uzan, J. (1996). "Asphalt concrete characterization for pavement performance prediction." *Journal of Association of Asphalt Paving Technologists*, 65, 573-607.

Van Eekelen, H. A. M. (1980). "Isotropic yield surfaces in three dimensions for use in soil mechanics." *International Journal for Numerical and Analytical Methods in Geomechanics*, 4(1), 89-101.

Wagoner, M., and Braham, A. (2008). "Anisotropic behavior of hot-mix asphalt at low temperatures." *Transportation Research Record: Journal of the Transportation Research Board*, No. 2057, Transportation Research Board of the National Academies, Washington, D.C., 83-88.

Walubita, L. F., Martin, A. E., Cleveland, G. S., and Lytton, R. L. (2006). "Computation of pseudo strain energy and paris law fracture coefficients from surface energy and uniaxial strain-controlled tension test data." *International Journal of Pavement Engineering*, 7(3), 167 - 178.

Wang, L., Hoyos, L. R., Wang, J., Voyiadjis, G., and Abadie, C. (2005). "Anisotropic properties of asphalt concrete: Characterization and implications for pavement design and analysis." *Journal of Materials in Civil Engineering*, 17(5), 535-543.

Wen, H., and Bahia, H. (2009). "Characterizing fatigue of asphalt binders with viscoelastic continuum damage mechanics." *Transportation Research Record: Journal of the Transportation Research Board*, No. 2126, Transportation Research Board of the National Academies, Washington, DC., 55-62.

Wineman, A. S., and Rajagopal, K. R. (2001). *Mechanical response of polymers, An introduction*, Cambridge University Press, New York, NY.

Witczak, M. W., Bonaquist, R., Von Quintus, H., Kaloush, K., and Aapt, A. A. (2000). "Specimen geometry and aggregate size effects in uniaxial compression and constant height shear tests." *Journal of the Association of Asphalt Paving Technologists*, 69, 733-793.

Witczak, M. W., Kaloush, K., Pellinen, T., and El-Basyouny, M. (2002). "Simple performance test for superpave mix design." *National Cooperative Highway Research Program (NCHRP) Report 465*, Transportation Research Board, National Research Council, Washington, D.C.

Wong, R. K. S., and Arthur, J. R. F. (1985). "Induced and inherent anisotropy in sand." *Geotechnique*, 35(4), 471-481.

Yang, Z. X., Lit, X. S., and Yang, J. (2008). "Quantifying and modelling fabric anisotropy of granular soils." *Geotechnique*, 58(4), 237-248.

Ye, J., Wu, F. Q., and Sun, J. Z. (2009). "Estimation of the tensile elastic modulus using brazilian disc by applying diametrically opposed concentrated loads." *International Journal of Rock Mechanics and Mining Sciences*, 46(3), 568-576.

Yoshimine, M., Ishihara, K., and Vargas, W. (1998). "Effects of principal stress direction and intermediate principal stress on undrained shear behavior of sand." *Soils and Foundations*, 38(3), 179-188.

You, Z., and Buttlar, W. G. (2004). "Discrete element modeling to predict the modulus of asphalt concrete mixtures." *Journal of Materials in Civil Engineering*, 16(2), 140-146.

Yun, T., and Kim, Y. R. (2011). "A viscoplastic constitutive model for hot mix asphalt in compression at high confining pressure." *Construction and Building Materials*, 25(5), 2733-2740.

Zhang, W., Drescher, A., and Newcomb, D. E. (1997). "Viscoelastic analysis of diametral compression of asphalt concrete." *Journal of Engineering Mechanics*, 123(6), 596-603.

Zhang, Y., Luo, R., and Lytton, R. L. (2011). "Microstructure-based inherent anisotropy of asphalt mixtures." *Journal of Materials in Civil Engineering*, 23(10), 1473-1482.

Zhang, Y., Luo, R., and Lytton, R. L. (2012a). "Anisotropic viscoelastic properties of undamaged asphalt mixtures." *Journal of Transportation Engineering*, 138(1), 75-89.

Zhang, Y., Luo, R., and Lytton, R. L. (2012b). "Characterizing permanent deformation and fracture of asphalt mixtures by using compressive dynamic modulus tests." *Journal of Materials in Civil Engineering*, 24(7), 898-906.

Zhang, Y., Luo, R., and Lytton, R. L. (2012c). "Mechanistic modeling of fracture in asphalt mixtures under compressive loading." *Journal of Materials in Civil Engineering*, American Society of Civil Engineers (ASCE), In Press, Available at: http://dx.doi.org/10.1061/(ASCE)MT.1943-5533.0000667.

Zhao, Y., and Kim, Y. R. (2003). "Time-temperature superposition for asphalt mixtures with growing damage and permanent deformation in compression." *Transportation Research Record: Journal of the Transportation Research Board*, No. 1832, Transportation Research Board of the National Academies, Washington, D.C., 161-172.

Zhou, F., and Scullion, T. (2002). "Discussion: Three stages of permanent deformation curve and rutting model." *International Journal of Pavement Engineering*, 3(4), 251-260.

Zhou, F., Scullion, T., and Sun, L. (2004). "Verification and modeling of three-stage permanent deformation behavior of asphalt mixes." *Journal of Transportation Engineering*, 130(4), 486-494.